AGEING CHARACTERISTICS OF

COPPER BASED SHAPE MEMORY ALLOYS

A THESIS SUBMITTED TO

THE GRADUATE SCHOOL OF NATURAL AND APPLIED SCIENCES

OF

THE MIDDLE EAST TECHNICAL UNIVERSITY

BY

ELİF TARHAN

IN PARTIAL FULFILLMENT OF THE REQUIREMENTS FOR THE DEGREE OF

DOCTOR OF PHILOSOPHY

IN

THE DEPARTMENT OF METALLURGICAL AND MATERIALS ENGINEERING

JANUARY 2004

Approval of the Graduate School of Natural and Applied Sciences.

Prof. Dr. Canan ÖZGEN
Director

I certify that this thesis satisfies all the requirements as a thesis for the degree of Doctor of Philosophy.

Prof. Dr. Bilgehan ÖGEL
Head of Department

We certify that we have read this thesis and in our opinion it is fully adequate, in scope and quality, as a thesis for the degree of Doctor of Philosophy.

Prof. Dr. Şakir BOR
Supervisor

Examining Committee Members:

Prof. Dr. Bilgehan ÖGEL

Prof. Dr. Bülent DOYUM

Assoc. Prof. Dr. Tamer ÖZDEMİR

Assoc. Prof. Dr. Kadri AYDINOL

Prof. Dr. Şakir BOR

ABSTRACT

AGEING CHARACTERISTICS OF
COPPER BASED SHAPE MEMORY ALLOYS

Tarhan, Elif

Ph.D., Department of Metallurgical and Materials Engineering

Supervisor: Prof. Dr. Şakir Bor

January 2004, 215 pages

Martensite$\leftrightarrows$Beta transformation temperatures of CuAlNiMn and CuAlNi shape memory alloys has been determined by differential scanning calorimetry (DSC). In CuAlNiMn alloys, each new betatizing treatment has resulted in randomly varying transformation temperatures on the same specimen and an anomalously diffuse and serrated Martensite$\rightarrow$Beta transformation peaks in the first cycle. Therefore, as quenched alloy samples were thermally cycled for three times in DSC prior to ageing to obtain thermally stable and reproducible transformation temperatures and to eliminate the anomalous effect of betatizing on the transformation temperatures.

CuAlNiMn alloys were aged in martensitic condition at temperatures in the range 80°C to 150°C for 24 hours to 312 hours ageing periods. Both A_s and A_f temperatures have increased with ageing temperature and time while M_s and M_f temperatures have not changed during martensite ageing. Transformation temperatures of CuAlNi alloys, on the other hand, have not changed during martensite ageing. In this respect, CuAlNiMn alloys were found to be more prone to martensite stabilization than the CuAlNi alloys. Through Transmission Electron

iii

Microscope investigation in the Cu-12.6wt%Al-5.9wt%Ni-1.8wt%Mn alloy aged at 150°C for 312 hours has revealed no sign of precipitate formation and it has been concluded that the "precipitates pinning martensite boundaries" mechanism could not be responsible of martensite stabilization.

Beta phase ageing of CuAlNiMn alloys at temperatures 200°C, 230°C, 250°C and 270°C, have drastically shortened the periods for stabilization to the extent that β→M transformation completely ceases. With regard to the Manganese content, highest Manganese bearing alloy was the one stabilized first and the lowest manganese containing one was the longest lasting alloy during beta phase ageing. Beta stabilization was not observed in any of the four CuAlNi alloys at the end of 96 hours ageing at 200°C while beta stabilization was realized after 26, 38 and 11 hours ageing at the same temperature in the three Mn containing alloys studied. In conclusion, on the basis of ageing studies at 200°C, with regard to beta stabilization, CuAlNi alloys were found to be more resistant to high temperature ageing than CuAlNiMn alloys.

Equilibrium γ_2 and α phases were observed with coupled-grown lamellar morphologies in Cu-13.6%Al-3.0%Ni alloy aged above 400°C.

Keywords: CuAlNiMn and CuAlNi shape memory alloys, Ageing, Martensite Stabilization, Beta stabilization, Differential Scanning Calorimetry, Transmission Electron Microscopy.

ÖZ

BAKIR ESASLI HAFIZALI ALAŞIMLARDA
YAŞLANMA DAVRANIŞI

Tarhan Elif

Doktora, Metalurji ve Malzeme Mühendisliği Bölümü

Tez Yöneticisi: Prof. Dr. Şakir Bor

Ocak 2004, 215 sayfa

CuAlNiMn ve CuAlNi hafızalı alaşımlarının Martensit⇆Beta dönüşüm sıcaklıkları Diferansiyel Taramalı Kalorimetri (DSC) yöntemiyle belirlenmiştir. CuAlNiMn alaşımlarında, her yeni betalaştırma işleminin aynı numunede rastgele değişen dönüşüm sıcaklıklarına ve birinci döngüdeki martensit→beta dönüşüm eğrisinde yayılma ve tırtıklanmalara sebep olduğu görülmüştür. Bu durumda, ısıl olarak kararlı ve tekrarlanabilir dönüşüm sıcaklıkları elde etmek ve betalaştırma işleminin dönüşüm sıcaklıklarında yarattığı beklenmedik düzensizlikleri ortadan kaldırmak için su verilmiş alaşımlar yaşlandırma çalışmaları öncesinde üç ısıl döngüye tabii tutulmuşlardır.

CuAlNiMn alaşımları martensit fazındayken, 80°C ile 150°C sıcaklık aralığında 24 saatten 312 saate kadar sürelerde yaşlandırılmışlardır. Artan yaşlanma sıcaklığı ve süresiyle A_s ve A_f sıcaklıklarının her ikisi de artarken, M_s ve M_f sıcaklıklarında bir değişiklik olmamıştır. Diğer taraftan, CuAlNi alaşımlarının dönüşüm sıcaklıkları martensit yaşlanması sırasında değişmemiştir. Bu açıdan, CuAlNi alaşımlarına oranla, CuAlNiMn alaşımlarında martensitin kararlılaşma eğilimi daha yüksektir.

150°C sıcaklıkta 312 saat süreyle yaşlandırılmış olan Cu-12.6wt%Al-5.9wt%Ni-1.8wt%Mn alaşımında yapılan geçirimli elektron mikroskop incelemeleri herhangi bir ikinci faz oluşumu göstermemiştir ve bu doğrultuda "ikinci faz parçalarının martensit sınırlarını kitlemesi" mekanizmasının martensit kararlılığından sorumlu olamayacağı sonucuna varılmıştır.

CuAlNiMn alaşımlarının 200°C, 230°C, 250°C and 270°C sıcaklıklarda beta fazında iken yaşlandırılmaları, Beta→martensit dönüşümünün tamamen durmasına yol açan bir kararlılık yaratarak bu alaşımların ömürlerini çok kısaltmıştır. Mangan içeriği bakımından, beta yaşlanması sırasında en fazla mangan içeren alaşım ilk kararlılaşan, en az mangan içeren alaşım ise en uzun süre dayanan alaşım olmuşlardır. 200°C'de 96 saat süreyle yaşlandırılan CuAlNi alaşımlarının hiçbirinde beta kararlılığı gözlenmemiş olması, bu alaşımların, 200°C'de 26, 38 ve 11 saatler sonunda beta kararlılaşmasına uğrayan Manganlı alaşımlara kıyasla oldukça daha dayanıklı olduğunu göstermektedir. Sonuçta, 200°C beta yaşlanması çalışmaları esasına dayanarak, CuAlNi alaşımlarının CuAlNiMn alaşımlarına göre yüksek sıcaklık yaşlanmasına daha dayanıklı olduğu söylenebilir.

400°C üzerinde yaşlandırılmış Cu-13.6%Al-3.0%Ni alloy alaşımında, γ_2 ve α denge fazlarının birlikte büyümüş lamellar morfolojide oldukları gözlenmiştir.

Anahtar Kelimeler: CuAlNiMn ve CuAlNi hafızalı alaşımları, yaşlanma, martensit kararlılığı, beta kararlılığı, Diferansiyel Taramalı Kalorimetri, Geçirimli Elektron Mikroskobu.

ACKNOWLEDGEMENTS

TABLE OF CONTENTS

CHAPTER 1

INTRODUCTION

In the last twenty years, considerable effort has been devoted to the study of ageing in copper based shape memory alloys since the shape memory performance is directly affected from the stabilization of both parent and martensite phases. Copper Based shape memory alloys are susceptible to low temperature ageing effects; variations in transformation temperatures i.e. A_s, M_s, and poor martensite reversibility are the common changes resulting from time dependent changes during ageing. Therefore, during service ageing induced changes alter the reproducibility and reliability of the alloys and hence limit their practical applications. For a reliable shape memory alloy in temperature sensitive component applications, alloy is expected to be stable, thus transformation temperatures should not change with shape memory cycles or with the holding duration in the martensitic condition. Consequently, the understanding of the ageing mechanism is not only an academic interest but also necessary to provide a better control and the development of those alloys for engineering applications.

Some of the common features of ageing phenomena in copper-based shape memory alloys are such that ageing is a time-dependent diffusional process and very sensitive to point defects. Furthermore, some structural changes in martensite such as long range order change are experimentally verified. Copper-based martensites are non-equilibrium phases, which can be obtained only by quenching and have ordered structures.

An as quenched alloy having subzero M_s temperature is in parent phase after betatizing and quenching to room temperature. It has been observed that in such alloys, ageing around room temperature results in a decrease in M_s temperature. Due to decreased M_s temperature, parent phase cannot transform into martensite upon cooling hence parent phase is said to be stabilized. For this phenomenon, known as parent phase stabilization, two mechanisms may be responsible; either ordering of the incompletely ordered parent phase due to quenching or formation of precipitates due to ageing.

Martensite stabilization is the increase of the stability of martensite with respect to the parent phase during ageing below M_s temperature. Significant rise of A_s and A_f temperatures during ageing prevents reversion of martensite back into parent phase upon heating. Martensite stabilization is a time and temperature dependent diffusional process that is accelerated by high concentration of quenched-in vacancies. Degree of stabilization is closely related to quenching conditions such that strong martensite stabilization induced after direct quenching is attributed to excess quenched-in vacancies and the increase in A_s and A_f temperatures is the measure of degree of martensite stabilization.

Grain size, alloy composition, lattice defects and heat treatments applied are some factors affecting stabilization. Fine grained materials are recognized to be less susceptible to stabilization due to higher proportion of grain boundaries acting as effective sinks for vacancies. Alloy composition is also critical in stabilization. In CuZnAl alloys for example, low Aluminium content accelerates α precipitation due to higher supersaturation while high Al content accelerates γ precipitation again because of higher supersaturation. It is well known that CuAlNi alloys are less prone to stabilization than CuZnAl alloys. The lower mobility of vacancies and the difficulty of formation of vacancy clusters in CuAlNi martensite making it less susceptible to stabilization may be related to the stronger bonding force between Al and Ni atoms. Lattice defects such as dislocations inhibit stabilization simply by acting as sinks for vacancies and reducing their amount and contribution to

2

diffusion. The purpose of application of a special heat treatment known as step quenching is to reduce the amount of excess quenched-in vacancies. The basis of stabilization control is simply elimination of the effects of the excess quenched-in vacancies.

In literature, two basic mechanisms are offered as possible origins of martensite stabilization. The first one is the model based on pinning of interfaces between parent and martensite phases and/or martensite variant boundaries by quenched-in vacancies and/or precipitates. Due to pinning of boundaries, an extra driving force is required for $M\rightarrow\beta$ transformation upon heating and to provide this extra driving force A_s and A_f temperatures increased. Actually, pinning mechanism does not cause a relative energy change between martensite and parent phases. The second mechanism is the models based on structural changes or atomic rearrangements in martensite. In the aged martensite structural changes such as long range order change, short range order change or reordering in martensite result in decreased energy of martensite as compared to parent phase and this causes an increase in A_s and A_f temperatures.

Since martensite stabilization is a diffusion-assisted phenomenon accelerated by quenched-in vacancies, methods for inhibition of stabilization are based on the principle to decrease the extent of diffusion by reducing vacancies. A usual way to avoid stabilization due to direct quenching is to perform quenching in a stepwise manner. By step quenching the quenched-in vacancies are annihilated and the optimum step quenching temperature range, which is below DO_3 ordering temperature and above M_s temperature, provides accomplishment of DO_3 ordering. Besides step quenching, hot rolling and thermal cycling are the other methods offered to inhibit stabilization. By hot rolling and thermal cycling dislocations introduced are as effective sinks for vacancies. Dislocations introduced by thermal cycling establish favoured nucleation sites for thermoelastic martensite through repeated thermal cycling. Changes in transformation temperatures reach saturation after a certain number of cycles so thermal cycling may be used in inhibition of

stabilization to a certain extent. Unfortunately, the importance of subjects on the early thermal cycling effects and the first cycle anomalies that are playing significant roles in stabilization of alloys are not given attention in literature. That is why these subjects are emphasized in the present study.

CuAlNi alloys, which are less prone to martensite stabilization, have found only limited application because of insufficient formability due to the brittle γ_2 precipitates. To increase formability of CuAlNi alloys, γ_2 precipitates are suppressed by decreasing Al content to 12%. Increase in M_s temperature due to the decrease in Al content has been compensated by addition of alloying elements such as Ni and Mn. Cu-Al-Ni-Mn-Ti alloys known by an acronym CANTIM, were introduced as potential candidates for high temperature shape memory alloy applications in the 1990's.

In this study, the ageing characteristics of CuAlNiMn and CuAlNi alloys has been investigated with emphasis on martensite stabilization effect to evaluate their suitability for high temperature shape memory applications. Precipitation of CuAlNiMn alloys in the martensitic matrix has been examined extensively at 150°C while precipitation of CuAlNi alloys in the beta phase at relatively higher temperatures, 200°C-400°C, has been to a limited extent by Transmission Electron Microscopy. Transformation temperatures of alloys prior to and latter to ageing have been determined by Differential Scanning Calorimetry. In addition to expected transformation temperature changes as a consequence of martensite ageing, unexpected transformation temperature changes after the routine betatizing treatment and anomalous effects upon application of three thermal cycles just after betatizing have been observed. Therefore, the study has focused on anomalous effects of betatizing and early thermal cycling on transformation temperatures of CuAlNiMn alloys in addition to the studies on the basis of martensite stabilization effect. Unsystematic changes in the transformation temperatures of the pre-aged alloys and the anomalous effects in early cycles have prevented the detailed understanding of the mechanisms except disproving the famous "precipitates

4

pinning martensite boundaries" proposal for martensite stabilization in CuAlNiMn alloys. Atomic rearrangements in martensite might be the reason of martensite stabilization but the question "exactly which structural change" has remained unanswered.

The previous experimental observations and predicted mechanisms on both parent and martensite stabilization of copper-based shape memory alloys resulting from ageing and the methods to inhibit stabilization are reviewed in Chapter Two. Chapter Three introduces the experimental technique. Experimental results are evaluated and discussed in Chapter Four. The concluding remarks are presented in Chapter Five. Finally, suggestions for future work are summarized in Chapter Six.

CHAPTER 2

THEORY

2.1. Shape Memory Effect in Copper-Based Alloys:

Shape memory alloys (SMA) employed in smart structures have found wide spread applications throughout the world during the last twenty years. Alloys undergoing thermoelastic martensitic transformations exhibit two unusual effects, namely Shape Memory Effect and Pseudoelasticity, because of the crystallographic reversibility of thermoelastic martensite. The shear nature of transformation provides that martensitic transformations can be induced either by undercooling or by application of stress. If a macroscopic deformation is applied when the material is in the martensitic state, and then the temperature is raised, the plastic strain will recover upon heating and the material will return back to its original shape. This phenomenon is called as Shape Memory Effect. The pseudoelastic behavior is a complete mechanical analogue of the shape memory effect. In this case, when the material is in the parent phase, martensitic transformation proceeds by the increasing stress and reverses continuously when the applied stress is reduced. Unloading will cause the material to revert to its original shape in a way similar to that in shape memory effect.

For a complete shape memory effect to occur the necessary condition is that the martensitic transformation must be crystallographically reversible, i.e.,

thermoelastic in nature. One of the main reasons for the reversibility of thermoelastic martensites is that there are inherently low elastic strains associated with the crystal structure change, so that the elastic limit of the parent phase is not exceeded and irreversible plastic deformation does not occur. Furthermore, the strains, which do build up as the martensite plates grow, are effectively cancelled out by forming groups of mutually accommodating plates. In addition, the individual plates themselves are internally twinned or faulted to accommodate the transformation strains. Thermoelastic martensites are soft and ductile since they deform by movement of twin or variant boundaries, which are not stabilized due to low shape strains. The boundaries do not posses elastic strain fields to interact and make their motion difficult. Additionally, twin boundaries are very low energy, high mobility interfaces. Total energy change in low hysteresis thermoelastic martensitic transformations can be characterized by the compromise between the Gibbs free energy change driving the transformation and the inhibiting elastic strain energy term. Once martensite crystals are nucleated below M_s temperature they grow at a velocity proportional to the cooling rate as the specimen is cooled. However, after reaching a certain size, when the decrease in Gibbs energy is counterbalanced by the increasing elastic strain energy due to growing plate, the growth is arrested. Once this thermal equilibrium has been attained, if specimen is further heated or cooled or external force is applied, the thermal equilibrium will be disrupted and martensite crystals once again begin either to grow or shrink. Besides the reversibility criterion, the other criteria necessary for a complete shape memory effect are that the lattice invariant deformation occurs by twinning rather than by slip and finally the martensite is formed from an ordered parent phase. Both conditions provides high resistance to slip yielding and supports the main reversibility condition of thermoelastic martensitic transformation whose major advantage is the absence of plastic yielding during accommodation of the shape deformation.

Even when the parent phase is a single crystal, number of martensites with different but crystallographically equivalent habit plane indices called, as variants will appear

throughout the specimen in a thermoelastic martensitic transformation. The basal plane of long period stacking order martensite originates from one of the {110} planes of the parent phase and that the inhomogeneous shear during transformation occurs on the basal plane. There are six {110} planes in the ordered parent phase and two possible shear directions for each {110} plane. Thus, there are 12 possible combinations of stacking planes and shear directions, each combination of which leads to two possible crystallographically equivalent unrotated and undistorted habit planes. Finally, 24 martensite variants can result from a single parent phase. During cooling below M_s, the single parent crystal transforms in a self-accommodating manner to minimize the total shape change. In fact, six groups of four variants form from the parent and the four variants have habit plane normals clustered about one of the six {110} poles of the parent. There are specific twin relations among these four self-accommodating variants. Even if all of the parent phase is transformed into martensite as the specimen is cooled below M_f and the 24 martensite variants will individually be subjected to shape deformations, the specimen as a whole will experience no shape change whatsoever due to the formation of the martensite crystals because self-accommodation comes into play. The origin of the shape memory effect is based on the fact that, when the SMA deformed below M_f is heated above A_f temperature, a parent phase with an orientation identical to that prior to deformation is created from the correspondence variants in accordance with the lattice correspondences between the original parent phase and each variant. This phenomenon causes the specimen to revert completely to the shape it had before the deformation. Generally, martensite is a lower symmetry phase than the parent phase with the consequence that, although there are several ways in which martensite can form from the parent phase, there is only one possible route to return to the parent phase.

TiNi alloys are the most popular of shape memory alloys with their excellent shape memory characteristics. However, they are very costly. Therefore, cheaper Cu-based i.e. CuZn and CuAl based, SMA's have been developed as an alternative to TiNi SMA's. Although CuZnAl alloys with better mechanical properties are the

most popular among the Copper-based SMA, they suffer from lack of sufficient thermal stability, while CuAlNi shape memory alloys, in spite of their better thermal stability, have found only limited application because of insufficient formability due to the brittle γ_2 precipitates. CuAlNi alloys are also less prone to martensite stabilization than CuZnAl alloys. TiNi and CuZnAl alloys cannot be used practically over 100°C. Therefore, in recent years Cu-Al-Ni-Mn-Ti (CANTIM) series alloys have been developed [1] as potential candidates for high temperature SMA applications.

M_s temperature of Cu-based SMA's is very strongly composition dependent and M_s temperature can be adjusted between –100 to +200°C by changing the composition. In CuZnAl alloys, increasing the zinc or aluminum contents causes a decrease in M_s temperature. In Cu-Al-4%Ni SMA's, transformation temperatures decrease steeply with slight increases in Al content, e.g., about 100°C per 1%Al. Although they also decrease with increasing Ni content, dependence of M_s temperature upon Ni content is much weaker than that on Al content. In CuAl binary systems with high concentrations of Al, precipitation of γ_2 phase cannot be prevented even with extremely rapid quenching and thermoelastic martensitic transformation disappears. Therefore, it is believed that addition of Ni suppresses the diffusion of Cu and Al and thus effectively stabilizes the β phase. If vertical cross-sections of ternary CuAlNi system for varying Nickel contents have been compared, the boundary between the β and the $\beta+\gamma_2$ phases is seen to be shifted towards higher aluminum concentrations with increasing nickel content. The range of composition at which CuAlNi and CuZnAl alloys can be used as a SMA is the region allowing β phase to exist alone at high temperatures and limited, approximately to, Cu-(12-14)wt%Al-(3-4)wt%Ni and Cu-(10-30)wt%Zn-(5-10)wt%Al as can be seen from the phase diagrams given in Figure 2.1 and Figure 2.2, respectively.

Recarte et al [2] have investigated the dependence of M_s transformation temperature on concentrations of Ni and Al and analyzed the influence of
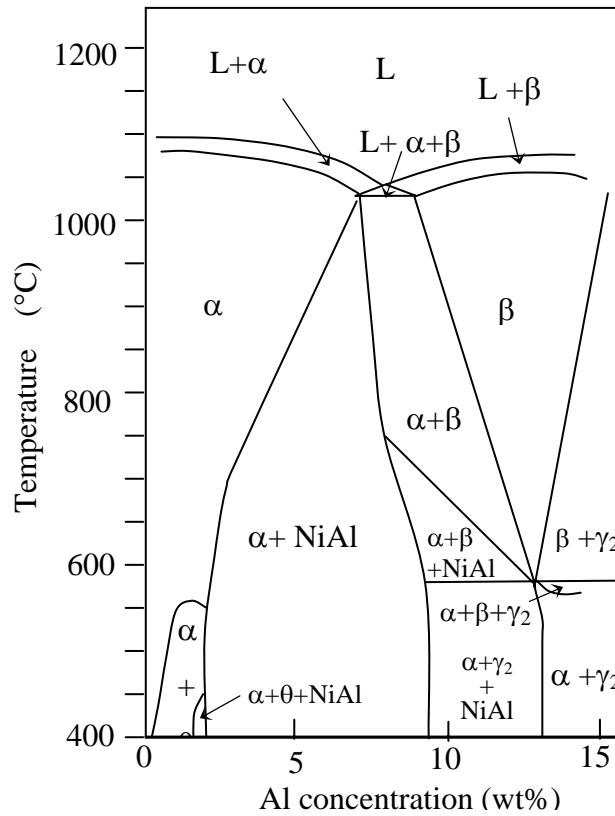
Figure 2.1: The phase diagram showing the vertical cross section of CuAlNi ternary systems with fixed 3wt%Ni [3].
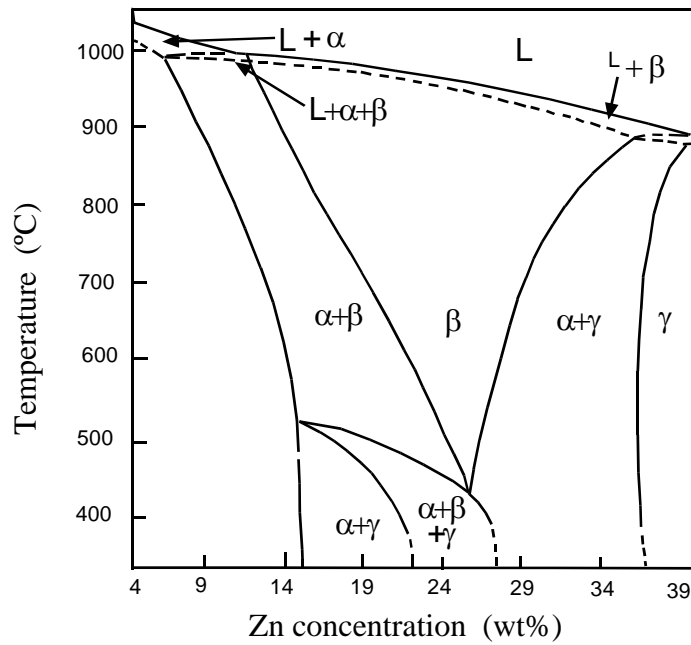
Figure 2.2: The phase diagram showing the vertical cross section of CuZnAl ternary systems with fixed 6wt%Al [4].
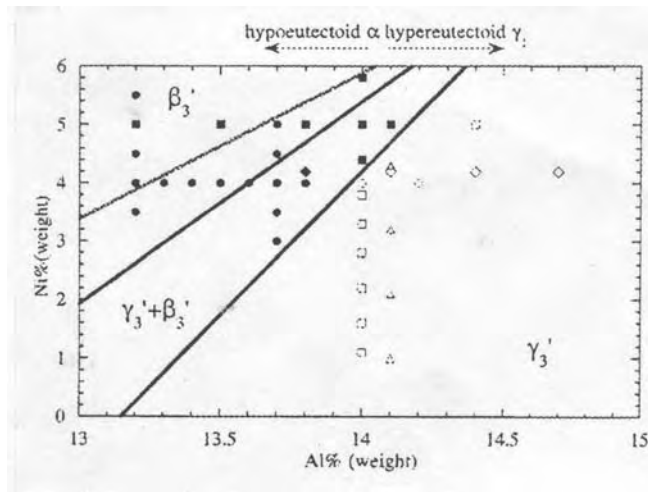
Figure 2.3: Schematic map of the kind of martensite according to changing aluminum and nickel contents [2].

concentration on the kind of martensite formed in CuAlNi single crystals and constructed a concentration-martensite phase map as seen in Figure 2.3. They have found that when aluminum content increases, keeping the nickel concentration constant, the transformation evolves from $L2_1 \rightarrow 18R$ to $L2_1 \rightarrow 2H$ transformation, showing an intermediate concentration range where both martensites coexist i.e., $L2_1 \rightarrow 18R+2H$ transformation is observed. On the other hand, an increase in nickel concentration for constant aluminum content results in an evolution from the mixed $L2_1 \rightarrow 18R+2H$ transformation to the $L2_1 \rightarrow 18R$ transformation. In Figure 2.3, the continuous lines are the boundaries between the stability regions of $\beta_3{}'(18R)$, $\gamma_3{}'(2H)$ and $\beta_3{}'+\gamma_3{}'$ martensites. The eutectoid line (dashed line) is also plotted. In the hypereutectoid region, to the right of this line, the primary precipitates are γ_2 phase and in the hypoeutectoid region, to the left of this line, the primary precipitates are α phase. From the calorimetric results, M_s has been fitted to a linear equation regardless of the kind of martensite:

$$M_s = 2433 - 169.9wt\%Al - 19.1wt\%Ni$$

The difference between the experimental and calculated values is ±8°C at most. They concluded that the transformation temperature depends strongly on

11

concentration, especially on aluminum content. Change of the kind of martensite from 18R into 2H type with increasing aluminum content in CuAlNi alloys has also been reported by C.M. Friend [5] and Friend, Ortin et al [6].

It is well known that the transformation temperatures of shape memory alloys decrease as the grain size is reduced [7, 8] but are independent of grain size for grain sizes larger than 100μm [9]. The effect of grain size on transformation temperature was suggested to be due to a grain constraint effect where grain boundaries retard the martensite transformation and lower the M_s temperature [10].

Cu-based shape memory alloys have disordered β phase at high temperatures. Upon cooling β→B2 ordering transition takes place such that even rapid quenching cannot prevent this ordering reaction. With further lowering of temperature B2→DO_3 ordering may take place depending on alloy composition and cooling rate. B2 ordering is a first order transformation whereas the DO_3 ordering is a second order transformation. In nucleation and growth controlled first order transformations, a substantial change in order takes place discontinuously at critical ordering temperature (T_C) and thermodynamically first derivative of Gibbs free energy changes discontinuously characterized also by discontinuous changes in entropy, S. On the other hand, for second order transformations, which are of the homogeneous type phase transformations, there is no sudden change in order at T_C, the second derivative of Gibbs free energy is discontinuous revealing a continuous change in entropy [11]. Ordering temperatures of various CuAlNi and CuZnAl alloys are tabulated in Table 2.1.

Recarte et al. [12] have calculated T_{B2} and T_{DO3} ordering temperatures theoretically by modifying the chemical interchange energies for binary Cu-Al alloys proposed by Inden and Pitsch for ternary CuAlNi alloys. They have found a good agreement between the theoretical ordering temperatures and experimental ordering

Table 2.1: Ordering temperatures of various Cu-Based alloys

Alloy (wt.%)	B2 (°C)	DO$_3$ (°C)
Cu-12,41%Al-3,14%Ni-2,02%Mn-0,03%B [13]	800±10	560±10
Cu-11,86 %Al-3,13%Ni-3,13%Mn-0,03%B [13]	700±10	550±10
Cu-13,05 %Al-4,48%Ni-0,04%B [14]	600±10	600±10
Cu-11,9 %Al-5%Ni-2%Mn-1%Ti [15]	500	≈460
Cu-13,4 %Al-3%Ni-1%Ti [15]	540	460
Cu-14,2 %Al-4,0%Ni [16]	605	550
Cu-14 %Al-3,99%Ni [12]	576	523
Cu-13,75 %Al-5%Ni [17]	630	508
Cu-18.18%Zn-7.4%Al [18]	537	367
Cu-20.69%Zn-6.79%Al [19]	536	330
Cu-14.2%Zn-8.5%Al [20]	480	260
Cu-26.32%Zn-4.14%Al [21]	517	277
Cu-26.17%Zn-4.0%Al [22]	≈500	260

temperatures measured by electrical resistivity. In Figure 2.4, the theoretically calculated and the experimental values of both T_{B2} and T_{DO3} ordering temperatures are presented. Nickel and Aluminum contents are given in atomic percentages that correspond approximately to 3-5% Nickel and 13-15% Aluminum in terms of weight percentages. With increasing Ni and Al concentrations the increase of T_{B2} temperature has been found to be larger than that of T_{DO3} temperature.

Rapacioli and Ahlers [23] have studied the ordering in CuZnAl alloys and B2 ordering temperature has been found to be changing slightly with Zn concentration while the DO$_3$ ordering temperature was strongly dependent on composition, i.e. decreasing steeply with increasing Zn concentration. Singh et al. [24] have calculated T_{B2} and T_{DO3} temperatures in ternary CuZnAl alloy by using the

Bragg-Williams-Gorsky approximation with the assumption of a pair-like chemical interaction between the nearest and the next nearest neighbor atoms. As can be seen in Figure 2.5, for a constant Zn concentration with increasing aluminum percentage T_{B2} increases. Change of DO_3 ordering temperature is shown in Figure 2.6. For a
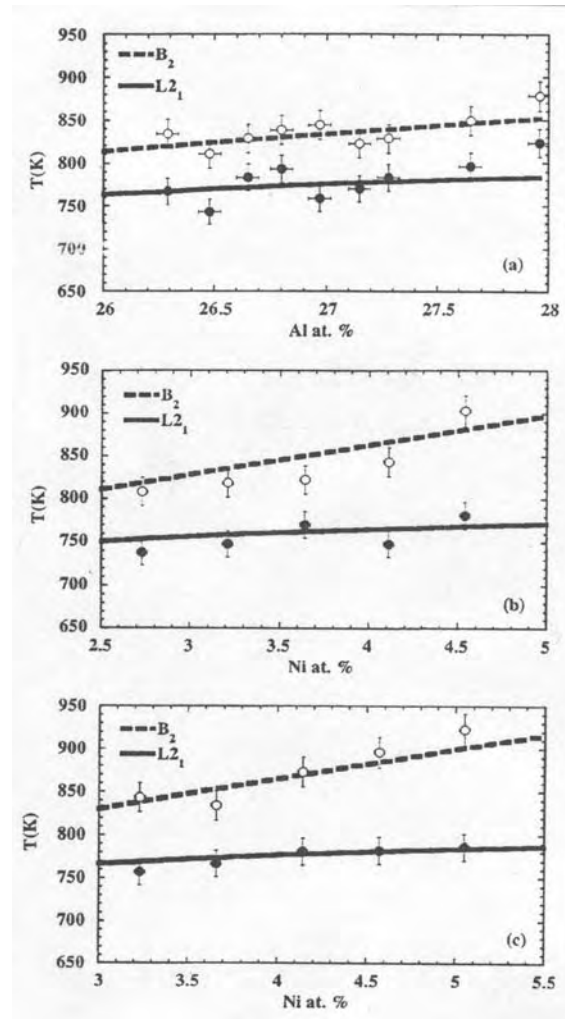
Figure 2.4: Dashed lines are the theoretically calculated T_{B2} temperatures and the open circles are the experimental values of T_{B2} temperatures. On the other hand, full lines are the theoretically calculated T_{DO3} temperatures and the full circles are the experimental values of T_{DO3} temperatures [12].
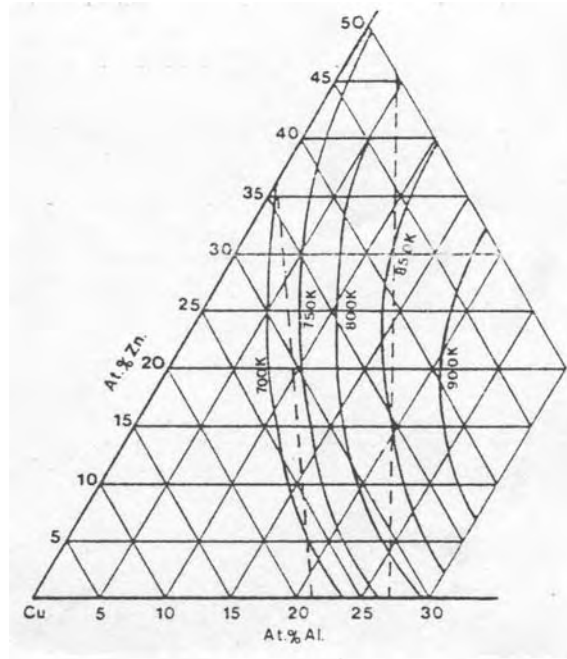
Figure 2.5: Calculated values of T_{B2} temperatures in the ternary CuZnAl alloy. The dotted lines define the β phase region at 800°C [24].

constant low Zn concentration, with increasing aluminum content, T_{DO3} increases while for a constant high Zn concentration, with increasing aluminum content T_{DO3} decreases. Schofield and Miodownik's [25] assumed model for B2→DO$_3$ ordering temperatures in CuZnAl alloys is schematically illustrated in Figure 2.7.

Approximately above 20%Zn, with increasing Al content B2→DO$_3$ temperature decreases. On the other hand approximately below 20%Zn, with increasing Al content B2→DO$_3$ temperature first increases and than decreases.

Wu and Wayman [26] proposed that the interpretation of long range order in CuZnAl alloys is in confusion such that L2$_1$ superlattice has often been

15
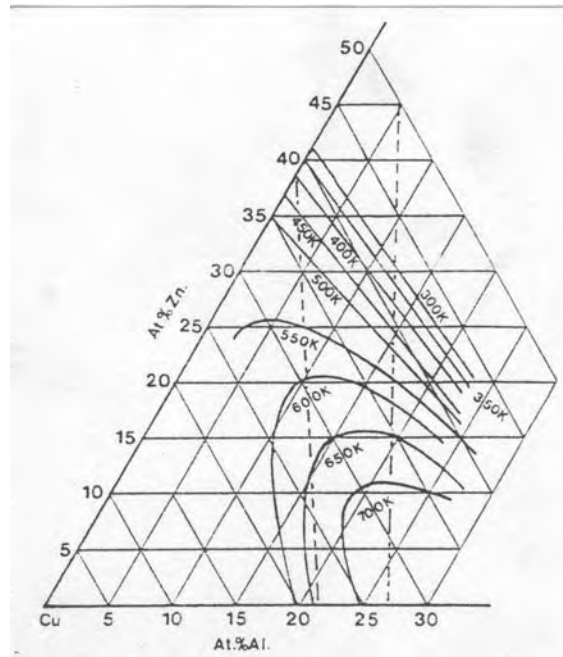
Figure 2.6: Calculated values of T$_{DO3}$ temperatures in the ternary CuZnAl alloy. The dotted lines define the β phase region at 800°C [24].
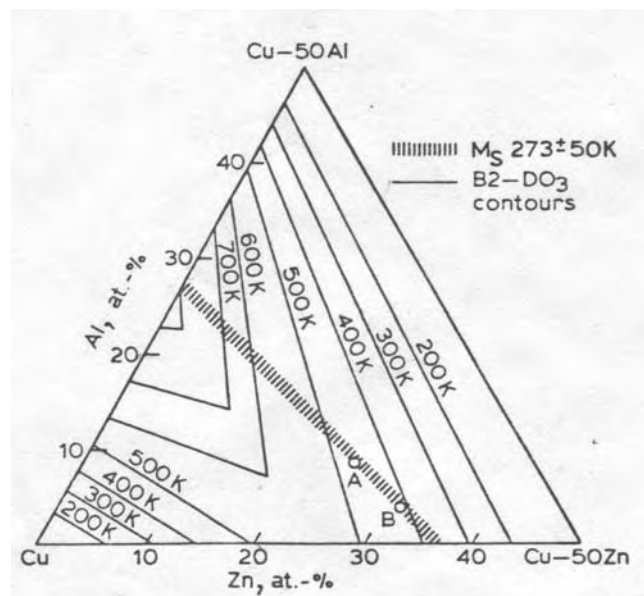
Figure 2.7: B2→DO$_3$ ordering temperatures in CuZnAl alloys [25].

misidentified as a DO_3 superlattice. In their study the criterion to differentiate between DO_3 and $L2_1$ superlattices is described. By using the convolution method, they calculated structure factors and intensities for B2, DO_3 and $L2_1$ crystal structures.

β phase lattice shown schematically in Figure 2.8 can be viewed as an fcc lattice with the lattice sites occupied by four kinds of atoms; A_1 at (0,0,0), A_2 at (1/2,0,0), A_3 at (1/4,1/4,1/4) and A_4 at (3/4,1/4,1/4). Three different crystal structures can be derived from this lattice are:

$$\beta_1(DO_3) \text{ when } A_1=A_2=A_3\neq A_4$$

$$\beta_2(B2) \text{ when } A_1=A_2\neq A_3=A_4$$

$$\beta_3(L2_1) \text{ when } A_1=A_2\neq A_3\neq A_4$$

For a B2 superlattice, the crystal structure is a cubic lattice with lattice constant of a/2. The structure factor, F of a (hkl) reflection of the β phase lattice can be calculated according to $F = F_B X F_F$, where

$$F_B = f_1 + f_2\exp2\pi i(h/2) + [f_3+f_4\exp2\pi i(h/2)] \times \exp2\pi i[(h/4)+(k/4)+(l/4)]$$

$$F_F = 1+\exp2\pi i[(h/2)+(k/2)]+\exp2\pi i[(k/2)+(l/2)]+\exp2\pi i[(h/2)+(l/2)]$$
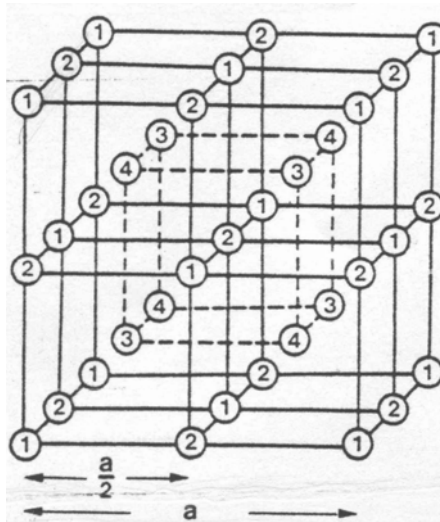
Figure 2.8: Schematic drawing of the four sites in a β phase lattice [26].

where F_B is the shape factor and F_F is the structure factor of FCC lattice. Actually DO_3 crystal structure is a four interpenetrating FCC lattices. The extinction rule of an fcc lattice must be obeyed due to F_F factor and hkl of the reflection must be all even or all odd.

When hkl are all even and h+k+l=4n (n integer):

$F_B=f_1+f_2+f_3+f_4$ and these are fundamental reflections.

When hkl are all even and h+k+l=4n+2:

$F_B=(f_1+f_2)-(f_3+f_4)$ since A_1, A_2 and A_3, A_4 are nearest neighbors, these reflections will be nearest neighbor superlattice reflections (NNSR).

When hkl are all odd:

$F_B=(f_1-f_2)+(f_3-f_4)$ because A_1 and A_2 also A_3 and A_4 are next nearest neighbors, these reflections will be called next nearest neighbor superlattice reflections (NNNSR).

The high temperature β phase possessing disordered bcc structure undergoes two ordering transitions upon cooling. The first one is a first nearest neighbor (NN) ordering which results in B2 superlattice. Further cooling induces next nearest neighbor (NNN) ordering and the crystal structure has been suggested to become DO_3 or $L2_1$ superlattice. The intensities of nearest neighbor superlattice reflections (NNSR) and next nearest neighbor superlattice reflections (NNNSR) contain all the information necessary to identify the correct order of state as discussed below:

B2: Since there are two types of atoms ($f_1=f_2\neq f_3=f_4$) in a B2 structure, NNNSR are extinct and only NNSR are present. However, because the lattice constant changes from a to a/2, the reflections should be indexed according to (h/2, k/2, l/2).

DO_3: In a DO_3 superlattice, $f_1=f_2=f_3\neq f_4$. $\left|F_b\right|^2 = (f_1- f_4)^2$ for both NNSR and NNNSR and they have identical intensities.

$L2_1$: Because $f_1=f_2\neq f_3\neq f_4$, the intensities of NNSR and NNNSR are different. For NNSR, $\left|F_b\right|^2 = (2f_1- f_3- f_4)^2$ and for NNNSR, $\left|F_b\right|^2 = (f_3- f_4)^2$.

Therefore, by comparing the intensities of NNSR and NNNSR, the order state of a homogeneous system can be identified.

Cu-based shape memory alloys with ordered B2 or DO_3 phases transform into one of the long period stacking order martensite (LPSO) structures such as 2H, 3R, 9R, and 18R through a thermoelastic martensite transformation. Crystal structures of DO_3 parent phase, 2H and $18R_1$ LPSO martensites are schematically drawn in Figure 2.9, Figure 2.10 and Figure 2.11, respectively. Long period stacking order martensite structures are formed by shearing of {110} parent phase planes, which become the basal planes of long period stacking order martensites, along <110> directions by an amount 1/6 a_{DO3}. Low symmetry of martensite structure provides formation of 24 crystallographic variants from the high symmetry parent phase. During cooling below M_s temperature the parent phase transform in a self-accommodating manner, in which the martensite variants are created side by side forming diamond like morphologies, to minimize the total shape change. Due to the displacive shear nature of martensitic transformation the crystal structure, atomic ordering and microstructural defects of parent phase are inherited by the product martensite phase.

2.2. Ageing of Copper-Based Shape Memory Alloys:

In recent years, considerable efforts are devoted to the study of ageing in copper based shape memory alloys since shape memory performance of the alloys are directly related to the stabilities of both parent and martensite phases. Copper Based shape memory alloys are susceptible to low temperature ageing effects that can alter their transformation behavior limiting their reliability in applications of temperature sensitive components. The time dependent ageing process producing changes in properties of martensite are not desired because they limit the technological applications of SMA's. Therefore, the understanding of the ageing mechanism is not only an academic interest but provides a better control and development of those alloys for engineering applications.
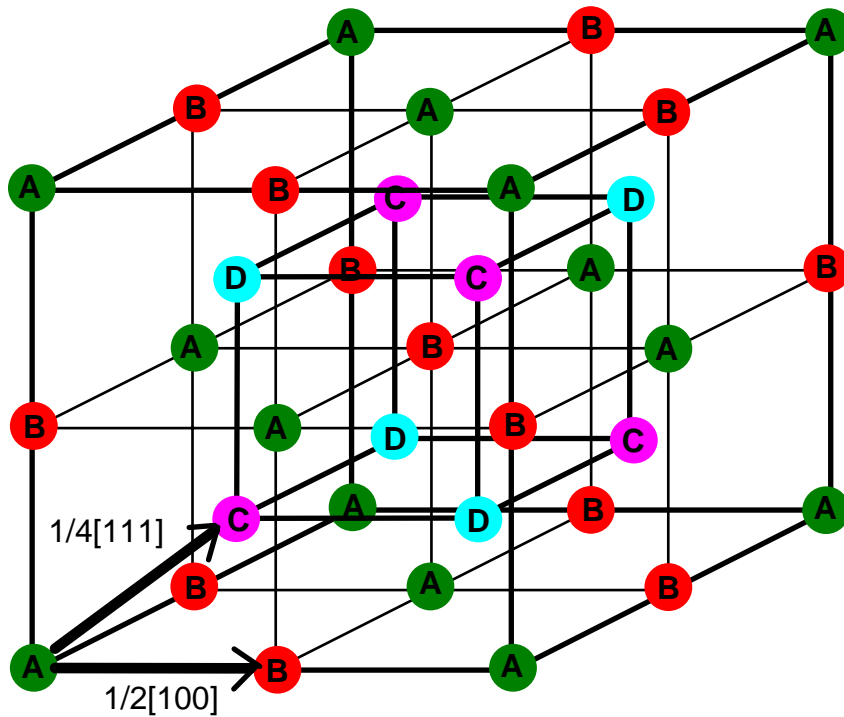
Figure 2.9: DO$_3$ unit cell showing position of atoms [11]

    A atoms: (000), (1/2,1/2,0), (1/2, 0, 1/2), (0,1/2, 1/2) - fcc sites

    B atoms: (1/2, 0, 0), (0, 1/2, 0), (0, 0, 1/2), (1/2,1/2,1/2) - fcc sites translated by [1/2, 0, 0]

    C and D atoms: on the eight (1/4, 1/4, 1/4) equivalent sites
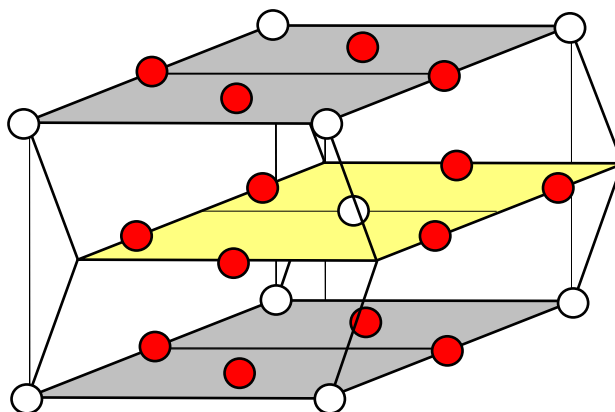
Figure 2.10: Long Period Stacking Order Structure of 2H Martensite [11].

20
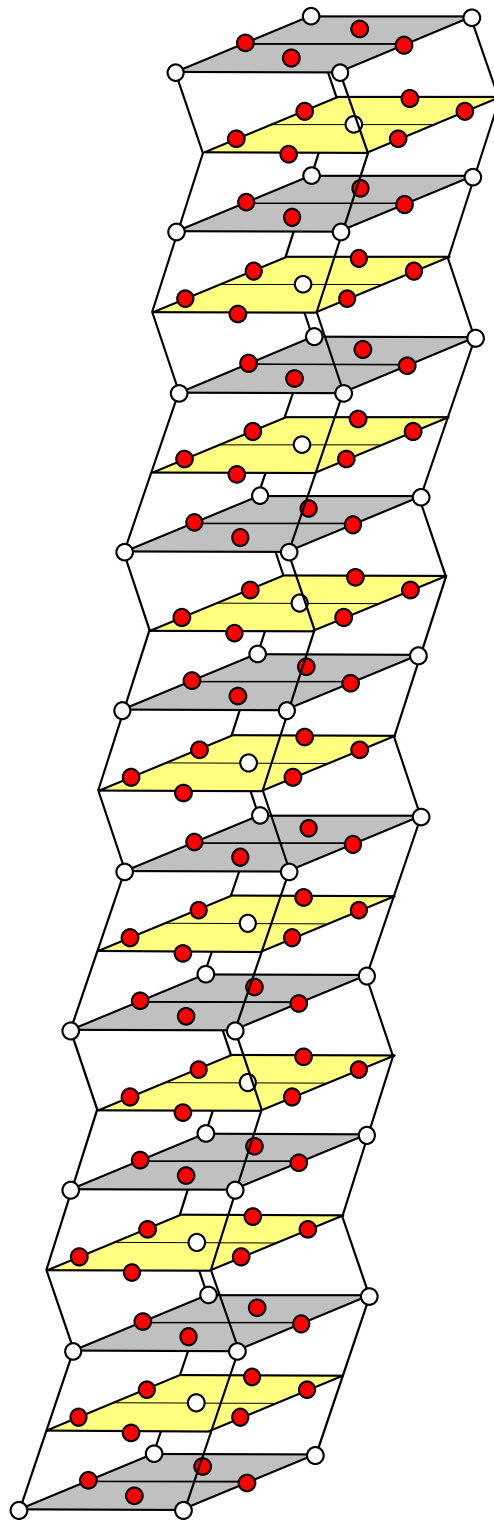
Figure 2.11: Long Period Stacking Order Structure of 18R$_1$ Martensite [11].

Use of a SMA in a temperature controlling device demands reliability and reproducibility of transformation temperatures with shape memory cycles or with the holding duration in the martensitic condition before the device operates at any given time. Some of the common features of ageing phenomena in copper-based SMA are as follows: Ageing is a time-dependent process such that it should be related with redistribution of atoms or defects, thus diffusion. Ageing has been observed to be very sensitive to point defects. Some changes in martensite i.e. in long range order, were experimentally verified. Variations in transformation temperatures and poor martensite reversibility are the common changes resulting from ageing.

The most important consequence of ageing in those alloys is stabilization of either parent or martensite phase. Among the previous studies, martensite stabilization has received much more attention, whereas literature on stabilization of parent beta phase has been relatively limited. The subjects of Parent phase stabilization and Martensite stabilization are sequentially discussed in sections 2.3 and 2.4.

2.3. Parent Phase Stabilization:

An as quenched alloy having subzero M_s temperature is in parent phase after betatizing and quenching to room temperature. It has been observed that in such alloys ageing around room temperature results in a decrease in M_s temperature. Due to the lowered M_s temperature, parent phase cannot transform into martensite upon cooling when the parent phase is stabilized. For this phenomenon, known as parent phase stabilization, there are two factors: Incomplete ordering during quenching and formation of precipitates [27].

Experimental observations of parent phase stabilization are summarized and the mechanisms of parent phase stabilization are explained below.

2.3.1. Experimental Observations of Parent Phase Stabilization:

Singh et al. [28, 29] have observed the transformation sequence in a Cu-14Wt%Al-4Wt%Ni alloy, which consists of a mixture of 2H martensite and DO_3 parent phase in the as-quenched condition, by ageing up to 550°C in TEM. In-situ hot stage TEM studies have shown that γ_2 phase has formed after isothermal ageing at 450°C for one hour. 72 hours ageing times resulted in coarsening of γ_2 phase by the migration of γ_2 interfaces and simultaneous partitioning of solute atoms takes place across the interface. The concentration of Aluminum in the γ_2 phase increases as a function of time. When the γ_2 phase reaches the nearly equilibrium condition, in the remaining matrix, which is enriched by Cu and Ni atoms, α phase is precipitated in the form of rods at 500°C to 550°C. In the study of Kuwano and Wayman [30], Cu-14Wt%Al-4Wt%Ni alloy having DO_3 structure in the as-quenched state, upon ageing at 400°C for 40 minutes revealed cuboidal precipitates of the γ_2 phase, which has a cubic crystal structure with lattice dimension $3a_{BCC}$. The M_s temperature of the aged alloy samples has been found to be much higher than that of as-quenched samples because of the reduced matrix solute content. Dvorack et al. [31] have reported decomposition of parent DO_3 phase into a two phase mixture of α and γ_2 above 275°C in a Cu-14.3Wt%Al-4.3Wt%Ni alloy. They have determined the crystal structures and lattice parameters of α and γ_2 phases by x-ray diffraction. It was found that α phase has FCC structure with lattice parameter of 0.372 nm and γ_2 phase has simple cubic structure with 0,872nm lattice parameter. Castro and Romero [19] have studied isothermal ageing of Cu-20.69Wt%Zn-6.79Wt%Al alloy in the temperature range 200-500°C, where the β phase decomposed into stable α and γ phases. They have constructed TTT diagram for the precipitation of α and γ phases as shown in Figure 2.12.

Lee and Kim [32, 33] have determined the β/α and β/γ solvus temperatures, T_s, and the composition dependence of ageing kinetics in five different CuZnAl shape
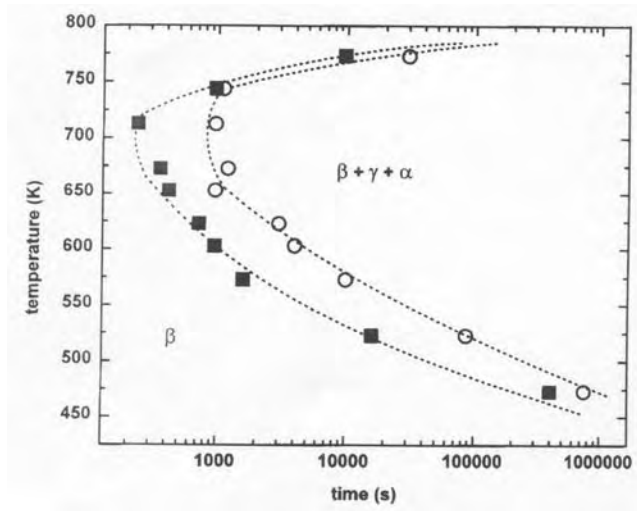
Figure 2.12: TTT diagram for the formation of α (o) and γ (□) precipitation in Cu-20.69Wt%Zn-6.79Wt%Al alloy [19].

memory alloys with different aluminum contents. Alloy with the highest T_s temperature most favored the decomposition of parent phase into α and γ phases, thereby exhibited faster ageing kinetics because the higher T_s temperature provided higher supersaturation at the respective ageing temperature. Therefore, the lower thermal stability of β phase at low aluminum contents in hypoeutectoid alloys can be improved by lowering the degree of supersaturation by increasing the aluminum content or decreasing the zinc content. Aluminum composition dependence of ageing kinetics of α precipitates in several CuZnAl alloys has also been studied by Leu and Hu [34] and accelerated α precipitation at low aluminum contents in hypoeutectoid CuZnAl alloys as compared to at high aluminum contents in hypereutectoid alloys has been observed during isothermal ageing at 450°C.

Kennon et al. [35] have isothermally aged Cu-15.1wt%Al-3.1wt%Ni alloy with M_s= -11°C, at temperatures between 200°C-450°C for ageing times up to approximately 10^6 seconds (12 days). Precipitates of α and γ_2 have been observed

24

after 24 hours ageing at 300°C. M_s temperature was observed to increase by about 20°C after ageing 28 hours at 200°C and by about 15°C after 17 minutes at 300°C. On the other hand, M_s temperature is observed to decrease by approximately 15°C after 5 minutes ageing at 400°C. Changes in M_s temperature at lower ageing temperatures has been attributed to incomplete B2→DO_3 ordering transition while the decrease in M_s temperature observed at higher ageing temperatures to the formation of solute lean precipitates that enrich the matrix and hence lower the M_s temperature. Additionally, hardness has been found to increase with increasing ageing time and has been attributed to precipitation of α and γ_2. For this property change, activation energy found as 80 kJ/mole was used to predict the life expectancy of alloys at lower temperatures. Predicted ageing times to lose shape memory capability are tabulated in Table 2.2. Lower stability of Cu-15.1%Al-3.1%Ni alloy as compared to Cu-14.2%Al- 2.9% Ni alloy stems from the fact that former is more supersaturated than the later. On the other hand, rapid ageing of Cu-21.2%Zn-6.0%Al alloy is due to bainite formation, which is particular to CuZnAl alloys, not observed in CuAlNi alloys. They concluded from their predictions that Cu-14.2%Al- 2.9% Ni alloy is the most resistant to degradation.

Table 2.2: Predicted ageing times to lose shape memory capability in CuAlNi and CuZnAl alloys [35].

Temperature	Cu-15.1%Al-3.1%Ni	Cu-14.2%Al-2.9% Ni	Cu-21.2%Zn-6.0%Al
100°C	12 days	3 years	42.5 days
50°C	240 days	69 years	5 years
20°C	6.5 years	744 years	82 years

Leu and Hu [34] have isothermally aged a parent phase Cu-27.4wt%Zn-3.72wt%Al alloy at room temperature for 18 hours. It has been found that M_s temperature has increased by about 20°C relative to that in the as-quenched condition. It has been confirmed with TEM that no precipitation is observed in this alloy after room temperature ageing for 18 hours. Therefore, the increase of M_s temperature has been attributed to the increase of the degree of ordering of the parent phase. In the study of Schofield and Miodownik [25], a Cu-25.55wt%Zn-3.72wt%Al alloy having parent beta phase at room temperature has been isothermally aged at 39°C, 52°C and 67°C for 100 minutes and M_s temperature has been found to decrease by 20°C and this is attributed to an incomplete B2→DO$_3$ ordering transformation.

2.3.2. Mechanisms of Parent Phase Stabilization:

In literature, parent phase stabilization phenomenon as usually manifested by a decrease in the M_s temperature is explained by two mechanisms; formation of precipitates and incomplete ordering during quenching [27].

Precipitation phenomena depress the martensitic transformation initially due to coherency strain fields around precipitates and/or due to the destruction of potential nucleation sites of martensites. However, accompanying the growth of precipitates, solute atoms in parent phase are enriched or depleted, depending on chemical compositions of precipitates. As a result, M_s temperature decreases or increases and the shape recovery is degraded due to the M_s change [36]. Degree of ordering of the parent Beta phase is also affected from ageing. Although β→B2 ordering cannot be suppressed due to its first order nature, the subsequent B2→DO$_3$ ordering is often incomplete during quenching because of its second order nature. Besides, excess quenched in vacancies are introduced in parent phase during quenching and inherited by the martensite phase as a result of diffusionless nature of the transformation. Upon ageing at intermediate temperatures, ordering reaction

26

transforms the Beta phase from incomplete to complete order accelerated by the migration of quenched in vacancies [36].

2.4. Martensite Stabilization:

In shape memory history, the subject of martensite stabilization has attracted much attention especially for the last twenty years. Many of the studies have been devoted to CuZnAl alloys suffering from severe stabilization effect. Although several mechanisms have been offered for martensite stabilization, the actual mechanism has remained mysterious. Martensite stabilization in Copper based SMA's has been critically reviewed first in 1986 [37] and later in 1995 [38]. Ren and Otsuka [39] have recently, 1999, reviewed previous mechanisms and they also offered a new model [40]. A review about ageing of CuZnAl martensites has been published in 2003 by Ahlers and Pelegrina [41].

Martensite stabilization is the increase of the stability of martensite with respect to the parent phase during ageing below M_s temperature. Significant rise of A_s and A_f temperatures during ageing prevents reversion of martensite back into parent phase upon heating. Martensite stabilization is a time and temperature dependent diffusional process that is accelerated by high concentration of quenched-in vacancies. Degree of stabilization is closely related to quenching conditions such that strong martensite stabilization induced after direct quenching is attributed to excess quenched-in vacancies and the increase in A_s and A_f temperatures is the measure of degree of martensite stabilization.

Grain size, alloy composition, lattice defects, heat treatments are some factors affecting stabilization. Fine grained material might be recognized less susceptible to stabilization, which stems from the reasoning that higher proportion of grain boundaries would act as effective sinks for vacancies, thereby reducing their contribution to diffusion.

Alloy composition is also critical in stabilization. For CuZnAl alloys, optimum Aluminum content is controversial from processing and stability points of view. A lower Al content is preferred for reasons of easier hot deformability. A higher Al content on the other hand, could provide a martensite more resistant to ageing. Low Aluminum containing CuZnAl alloys accelerates α precipitation due to higher supersaturation hence they are thermally less stable as compared to high Al content alloys. On the other hand, high Al content accelerates the precipitation of γ. It is well known that CuAlNi alloys are less prone to stabilization than CuZnAl alloys. The lower mobility of vacancies and the difficulty of formation of vacancy clusters in CuAlNi martensite making it less susceptible to stabilization may be related to the stronger bonding force between Al and Ni atoms. The mobility of vacancies in CuAlNi martensite is much less than that in CuZnAl martensite.

Lattice defects such as dislocations inhibit stabilization simply by acting as sinks for vacancies and reducing their amount and contribution to diffusion. The purpose of application of a special heat treatment known as step quenching is to reduce the amount of excess quenched-in vacancies. In brief, the basis of stabilization control is simply elimination of the effects of the excess quenched-in vacancies.

2.4.1. Experimental Observations of Martensite Stabilization:

Morawiec and Gigla [42] has studied the ageing of a Cu-13.42wt%Al-3.1wt%Ni-0.25wt%Ti-0.063wt%B alloy at temperatures 80°C, 120°C, 160°C and 200°C for times from 15 minutes to 312 hours. After 2 hours ageing of as quenched alloy with 2H martensite structure at 200°C coherent γ_2 phase appeared and extended 66 hours ageing at the same temperature resulted in increase of size of γ_2 precipitates and loss of their coherency. They concluded that ageing in this alloy proceeds in three stages. In the first stage, transformation temperatures and hardness decreased and this stage is interpreted as annealing out of vacancies and increase in parent phase order. In the second and third stages, transformation temperatures and hardness

28

increased. The second and third stages are explained in relation to the formation of coherent and incoherent γ_2 precipitates, respectively. Rodriguez and Guenin [43] have studied martensite ageing in a Cu-12.9wt%Al-4wt%Ni alloy, which has 18R martensite in the as-quenched condition. The transformation enthalpy for M$\rightarrow\beta$ is measured as 10-11 J/gr and the transformation hysteresis as 12°C. Ageing at 220°C for 750 hours exhibited very fine microstructure by TEM. This observed precipitation phenomenon is interpreted as a step towards the formation of the equilibrium phases α and γ_2. They concluded that the very beginning of this precipitation is the cause of the increase in A_s and A_f temperatures. Pelosin and Riviere [44] have studied annealing effects on the martensitic structure of a water quenched Cu-12wt%Al-3wt%Ni alloy by X-ray diffraction. The as quenched alloy with 18R martensite crystal structure was subjected to two hours isochronal annealing in the range 100°C to 515°C. Martensite decomposition into equilibrium phases of α and γ_2 has been observed above 415°C. The ageing of the martensite at increasing temperatures leads to its stabilization followed by its degradation into equilibrium phases that prevents the alloy from a reversible martensitic transition. Wei et al [45] have studied the precipitation sequence in a Cu-11.9wt%Al-5.1wt%Ni-1.7wt%Mn-1.0wt%Ti alloy by differential scanning calorimetry. Precipitation of γ_2 phase has been observed at 500°C and α precipitation occurred at a higher temperature than that of γ_2. They stated that the formation of martensite ($\beta\rightarrow$M transformation), atomic ordering, precipitation of equilibrium phases are exothermic reactions whereas M$\rightarrow\beta$ transformation and atomic disordering are endothermic reactions.

Generally, grain refiner added Copper–based shape memory alloys contain grain-refiner rich precipitates. Grain refined CuAlNiMnTi alloys exhibit χ phase precipitates in the as-quenched condition. Based on their size and shape, three types of χ phase precipitates have been observed in CuAlNiMnTi shape memory alloys. The larger ones, few micron size are known as χ_L, the small ones, several tens of nanometer size are the cuboidal χ_s precipitates and the very small ones, 3-5 nm size, are the χ_{ss} precipitates [46- 49]. In a similar manner, Chung et al [50, 51] have

identified the two kinds of zirconium rich precipitates formed in the Cu-21wt%Zn-5.98wt%Al-1.02wt%Mn-0.46wt%Zr alloy, which has 18R martensite in the as-quenched condition.

Wei et al [52] have investigated the isothermal ageing effects in an as quenched Cu-1.88wt%Al-5.06wt%Ni-1.65wt%Mn-0.96wt%Ti alloy revealing M18R martensite structure in the temperature range of 250°C to 400°C. Changes in hardness, electrical resistivity and transformation temperatures with ageing time at 250°C, 300°C, 350°C and 400°C, which are illustrated in Figure 2.13, have shown three distinct stages: In stage 1, there is no significant change in hardness but electrical resistivity decreases and transformation temperatures increase. In stage 1, the as quenched alloy with a nonequilibrium state of long range atomic order tends to reach an equilibrium state, hence martensitic transformation temperatures shift upwards. In stage 2, hardness increases abruptly, resistivity increases drastically and transformation temperatures start to decrease. Stage 2 was attributed to the formation of bainite. Since the bainitic transformation is irreversible, formation of bainite also implies a decrease in the fraction of thermoelastic martensite, an increase in transformation hysteresis and a degradation of shape memory effect. In stage 3, hardness and resistivity are almost stable and decrease in transformation temperatures continues. Stage 3 was explained as dissolution of bainite into equilibrium phases of α and γ_2. Once the parent phase totally decomposes into the metastable bainite and disordered equilibrium phases, the shape memory effect of the alloy will be completely destroyed.

Cu-28.02wt%Zn-3.22wt%Al alloy samples betatized at 870°C for 5 minutes and quenched into RT water, were heated at an intermediate temperature T_q for few seconds and quenched into iced water in the study of Marukawa et al. [53]. Then they were aged at different T_a temperatures, where they are martensitic, in a silicon oil bath or molten salt bath. Transformation temperatures were determined by electrical resistivity measurement. Figure 2.14 shows the rise in A_s temperature as a function of ageing time. Quenching temperatures T_q (180 or 280°C) and ageing
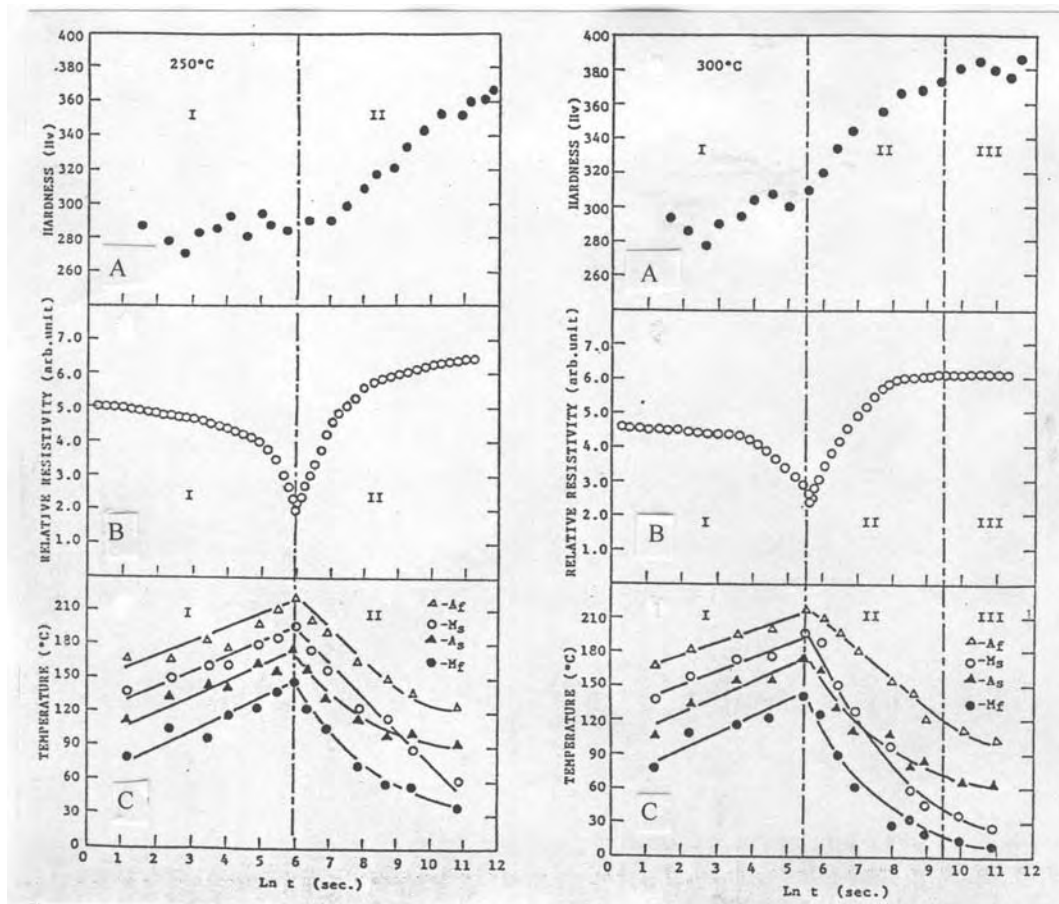
(a)   **(b)**

Figure 2.13: The changes in hardness (A), electrical resistivity (B) and transformation temperatures(C) in Cu-11.88Wt%Al-5.06Wt%Ni-1.65Wt%Mn-0.96Wt%Ti alloy after ageing at a) 250°C, b) 300°C, c) 350°C and d) 400°C [52].

31
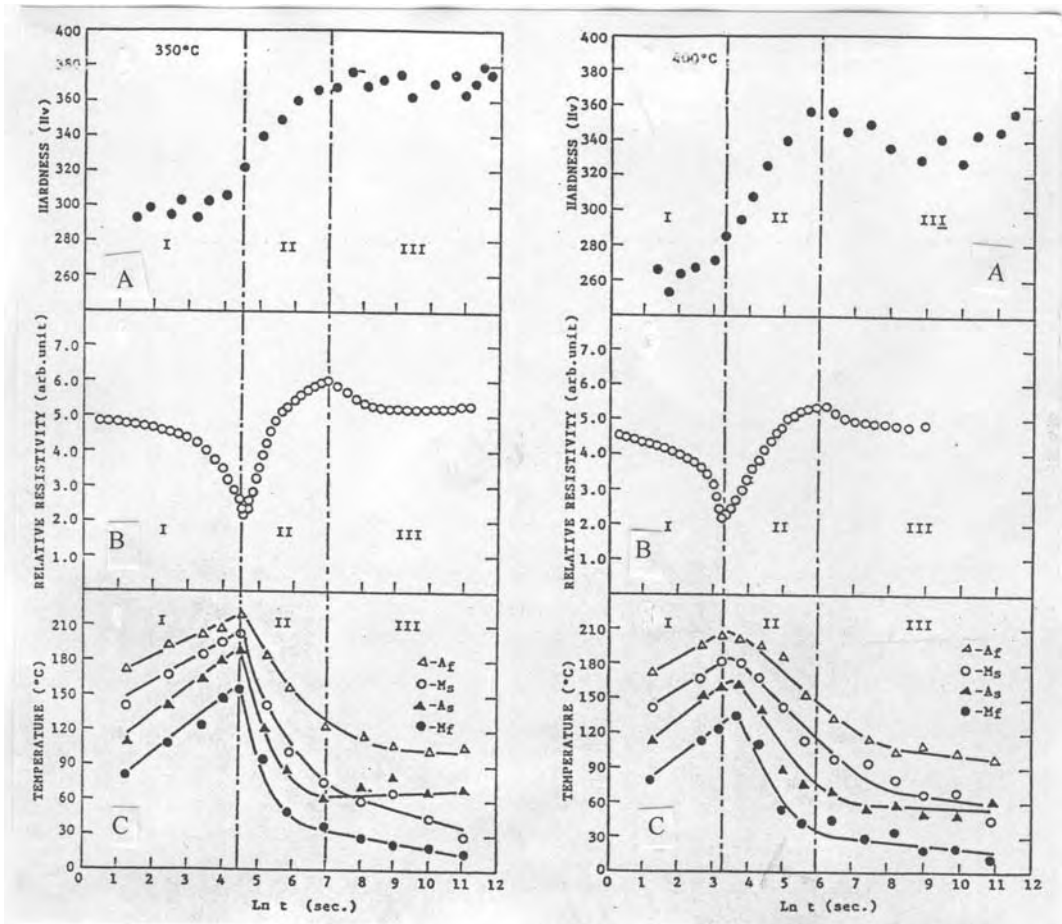
(c)   (d)

Figure 2.13: Continued.

temperatures T_a (20, 35, 40 or 50°C) are denoted in parenthesis. It is clear that higher quenching temperatures cause a rapid change in transformation temperature by subsequent ageing. Also higher ageing temperature leads to a faster change in transformation temperature. It can be deduced that a higher vacancy concentration in the sample quenched from higher T_q promotes the diffusion of solute atoms and higher the ageing temperature higher is the increase in A_s temperature. In Figure 2.15, change of M_s and A_s temperatures with respect to T_q, which is in the parent phase region, is plotted. A higher quenching temperature results in lower transformation temperature. This indicates that the initial condition probably atomic configuration of parent phase affects the transformation temperature.
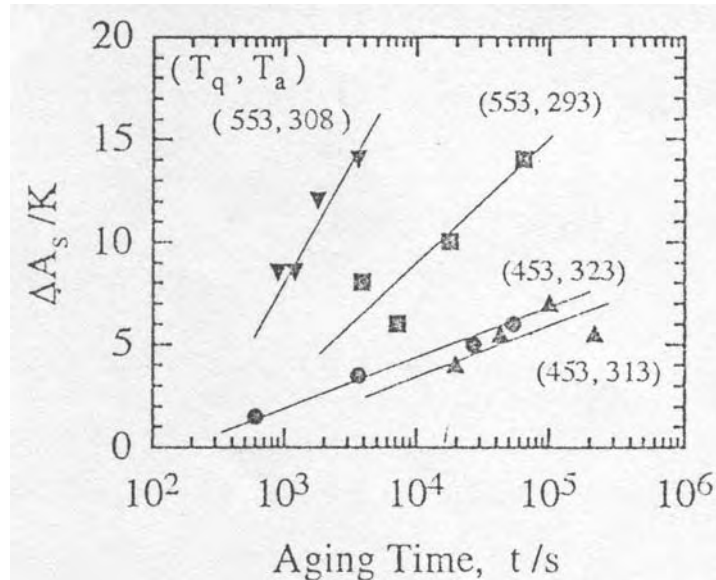
Figure 2.14: Increase in A_s as a function of ageing time for various quenching temperatures, T_q and ageing temperatures, T_a [53].

In the study of Nakata et al. [54] Cu-12.73wt%Zn-8.02wt%Al alloy sample betatized at 850°C for 5 minutes and directly quenched into water was martensitic at room temperature but has not shown M→β transformation during subsequent heating. Therefore, after betatizing instead of direct quenching it is step quenched

33
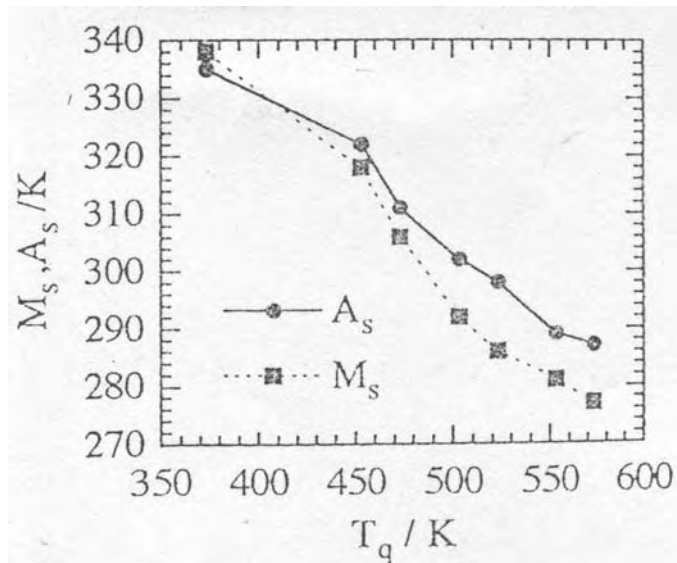
Figure 2.15: M_s and A_s temperatures as a function of quenching temperature T_q [53].

into an oil bath at 150°C for 5 minutes and then to room temperature. DSC curve of as step quenched alloy and after subsequent ageing at 100°C for 56 days can be seen from Figure 2.16 a and b, respectively. The shift of M→β transformation to higher temperatures after ageing is clearly seen. The A_s and A_f temperatures have been measured in specimens aged at 80°C, 90°C and 100°C for several period of times and the change in those temperatures with increasing ageing time has been plotted in Figure 2.17. It is obvious from this figure that transformation temperatures increases with increasing ageing temperature and time.

The microstructure of a Cu-23.6wt%Zn-4.47wt%Al-0.23wt%Mn-0.17wt%Ni SMA that is aged in martensite phase for one year were investigated by TEM [55]. Although the sample, which was betatized at 840°C for 20 minutes and step quenched into boiling water for 30 minutes and air cooled, were revealing high stacking fault density, after one year martensite ageing stacking faults become indistinct and decreased in amount and equilibrium fcc α phase was observed at martensite plate boundaries as well as in the plates. They explained the degradation

34
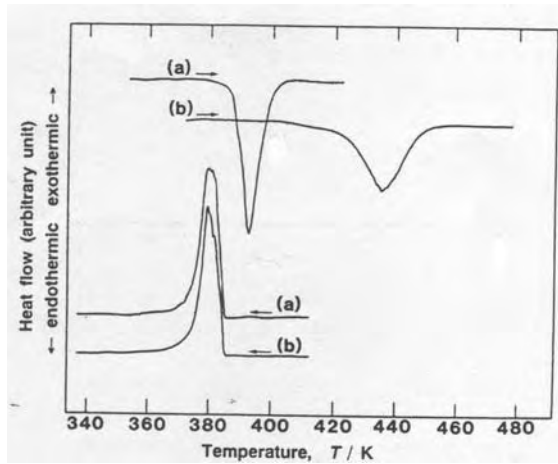
Figure 2.16: DSC curve of step quenched Cu-12.73wt%Zn-8.02wt%Al alloy for a) as step quenched condition and b) after subsequent ageing at 100°C for 56 days [54]
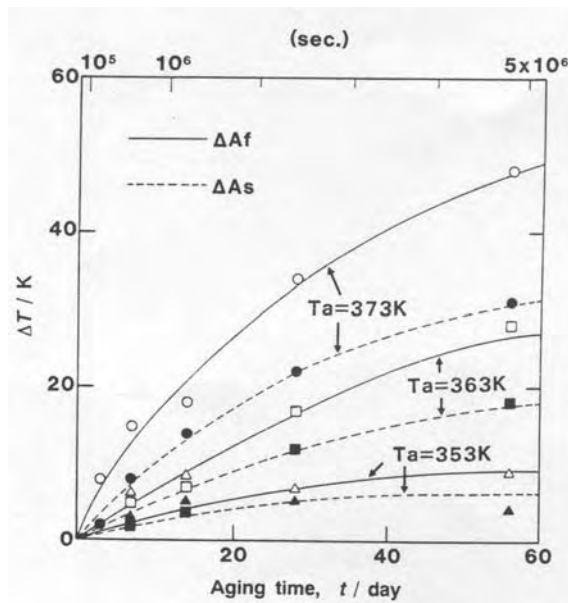
Figure 2.17: A_s and A_f temperatures as a function of ageing time [54].

35

of shape memory property and increase in transformation temperatures by the decreased stacking fault density after martensite ageing. Similarly, Nakata et al. [54] have observed a change in stacking fault density during martensite ageing in a Cu-12.73wt%Zn-8.02wt%Al alloy. TEM studies have revealed M18R martensite crystal structure, many stacking faults and absence of precipitates in alloys which were either directly quenched into iced water after betatizing at 850°C for 5 minutes or step quenched into 150°C for 5 minutes and subsequently quenched into water, or aged at 100°C for 56 days after step quenching. Even though the morphology and crystal structure have not changed during ageing, decrease in stacking fault density after ageing was clearly observed. However, stacking fault density could not correlated with the degree of stabilization. In fact, the density of stacking faults is lowest in aged alloys while stabilization is most promoted in directly quenched alloys, which has lower stacking fault density than step quenched one.

2.4.2. Mechanisms of Martensite Stabilization:

In literature, two basic mechanisms are offered as possible origin of martensite stabilization: 1. Pinning of interfaces between the parent and martensite phases and/or martensite variant boundaries by quenched-in vacancies and/or precipitates and 2. Structural changes or atomic rearrangements in martensite such as long range order change, short range order change or reordering in martensite resulting in some change in the relative stability between parent and martensite. A very recently offered Symmetry Confirming Short Range Order (SC-SRO) Model is based on the atomic rearrangements mechanism rather than boundary or pinning effect.

2.4.2.1. Model Based On Pinning of Interfaces:

Pinning of interfaces between parent and martensite phases and/or between martensite variant boundaries by precipitates or excess quenched-in vacancies is the

first mechanism that is offered to be responsible of martensite stabilization. When martensite interfaces are pinned by precipitates, the martensite to beta transformation becomes more difficult and upon heating M$\rightarrow\beta$ transformation requires extra driving force, which is supplied by increasing the A_s and A_f temperatures. TEM observations in stabilized CuZnAl alloys have shown the presence of small precipitates at the variant boundaries as well as in the bulk martensite plates. Precipitates were identified as γ_2 in the samples aged at 100°C for 2 weeks and at 200°C for 3 days [56, 57].

Stabilization kinetics is mainly controlled by vacancy concentration. Vacancy pinning of interfaces as a result of migration of excess quenched-in vacancies into martensite plate boundaries [58-61] and partially immobilizing them requires an extra driving force for M$\rightarrow\beta$ transformation upon heating. Since pinning of boundaries do not cause a change in relative stability of martensite and parent phases, T_0 remains the same. Therefore an increase in A_s temperature i.e., superheating $\Delta T = A_s - T_o$, is necessary to supply the extra driving force. Migration energy of quenched-in vacancies in CuZnAl alloys has been measured by positron annihilation, which is a direct technique to measure vacancy concentration and its change during stabilization. Migration energy of vacancies in beta phase and in martensite phase are found as 0.65±0.03 eV [62] and 0.80±0.03 eV [63], respectively. Wang et al. [64] examined the behavior of quenched-in vacancies in a Cu-25.75wt%Zn-4.01wt%Al alloy by positron annihilation technique. After betatizing at 850°C for 10 minutes, the samples were either quenched directly into ice water or step quenched into 150°C for 3 minutes and then into ice water. According to their experimental results, high quenched-in vacancies and vacancy clusters remained at room temperature in directly quenched samples. Encounter of those vacancies and clusters with moving coherent boundaries in thermoelastic martensite causes destruction of coherence of the interface thus weakening the shape memory effect of samples. Vacancies annihilated and vacancy clusters collapsed to become dislocation loops with increasing temperature. Dislocation loops also obstruct the reverse transformation deteriorating shape memory property.

Conversely, in step quenched samples while holding at step quenching temperature vacancies with enough energy and mobility migrate long distances to the vacancy sinks rather than merging into vacancy clusters. Migration of vacancies also enables the parent phase to reach an equilibrium degree of ordering, which is inherited by martensite. Therefore, stabilization cannot occur easily in step quenched martensites. Kong et al. [65, 66] compared the vacancy behavior in Cu-26wt%Zn-4wt%Al and Cu-14wt%Al-4wt%Ni alloys during low temperature ageing by means of positron annihilation and electrical resistivity measurements. They have made use of the Doppler broadening parameter (s parameter), which reflects the vacancy concentration and its change in a way that the increase of the dimension of vacancy clusters can induce, an increase of s parameter. During ageing in the martensitic state after direct quenching, experimental results show that s parameter of CuZnAl alloys first increases and then decreases while that of CuAlNi alloys remains unchanged. For directly quenched CuZnAl alloys electrical resistivity increases with ageing time when they are aged below A_s temperature, in contrary, no obvious change in resistivity is detected in CuAlNi martensites during ageing at low temperatures. From s parameter measurements the formation energy of vacancy clusters in CuZnAl alloys is found as 0.41 eV. They concluded that clustering of vacancies in the early stage of ageing in directly quenched specimens resulting in the reduction in degree of ordering is the main factor responsible of martensite stabilization in the CuZnAl alloys. No vacancy clustering occurs in CuAlNi alloys during low temperature ageing as indicated by both unchanging s parameter and resistivity values. The immobility of vacancies and difficulty of vacancy cluster formation in CuAlNi martensite may be related to crystal structure and strong bonding force between Al and Ni atoms. These results clearly explain the lower stabilization susceptibility of CuAlNi alloys.

Xuan et al. [67] observed a large number of Moiré patterns together with partial dislocations and prismatic dislocation loops in a directly quenched Cu-25.83wt%Zn-3.96wt%Al alloy. They suggested that the observations may be associated with clustering of quenched-in vacancies on close packed $(001)_M$ planes

causing distortion of neighboring lattice planes by forming partial dislocations or producing sessile dislocation loops by collapse of vacancies. All these factors act as impediments to atomic movements during reverse transformation and result in stabilization of martensite. In step quenched alloys fewer Moiré patterns observed since annealing of vacancies during step quenching does not allow clusters on close packed planes.

2.4.2.2. Models Based On Structural Changes In Martensite:

Neither Martensite nor Beta is equilibrium phases in reversible, diffusionless M$\leftrightarrow\beta$ transformations. Therefore, it is not surprising to observe structural changes or atomic rearrangements in these states during ageing manifested by martensite stabilization that is reflected as increase in A_s and A_f temperatures. The most cited structural changes in literature are Long Range Order (LRO) Change [54, 68-72], Short Range Order (SRO) Change [53, 73-75] and martensite reordering [26, 76-78]. When one of these arrangements takes place during martensite ageing, relative stability of martensite increases as compared to the parent phase and A_s and A_f temperatures increase. In the following, models based on LRO change, SRO change, reordering in martensite and finally Symmetry-Conforming Short Range Order (SC-SRO) [39, 40, 79-81] are summarized.

LRO change: Martensites of Copper-based alloys are not thermodynamic equilibrium phases and they can be obtained only by quenching. Thus they decompose into equilibrium or more stable states whenever diffusion is possible i.e. ageing. Equilibrium LRO for parent phase may not be the equilibrium LRO for martensite when inherited to martensite through diffusionless transformation during quenching. During ageing, the as quenched martensite changes its degree of LRO until reaching the equilibrium state for martensite. The new equilibrium attained causes a change in free energy of martensite and lowered free energy of martensite

39

results in rise of A_s and A_f temperatures. In CuZnAl alloys, stabilization is described by the interchange of Cu and Zn atoms on nearest neighbor sites, leading to a decrease in long range order [41, 68]. Nakata, Yamamoto and Shimizu [54] have determined the atom sites by Alchemi method [82-85] in a martensitic Cu-12.73wt%Zn-8.02wt%Al alloy. When step quenched and directly quenched alloy samples were aged at 100°C for 28 days, first nearest neighbor Cu and Zn atoms changed their positions during ageing. However, atom arrangement of β phase did not change in a parent phase Cu-13.09wt%Zn-8.86wt%Al alloy aged at 200°C for 30 minutes. Observed increase in A_s and A_f temperatures after ageing in martensite phase, which is not observed after ageing in parent phase has been ascribed to interchange between first nearest neighbor Cu and Zn atoms. In a Cu-14.58wt%Al-4.10wt%Ni alloy Ni atoms were found to be occupying nearest neighbor sites around Al atoms according to Alchemi results. This preferential occupation of Ni atoms is related to the strong binding force between Ni and Al atoms. Increase in transformation temperatures after ageing at 250°C for 1 hour has been attributed to ordering between next nearest neighbor Cu and Al atoms, in other words, progress of ordering from DO_3 into $L2_1$ [72]. Hosihiguchi et al. [69] have observed a decrease in degree of LRO by X-ray studies in a Cu-26.84wt%Zn-3.76wt%Al alloy that is aged at room temperature. Decrease of LRO makes the transformation of disordered martensite into parent phase difficult and A_s temperature increases reducing the shape memory capacity. In the study of Cook and Brown [70] Cu-26wt%Zn-4wt%Al alloys, which are aged at 123°C and 140°C for 96 hours after water quenching from 800°C, show rise of transformation temperatures. They tentatively accepted order change is responsible for stabilization and they found an activation energy of 65±5 kJ/mole for changes in order. Recarte et al [71] aged a Cu-13.75wt%Al-5wt%Ni alloy at 200°C for 20 hours to 44 hours. They observed martensite crystal structure of 18R in the as quenched state while existence of both 18R and 2H in the aged samples. A_s and M_f temperatures observed to be increasing with increasing ageing time during ageing at this temperature. In internal friction spectra, two separated peaks were observed during heating run in the sample aged 20 hours at 200°C, contrary to single peak of the as quenched sample. Increase in

transformation temperatures attributed to two kinds of processes: either the precipitation of stable γ_2 phase or ordering reactions of metastable β phase. To distinguish the mechanism in progress, flash heating after ageing is applied to some of the samples. Flash heating temperature is chosen between B2 ordering temperature of 630°C and DO$_3$ ordering temperature of 508°C and also below the eutectoid temperature of 585°C. Internal friction curve of flash heated sample revealed the same spectrum obtained in the as quenched state, completely invalidating the effect of 44 hours ageing. Since the flash heating temperature was lower than eutectoid temperature, precipitation of stable α and γ_2 phases were expectable. But, since the accelerated shift of transformation temperatures expected to take place in case of γ_2 precipitation was not experimentally confirmed, they concluded that increasing degree of order at next nearest neighbor has stabilized the martensite with respect to β phase and caused rise of transformation temperatures.

SRO change: Short Range Ordering Model was first proposed by Ahlers, Barcelo and Rapacioli [73] to explain the rubber like behavior of SMA. Later, Marukawa et al. [53, 74, 75] used this model to elucidate both the martensite stabilization effect and the rubber like behavior. During B2→3R(L1$_0$) martensitic transformation, diffusionless lattice distortion brings some second nearest neighbor atoms of parent phase into first nearest neighbor positions of martensite, that alters the probability of finding a type of atom around the first nearest neighbor shell of a given atom. That is to say, martensitic transformation leads to a sudden change in short range order. According to this model, martensite has the same tendency to form more unlike atom pairs similar to parent and this tendency is the origin of martensite ageing. Consequently the disrupted degree of short range order increases again during martensite ageing. Such a change lowers the energy of the aged martensite with respect to original one and results in martensite stabilization. The basis of this model is the change of bond probability during martensite ageing. They predicted that the shear occurs along <100> direction of B2 instead of <110> and this brings about the changes in nearest neighbor relations of each atom so that number of

nearest neighbors increased from eight to twelve. Generally just after B2→3R transformation, the site occupation probability and the pair (bond) probability on neighboring sites may be far from the equilibrium values. Prolonged ageing brings the system to equilibrium. In other words, ageing results in short range order changes. However, in an ordered alloy, pair probability also determines the long range order parameter. Therefore, change of SRO inevitably causes a LRO change, too.

Martensite reordering: Reordering in martensite is suggested by the fact that x-ray measurements indicate change of lattice parameters of martensite reflecting the orthorhombic distortion in the basal plane due to changes in ordering during ageing [77, 78, 86-88]. In long period stacking order martensite structures, when the atoms in the close packed {110} planes of β phase are arranged in a hexagon forming the basal plane of martensite the first and second layers shift by at 1/3 and 2/3 respectively, relative to the 0th layer along the [-110] direction of the parent phase, i.e., the [100] direction of the martensite phase. Consequently, the height of the unit cell along the c-axis can be determined from the number of close packed layers in different long period stacking orders. Moreover, since the c-axis forms a right angle relative to the 0th layer, long period stacking structures are generally described as "orthorhombic lattices". However, since the radii of two kinds of atoms forming the superlattice are generally unequal, the close packed planes of this long period stacking order structures form a close packed structure, which is, strictly speaking, slightly deformed. To be precise, the atoms within the close packed planes are not arranged in exact hexagons. The first and second layers are therefore stacked in positions slightly displaced from 1/3 and 2/3 relative to the 0th layer. Consequently, the c-axis cannot maintain a right angle relative to the 0th layer and a slightly inclined monoclinic lattice results. [89, 90]. Thus most of the martensites with long period stacking order structures, which occur in β phase alloys are not orthorhombic, but instead monoclinic structures [91].

Suzuki et al. [77] have investigated the martensite stabilization in a Cu-11.51wt%Zn-9.02wt%Al alloy by x-ray studies. Splitting distance ρ between (12-2) and (202) peaks of 18R martensite demonstrates the magnitude of the orthorhombic distortion and is expressed as $\rho=(\sin^2_{\theta 1} - \sin^2_{\theta 2})$ [78, 87, 88]. It has been known that the extent of distortion in the close-packed plane increases with increasing degree of B2 order or with decreasing degree of $L2_1$ order and the nonideal axial ratios of the modified structure of martensite due to distortion in close packed planes result in splitting of certain diffraction peaks, which overlap in undistorted structure [92]. They have observed that orthorhombic distortion decreases in stabilized martensite with increasing temperature. They suggested that this distortion decreases with increasing degree of DO_3 order but the reason is not known. In the absence of orthorhombic distortion, (12-2) and (202) peaks of 18R martensite peaks coincide. Meanwhile, splitting of peaks in the stabilized condition can be explained as the decreased degree of DO_3 order, which stabilizes the martensite with respect to parent phase.

Scarsbrook et al [86, 93] have found a change in the monoclinic angle β during ageing of a stabilized M18R CuZnAl martensite. Deleay et al. [87] have observed increase in monoclinic angle β approaching 90° in stabilized CuZnAl alloys.

Symmetry Confirming Short Range Order: Ren and Otsuka [39] have categorized the common features of martensite ageing phenomena in their review. For the sake of finding one unified theory that explains all aspects of martensite stabilization effect and rubberlike behavior, simultaneously and can be applicable to all shape memory alloys they determined certain ageing criteria to illustrate, ageing should not be dependent on a change of martensite structure such as change of long range order and ageing must be common to many thermoelastic alloys, irrespective of their crystal structure or order-disorder state. Disregarding different aspects of ageing observed in different shape memory systems they tried to create a general and a simple mechanism insisting on generality being the most important criterion

for the prediction of a correct ageing mechanism, which governs their mentioned common features of ageing.

To explain their symmetry confirming short range order (SC-SRO) principle [40], they have started with their short range order parameter. Usually defined SRO parameters were in terms of the probability of finding one kind of atom in the nth (n=1,2,3….) nearest neighbor shell of a given atom, that can not describe atomic rearrangement within the same shell whereas it is this kind of atomic rearrangement responsible from martensite ageing. Therefore, SRO was defined in terms of the probability of finding one kind of atom or defect at some interatomic vector from a given atom.

$$\alpha_{lmn} = 1 - (P_i^B \mid_j^A)/x_B$$

where lmn are the coordinates of the interatomic vector between site i,j; $(P_i^B \mid_j^A)$ is the conditional probability that there is a B atom at site i if there is an A atom at j; x_B is the average concentration of B. Such shell probability based SRO parameters are established on crystal lattice and naturally they should posses certain symmetry properties. For simplicity, a schematic two-dimensional structure as seen in Figure 2.18 has been used to explain the SC-SRO principle but it is applicable to any three-dimensional structure because it is only related to symmetry.

For the defect B given in a high symmetry, square lattice, Figure 2.18-a, the four nearest neighbor sites 1,2,3,4 are equivalent to defect B. Thus, it is natural to expect that the probability of finding another defect B around the defect at site 0 has the same fourfold symmetry as the crystal symmetry, i.e. $P_1^B = P_2^B = P_3^B = P_4^B$, when in equilibrium. On the other hand, if the crystal has lower symmetry, rectangular lattice, the environment around B becomes less symmetrical and it is expected that $P_1^B = P_2^B \neq P_3^B = P_4^B$ when in equilibrium following the twofold crystal symmetry, Figure 2.18-b. Apparently, this symmetry consideration also applies to farther sites from B but the effect becomes weaker due to weakening of the influence of B on farther sites, which means a short range effect. In brief, when in equilibrium, the

44
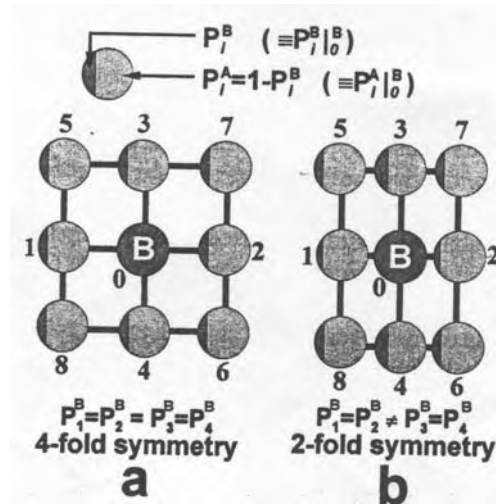
Figure 2.18: SC-SRO principle of point defects in crystals [40, 79].

probability of finding another point defect around a given point defect possesses the same symmetry as the crystal symmetry. This is the symmetry confirming short range order (SC-SRO) principle.

The mechanism of martensite ageing effect based on this SC-SRO principle can be explained by following the schematic illustration showing the statistical atomic configuration of an imperfectly ordered A-B alloy, Figure 2.19. Due to the fourfold symmetry of structure, the probability of finding a B atom around the A atom must hold the same fourfold symmetry in accordance with SC-SRO principle, i.e. $P_1^B = P_2^B = P_3^B = P_4^B$ and $P_5^B = P_6^B = P_7^B = P_8^B$ so Figure 19-a is the equilibrium parent phase. The martensite has a lower symmetry, so the equilibrium occupation probability of atoms should have the same symmetry as the structure about the A atom, i.e. $P_1^B = P_3^B \neq P_2^B = P_4^B$ and $P_5^B = P_7^B \neq P_6^B = P_8^B$ (after symmetry change, sites 1 and 3 are away from A atom while sites 2 and 4 are closer and in closer sites conditional probability of B atoms increase). When the parent phase shown in Figure 19-a transforms diffusionlessly into martensite, all the probabilities must

45

remain unchanged despite the symmetry change as seen in Figure 2.19-b. However, the occupation probability of the high symmetry configuration is no longer a stable configuration for the lower symmetry martensite structure. Then during ageing, such a configuration gradually changes by atomic arrangements into a stable one that conforms to martensite symmetry, Figure 2.19-c. When the stabilized martensite, Figure 2.19-c, is heated up and transforms back into the parent phase diffusionlessly, the stable SRO configuration for the martensite is inherited into the parent as seen in Figure 2.19-f which is not a stable configuration for the parent. From a thermodynamic point of view, this corresponds to an increased reverse transformation temperature. This is the origin of martensite stabilization.
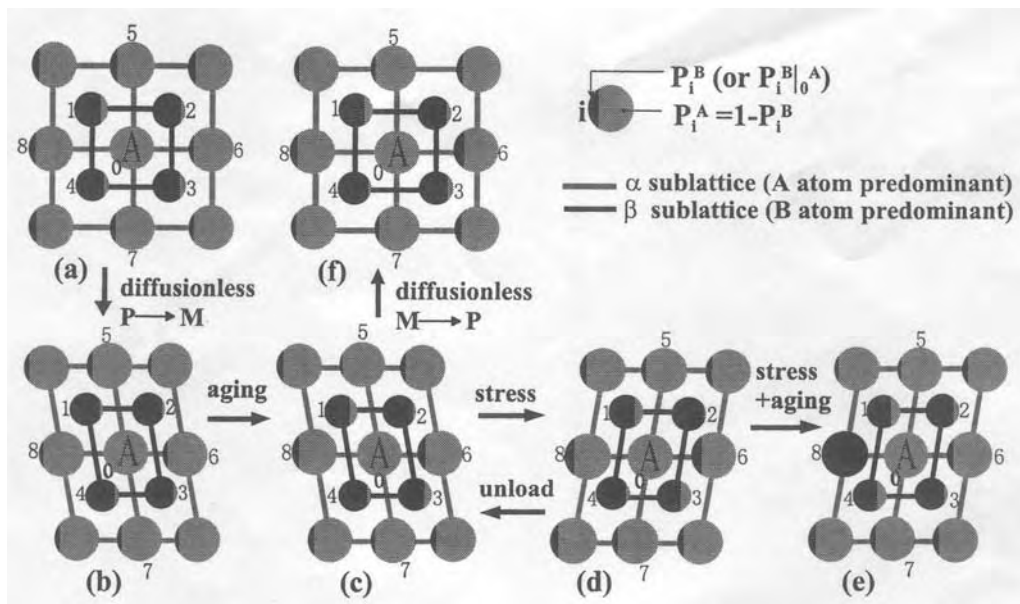
Figure 2.19: Schematized symmetry-confirming short-range order mechanism explaining martensite ageing effect and rubber like behavior [39].

They also explained the rubber like behavior [80]: When the stabilized or aged martensite, Figure 2.19-c, is deformed, it changes into another twin related variant. Since this twinning is also diffusionless, the atomic occupation probabilities shown in Figure 2.19-c are inherited into the variant as shown in Figure 2.19-e. When the external stress is released immediately after the loading, the new variant (2.19-d) reverts into the original one (2.19-c) by de-twinning because SRO of the new variant is not the equilibrium one. By this mechanism, the aged martensite can be deformed like a rubber. This is the origin of rubber like behavior. If the stress is held for some time, the atomic configuration in Figure 2.19-d has enough time to change into a stable configuration, Figure 2.19-e and no rubber like behavior will occur upon unloading.

Ren and Otsuka [80] have experimentally shown that no change in LRO occurs during isothermal ageing of AuCd alloy. Due to great sensitivity of electrical resistivity to changes in LRO in alloys, they used a four terminal electrical resistivity measurement to observe possible changes in LRO of AuCd alloy. However, no remarkable change in resistivity has been monitored and it has been concluded that if there was a change in LRO of martensite during isothermal ageing, this could have been observed as an obvious change in resistivity values.

2.5. Inhibition of Stabilization:

The main mechanism responsible from stabilization remaining without a definite answer drived researchers to develop practical methods for the prevention of stabilization. Since martensite stabilization is a diffusion-assisted phenomena accelerated by quenched-in vacancies, methods for inhibition of stabilization are based on the principle of reducing the extent of diffusion by immobilizing or reducing the concentration of vacancies. A usual way to avoid stabilization due to direct quenching is to perform quenching in a stepwise manner. Thus first quenching from betatizing temperature into a temperature generally $M_s < T_{SQ} < T_{DO3}$

and than quenching into water. This commonly used process is the very well known step quenching. Besides step quenching, hot rolling and thermal cycling are the methods offered to inhibit stabilization. By step quenching the quenched-in vacancies are annihilated, by hot rolling and thermal cycling dislocations introduced are as effective sinks for vacancies.

Leu and Hu [34] investigated the effects of different heat treatments i.e. direct quenching (DQ), Up-quenching (UQ), Step Quenching into Water Bath (SQWB) and Step Quenching into Oil Bath (SQOB) on shape memory property of a Cu-28.2wt%Zn-3.14wt%Al alloy. After betatizing all samples at 850°C for 5 minutes, they were directly quenched into RT water for DQ. For UQ, betatized and water quenched samples were immediately up quenched into an oil bath at 100°C for 10 minutes and quenched into RT water. For SQWB and SQOB, betatized samples were quenched into boiling water and oil bath at 100°C, respectively, for 10 minutes after betatizing and finally quenched into RT water. Heat treatments applied are schematically illustrated in Figure 2.20. Step quenching temperature below DO_3 ordering temperature and above M_s temperature provides accomplishment of DO_3 ordering and yields best results in terms of prohibition of martensite stabilization. Shape recovery of alloys has been tested by room temperature tensile tests. DQ and SQWB resulted in poor shape recovery due to martensite stabilization and α precipitation. After UQ and SQOB, excellent and stable shape recovery has obtained. Lu and Cao [76] determined the effective temperature range for step quenching to reduce martensite stabilization extensively. In a Cu-14.84wt%Zn-7.75wt%Al alloy, after betatizing the specimens at 800°C for 5 minutes, they were step quenched into salt or oil bath at different temperatures for 2 or 5 minutes and finally quenched into RT water. Afterwards their resistances measured and resistance vs. temperature curves was prepared and variations of relative amount of martensite reversion (RAMR) and transformation temperatures were determined by these curves. They found that step quenching temperature (T_s) below M_f or above T_{DO3} is similar to direct quenching and martensite stabilizes as implied by zero RAMR. When T_s is between M_s and M_f or between DO_3 ordering

48
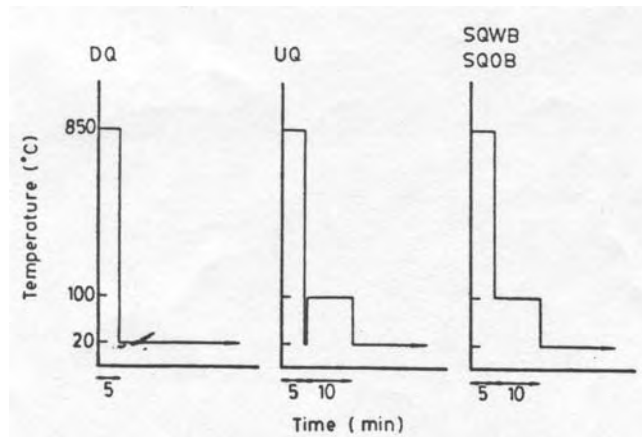
Figure 2.20: Schematics of various heat treatments [34].

start and finish temperatures, part of the martensite stabilizes as indicated from change of RAMR and A_s, A_f temperatures. If T_s is between M_s and DO_3 ordering finish temperatures, stabilization is completely avoided as can be understood by maximum RAMR and stable transformation temperatures. They suggested that in this temperature range equilibrium ordering DO_3 structure will be attained hence martensite obtained subsequent to step quenching will have equilibrium degree of ordering and will be stable. Scarsbrook et al. [93] interpreted the step quenching and direct quenching in an aged CuZnAl alloy as follows: when the material is quenched to above M_s temperature, the quenched-in vacancy population allows the parent phase to achieve its equilibrium order and then rapidly decays. This rapid decay of vacancy population provides that on the subsequent martensite transformation the vacancies are not high enough to allow rapid reordering of this martensite to one of the higher stability one. On the other hand, quenching directly into martensite results in the retention of a high vacancy population, which may activate any structural change lowering its energy and rising transformation temperatures.

Xuan et al. [67] investigated the extent of ordering and its relation to step quenching. In a Cu-25.8wt%Zn-3.96wt%Al alloy, they estimated the lattice spacing difference Δd of some pairs of diffracting planes with indices satisfying the relation $(h_1^2 - h_2^2)/3 = (k_2^2 - k_1^2)/n$, which reflects the degree of ordering in martensite. Since Δd increases with the degree of ordering, it can be used to express the degree of ordering of the β type martensites. They found that degree of DO_3 ordering evidenced from increase of Δd, increases with the holding time at step quenching temperature. During step quenching between M_s and T_{DO3} temperatures $B2 \rightarrow DO_3$ ordering occurs. They optimized the holding time at step quenching temperature as 1000 seconds, ≈ 17 minutes.

One of the most interesting finding on the inhibition of stabilization has been reported by Duan and Stobbs [94]. They have shown that hot rolled Cu-Zn-Al alloys are hardly stabilized even after ageing for one and a half years. Stabilization is inhibited in the presence of high density line defects since they act as sinks and reduce the amount of vacancies that could otherwise accelerate and contribute to diffusion. They observed lowering of the transformation temperatures in the hot rolled samples as compared to step quenched ones and attributed this to the higher elastic stored energy of both parent and martensite phases due to the presence of dislocations generated by hot rolling. Nevertheless, not all kinds of dislocations seems to be inhibiting stabilization as Duan and Stobbs have reported that dislocations introduced by low temperature fatigue do not seem to cause inhibition as much as rolling does. Wolska et al. [95] have extended this work to determine whether the temperature of rolling and the amount of deformation also play a role in inhibiting stabilization. Their results can be summarized as: for a given deformation temperature, the material that is deformed more is less prone to stabilization and for a given amount of deformation, the material that is deformed at a lower temperature suffers less from stabilization. In brief, higher amounts of deformation and lower deformation temperatures provide the best combination to inhibit stabilization according to Wolska's study.

The stability of transformation characteristics can be gained by successively repeated forward and reverse transformation, i.e. thermal cycling. Changes of transformation temperatures resulting from thermal cycling will be explained in the following section. Electrical resistivity and DSC studies indicate that thermal cycling stabilizes part of martensite plates. It has also been demonstrated that thermal cycling introduces dislocations. The locations where martensite crystals are nucleated can be determined by the structure of these dislocations. Moreover, the final crystals disappearing during reverse transformation correspond to the same locations where they nucleated. Briefly, nucleation processes are strongly affected by thermal cycling. Since the dislocations introduced during thermal cycling harden the parent phase and raise the critical stress for slip, the dislocations become more difficult to move as the number of cycles increase. As a result, after about ten cycles, slip deformation becomes more difficult to induce in the forward and reverse transformations and the density of dislocations settles to a constant value. Further changes in transformation temperatures can hardly be detected. Thus, stabilized properties can be obtained by thermal cycling a specimen prior to use in an application. The origin of the effects of thermal cycling is basically creation of dislocations [96].

In brief, because of decreasing the concentration of excess quenched-in vacancies step quenching is preferable over direct quenching. The optimum step quenching temperature range is between M_s and T_{DO3} temperatures and the optimized step quenching time is 15-20 minutes. When step quenching is done above M_s temperature, excess quenched in vacancy concentration is not as much as that in the direct quenching but high enough to allow the parent phase achieves its equilibrium order. On the other hand, during direct quenching retention of excess quenched-in vacancies may activate any structural change in martensite and lower the energy of martensite relative to parent phase so that transformation temperatures increase. The logic behind hot rolling and thermal cycling used in the inhibition of stabilization is the introduction of dislocations, which are effective sinks for vacancies and easy nucleation sites for martensite.

2.6. Thermal Cycling Effects in Copper Based Shape Memory Alloys:

In literature of thermal cycling effects in copper-based SMA's, cycling experiments are mostly devoted to life prediction and enhancement efforts and hence involve large number of cycles. There is only very limited study on early stages of thermal cycling and first peak anomalies. It has been shown many times that thermal cycling introduces dislocations, which establish favored nucleation sites for thermoelastic martensite through repeated thermal cycling. Changes in transformation temperatures have been reported and those changes reach saturation after a certain number of cycles so thermal cycling may be used in inhibition of stabilization to a certain extent. In CuZnAl alloys, M_s and A_f temperatures increase while M_f and A_s temperatures remain constant with increasing number of thermal cycles, i.e. couple of hundreds cycles, as opposed to controversial results in CuAlNi alloys where decrease in M_s and A_f temperatures [97], increase in all temperatures [98], increase in M_s and A_s temperatures [99] by thermal cycling are some of the contradictory examples from CuAlNi alloys. Briefly, whatsoever the sense of transformation temperature change in alloys due to thermal cycling, it has been mostly attributed to enhancement of martensite nucleation due to dislocations introduced by thermal cycling.

2.6.1. Changes Observed After Thermal Cycling:

The transformation temperatures and thermal hysteresis behavior of a Cu-29wt%Zn-3wt%Al alloy have been determined by electrical resistance measurement [100]. Specimens were cyclically transformed between 38°C and -20°C for 400 cycles. Electrical resistance versus temperature hysteresis behavior of the alloy for 3rd, 60th, 180th, 300th and 400th thermal cycles can be seen in Figure 2.21. It is apparent that transformation temperature characteristics have changed during cycling as follows: M_s and A_f temperatures increased while M_f and A_s temperatures remained constant. Additionally, the area of the hysteresis loop

decreased with cycling. Finally, with increasing number of cycles, the electrical resistance of beta phase increased whereas electrical resistance of martensite remained constant. The resistance change has been explained as the martensite to beta reversion being incomplete and some martensite retaining above the A_f temperature Martensite retained with cycling reduces the total extent of thermoelastic transformation. The unrelaxed elastic strain accompanying the transformation could act to stabilize the martensite. The relative amount of this retained martensite can be estimated from Figure 2.21 such that the height between A_s and M_s temperatures should be proportional to the amount of martensite undergoing reversible transformation. Variation of M_s and A_f temperatures and relative amount of transforming martensite as a function of number of cycles are shown in Figure 2.22. It is clear from this figure that those changes resulting from cycling ceased at approximately 300 cycles.
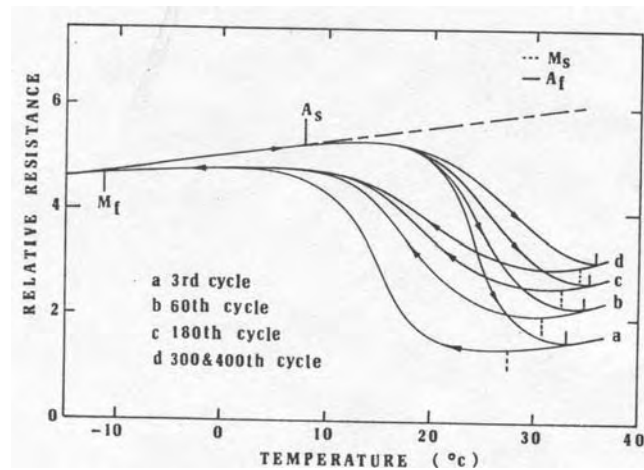
Figure 2.21: Electrical resistance versus temperature hysteresis behaviour of the Cu-29wt%Zn-3wt%Al alloy for 3rd, 60th, 180th, 300th and 400th thermal cycles [100].
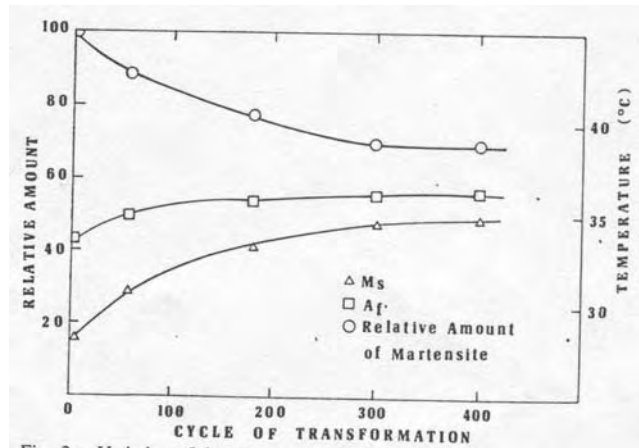
Figure 2.22: Variation of M_s and A_f temperatures and relative amount of transforming martensite as a function of number of cycles in the Cu-29wt%Zn-3wt%Al alloy [100].

Perkins and Muesing [101] have studied thermal cycling effects on transformation temperatures and transformation characteristics of a Cu-26.75wt%Zn-4wt%Al alloy. After betatizing at 900°C for 15 minutes and water quenching, the alloy samples were thermally cycled between -33°C and 67°C about 20 times. Temperature changes in the DSC profiles with cycling are schematically shown in Figure 2.23. As a result of thermal cycling, calorimetric data have revealed that M_s and A_f temperatures increased, M_f decreased and A_s is virtually unaffected. The increasing width of the martensite and parent peaks is related mainly to shifts of M_s and A_f temperatures. Changes of M_s, A_f, M_f and A_s temperatures with increasing number of cycles are illustrated in Figure 2.24. TEM observations indicated generation of dislocations in multiple-cycled samples. Through repeated transformation those substructural dislocations are believed to establish favored nucleation sites for thermoelastic martensite. It is very well known and shown many times that one of the characteristics of thermoelastic martensitic transformation is that each plate in the microstructure appears in the same place each time during

54

cooling the alloy from M_s to M_f. The plates appear in the same sequence on cooling and revert from the exact position on heating i.e. the first plate formed is the last to revert and so on. Finally, the increase in M_s temperature is explained by the argument that as the preferred sites are stimulated by repeated cycling, they become more prominent so that martensite nucleates more readily, thus M_s increases. As can be clearly seen from Figure 2.24, the shift of M_s temperature is much more than that of A_f temperature. This can be explained by considering that $\beta \rightarrow M$ transformation depends on nucleation of new martensite crystallites from the parent beta phase whereas the $M \rightarrow \beta$ transformation does not. Instead, $M \rightarrow \beta$ reversion takes place simply by the shrinkage of the existing martensite crystallites back to parent phase. After about 10-12 thermal cycles, the cycling effects have been observed to saturate. Generation of dislocations with cycling has been shown by TEM studies in CuZnAl alloys, which are thermally cycled 50 [102] and 250 [103] times.
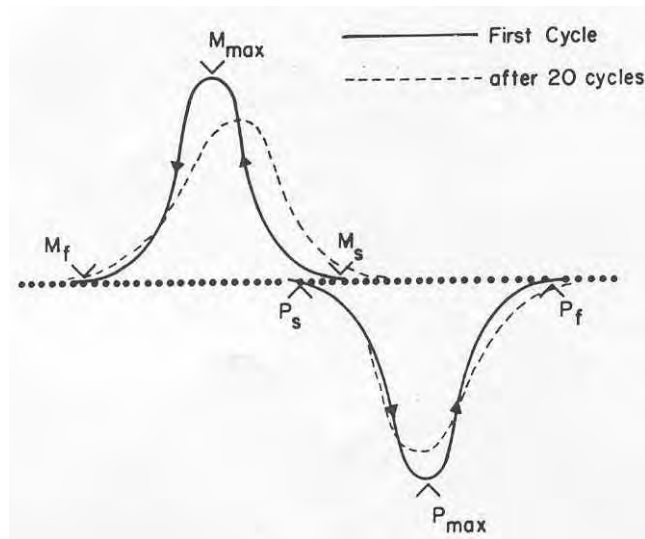
Figure 2.23: Summary of changes in M_s, M_f, A_s, A_f temperatures of a Cu-26.75wt%Zn-4wt%Al alloy after 20 thermal cycles on a schematic DSC curve [101].
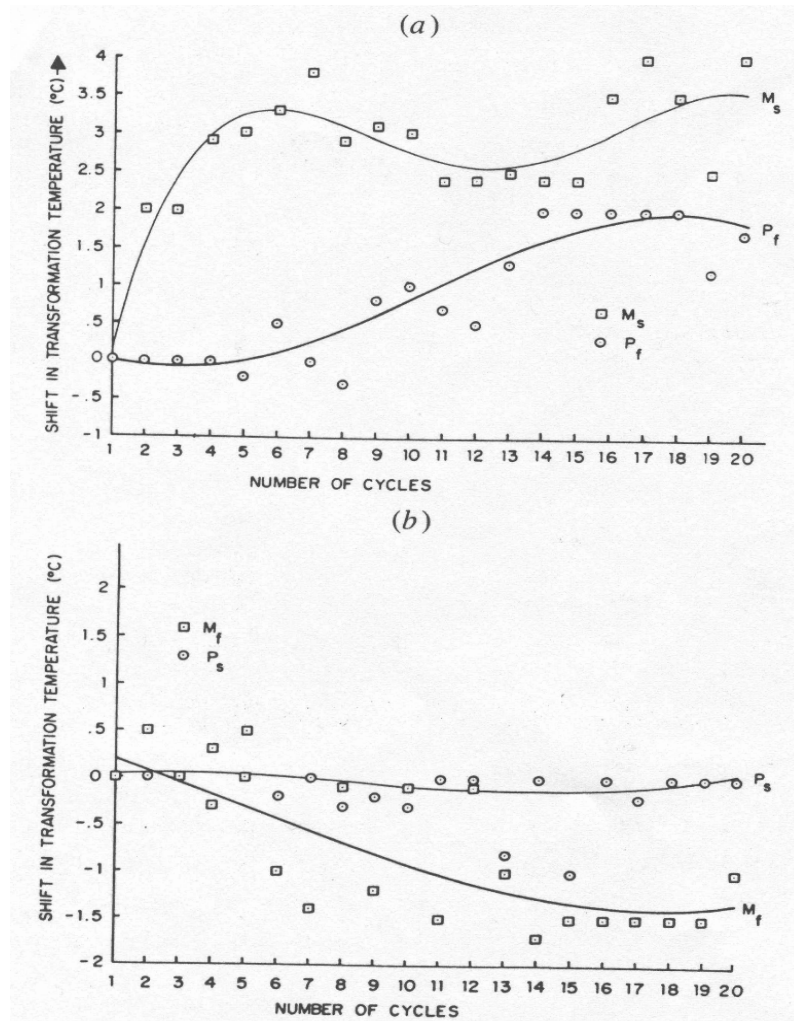
Figure 2.24: Variation of a) M_s, A_f, b) M_f and A_s temperatures with increasing number of cycles in a Cu-26.75wt%Zn-4wt%Al alloy [101].

Tadaki et al [104] have examined the thermal cycling effects in a Cu-14.4wt%Zn-9.2wt%Al having DO_3 structure with M_s= -93°C and a Cu-30.8wt%Zn-2.9wt%Al having B2 structure with M_s= -18°C. They have concluded that, with increasing thermal cycle, M_s temperature of B2 alloy increases while that of DO_3 alloy decreases. Amount of change is at most 10°C and 15°C after 10^3 cycles, respectively. High dislocation densities are accumulated in parent phases of both alloys with cycling. The dislocation density appears to be much higher for B2 alloy than DO_3 alloy. By thermal cycling, disordering is found to occur in parent phases

56

of both B2 and DO$_3$ alloys as manifested from the change in intensity of superlattice reflections with cycling. Above mentioned changes in M$_s$ are considered to be due to disordering.

Pons et al. [105] analyzed the dislocations formed in a Cu-17.48wt%Zn-7.5wt%Al alloy, which has been thermally cycled up to 200 times. The dislocations produced by thermal cycling were mixed type dislocations with u=<111> and b=<100>. Dislocation density is observed to increase with increasing number of cycles. Optical microscopy observation of the martensite plates of the non-cycled and 200 times cycled samples have revealed that the cycled samples showed more uniformly distributed and thinner martensite plates as expected from high density of dislocations. The role of dislocations in changing transformation temperatures has been mainly associated with relative chemical free energy changes of parent and martensite phases due to the different energies of dislocations when they are embedded in each phase and to the energy of additional faults created in martensite by some of these dislocations.

Font et al. [106] have studied thermal cycling effects in three alloys with compositions Cu-12.4wt%Al-3.2wt%Ni-2wt%Mn-0.03wt%B (alloy A), Cu-11.8wt%Al-3.1wt%Ni-3.1wt%Mn-0.03wt%B (alloy B) and Cu-13wt%Al-4.5wt%Ni-0.004wt%B (alloy C) which have been subjected to one of the following heat treatments: 1) annealing at 797°C for 20 minutes and water quenching, 2) treatment one followed by ageing at 297°C for 15 minutes in a molten salt bath and water quenching, 3) annealing at 797°C for 20 minutes and air cooling. For alloys A and B, peak transformation temperatures measured in DSC show an increase of 7°C independent of thermal treatment after 60 thermal cycles. For alloy C, for heat treatment 1 the same increase of 7°C was detected but for treatment 2 a very slight increase with cycling was observed. The CuAlNiMnB alloys were also thermally cycled in temperature range of 130°C-230°C, which can be high enough to activate the diffusional processes in the beta phase. The process most likely to occur is the improvement of the degree of next-nearest neighbor ordering by reorientation of

wrong pairs of atoms. The exchanged pairs of atoms are retained after the completion of one cycle. When the new cycle begins, the parent phase would start having a slightly better degree of order than previous cycle and leading slightly higher transformation temperatures. For a repetitive thermal cycling, this effect is cumulative, causing a step-by step ageing of parent phase that could be responsible for gradual increase of transformation temperatures.

Nakata et al. [97] have examined the thermal cycling effects in a Cu-13.7wt%Al-4wt%Ni alloy having M_s= 24°C. Both M_s and A_f temperatures decreased gradually with increasing number of cycles; a decrease of 40°C after 10.000 cycles was found. The rate of decrease in transformation temperatures has slowed down after about 4000 cycles. TEM investigation has resulted in increased dislocation density with cycling. At the end of 10.000 cycles, there was no characteristic structure other than dislocations. Moreover, martensite plates tend to become smaller with increasing number of cycles. They found that the degree of DO_3 order decreases with thermal cycling and this fact leads to decrease of transformation temperatures. In order to determine the change in the degree of order by cycling, intensity ratios of four superlattice reflections to the one fundamental reflection have been measured as a function of number of cycles. The degree of DO_3 order decreased after thermal cycling. Decreasing rate of change in transformation temperatures after about 4000 cycles has been explained as disordering of DO_3 structure. Gao et al. [98] have investigated the effect of thermal cycling on transformation temperatures of a C-15wt%Al-7wt%Ni-0.5wt%Mn-0.5wt%V alloy. All transformation temperatures increased about 20°C after 50 thermal cycles. Observed Vanadium –rich precipitates in the as-quenched samples were held responsible from the increase of the transformation temperatures due to cycling. Morris and Gunter [99] have studied the effect of heat treatment and thermal cycling on transformation temperatures of a Cu-12wt%Al-4wt%Ni-3wt%Mn-0.1wt%B alloy. Alloy samples were either betatized at 820°C for 30 minutes and directly quenched into water or this treatment is followed by an additional annealing at 300°C for 30 minutes and air cooling and they were thermally cycled 8-10 times.

At the end of eight thermal cycles, they have observed 10-20°C increase in M_s and A_s temperatures in the directly quenched alloys on the other hand in the annealed and air cooled samples the increase was only 5-7°C. The increased stability of transformation temperatures observed in the annealed specimens has been attributed to the increase of order obtained by annealing treatment. The incomplete order obtained by the direct quenching leads to a fast change in transformation temperatures during cycling of quenched samples. The post-quench increase in transformation temperatures in CuZnAl alloys has also been attributed to incomplete $L2_1$ ordering resulted from direct quenching [107].

2.6.2. Early Thermal Cycling Effects:

Subjects of early stage cycling and anomalous first DSC cycle peaks in relation to thermal cycling effects in copper-based alloys are not emphasized sufficiently in literature and the importance of subject is overlooked.
.
Perkins and Muesing [101] have mentioned, but not in detail, that DSC peaks were quite noisy during initial cycling before reaching saturation. But the peaks smooth out as cycling proceeds. But, they have not introduced any experimental result, i.e. a DSC curve showing the noisy background. This was explained by a simple analogy of creating a trail through initially unbroken forest. The first time the path is taken, travel is difficult. However, as the path is traveled back and forth several times, the trail becomes more and more established and no further significant improvements in the trail are possible. Hsu, Wang and Wayman [10] have studied thermal cycling effects in α/β CuZn brasses. M_s temperature increases about 8°C in the second cycle and then increases very gradually on further cycles. The large difference in M_s temperature between the first and second cycles is considered to be due to a change of internal strain field. The α phase is softer than β matrix, thus deformed by shape strain of martensitic transformation. On the other hand, α particles retard the martensitic transformation, which increases the elastic strain energy of the system.

Thus, a larger driving force, i.e. a lower M_s temperature, is required for transformation in the first cycle. Extra strain energy is released by plastic deformation of α particles, i.e. after the first cycle, internal strain field of system is changed due to deformation of them. Hence, no extra driving force is needed for overcoming the strain energy of deformation of α particles on further thermal cycles. That is the reason why M_s temperature is shifted higher in the second cycle but not in further cycles. Moreover, with increasing thermal cycles, the dislocation density is also increased which is closely related to the high reproducibility of martensite plate formation.

The first peak anomaly has been observed in the studies of Segui and Cesari [14] and Morris and Lipe [108]. A Cu-12.41wt%Al-3.14wt%Ni-2.03wt%Mn alloy [14] that is directly water quenched from 800°C. They showed that the first $M \rightarrow \beta$ transformation occurs at higher temperatures and spreads over a broader temperature range in the first thermal cycle as can be seen from Figure 2.25. It has been suggested that $L2_1$ quenched-in disorder was responsible of observed temperature shift. Quenching stresses may have partial contribution because air-cooled samples do not show temperature shift.

A Cu-12wt%Al-4wt%Ni-3wt%Mn-0.04wt%B alloy [108] quenched from 820°C has revealed a DSC curve with different behaviour between the first and second thermal cycles as clearly seen in Figure 2.26. They concluded that in the first cycle, martensite is stabilized subsequent to quenching probably because of excess strain energy accumulated at the interfaces hence reverse transformation requires increased transformation temperatures.

In the study of Font et al. [106], DSC curves of three alloys namely, A, B, C which are directly water quenched from 797°C and thermally cycled 60 times have shown temperature shifts about 30°C between first and second cycles as can be clearly seen from Figure2.27-a, b, c respectively. The authors have not made any comments on the mechanism occurring in the very early first and second cycles but only

considered changes starting from third cycle, disregarding the first two anomalous cycles.
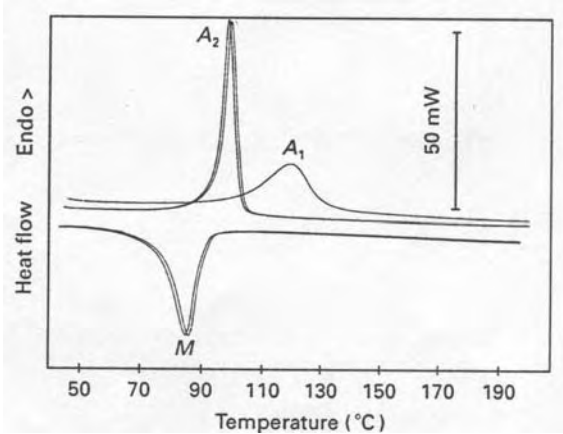
Figure 2.25: DSC curves of Cu-12.41wt%Al-3.14wt%Ni-2.03wt%Mn alloy showing two thermal cycles performed between 40-200°C [14].
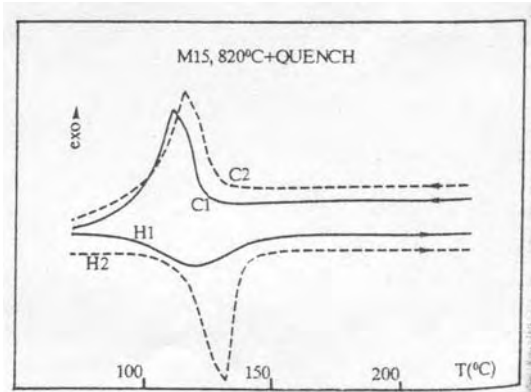
Figure 2.26: DSC curve of Cu-12wt%Al-4wt%Ni-3wt%Mn-0.04wt%B alloy showing two thermal cycles [108].
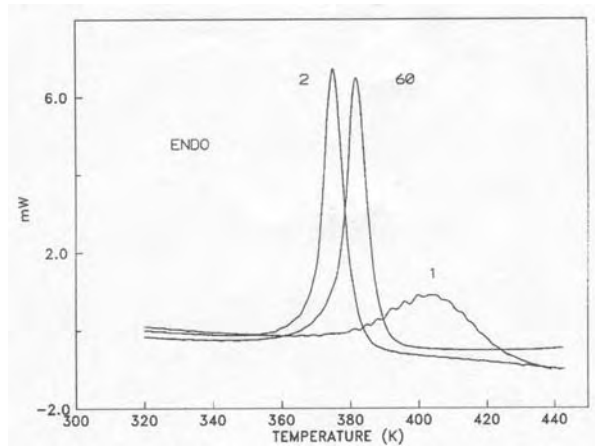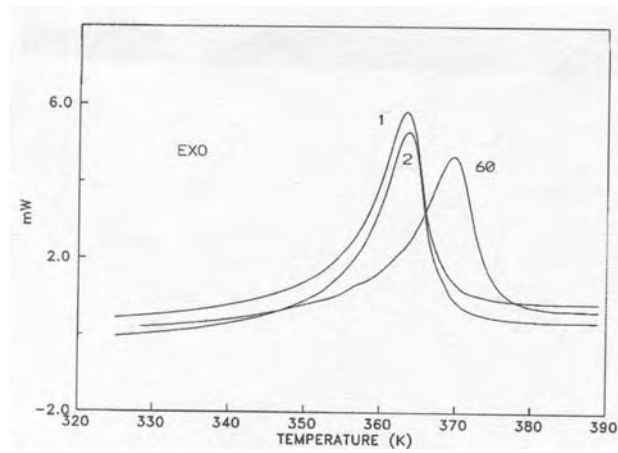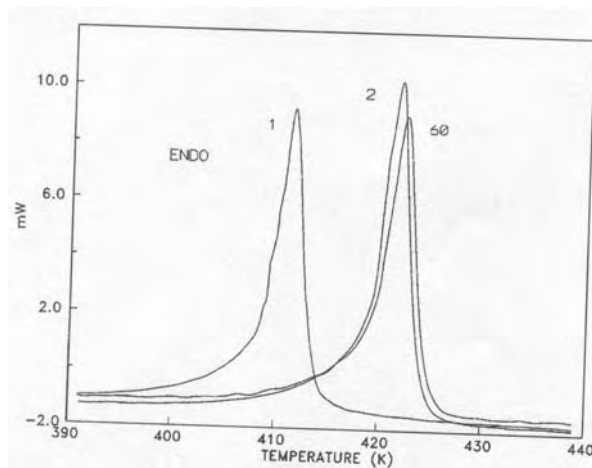
Figure 2.27: DSC curves of a) Cu-12.4wt%Al-3.2wt%Ni-2wt%Mn-0.03wt%B (alloy A), b) Cu-11.8wt%Al-3.1wt%Ni-3.1wt%Mn-0.03wt%B (alloy B) and c) Cu-13wt%Al-4.5wt%Ni-0.004wt%B (alloy C) alloys for cycles 1,2 and 60 [106].

CHAPTER 3

EXPERIMENTAL TECHNIQUE

3.1. Alloys:

CuAlNiMn and CuAlNi alloys investigated in the present study were produced from elemental metals in a laboratory type induction melting and centrifugal casting unit, namely Manfredi Neutromag Digital, under argon atmosphere at 1300°C and 1250°C, respectively, from charges of 25 gr. They were cast into 8 mm diameter cylindrical copper moulds. Composition of CuAlNiMn and CuAlNi alloys produced are shown in Table 3.1 and Table 3.2, respectively. Optical examination has revealed that the room temperature microstructure of all alloys is martensitic. Additionally, a Cu-18.5wt%Zn-6.4wt%Al alloy produced by melting electrolytic copper, electrolytic aluminum and commercially pure zinc in an induction furnace

Table 3.1: CuAlNiMn alloys and their compositions.

Alloy Code	Nominal Composition	EDS Composition
VD5	Cu-12%Al-5%Ni-2%Mn-0.6%TiB_2	Cu-12.7%Al-5.4%Ni-1.9%Mn-0.6%TiB_2
VD11	Cu-12.0%Al-5.0%Ni-2.0%Mn	Cu-12. 6%Al-5.9%Ni-1.8%Mn
VD12	Cu-12.4%Al-5.1%Ni-2.0%Mn	Cu-12.6%Al-4.8%Ni-1.1%Mn
VD13	Cu-11.9%Al-5.1%Ni-2.0%Mn	Cu-12.9%Al-5.0%Ni-2.2%Mn

Table 3.2: CuAlNi ternary alloys and their compositions.

Alloy Code	Nominal Composition	Composition
V1	Cu-13.0%Al-3.0%Ni	Cu-14.0%Al-2.5%Ni
V2	Cu-14.0%Al-3.0%Ni	Cu-13.9%Al-4.2%Ni
V3	Cu-13.0%Al-3.0%Ni	Cu-14.2%Al-2.7%Ni
V4	Cu-13.0%Al-3.0%Ni	Cu-13.6%Al-3.0%Ni

open to atmosphere, has been used for the preparation of kikuchi map of $18R_1$ martensite crystal structure.

3.2. Shaping of The Alloys:

Cast CuAlNiMn and CuAlNi alloy rods 8 mm in diameter were hot swaged down to 4.75 mm in two steps of about equal reductions about 40%, at 950°C.

Hot swaged CuAlNiMn and CuAlNi alloys were then hot rolled from 4.75 mm diameter down to 0.4 mm thickness in 11 steps by intermediate anneals at 950°C and 20% deformation between each step.

3.3. Metallography:

Specimens cut from alloys of each composition were betatized at 950°C for 10 minutes prior to water quenching to room temperature. Specimens were mounted, grinded, polished in two steps with 1 μm and 0.1 μm alumina and finally etched by a mixture of 15 gr $FeCl_3$ + 10 ml HCl + 120 ml alcohol.

Samples were examined under Vickers optical microscope and Jeol 6400 Scanning Electron Microscope. In SEM, also, areal EDS analysis were taken from three different regions to determine the approximate chemical composition.

3.4. Grain Refinement in Production of CuAlNiMn Alloys:

For grain refinement $AlTiB_2$ was also added to the charge but SEM studies showed that TiB_2 particles were not distributed homogeneously and remained as agglomerates throughout the matrix. TiB_2 particle clusters in Cu-12.7%Al-5.4%Ni-1.9%Mn0.6%TiB_2 alloy and their corresponding backscatter image are seen in Figure 3.1-a and b respectively.

<table>
<tr><td>a)</td><td>b)</td></tr>
</table>
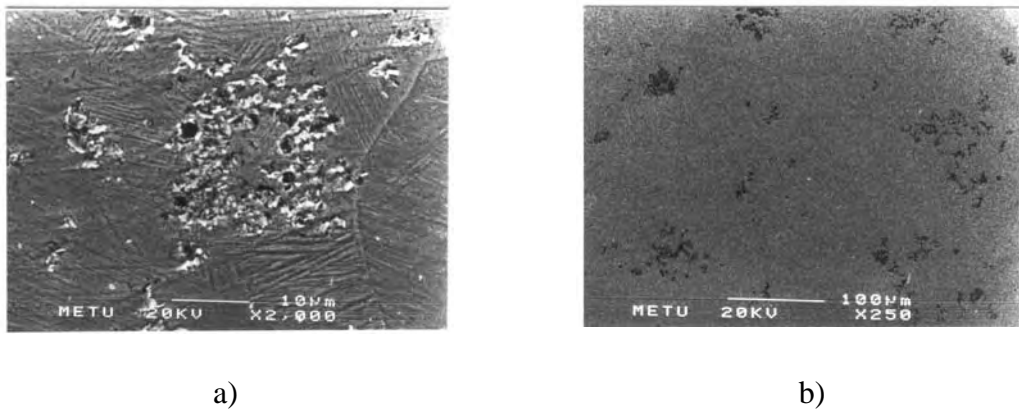
Figure 3.1: SEM microstructure of Cu-12.66%Al-5.43%Ni-1.94%Mn-0.6%TiB_2 alloy a) TiB_2 clusters in the martensite matrix, 2000X. b) backscatter image of TiB_2 clusters, 250X.

Martensite microstructure of grain refiner free Cu-12.6%Al-5.9%Ni-1.8%Mn alloy is seen in Figure 3.2. SEM studies have shown that grain refinement of CuAlNiMn alloys were unsuccessful and the alloys were produced without $AlTiB_2$ addition except the Cu-12.66%Al-5.43%Ni-1.94%Mn-0.6%TiB_2 alloy (VD5).
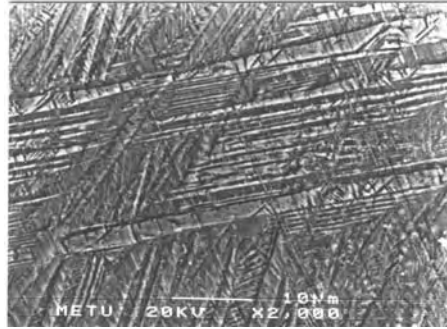
Figure 3.2: SEM image of martensite matrix in Cu-12.56%Al-5.93%Ni-1.78%Mn alloy, 2000X.

3.5. X-Ray Diffraction:

Crystal structures of the alloys were determined from X-ray diffractogrammes taken in a Phillips Diffractometer PW 1352/20 DY871 (Model 1967) by Co-K_α radiation with a wavelength of 1.788965Å. Diffractogrammes in the $2\theta=20°-100°$ range were indexed by comparison with the master charts prepared for the possible martensite 2H, $18R_1$ and parent DO_3 crystal structures [10].

3.6. DSC Measurements:

Transformation Temperatures, i.e. M_s, M_f, A_s and A_f of the alloys were measured in Setaram DSC131 Differential Scanning Calorimeter under Nitrogen gas atmosphere. From the preliminary tests, temperature range of 30°C to 250/300°C, heating rate of 20 K/min and cooling rate of 10 K/min were found to be the optimum conditions for DSC testing of CuAlNiMn and CuAlNi alloys to determine the transformation temperatures. Due to strong composition dependence of the transformation temperatures of alloys, appropriate heating/cooling temperature ranges of each alloy were determined individually. Alloys have not been heated to

temperatures much higher than A_f to prevent unexpected and uncontrolled ageing. Heating rates had to be optimized because high heating rates often decrease the resolution of the adjacent peaks and at very low heating rates sensitivity decreases and even the peaks may completely disappear. Cooling rates were limited to 10 K/min since at higher rates the detection of M_s and M_f temperatures becomes impossible due to reduced response time of the instrument.

All DSC curves were blank test corrected. Sample sizes were between 20-60 mg. Figure 3.3 shows the transformation temperatures on a schematic DSC curve during heating and cooling runs. Transformation temperatures are determined by use of the software program of the Setaram DSC131 instrument. Extrapolated onset and extrapolated offset temperatures (see Appendix A) of M→β and β→M transformation curves are taken as A_s, M_s and A_f, M_f temperatures, respectively.

3.7. Ageing Experiments:

A laboratory type furnace with a resistance embedded heating cell produced from castable alumina was used for the ageing experiments carried out at temperatures up to 300°C. A 12 cm diameter stainless steel reservoir was used as silicon oil bath. Because of the high heat capacity and low thermal conductivity of silicon oil, furnace temperature remained stable even in case of temporary power shortage. Temperature control of ageing furnace was done by a Copper-Constantan thermocouple activated on-off temperature controller and an electronic variac.

Ageing experiments were done mainly in two groups: Martensite phase ageing and Beta phase ageing. For Martensite phase ageing, both CuAlNiMn and CuAlNi alloy samples were aged at selected temperatures of 80°C, 100°C, 120°C and 150°C, where they were martensitic ($T<M_f$), for 24, 72, 144 and 312 hours. For Beta phase ageing, CuAlNiMn and CuAlNi alloy samples were aged at selected temperatures
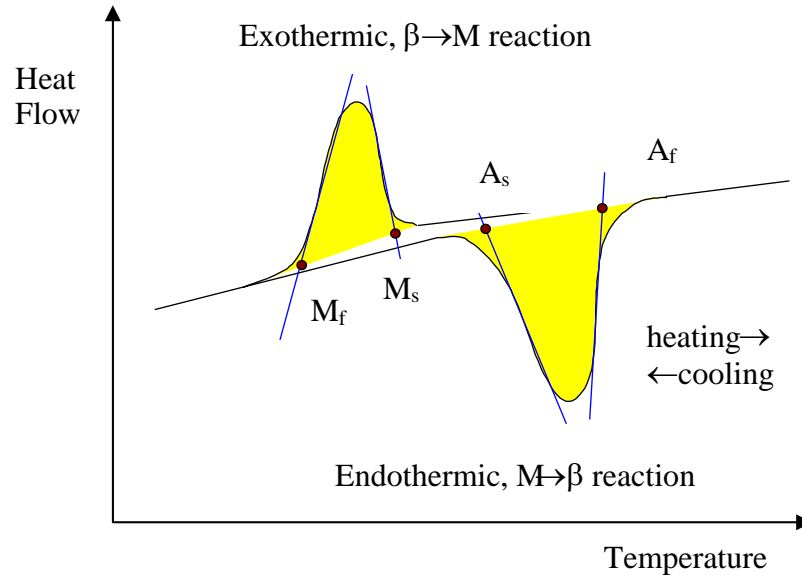
Figure 3.3: Schematic DSC curve showing critical transformation temperatures.

of 200°C, 230°C, 250°C and 270°C, where they were Beta (T>A$_f$), for times up to few hours depending on the chosen ageing temperature.

Ageing times were cumulative for each sample to prevent the unexpected random changes in transformation temperatures observed after each betatizing treatment on the same sample as will be explained in section 4.3. In other words, each isothermal ageing has been carried out on the same sample of the alloy by taking ageing times cumulatively, which is contrary to the conventional practice of using a new sample of the alloy for each selected ageing period in isothermal ageing experiments. This is to prevent random changes in transformation temperatures due to betatizing treatment. Prior to ageing experiment, each of the betatized and water quenched alloy sample was thermally cycled three times to obtain reproducible transformation temperatures and the same sample is used throughout the isothermal ageing experiments for varying times.

Since eight different temperatures, namely, 80°C, 100°C,120°C, 150°C, 200°C, 230°C, 250°C and 270°C were choosen for ageing experiments, there were eight different samples of the same alloy having eight different transformation temperatures at the end of thermal cycling. Transformation temperature of a particular alloy is determined by taking the transformation temperatures referring to the end of third thermal cycle and averaging those eight temperatures. For eight different samples of the same alloy, average of first cycles is taken as the transformation temperatures of the first thermal cycle. The same approach has been repeated for the second and the third cycles. Transformation entalphies of alloys for M→β and β→M transformations has been calculated by the same method.

3.8. Transmission Electron Microscopy:

TEM studies were performed in a Jeol JEM 100 CX-II Transmission Electron Microscope equipped with a side entry double tilt goniometer with a tilt capacity of ±30° and operated at 100 kV. Specimens to be subjected to crystallographic and morphological studies in TEM were prepared by first punching into 3 mm discs from hot rolled 0.4 mm thick alloy strips and then grinding them down to 100μm thickness. Thin foils were perforated by electropolishing with an electrolyte of 35%HNO_3+65%Methanol at about -30°C with 0.8 ampere, 8V, flow rate of 3 and sensitivity of 8-9 in a Struers-Tenupol-3 Double Jet Electropolisher. Perforated thin foils were finally washed in methanol.

Two beam bright field (BF) and centered dark field (DF) imaging techniques were used to investigate the microstructure and morphology of the phases of interest.

CHAPTER 4

RESULTS AND DISCUSSION

4.1. Transformation Temperatures of Alloys:

The average transformation temperatures of the three CuAlNiMn and four CuAlNi alloys prior to ageing at eight different temperatures were presented in Table 4.1. To obtain reproducible transformation temperatures, prior to ageing each alloy has been subjected to three thermal cycles in the range RT to 250°C (see section 4.4). This resulted in eight different samples of the same alloy having eight different sets of transformation temperatures. Average transformation temperatures presented in
.

Table 4.1: Average transformation temperatures of CuAlNiMn and CuAlNi alloys.

Alloy	A_s	A_f	M_s	M_f
VD11	152±4	174±5	158±4	141±2
VD12	145±4	166±5	149±5	133±5
VD13	180±6	198±6	179±4	165±5
V1	225±1	240±1	225±1	210±1
V2	108±5	124±6	110±5	95±4
V3	127±2	146±2	132±3	116±3
V4	164±2	182±2	168±2	152±2

Table 4.1 were calculated by taking the transformation temperatures of each sample referring to the end of third thermal cycle and averaging them.

Transformation temperatures of alloys were calculated by use of the software program of DSC instrument. A_s, M_s, and A_f, M_f temperatures were determined from the conventionally used extrapolated onset and offset temperatures, respectively. Although the use of extrapolated onset and offset temperatures was universal in thermal analysis community, where mostly chemical reactions rather than phase transformations have been studied, it might have been better to use onset and offset temperatures (point of deviation from baseline) rather than extrapolated temperatures for the interpretation of anomalous effects in DSC curves of diffusionless martensitic transformations. But to prevent the subjectiveness of the choice of deviation point and obey the general trend in DSC community, extrapolated values were used. The transformation temperatures of the individual CuAlNiMn and CuAlNi alloys corresponding to the end of third cycle were shown in Appendix B.

Transformation temperatures of alloys VD11, VD12, V2, V3 and V4 followed the order of $M_f < A_s < M_s < A_f$ and that of alloys VD13 and V1 followed the relation $M_f < A_s \approx M_s < A_f$ as shown schematically in Figure 4.1. The extent of thermal hysteresis and slopes of thermoelastic curves were presented in Table 4.2.
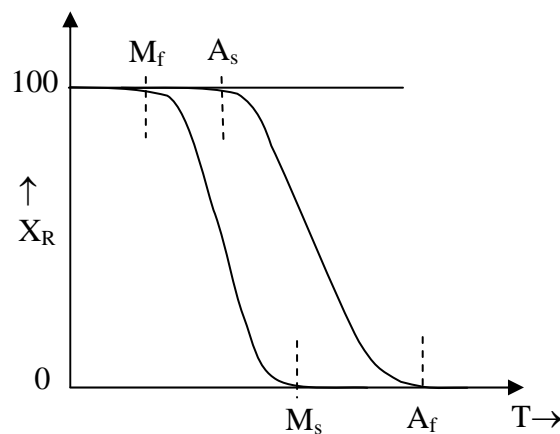
Figure 4.1: Schematic Fraction Transformed (%X_R) versus Temperature curve, showing transformation temperatures of A_s, A_f, M_s and M_f.

71

Table 4.2: Thermal hysteresis and slopes of thermoelastic transformation curves.

Alloy	$(M_s - M_f)$	$(A_f - A_s)$	$(A_s - M_f)$	$(A_f - M_s)$
VD11	17	22	11	16
VD12	16	21	12	17
VD13	14	18	15	19
V1	15	15	15	15
V2	15	16	13	17
V3	16	19	11	14
V4	16	18	12	14

Thermal hysteresis of thermoelastic curves for CuAlNiMn and CuAlNi alloys was 10-15°C in terms of the difference $(A_s - M_f)$ and 15-20°C in terms of the difference $(A_f - M_s)$ and did not show variation with alloy composition. $(A_s - M_f) \neq (A_f - M_s)$ indicates that slopes were different, which implied a difference in shape strains and unidentical transformation characteristics in forward and reverse reactions. Moreover, the difference of $(A_f - A_s)$ being greater than the difference of $(M_s - M_f)$ showed that shape strains formed during heating were greater than that of cooling. For thermoelastic martensitic transformations, $(A_s - M_f)$ and $(A_f - M_s)$ differences were the measure of hysteresis width and $(M_s - M_f)$ and $(A_f - A_s)$ differences are proportional to the slope of the transformation curve, which is the measure of transformation temperature interval, as can be seen from Figure 4.1. In nucleation and growth controlled first order martensitic transformations, thermodynamic equilibrium temperature between the martensite and the parent beta phase is T_0 where Gibbs free energy of both phases are equal and it is defined as $T_0 = 1/2 (M_s + A_f)$. Supercooling $\Delta T = T_0 - M_s$ is the undercooling necessary to initiate the nucleation of martensite. In a similar manner, a superheating is required for the reverse transformation. Starting of martensite nucleation is related mainly to the

magnitude of the driving force and availability of favorable nucleation sites. However, detailed mechanism of martensite nucleation is not yet well known and documented. Small hysteresis indicates that driving force necessary to compensate the shape strains are small and evidenced by steeper slope of martensite fraction transformed (X_M) versus temperature curve. Further undercooling supplied below M_s temperature is required for the growth of nucleated martensites. During growth of martensites formed in plate shapes, strain produced around the growing martensite plate increases volumetrically while the martensite volume increases planarly. Therefore, strain energy term will be the fast increasing term in proportion to r^3 while the bulk free energy term is proportional to r^2. If shape strain is large, plastic accommodation takes place around parent phase during growth and martensite interface loses its glissile nature due to plastic yielding and defects produced serve as nucleation sites for new martensite plates. Upon cooling, individual martensite plates grow quickly into their final size, no further growth occurs by drop of temperature instead new nucleation events occur and the slope of X_M versus temperature curve declines gently as well as increasing hysteresis width. In the case of small shape strain, shape deformation is accommodated elastically so that interfacial motions are reversible. Martensite crystals grow as the specimen is cooled until they meet another plate or grain boundary and then thicken until a thermoelastic force balance between Gibbs free energy change and elastic strain energy of martensite are maintained. Further cooling disrupts the equilibrium attained and martensite crystals begin to grow again. Even with ideal interfacial reversibility, there is a departure from reversibility due to lattice friction encountered by moving interface. This extra force requirement introduces hysteresis in the growth. Thus anything that raises the friction stress such as lattice defects due to plastic yielding will increase the transformational hysteresis. When shape strains are small, the slope of X_M versus temperature curve is steep and hysteresis width is small, i.e., ($M_s - M_f$) and ($A_f - A_s$) differences are small. Although both hysteresis and slopes is the indicator of martensite shape strain, hysteresis width is proportional to undercooling essential for nucleation of martensite while the slopes are related solely to shape strain generated during martensite growth.

4.2. Enthalpy Changes of Martensite→Beta and Beta→Martensite Transformations of Alloys:

Table 4.3 has been showing the average transformation enthalpies of alloys which were calculated for each particular alloy by averaging the enthalpy values of the eight samples for eight ageing temperatures at the end of the first, second and third thermal cycles. For the specific values see Appendix C. Enthalpy values were calculated from peak areas of DSC curves (peak area= m.K.ΔH) as J/gr. It has been observed that Martensite to Beta transformation (M→β) occurs by an endothermic reaction during the heating run while the reverse Beta to Martensite (β→M) transformation takes place by an exothermic reaction during the cooling run.

It was clear that, for all alloys, M→β transformation enthalpies were greater than that for the corresponding reverse β→M transformation. M→β and β→M transformations both occur diffusionlessly in thermoelastic alloys, following almost the same transformation paths during heating and cooling; in other words, in an ideally thermoelastic transformation, hysteresis and slopes are expected to approach to zero and infinity, respectively. The difference of enthalpies of the forward and backward transformations could have been attributed to the transformation temperature difference (≈15°C) if $(C_p)_\beta$ was greater than $(C_p)_M$. But nonexistence of a difference between the levels of the heat flow before and after transformation in DSC curves, indicated that, within the range of experimental errors C_p for Beta and Martensite were the same. Another reason for the enthalpy difference may be partial β→M transformation while all existing martensite transforms completely into Beta upon heating. This possibility, which requires a decrease in enthalpy with number of cycles, was not verified as seen in Table 4.3. And the last possibility was the inherent difference of the M→β and β→M transformations. As mentioned in section 4.1, $(A_f - A_s) > (M_s - M_f)$ showed transformation range of M→β transformation was wider than reverse transformation indicating that the transformation characteristics of M→β and β→M transformations were not identical. Higher enthalpies of M→β than β→M might be resulting from this fact,

Table 4.3: M→ β and β→ M transformation enthalpies of alloys for corresponding applied thermal cycles.

Alloy	Average sample mass (mg)	First Cycle		Second Cycle		Third Cycle	
		$\Delta H_{M\to\beta}$ (J/gr)	$\Delta H_{\beta\to M}$ (J/gr)	$\Delta H_{M\to\beta}$ (J/gr)	$\Delta H_{\beta\to M}$ (J/gr)	$\Delta H_{M\to\beta}$ (J/gr)	$\Delta H_{\beta\to M}$ (J/gr)
VD11	41.4±11.4	6.5±0.8	-6.9±0.8	8.5±0.4	-6.8±0.8	8,7±0.4	-7,2±0.7
VD12	38.7±3.1	7.1±0.8	-7.9±0.6	8.9±0.4	-8.0±0.7	8,8±0.4	-7,8±0.5
VD13	42.2±7.9	6.1±1.2	-7.0±1.1	7.8±1.1	-6.8±1.3	7,6±1.1	-6,4±1.1
V1	32.3±4.9	9.7±0.9	-8.7±0.5	10.8±0.4	-8.5±0.6	10,7±0.4	-8,8±0.6
V2	40.4±9.4	7.1±0.5	-6.4±0.7	7.5±0.3	-6.6±0.5	7,4±0.3	-6,5±0.4
V3	52.4±10.5	7.8±0.2	-7.8±0.9	8.4±0.3	-7.1±0.7	8,5±0.3	-7,0±0.5
V4	33.4±6.4	8.7±0.5	-8.1±0.4	9.6±0.5	-8.0±0.4	9,5±0.6	-8,0±1.0

and not related to martensite stabilization effect since enthalpy values were from unaged, only as quenched and thermally cycled alloy samples.

4.3. Effect of Betatizing on Transformation Temperatures of CuAlNiMn Alloys:

While checking the reproducibility of transformation temperature measurements, in addition to an increase in transformation temperatures of A_s and A_f in the M→β transformation by about 15-20°C between the first and second thermal cycles, it is observed that the same DSC sample yields different transformation temperatures after each betatizing treatment. One sample of Cu-12.6Wt%Al-5.9Wt%Ni-1.8Wt%Mn alloy has been three times successively subjected to the following series of treatments: betatizing at 950°C for 10 minutes, quenching into water and then thermal cycling twice in DSC. Transformation temperatures are found to change

inconsistently with each betatizing treatment. It is seen from Figure 4.2 that the M$\rightarrow\beta$ transformation in the first cycle takes place in a wide temperature range yielding an anomalous diffuse and serrated peak shape. Starting from second thermal cycle, M$\rightarrow\beta$ transformation curves become better defined and smooth as normally expected. Such diffuse and serrated peaks are not observed in $\beta\rightarrow$M transformation curves because the first $\beta\rightarrow$M transformation that occurs during quenching from betatizing temperature could not be recorded. The first $\beta\rightarrow$M transformation curves of Figure 4.2 are actually of the second $\beta\rightarrow$M transformation.

It is clear from Figure 4.2 that the transformation curves obtained after three successive betatizing treatments on the same sample are far from the anticipated similarity for the three cases and the variations are not systematic. Besides the aforementioned peculiarity of the peak shapes of the first Martensite$\rightarrow$Beta transformation, with each betatizing treatment the peaks of the second transformation are seen to be randomly shifted by as much as $\pm20°C$ relative to each other. To ensure that the observed discrepancy between experiments that differ only by a betatizing treatment is not an instrumental or experimental artifact, betatizing treatments under controlled argon atmosphere are repeated under closely controlled conditions, for different specimen geometries and sizes but the results has not changed.

Healing in shape of M$\rightarrow\beta$ curves with increasing number of thermal cycles can be interpreted as thermoelastic martensitic transformation can not takes place properly in the first cycle, complete thermoelastic nature can be gained only after second thermal cycle. The mechanism preventing thermoelastic martensite formation in the first cycle is not clear. Observed serrations imply the presence of a phenomenon producing obstacles in the martensite interface front, making transformation difficult and leaving those serrations behind. Early thermal cycling effects, diffuse and serrated first cycle DSC curve peaks are discussed further in section 4.4.
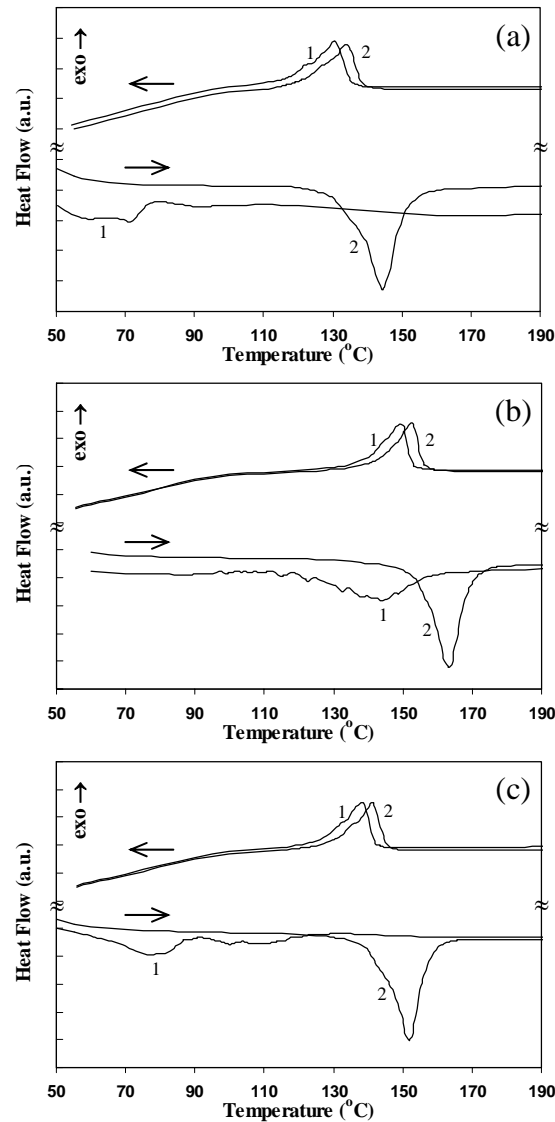
Figure 4.2:　　DSC curves of two thermal cycles of the same sample of alloy Cu-12.6wt%Al- 5.9wt%Ni-1.8wt%Mn after three successive betatizing treatments.

Obtaining random transformation temperatures on the same specimen may imply that each betatizing produces a new, different orientation distribution among the grains, which changes the constraining forces from neighboring grains during transformation. Although martensite variants will be forming in self-accommodating manner, each time a different strain distribution takes effect. As a result, after each betatizing, same sample yields different transformation temperatures.

There seems to be a contradiction that anomalies in peak shapes of first thermal cycles are only seen during M→β transformation. If this anomaly is attributed to formation of a new beta grain orientation, the same should be observed during β→M transformation but it was not. That is because the first martensite transformation while quenching from 950°C could not be observed in DSC and therefore not detected. If one would be able to observe actual first Beta→Martensite transformation curve, one would most probably observe the same unexpected, diffuse transformation range and serrations in the first martensite cycle as well. What are recognized as the first β→M transformation curves in Figure 4.2 are really the second β→M transformation curves.

Transformation temperatures of CuAlNi and CuAlNiMn alloys can be determined by DSC measurements even in the directly water quenched alloy samples as opposed to CuZnAl alloys, which suffer from strong martensite stabilization after direct water quenching and transformation temperatures can not be monitored during DSC runs in the as quenched samples and mostly transformation temperatures of those alloys could be displayed only after step quenching.

4.3.1. In-situ DSC Ageing Experiments:

Diffuse and serrated first cycle M→β transformation peaks of the DSC curves mentioned above, in view of the fact that they generally occur at low temperatures around 80°C, have been suspected to be a consequence of low temperature ageing itself during heating in DSC. To find out the basis of the serrations, in-situ DSC low temperature ageing experiment has been carried out on a VD11 alloy sample, which was in-situ aged at 80°C for 20 minutes, 1 hour, 2 hours and 3 hours. All experiments have been conducted on the same sample, which was rebetatized prior to each ageing experiment. Using the same sample eliminates the sample based variations but introduces betatizing and quenching effects, which might be the other alternative responsible of the occurrence of serrations. Upon completion of ageing
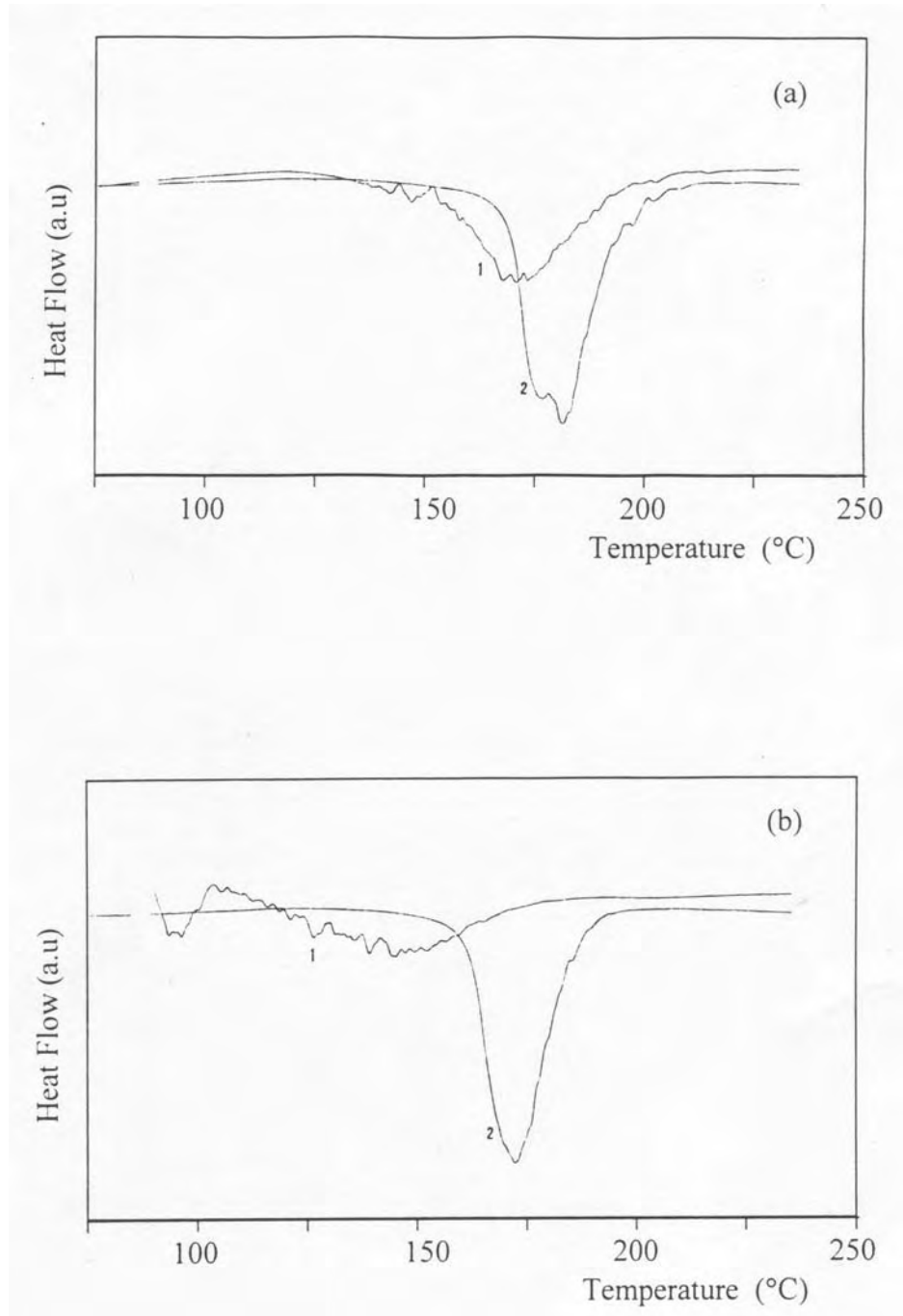
Figure 4.3: M→β transformation peaks of the VD11 alloy sample, which is in-situ DSC aged at 80°C a) just after betatizing and quenching prior to ageing, and after ageing at 80°C for b) 20 minutes, c) 1 hour, d) 2 hours and e) 3 hours, for the two applied thermal cycles.
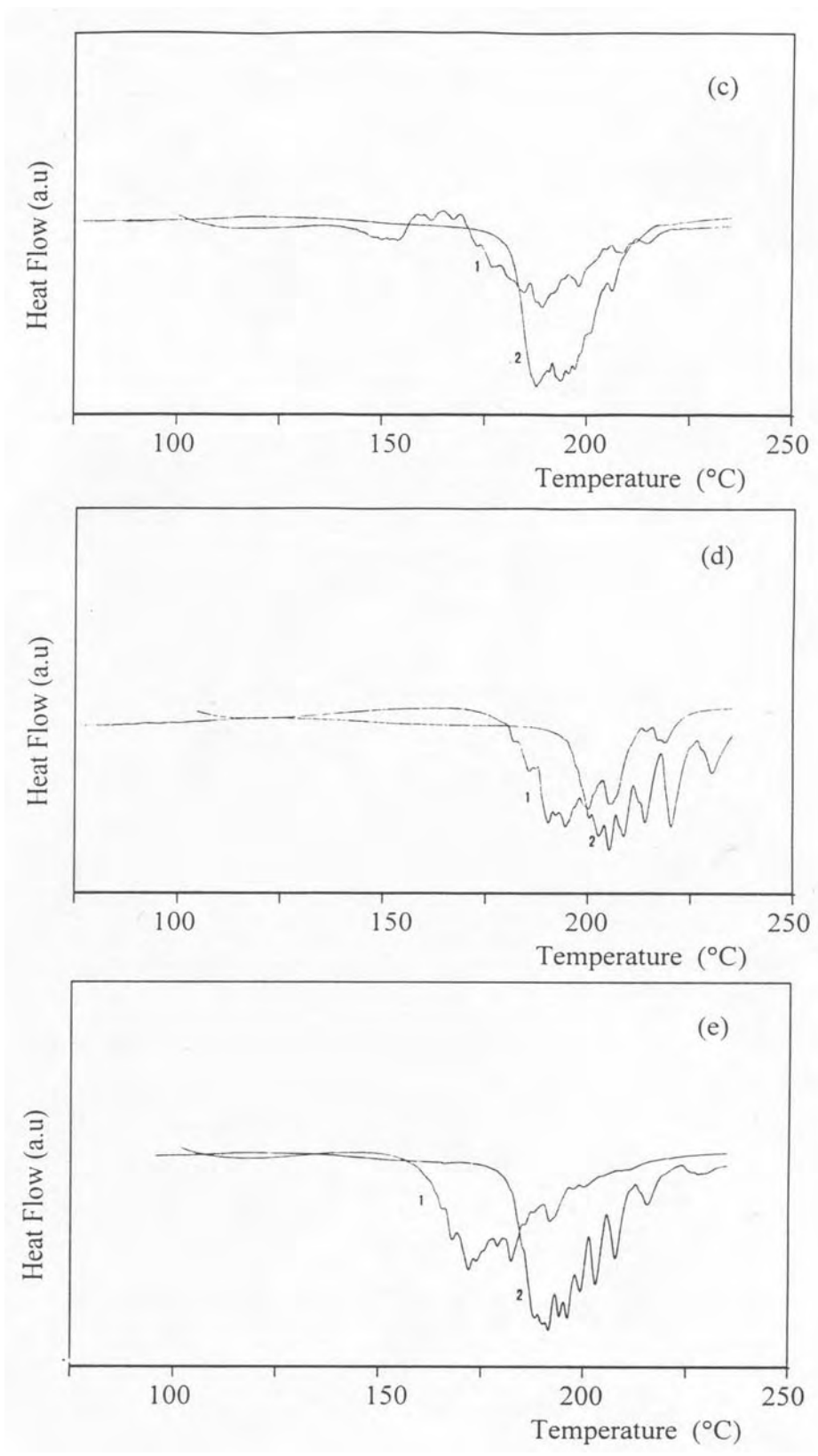
Figure 4.3: Continued.

periods in the DSC, without removing, the samples were heated and cooled to 250°C and 30°C to monitor the M→β and β→M transformations, respectively. This thermal cycling successively applied twice. Figure 4.3 shows M→β transformation peaks of the VD11 alloy sample just after betatizing and quenching prior to ageing, and after ageing at 80°C for 20 minutes, 1 hour, 2 hours and 3 hours, for the two applied thermal cycles. If microstructural changes due to low temperature ageing during heating were the origin of serrations, those changes would be completed during ageing prior to thermal analysis so that serrations observed during heating in DSC would disappear. However, experimental observations did not support the ageing model. It was clear in Figure 4.3 that serrations still existed after ageing as well as prior to ageing. Although in the non-aged and short time aged samples, serrations were absent in the second cycles, serrations persisted in the second cycle in sample aged for longer periods. It has been recognized that betatizing and quenching was the main factor for the existence of serrations, it should also be kept in mind that extended ageing at low temperatures might be contributing to activate serrations. Origin of serrations will be further discussed in section 4.4. One final remark with regard to Figure 4.3 was the effect of betatizing on transformation temperatures: through Figure 4.3 a to e, transformation temperatures of the same sample for the first cycles displayed five different values.

4.4. Early Thermal Cycling Effects on Transformation Temperatures of Alloys:

Prior to ageing experiments, each as quenched alloy sample has been thermally cycled three times in DSC to obtain thermally more stable, reproducible transformation temperatures and to eliminate the aforementioned anomalous effect of betatizing on the transformation temperatures. The term thermal cycling, here corresponds to heating and then cooling in Setaram DSC131 instrument in the temperature range of 30°C-250/300°C at a heating rate of 20 K/min and cooling rate of 10 K/min. Transformation temperatures recorded during the three thermal cycles

applied to CuAlNiMn and CuAlNi alloys are tabulated in Appendix D and E, respectively.

Superimposed DSC curves of M→β transformation during the first three thermal cycles for the eight samples (prior to ageing at eight different temperatures of 80°C, 100°C, 120°C, 150°C, 200°C, 230°C, 250°C and 270°C) of each of the three CuAlNiMn alloys are illustrated in Figure 4.4. For all three CuAlNiMn alloys, a rise of 15-20°C has been observed in A_s and A_f temperatures between the first and second thermal cycles. The rise in the transformation temperatures is observed to decrease progressively after second cycle and there was only 1-2°C rise in A_s and A_f temperatures between the second and third thermal cycles. As mentioned in section 4.3, first cycle peak anomalies disappear after the first cycle. Transformation temperatures tabulated in Table 4.4 and illustrated in Figure 4.5 for all three cycles are the averages of the values from eight samples of the same alloy. Compared to M→β transformation temperatures that increase by 15-20°C between the first two cycles, during the first two cycles of β→M transformation M_s and M_f temperatures have been observed to change only by 1-2°C. As mentioned previously, this is because the first DSC cycle of β→M transformation is, in reality, recalling the β→M transformation during quenching from 950°C, is the second β→M transformation. Hence, the three cooling DSC cycles are in fact the second, third and fourth β→M transformation cycles of the samples.

CuAlNi alloys, as opposed to CuAlNiMn alloys, do not exhibit any serrations or diffuse transformation ranges for the first thermal cycle i.e., the shape of the first thermal cycle is smooth and free from anomalies. Superimposed DSC curves of M→β transformation during the first three thermal cycles for the eight samples (prior to ageing at eight different temperatures of 80°C, 100°C, 120°C, 150°C, 200°C, 230°C, 250°C and 270°C) of each of the four CuAlNi alloys are illustrated
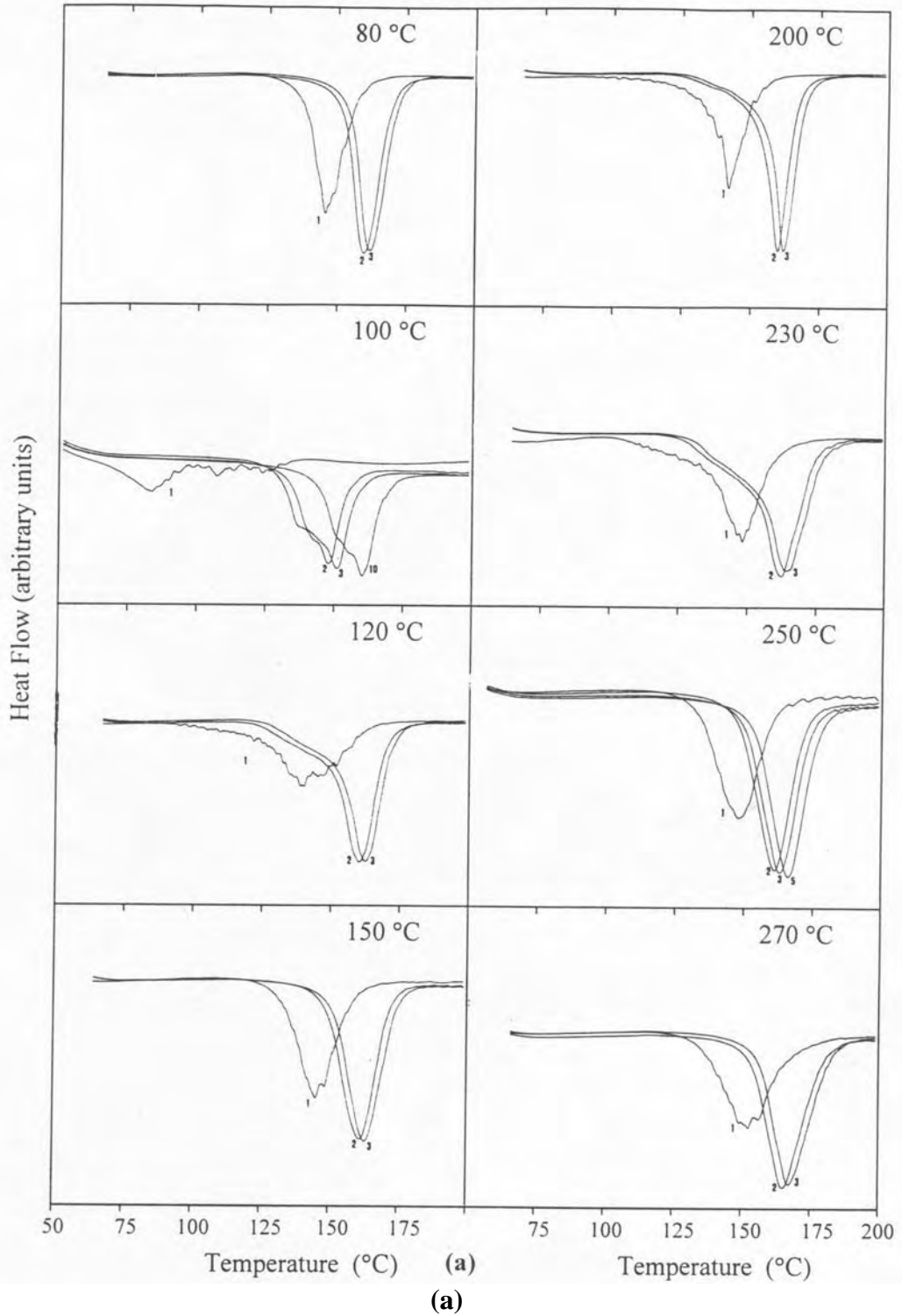
Figure 4.4: Superimposed DSC curves of M→β transformation during the first three thermal cycles for the eight samples (prior to ageing at eight different temperatures of 80°C, 100°C, 120°C, 150°C, 200°C, 230°C, 250°C and 270°C) of each of the three CuAlNiMn alloys a) VD11, b) VD12, c) VD13.

83
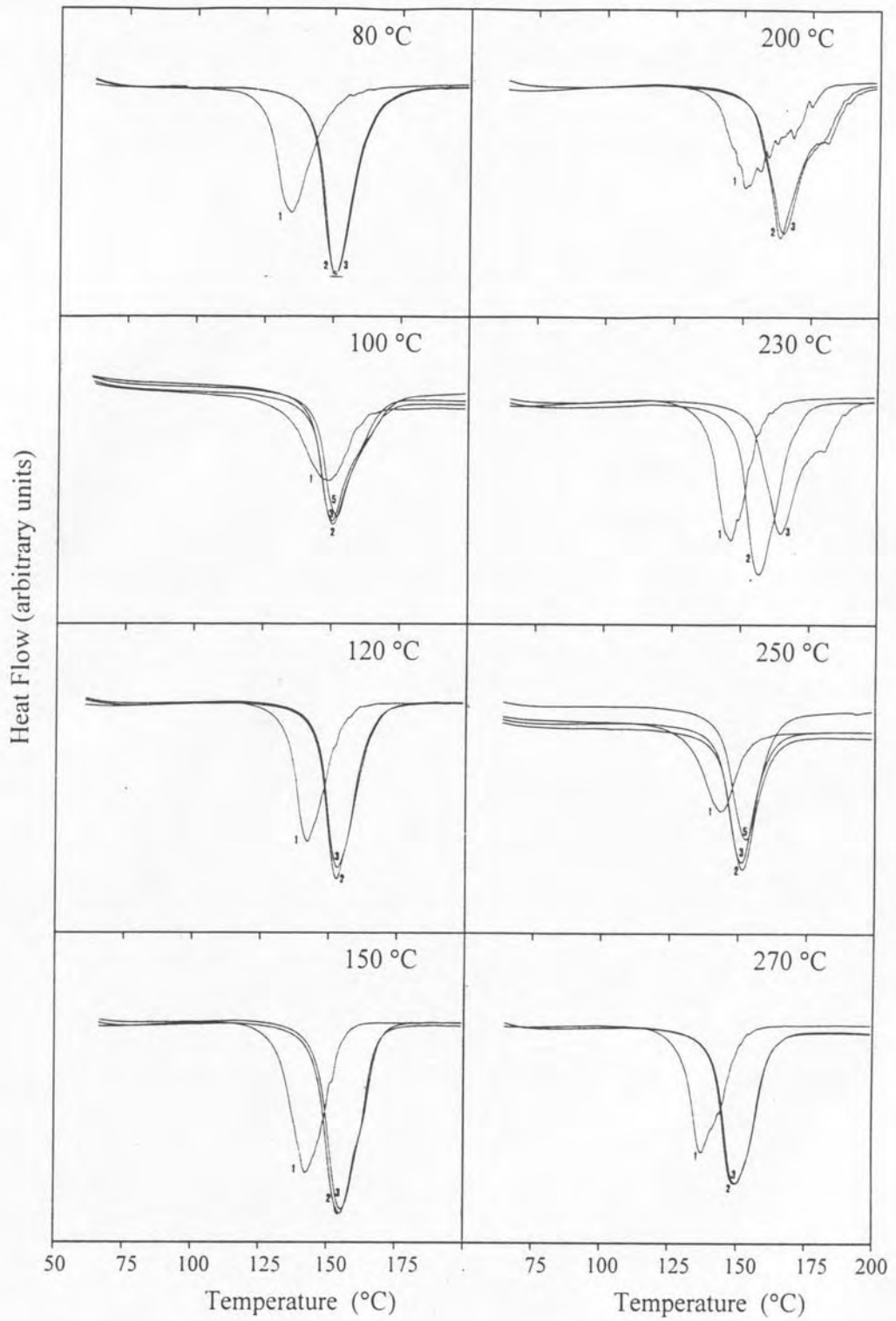
(b)

Figure 4.4: Continued
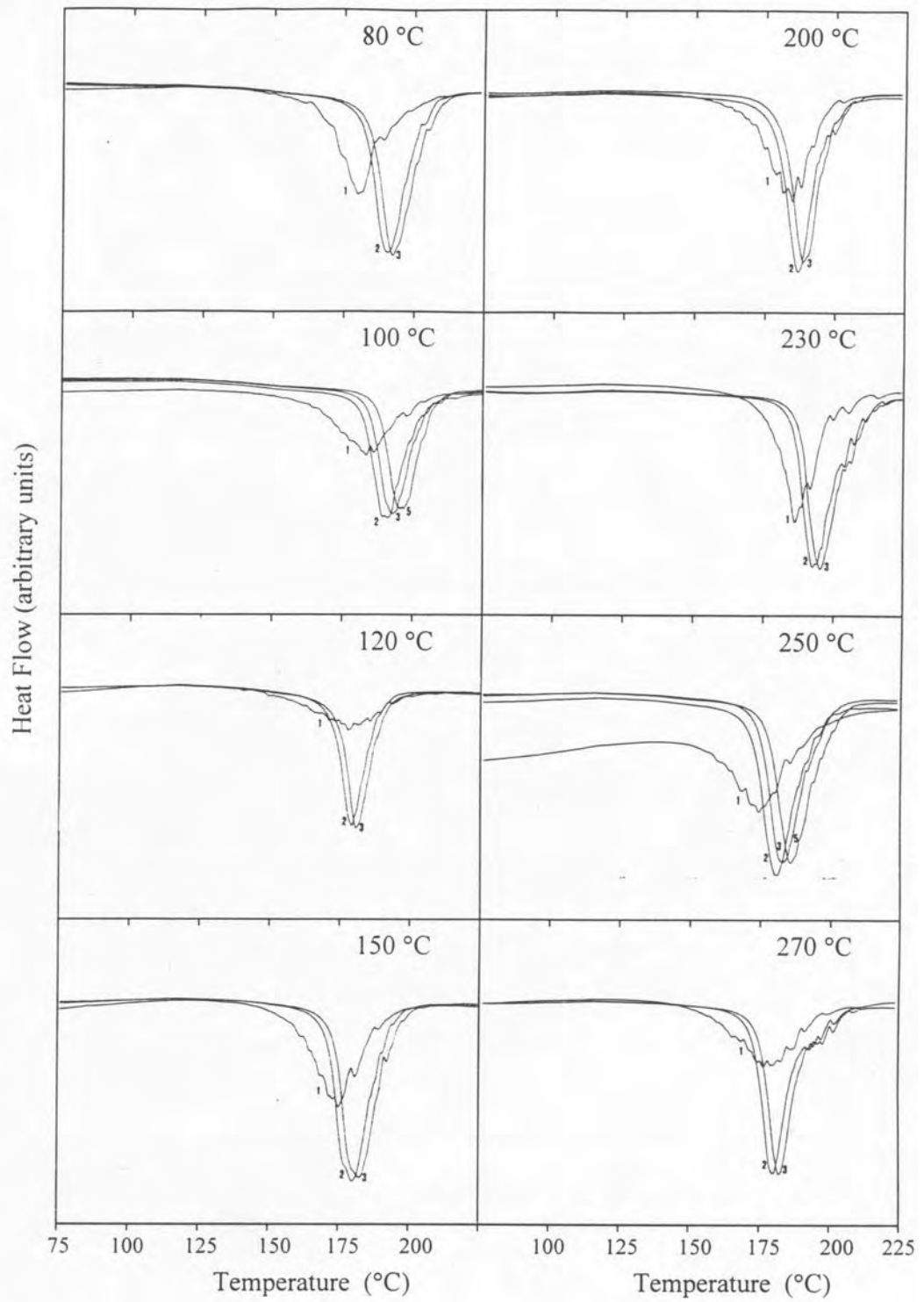
(c)

Figure 4.4: Continued

Table 4.4: For each applied thermal cycle, average transformation temperatures of the three CuAlNiMn and four CuAlNi alloys.

VD11	A_s	A_f	M_s	M_f
Cycle1	135±4	156±6		
Cycle2	148±8	169±10	155±2	137±3
Cycle3	152±4	174±5	154±5	139±5
Cycle4			158±4	141±2
VD12	A_s	A_f	M_s	M_f
Cycle1	133±5	154±5		
Cycle2	145±5	165±6	148±5	132±5
Cycle3	145±4	166±5	149±6	132±4
Cycle4			149±5	133±5
VD13	A_s	A_f	M_s	M_f
Cycle1	149±5	167±4		
Cycle2	177±6	194±6	176±4	140±5
Cycle3	180±6	198±6	155±4	142±5
Cycle4			179±4	165±5
V1	A_s	A_f	M_s	M_f
cycle1	221±3	257±7		
cycle2	222±2	237±1	221±1	206±2
cycle3	225±1	240±1	223±1	209±2
Cycle4			225±1	210±1
V2	A_s	A_f	M_s	M_f
cycle1	94±6	110±6		
cycle2	106±5	123±7	106±6	92±5
cycle3	108±5	124±6	108±6	94±5
Cycle4			110±6	95±4
V3	A_s	A_f	M_s	M_f
cycle1	120±2	139±1		
cycle2	124±3	142±2	127±2	110±3
cycle3	127±2	146±2	130±2	113±3
Cycle4			132±3	116±3
V4	A_s	A_f	M_s	M_f
cycle1	160±2	180±4		
cycle2	162±2	181±2	165±3	149±2
cycle3	164±2	182±2	167±3	151±2
Cycle4			168±3	152±2

(a) VD11

(b) VD12
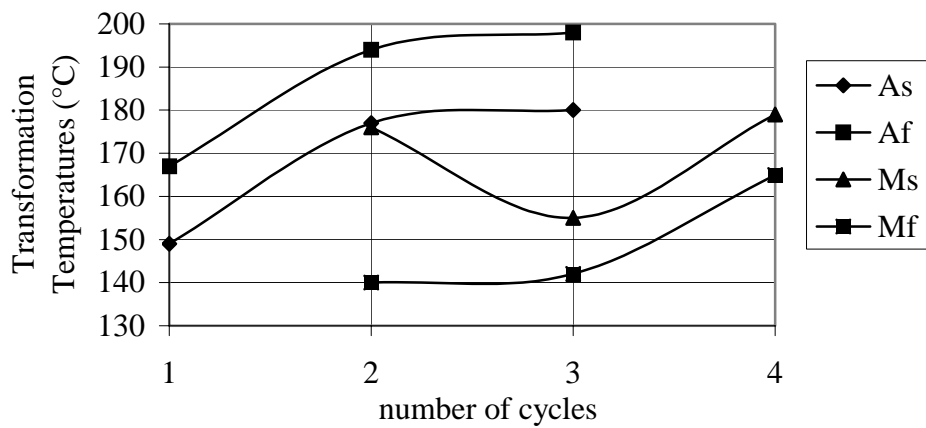
(c) VD13

Figure 4.5: Change of transformation temperatures versus number of thermal cycles for three CuAlNiMn alloys; a) VD11, b) VD12, c) VD13.

in Figure 4.6. Change of transformation temperatures in these alloys with thermal cycling after the second cycle is quite similar to that in CuAlNiMn alloys. However, the transformation temperatures during the first two cycles change non systematically, e.g., A_f temperatures increases by 1-2°C in two of the alloys, increase by 12°C in one of the alloys and decrease by 20°C in another alloy. The change of transformation temperatures with three thermal cycles in CuAlNi alloys is illustrated in Figure 4.7. Change of A_s and A_f temperatures for the seven samples of Cu-12. 6%Al-5.9%Ni-1.8%Mn alloy with thermal cycles is shown in Figure 4.8. Upper temperature bundle is A_f temperatures and lower temperature bundle is A_s temperatures. The values for seven different samples of the same alloy are coincident and do not scatter.

To observe the trend during the later thermal cycles, one Cu-12.6wt%Al-5.9wt%Ni-1.8wt%Mn alloy sample is cycled ten times, Figure 4.9. As expected, while the rise in A_s and A_f temperatures between first and second cycles is 15-20°C, after second cycle, the rise has been detected to be only 1-2°C and rise in transformation temperatures has been found to decrease with increasing number of thermal cycles but not cease totally even after ten cycles. Change of transformation temperatures in Cu-12.6wt%Al-5.9wt%Ni-1.8wt%Mn alloy after ten cycles is presented in Figure 4.10. Starting from third cycle until to the end of tenth cycle, A_s and A_f temperatures increase about 10°C while M_s and M_f temperatures increase approximately by 7°C. To get stabilized and reproducible transformation temperatures in CuAlNiMn and CuAlNi shape memory alloys prior to ageing experiment, three thermal cycles have been decided to be enough.

Present section focused on the microstructural developments in the very early stages of cycling as opposed to the literature, where cycling experiments are mostly devoted to life prediction and enhancement efforts and hence involve large number of cycles. Understanding of the progress in the early stages is crucial for the interpretation of thermal cycling studies and stability of alloys prior to any treatment.
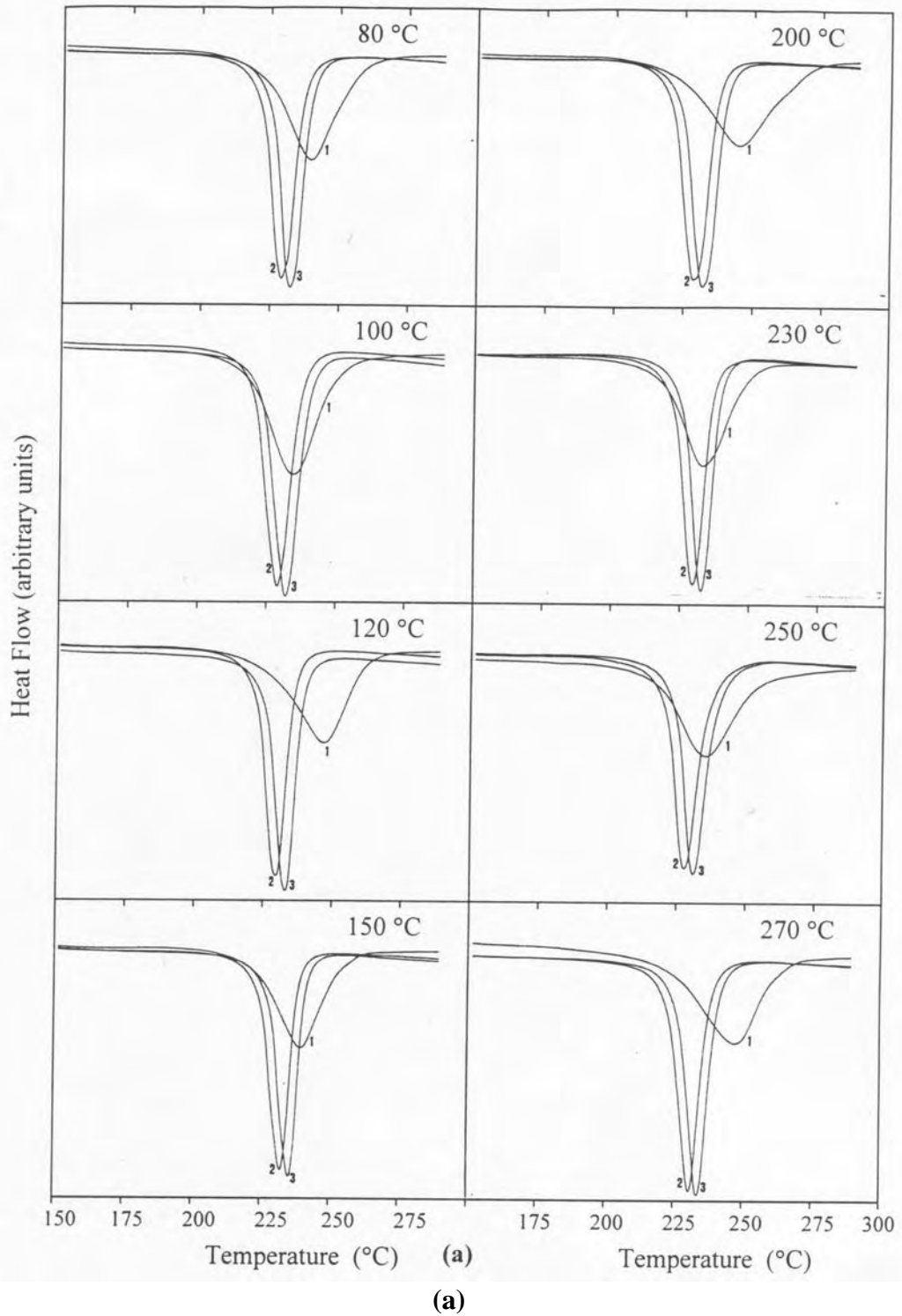
Figure 4.6: Superimposed DSC curves of M→β transformation during the first three thermal cycles for the eight samples (prior to ageing at eight different temperatures of 80°C, 100°C, 120°C, 150°C, 200°C, 230°C, 250°C and 270°C) of each of the four CuAlNi alloys a) V1, b) V2, c) V3 and d) V4.
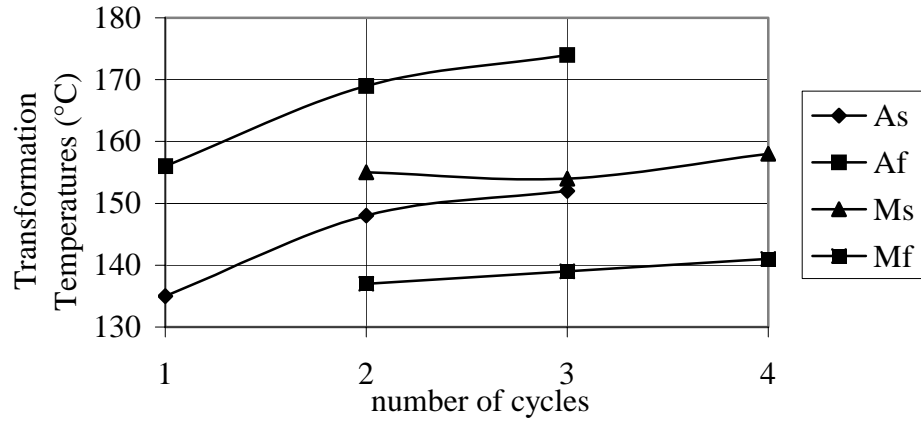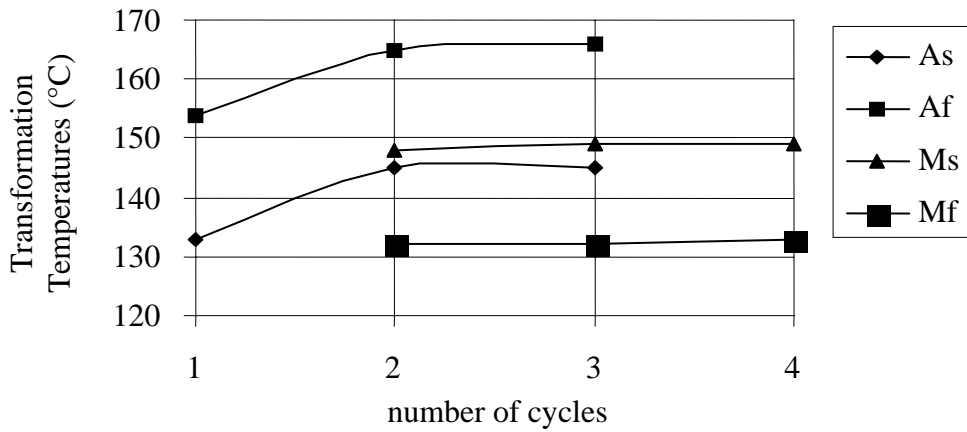
89
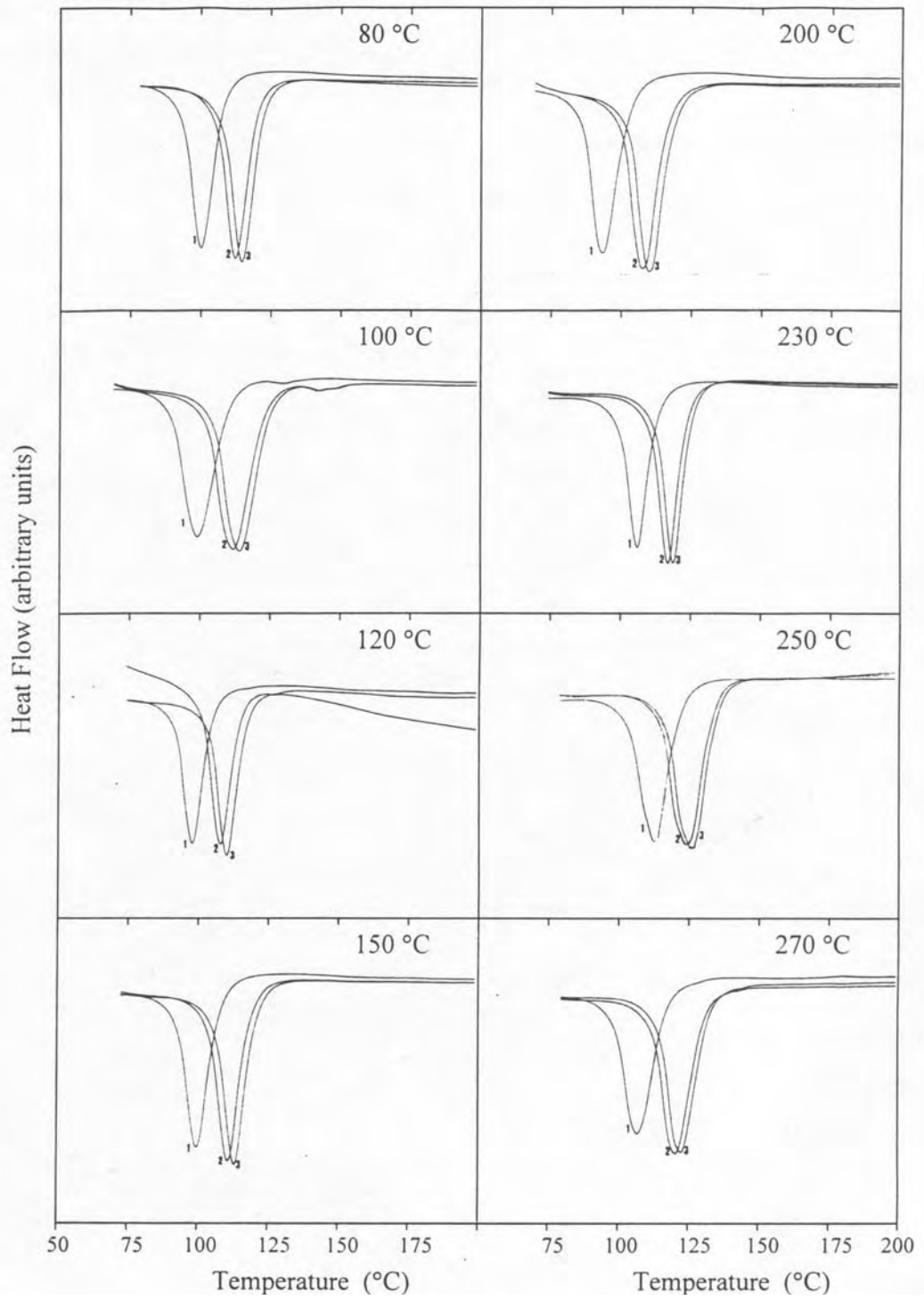
(b)

Figure 4.6: Continued
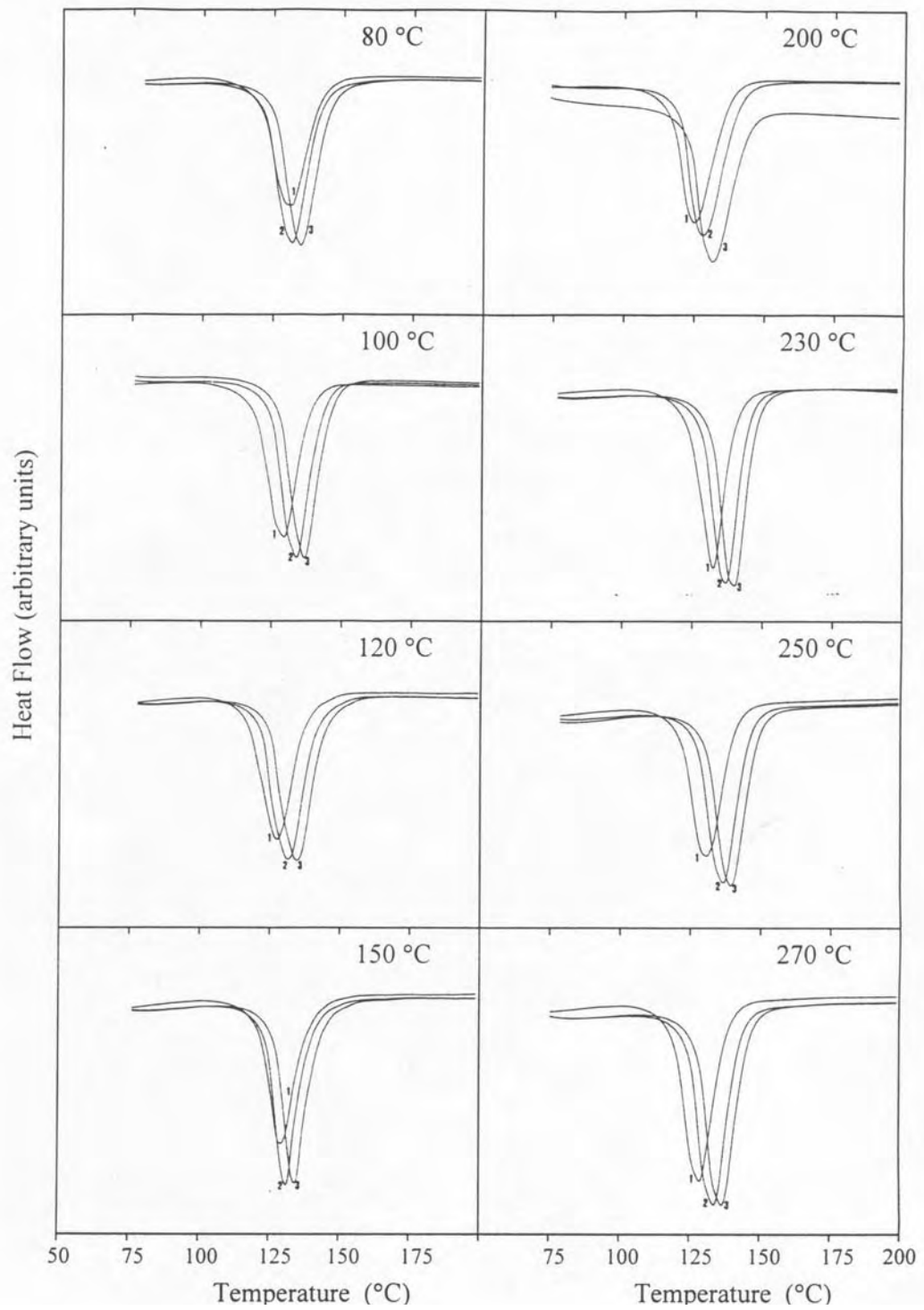
(c)

Figure 4.6: Continued
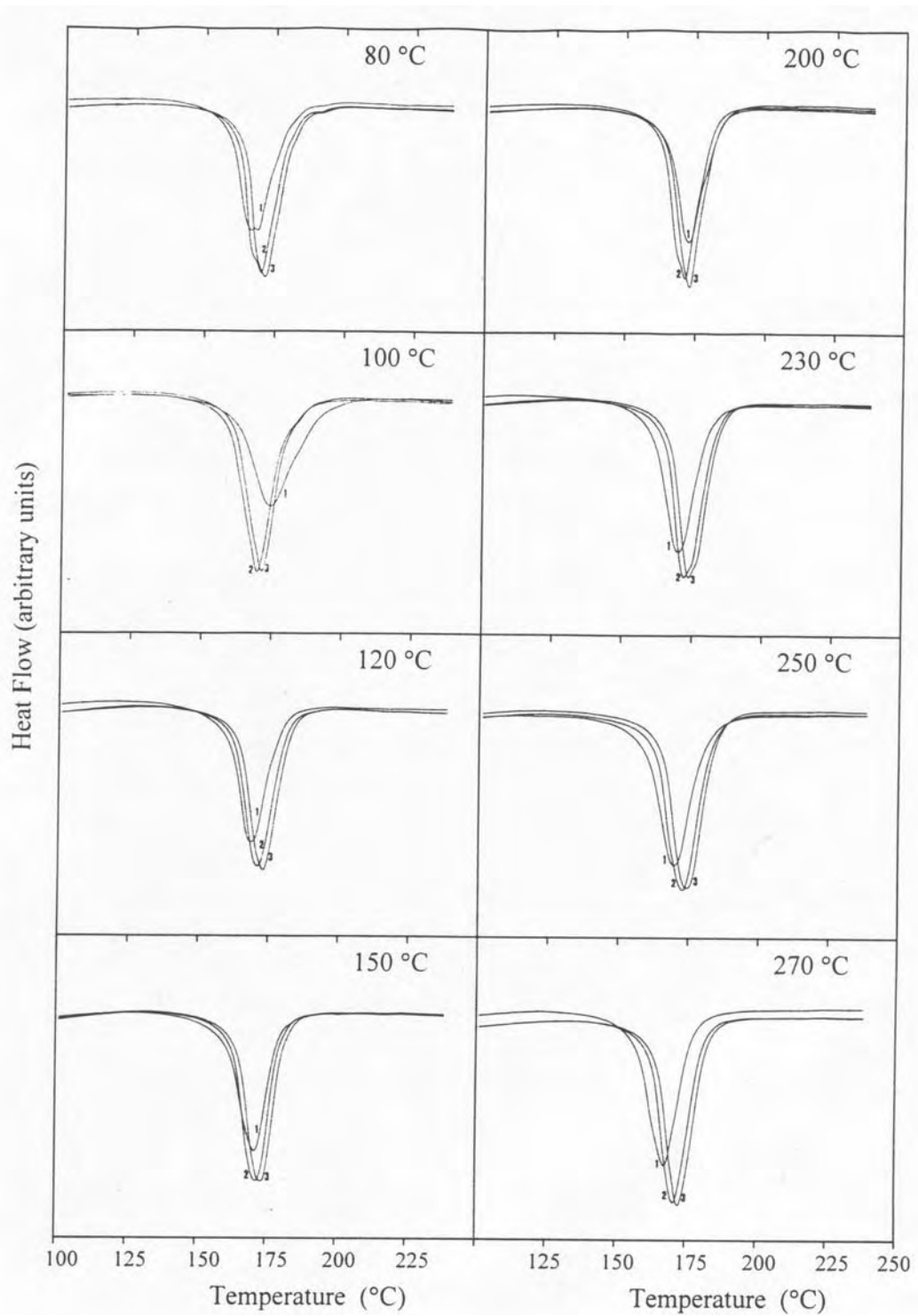
(d)

Figure 4.6: Continued
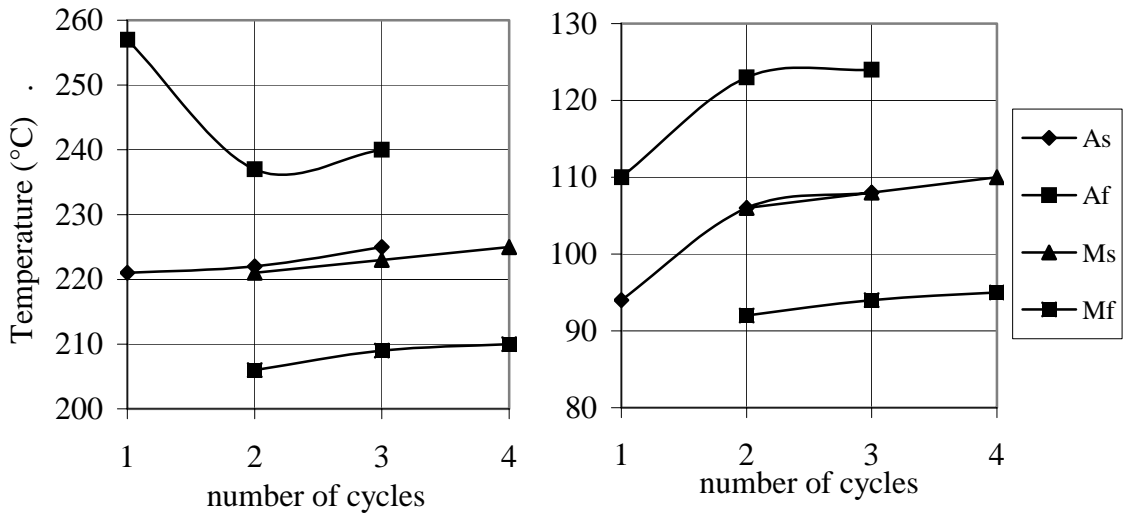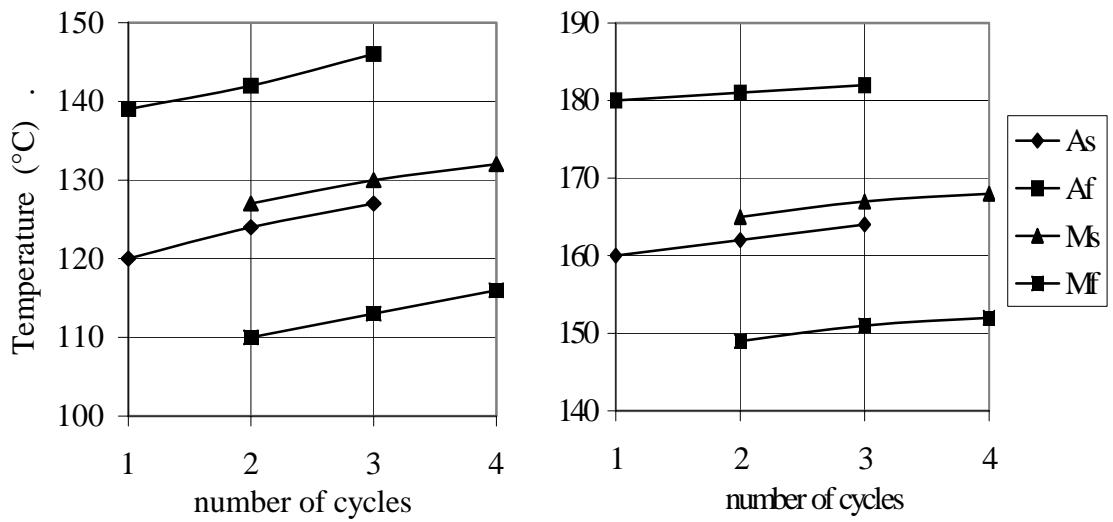
Figure 4.7: Change of transformation temperatures versus number of thermal cycles for four CuAlNi alloys; a) V1, b) V2, c) V3, d) V4.
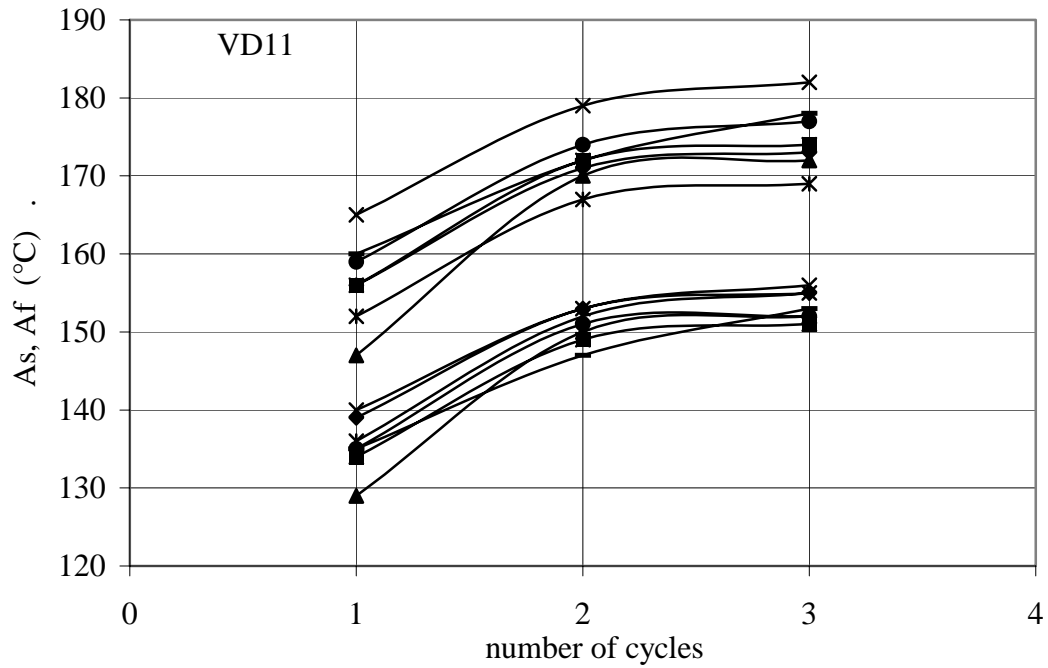
Figure 4.8: Change of A_s (lower group) and A_f (upper group) temperatures for the seven samples of Cu-12. 6%Al-5.9%Ni-1.8%Mn alloy with thermal cycles.

Actually, two basic and distinct phenomena stand out among the early cycling effects: One is the anomalous (serrated and diffuse) first cycle and the other is the increasing transformation temperatures with increasing number of cycles. Martensite nucleation does not obey the rules of classical diffusional nucleation. Martensite nucleates from crystal defects specific to the nature of the shear mechanism operating during the transformation. Once it is nucleated, as the preferred sites are stimulated by repeated cycling, nucleation of martensite becomes easier each time, and hence an increase in the M_s and M_f temperatures, i.e., transformation at temperatures closer to the equilibrium, seems to be reasonable.
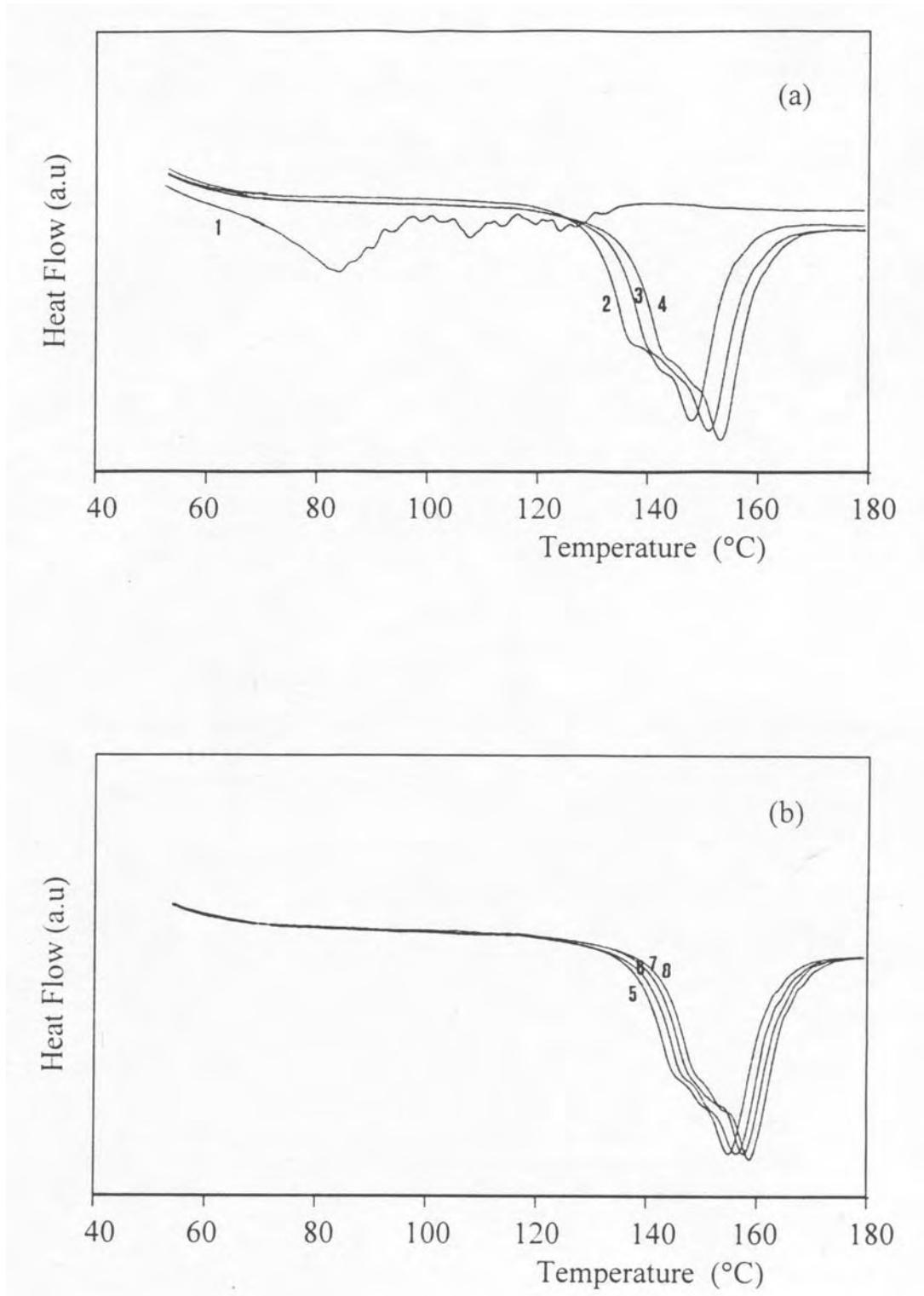
Figure 4.9: Superimposed DSC curves of Cu-12.6wt%Al-5.9wt%Ni-1.8wt%Mn alloy sample, which is thermally cycled ten times a) thermal cycles 1 to 4, b) thermal cycles 5 to 8.
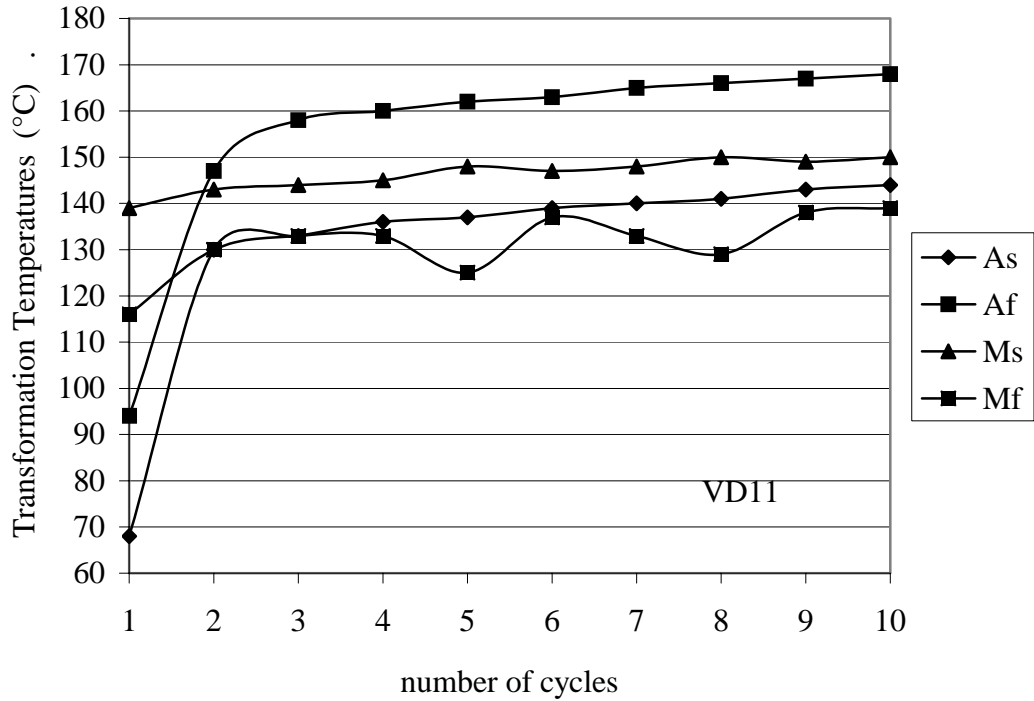
Figure 4.10: Change of transformation temperatures in Cu-12.6wt%Al-5.9wt%Ni-1.8wt%Mn alloy after ten cycles.

However, the same path of reasoning would require the A_s and A_f temperatures to decrease, which is in contradiction with the observations. Since all transformation temperatures are observed to increase, although to slightly different extents, with cycling, there must be a rise in equilibrium temperature T_0 as can be visualized on the schematic Gibbs Free Energy versus Temperature curves of martensite and beta phases, Figure 4.11. Any decrease in free energy of martensite shifts T_0 to higher temperatures leading to a rise in all M_s, M_f, A_s and A_f temperatures. Although it is difficult to account for the lowering of the free energy of martensite (no composition change, change in degree of order would affect both phases equivalently), one may speculate that defected structure generated by cycling may be the reason of lowering of martensite free energy.

96
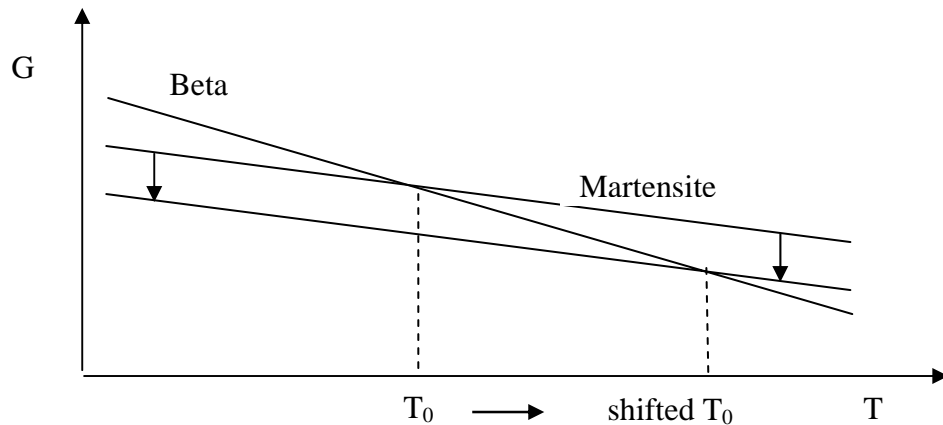
Figure 4.11: Schematized Gibbs free energy versus Temperature diagram of martensite and beta.

Observation of diffuse and serrated first cycle peaks only in CuAlNiMn alloys, but not in Mn free CuAlNi alloys rises a question on the role of Manganese in the occurrence of the first cycle peak anomalies. It is clear from Figure 4.4 that the jerky nature of the first cycle peak is least in the least Mn-bearing Cu-12.6%Al-4.8%Ni-1.1%Mn alloy (VD12), and more obvious in Cu-12.6%Al-5.9%Ni-1.8%Mn (VD11) and Cu-12.9%Al-5.0%Ni-2.2%Mn (VD13) alloys with medium and highest Manganese contents. Serrations remind repeating attempts for shrinkage of martensite crystals upon heating and their successive suppression by a mechanism involving the manganese atoms. Manganese atoms may be interacting with excess quenched-in vacancies and producing Mn-vacancy couples, which pin the shrinking martensite boundaries and result in the observed serrations. This mechanism is analogous to well known manganese-carbon interaction to form couples that cause strain aging in steels. If such a mechanism is really operative, upon heating the samples above A_f temperature at the end of the first cycle, excess vacancies would anneal out diminishing the Manganese-vacancy interactions and serrations would disappear as observed. Moreover, peak shape becomes non-diffuse and regular like the following cycles.

In brief, during very early few thermal cycles, CuAlNiMn alloys exhibit systematically repeating 15-20°C rise in A_s and A_f temperatures between first and second cycles whereas changes in A_s and A_f temperatures of CuAlNi alloys between the first two cycles are random. Relative to A_s and A_f temperatures, M_s and M_f temperatures of both CuAlNiMn and CuAlNi alloys hardly change in the first three cycles, which is explained by the experimental fact that the actual first cycle referring to first $\beta \rightarrow M$ transformation takes place during quenching from 950°C that can not be monitored during DSC measurements.

Literature on early cycling effects is scarce and the only related article is the one published by Segui and Cesari [14]. They have observed that the $M \rightarrow \beta$ transformation takes place at a lower temperature in the second heating run compared to the first during the DSC studies on a Cu-12.41wt%Al-3.14wt%Ni-2.03wt%Mn alloy room temperature water quenched from 800°C, while no shift was observed in the samples air cooled from 800°C. They attributed the decrease of temperatures to incomplete ordering due to quenching and/or to the quenching stresses. Since this paper is the only available reference on the subject, for a comparison with it, in the present study, a Cu-12. 6%Al-5.9%Ni-1.8%Mn alloy sample is betatized at 950°C for 10 minutes and air cooled instead of directly water quenching. Although completely martensitic microstructure after air cooling has been observed by optical microscopy, during the DSC studies neither $M \rightarrow \beta$ nor $\beta \rightarrow M$ transformations could be observed. The results of air cooled samples have not changed by repeated experiments in different alloy samples. When the same air cooled samples have been rebetatized and water quenched, they have shown both transformations thermoelastically. To conclude, betatized and air cooled CuAlNiMn martensites are not thermoelastic in nature as evidenced by the absence of $M \rightarrow \beta$ and $\beta \rightarrow M$ transformations upon heating and cooling. In conclusion, the physical basis of early thermal cycling effects and first cycle anomalies are not totally clarified. In fact, this subject, which has not been even notified in the literature, has central importance in understanding the stability of copper based martensites to be used in explaining martensite stabilization effect.

4.5. Crystal Structure of Alloys:

X-ray diffraction studies have shown that, Appendix F, crystal structures of alloys were mixture of $18R_1$ and 2H long period stacking order (LPSO) martensite structures. However, quantitative amounts of each crystal structure was not assessable due to texture effect. Qualitatively, on the basis of aluminium and nickel amounts, dominant $M18R_1$ structure in relatively lower aluminium content and higher nickel content CuAlNiMn alloys and abundant 2H structure in relatively higher aluminium and lower nickel content CuAlNi alloys were in accordance with literature.

Approximately, crystal structures of Mn containing VD11, VD12, VD13 alloys were mostly $18R_1$ with very limited 2H. It has been shown in literature that, decreased aluminum contents and increased nickel amounts increase the possibility of $18R_1$ crystal structure in ternary CuAlNi alloys while the possibility of 2H crystal structure increases with the increased aluminum contents and decreased nickel amounts and those possibilities has been visualized on a schematic map of the kind of martensite with changing aluminum and nickel contents [2]. In Mn containing alloys, Manganese has a similar effect with Nickel therefore; dominancy of $18R_1$ crystal structure in CuAlNiMn alloys with decreased aluminum amounts is quite expectable. On the other hand, Manganese free CuAlNi ternary alloys, which has relatively higher aluminum and lower nickel contents than CuAlNiMn alloys, have mainly 2H crystal structure.

Kikuchi map of diffraction patterns of $18R_1$ LPSO martensite structure for a Cu-18.5%Zn-6.4%Al alloy was illustrated in Figure 4.12.

TEM diffraction studies on crystal structures of betatized and as quenched Cu-12.6%Al-5.9%Ni-1.8%Mn alloy (VD11) and Cu-13.6%Al-3.0%Ni alloy (V4) have verified the X-Ray studies and revealed the same results: Some characteristic selected area diffraction patterns of $18R_1$ and 2H crystal structures for Cu-12.
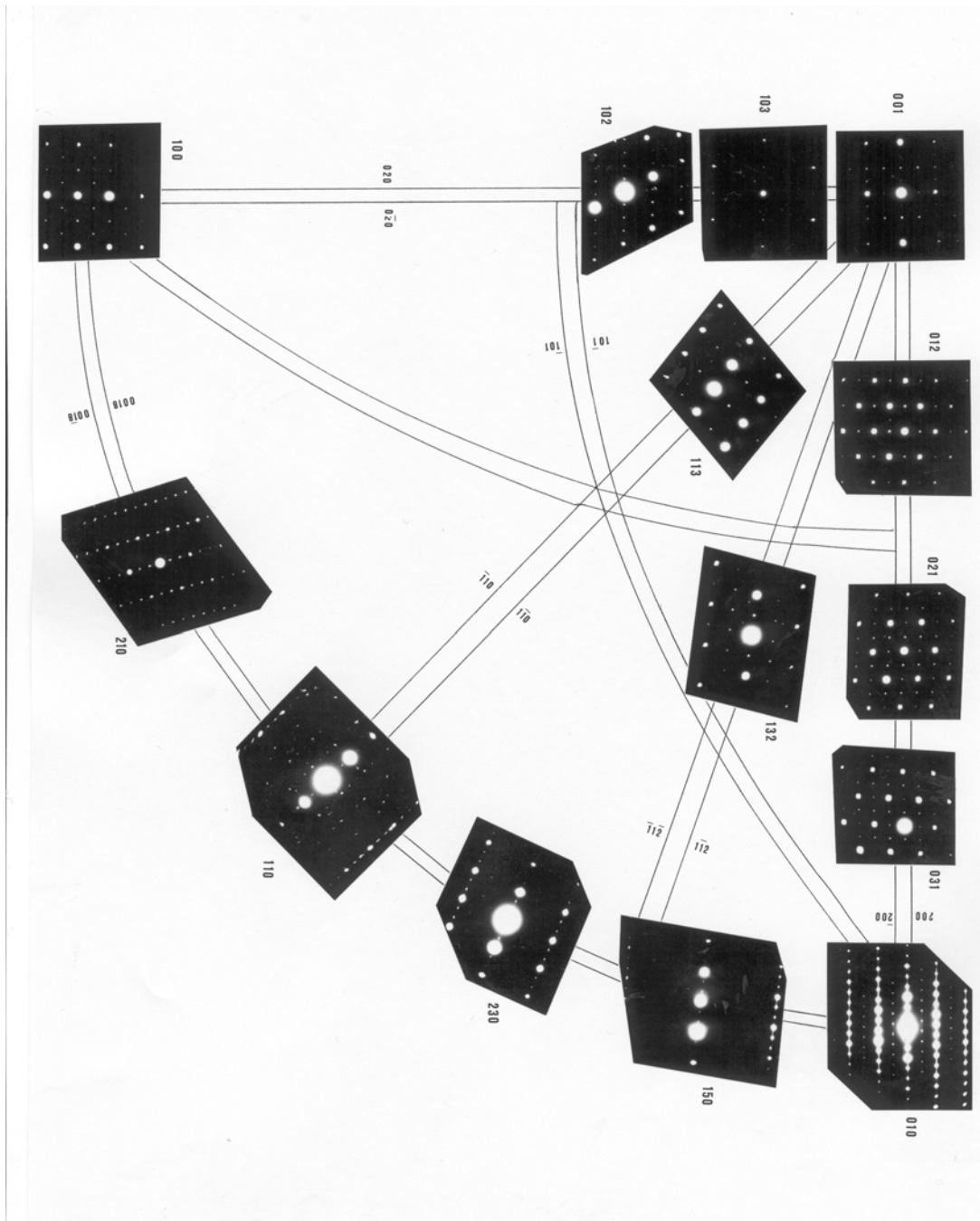
Figure 4.12: Kikuchi map of diffraction patterns of 18R1 LPSO martensite structure for a Cu-18.5%Zn-6.4%Al alloy.

6%Al-5.9%Ni-1.8%Mn alloy were illustrated in Figure 4.13. Wide plates of neighboring $18R_1$ and 2H martensite crystals a characteristic feature of the microstructure of the alloy were shown in Figure 4.14. (High density of crystal faults in the plates was the reason of absence of the Kikuchi lines). Some characteristic selected area diffraction patterns of 2H and $18R_1$ crystal structures for Cu-13.6%Al-3.0%Ni alloy were given in Figure 4.15. Twin related martensite variants of Cu-13.6%Al-3.0%Ni alloy were illustrated in Figure 4.16.

(a)
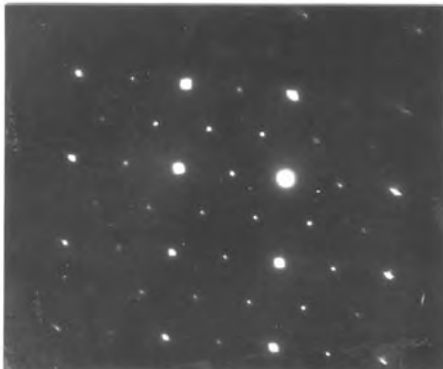
(b)

(c)

Figure 4.13: Some characteristic selected area diffraction patterns of $18R_1$ and 2H crystal structures for Cu-12. 6%Al-5.9%Ni-1.8%Mn alloy, as quenched condition. a)) $[110]_{18R}$, b) $[100]_{18R}$, c) $[010]_{18R}$, d) $[001]_{18R}$, e) $[230]_{18R}$ f) $[001]_{2H}$, g) $[011]_{2H}$,

(d)
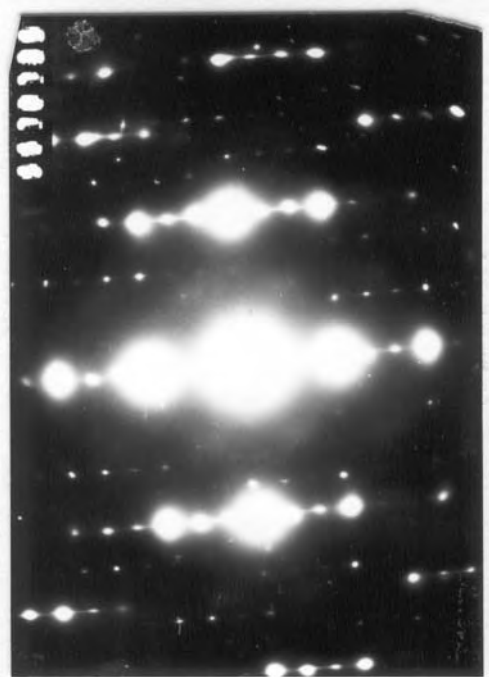
(e)
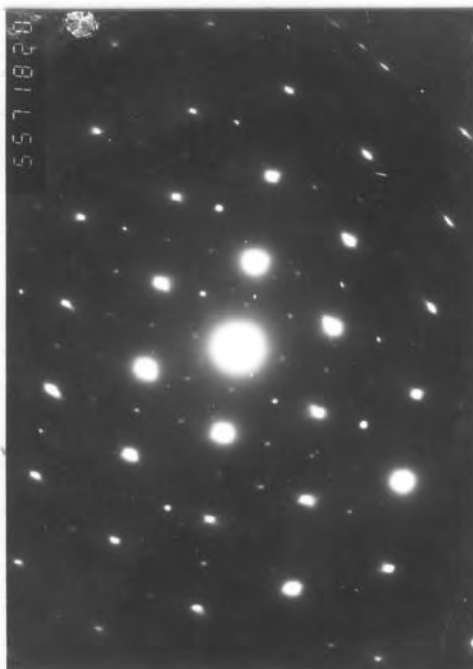
(f)
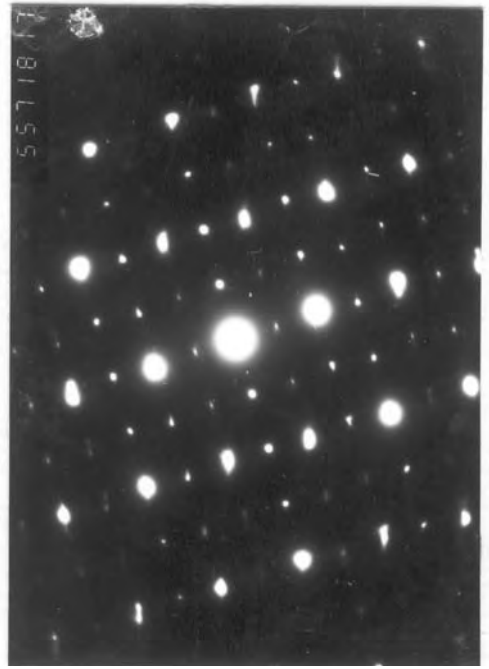
(g)

Figure 4.13: Continued.

(a)	**(b)**
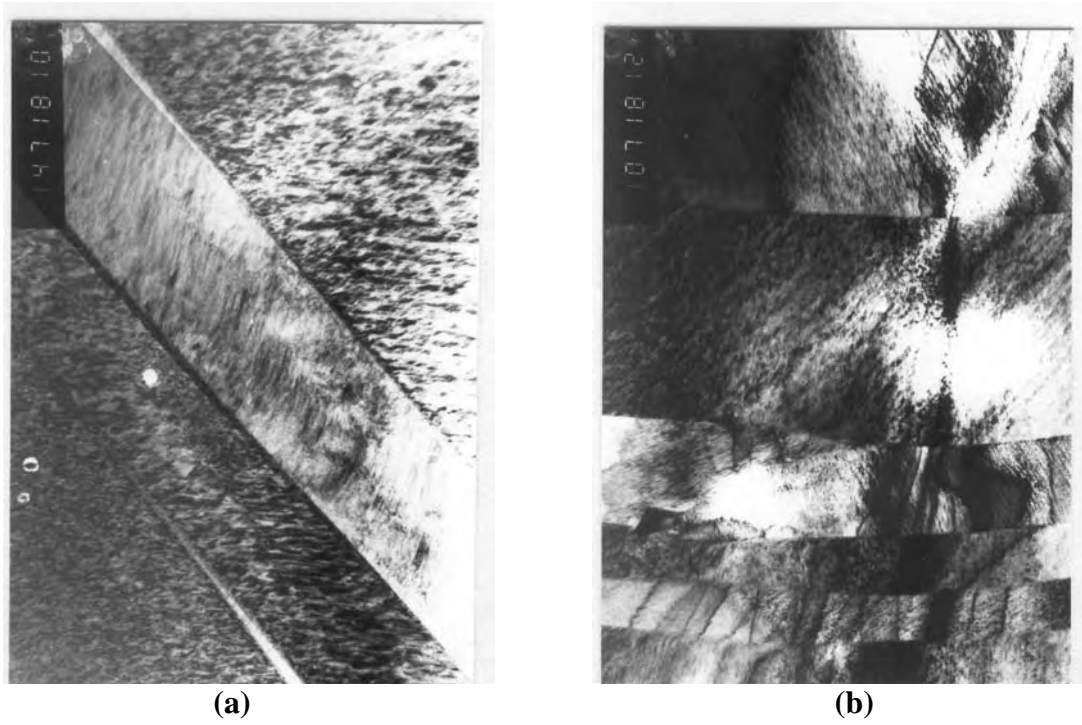
Figure 4.14: Coarse martensite plates in Cu-12. 6%Al-5.9%Ni-1.8%Mn alloy as quenched condition a) BF, 14 kX, b) BF, 10 kX.
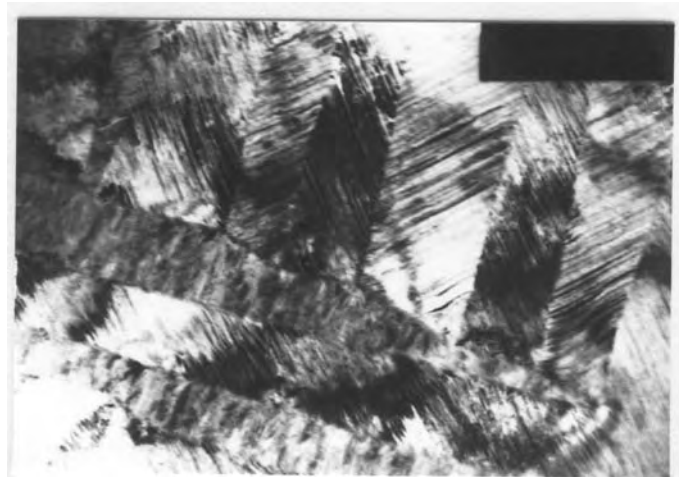
Figure 4.16: Twin related martensite variants of Cu-13.6%Al-3.0%Ni alloy, as quenched condition, BF, 36 kX

(a)
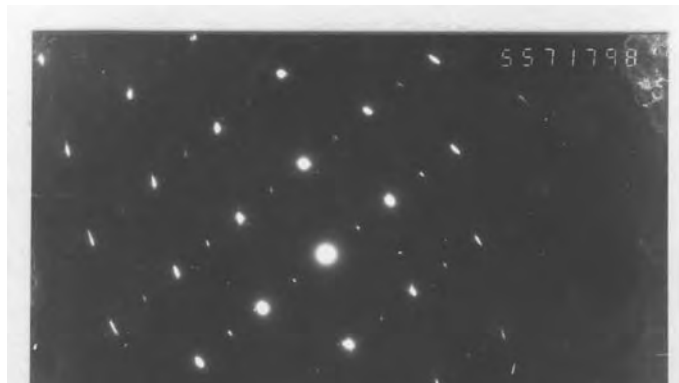
(b)

(c)

Figure 4.15: Some characteristic selected area diffraction patterns of $18R_1$ and 2H crystal structures for Cu-13.6%Al-3.0%Ni alloy, as quenched condition a) $[001]_{2H}$, b) $[012]_{2H}$, c) $[230]_{18R}$.

4.6. Martensite Ageing of CuAlNiMn Alloys:

CuAlNiMn Alloys were aged at selected ageing temperatures of 80°C, 100°C, 120°C and 150°C, where they were martensitic (T<M_f), for ageing times of 24, 72, 144 and 312 hours. Corresponding Transformation Temperatures (A_s, A_f, M_s, M_f) determined by DSC after each ageing time were tabulated in Appendix G.

The change of each particular transformation temperature with ageing times for four ageing temperatures were plotted in Figure 4.17, Figure 4.18 and Figure 4.19 for Cu-12.6%Al-5.9%Ni-1.8%Mn (VD11), Cu-12.6%Al-4.8%Ni-1.1%Mn (VD12) and Cu-12.9%Al-5.0%Ni-2.2%Mn (VD13) alloys, respectively. Each graph was fitted to a logarithmic curve and the slopes (dT/dlnt) of these fitted lines were indicated on the plots. What remarkable on these plots was the random variation of transformation temperature for the zero ageing time corresponding to as-quenched transformation temperatures and the curves corresponding to different ageing temperatures were randomly positioned in the vertical axis with respect to each other in each graph. This stems from the reasoning that different samples of the same alloy were used for each ageing temperature due to the previously mentioned betatizing anomaly. From these figures it was concluded that M_s and M_f temperatures were not changing at all with increasing ageing time for all four ageing temperatures. On the other hand, both A_s and A_f temperatures were increasing with increasing ageing temperature as can be seen from the steeper slopes with increasing temperature. The most remarkable increase of both temperatures was observed at the highest ageing temperature 150°C that has also shown the steepest slope. There was no clear rise of A_s and A_f temperatures corresponding to relatively lower ageing temperatures of 80°C, 100°C and 120°C. The most obvious increase in A_s and A_f temperatures observed during 150°C were approximately 40-45°C at the end of the total 312 hours ageing period. Increase in A_s temperature was more than that of A_f temperature according to the comparison of the fitted line slopes. The most obvious increase in A_s and A_f temperatures has been exhibited by VD11 alloy among the three CuAlNiMn alloys.

(a) As Change for VD11

7,6066

2,0326

1,1521

0,9482

As Temperature (°C)

ln [ageing time (hours)]

Legend: 80°C, 100°C, 120°C, 150°C

(b) Af VD11

6,8353

2,7104

,2508

0,6619

Af Temperature (°C)

ln [ageing time (hours)]
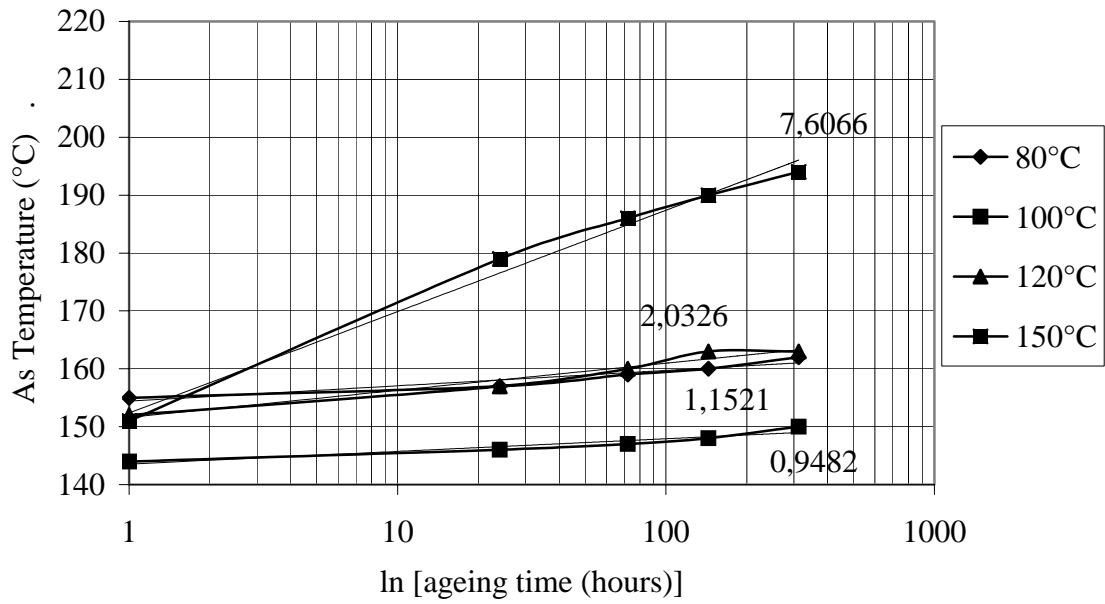
Legend: 80°C, 100°C, 120°C, 150°C
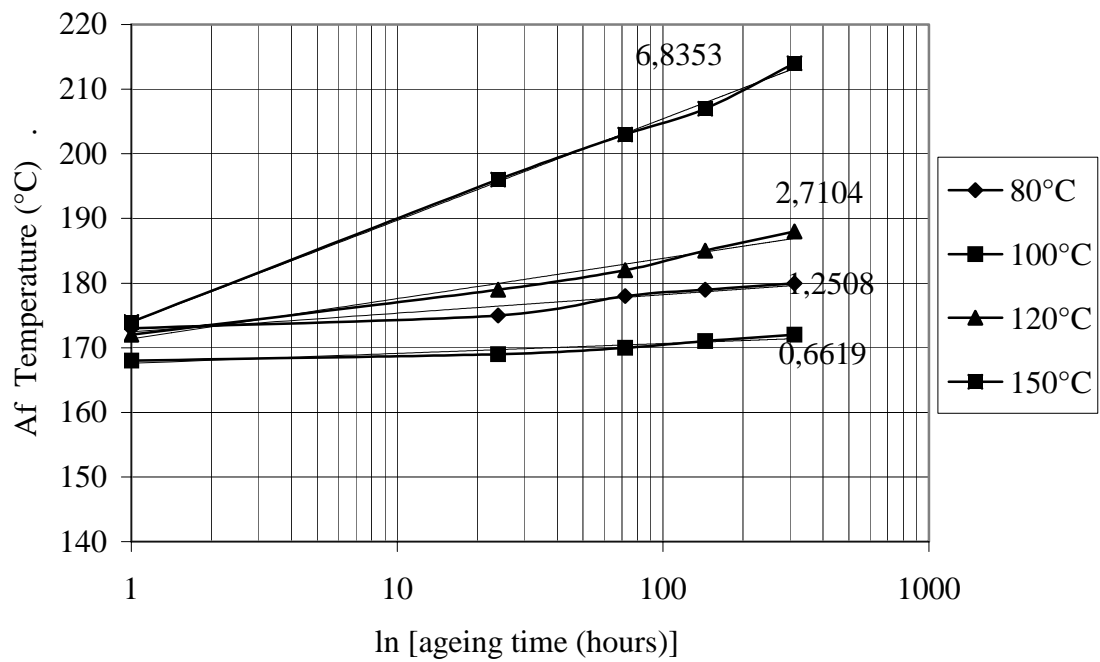
Figure 4.17: The change of transformation temperatures a) A_s b) A_f c) M_s d) M_f with ageing times for the ageing temperatures of 80°C, 100°C, 120°C, 150°C in Cu-12.6%Al-5.9%Ni-1.8%Mn alloy.

106
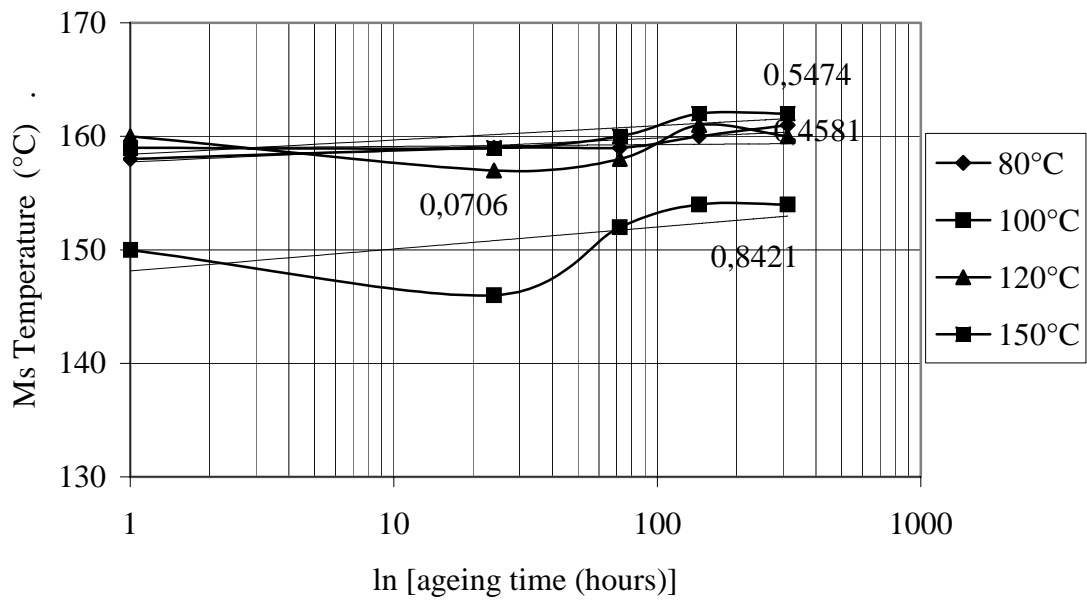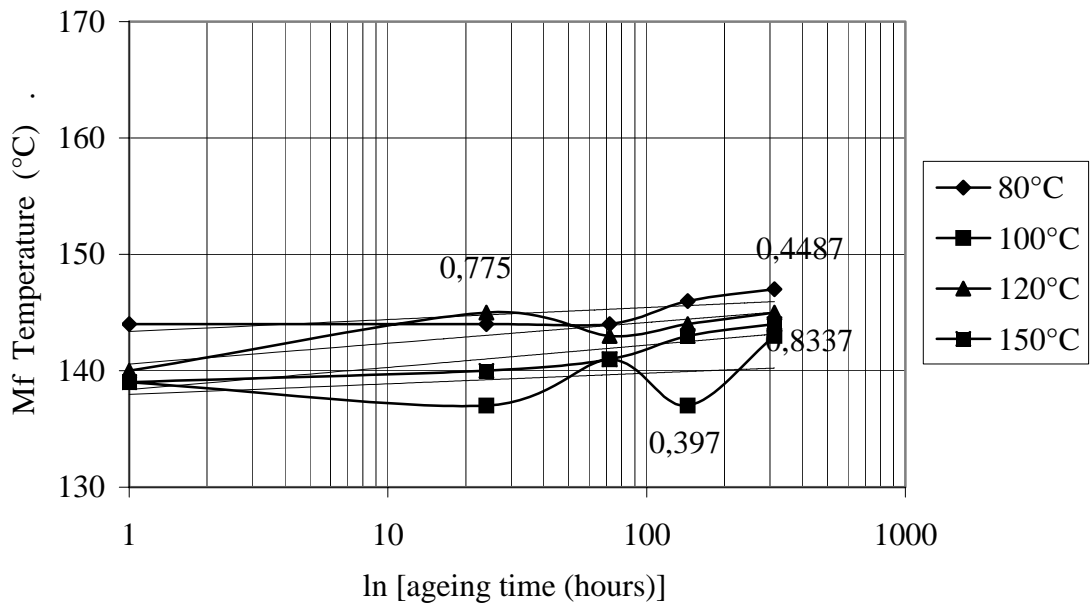
(c) Ms VD11

(d) Mf VD11

Figure 4.17: Continued

(a) As VD12
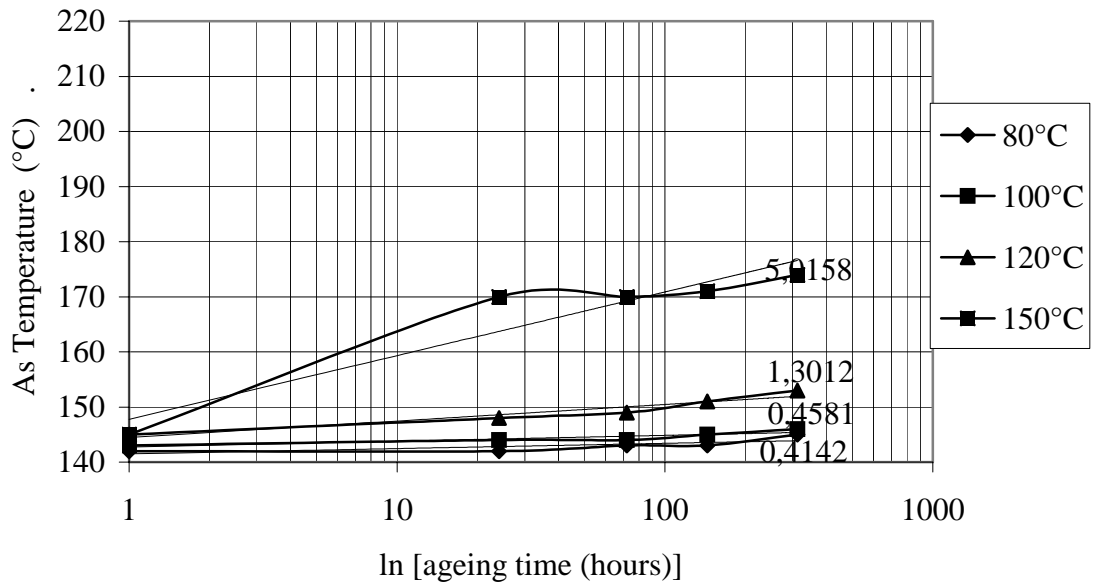
(b) Af VD12
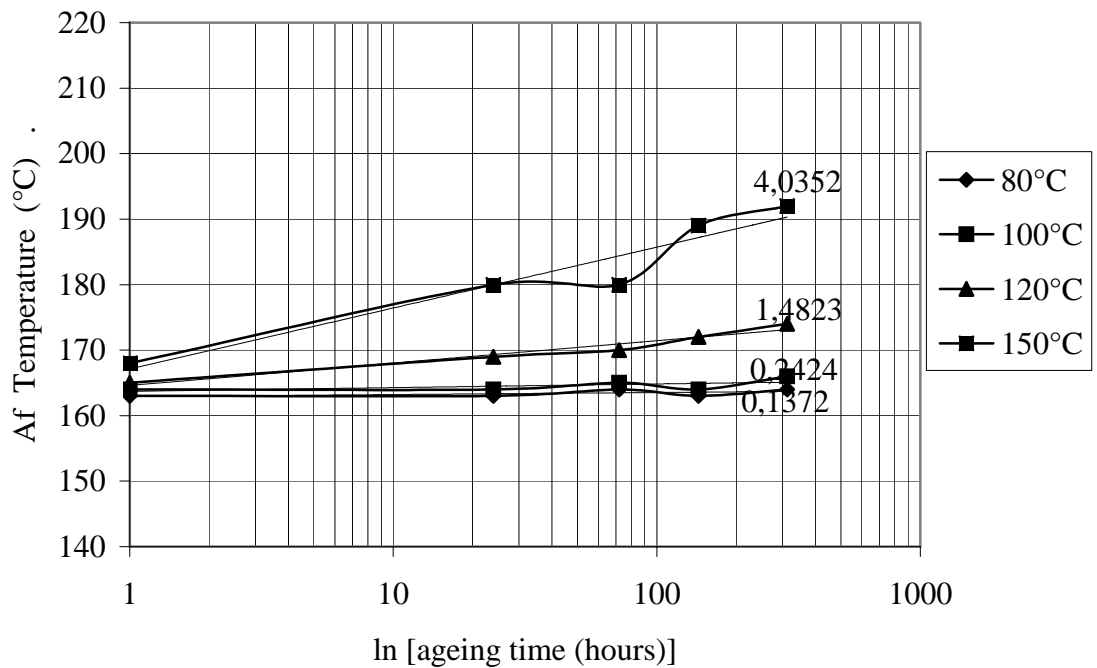
Figure 4.18: The change of transformation temperatures a) A_s b) A_f c) M_s d) M_f with ageing times for the ageing temperatures of 80°C, 100°C, 120°C, 150°C in Cu-12.6%Al-4.8%Ni-1.1%Mn alloy.

108
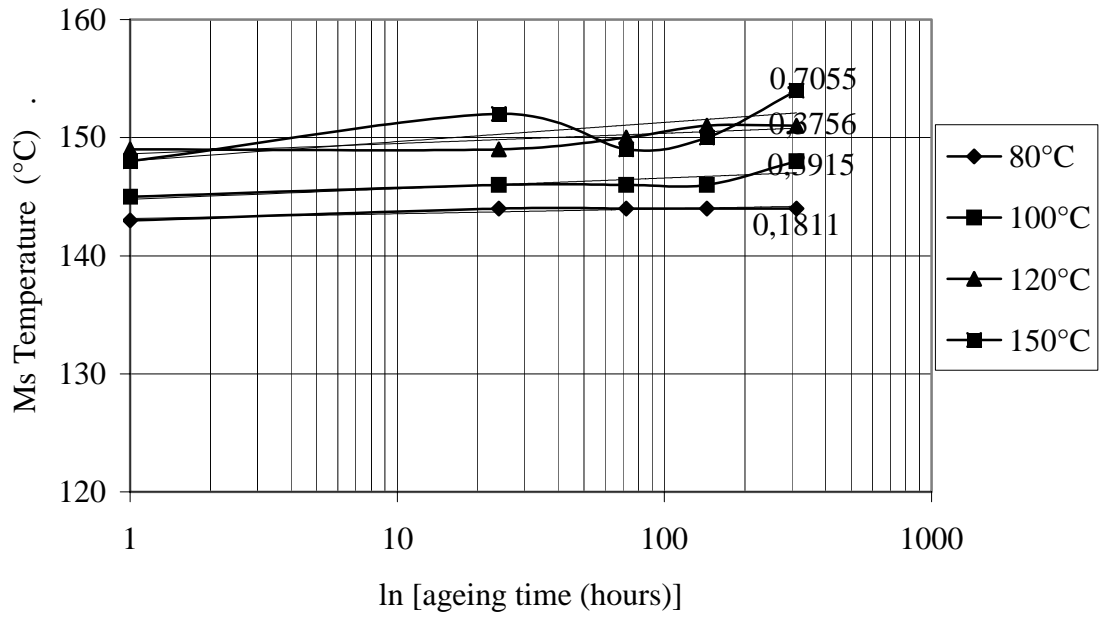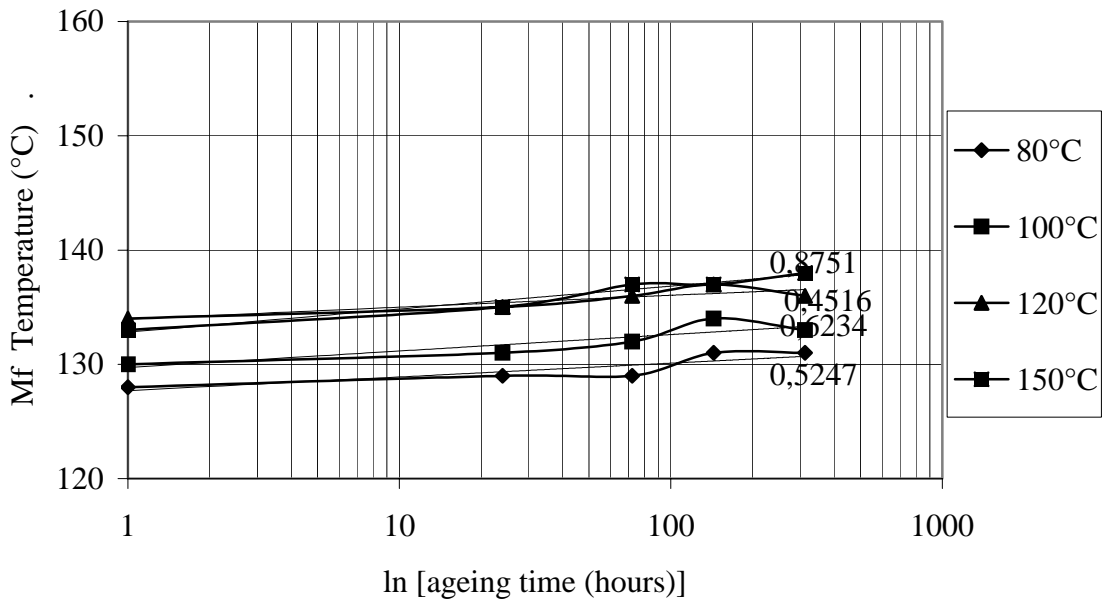
(c) Ms VD12

(d) Mf VD12

Figure 4.18: Continued.

(a) As VD13
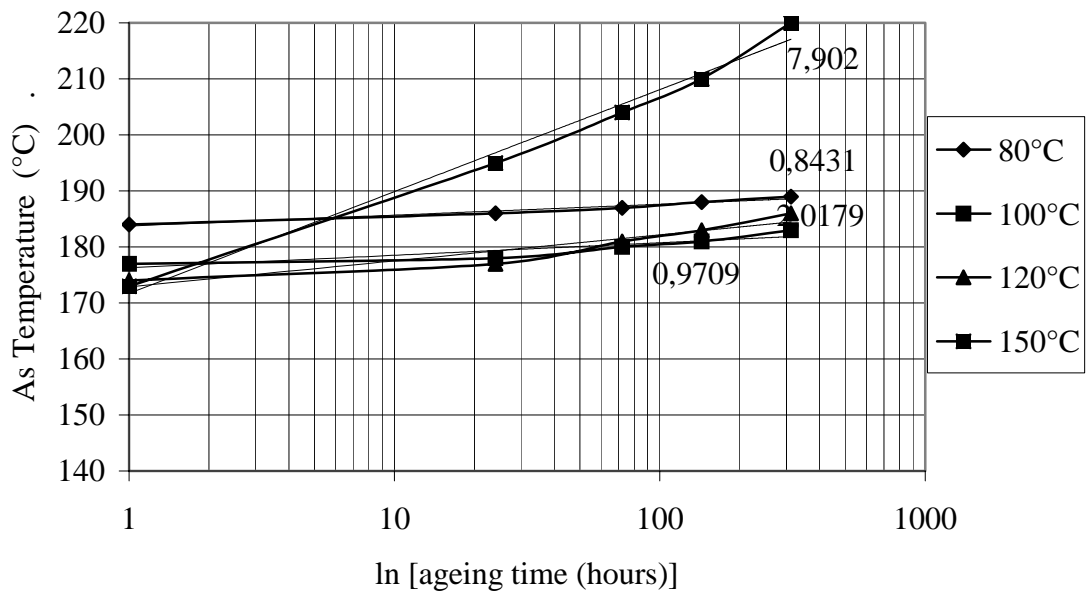
(b) Af VD13
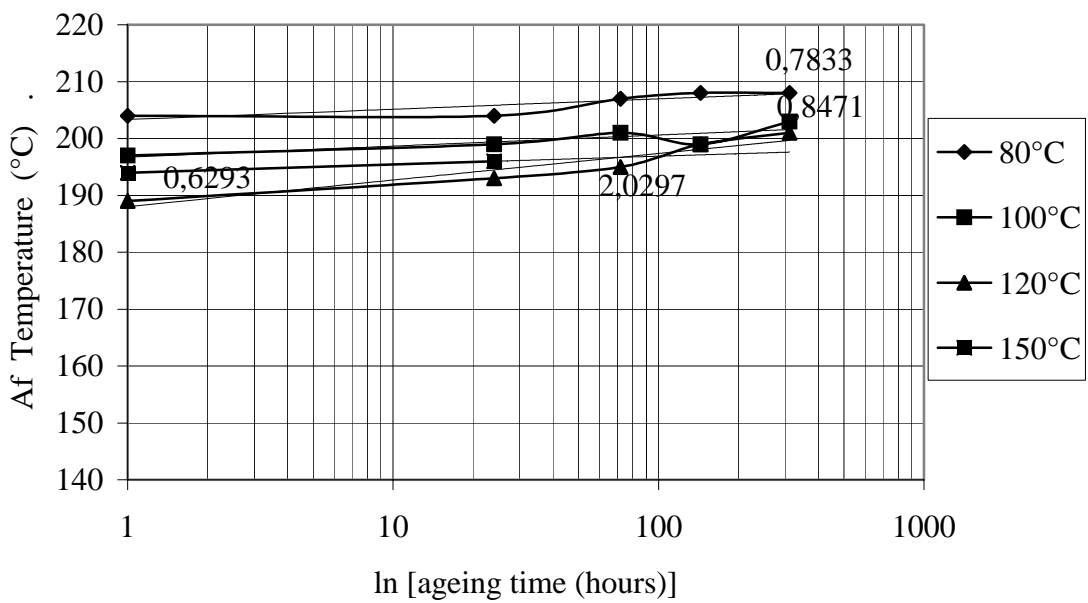
Figure 4.19: The change of transformation temperatures a) A_s b) A_f c) M_s d) M_f with ageing times for the ageing temperatures of 80°C, 100°C, 120°C, 150°C in Cu-12.9%Al-5.0%Ni-2.2%Mn alloy

(c) Ms VD13
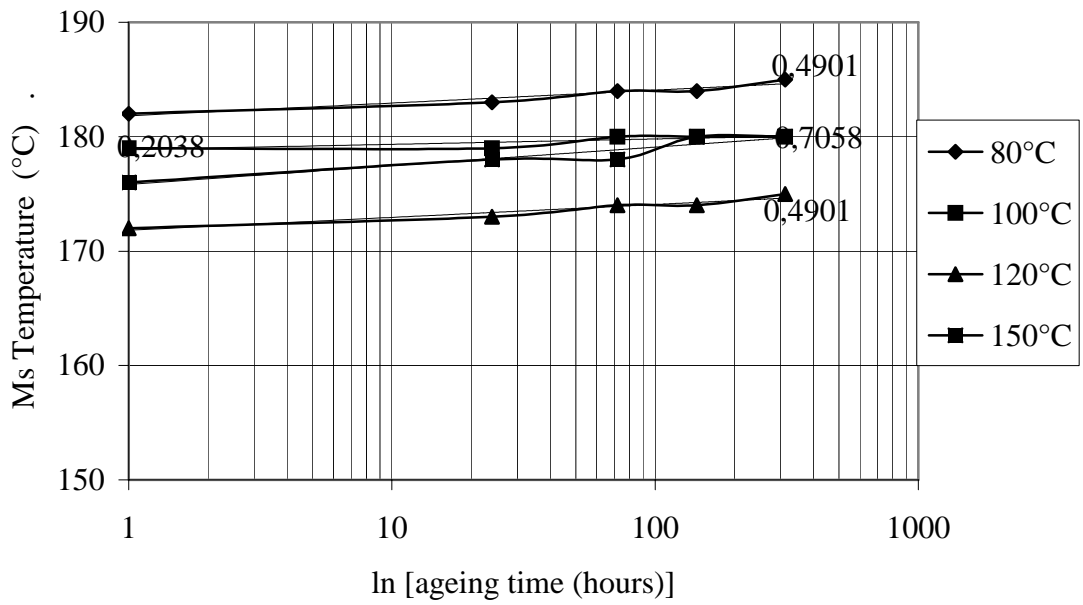
(d) Mf VD13
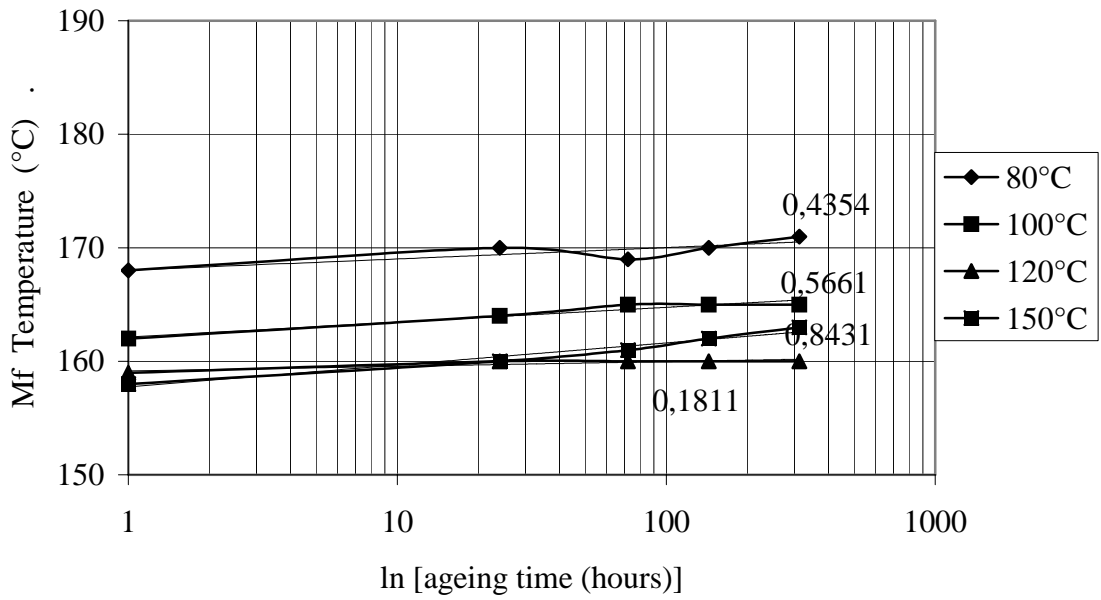
Figure 4.19: Continued.

Additionally, CuAlNiMn alloys were aged at room temperature (RT) for 168, 336, 672, 2016 and 4032 hours. Transformation temperatures of CuAlNiMn alloys aged at RT were tabulated in Appendix H and the transformation temperatures versus ageing time curves of three CuAlNiMn alloys were sketched in Figure 4.20. As can be seen from Appendix H, two measurements, namely cycle 1 and cycle 2, were done corresponding to each ageing period. Between the two measurement cycles A_s and A_f temperatures increased about 15-20°C while M_s and M_f temperatures increased by 2-3°C. Since RT ageings were not carried out cumulatively and different samples of the same alloy were used for each ageing time, the observed variations of temperatures in Figure 4.20 has occurred as a consequence of the each applied betatizing and quenching treatments. As a result, transformation temperatures do not change at all with increasing RT ageing times; the observed changes were attributed to randomly varying transformation temperature due to each betatizing treatment as clarified previously in section 4.3. In conclusion, apart from the effect of betatizing on transformation temperatures, CuAlNiMn alloys were quite stable during RT ageing.

4.7. Martensite Ageing of CuAlNi Alloys:

CuAlNi alloys were aged for 24, 72, 144 and 312 hours at selected ageing temperatures of 80°C and 100°C where they were martensitic ($T<M_f$). Transformation Temperatures (A_s, A_f, M_s, M_f) of the four investigated alloys, recorded after martensite ageing for the indicated periods were tabulated in Appendix J and plotted in Figure 4.21 to Figure 4.24. The relatively small change of the transformation temperatures with increasing ageing time can also be seen from the slopes (dT/dlnt) of the best fitted lines in Figures 4.21 to 4.24. Slopes of these figures also implied that time dependence of the transformation temperatures was very slightly stronger for the A_s and A_f temperatures compared to the M_s and M_f temperatures.

(a) RT-VD11
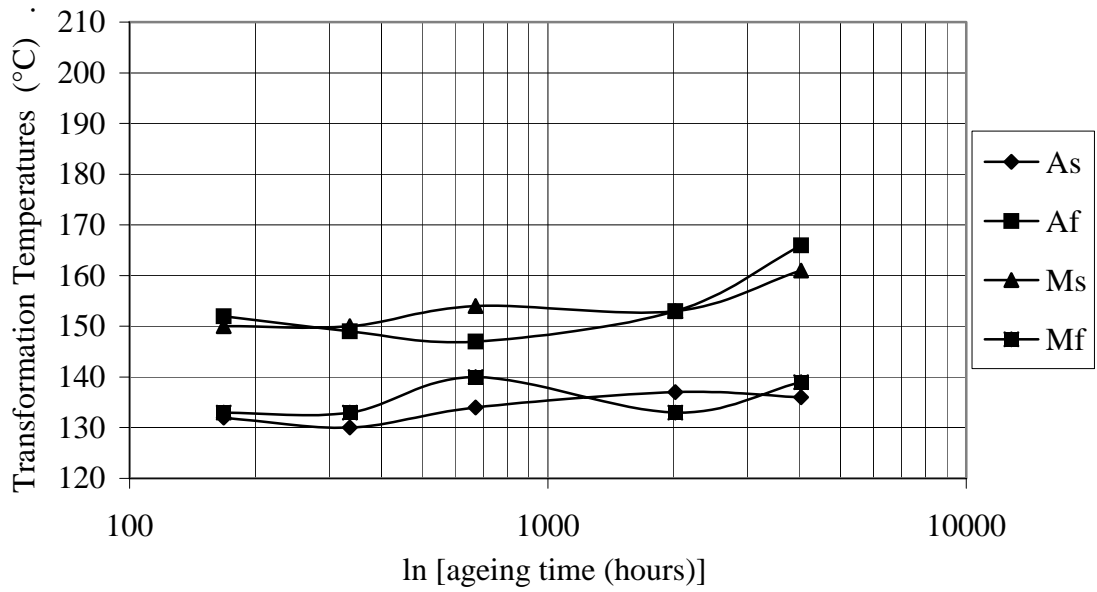
(b) RT-VD12
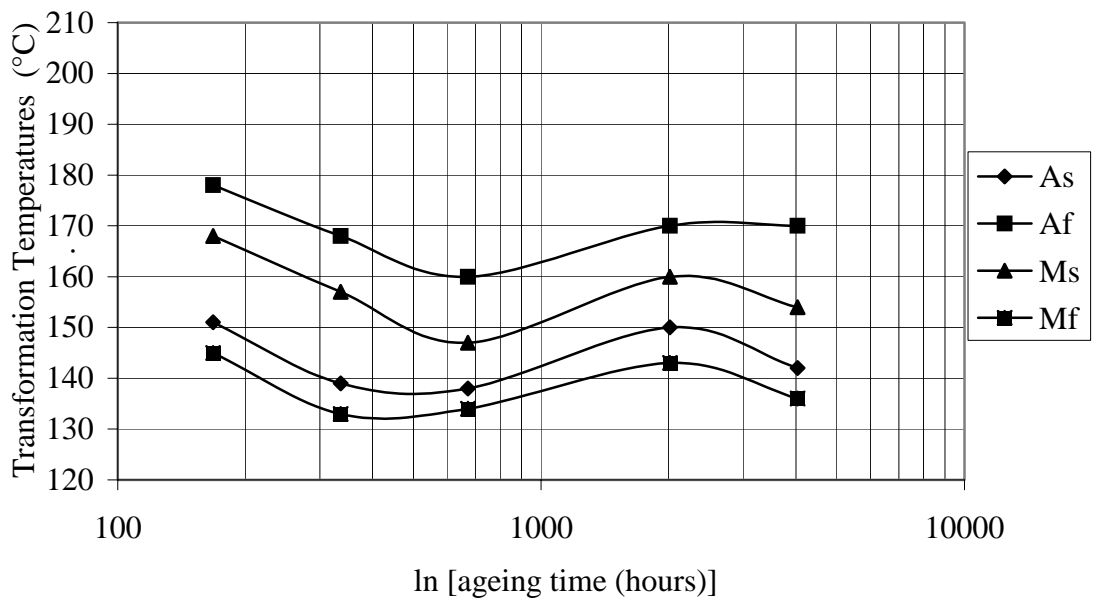
Figure 4.20: The change in A_s, A_f, M_s, M_f temperatures of the a)Cu-12. 6%Al-5.9%Ni-1.8%Mn, b) Cu-12.6%Al-4.8%Ni-1.1%Mn, c) Cu-12.9%Al-5.0%Ni-2.2%Mn alloys with ageing times 168, 336, 672, 2016 and 4032 hours after ageing at Room Temperature.

(c) RT-VD13
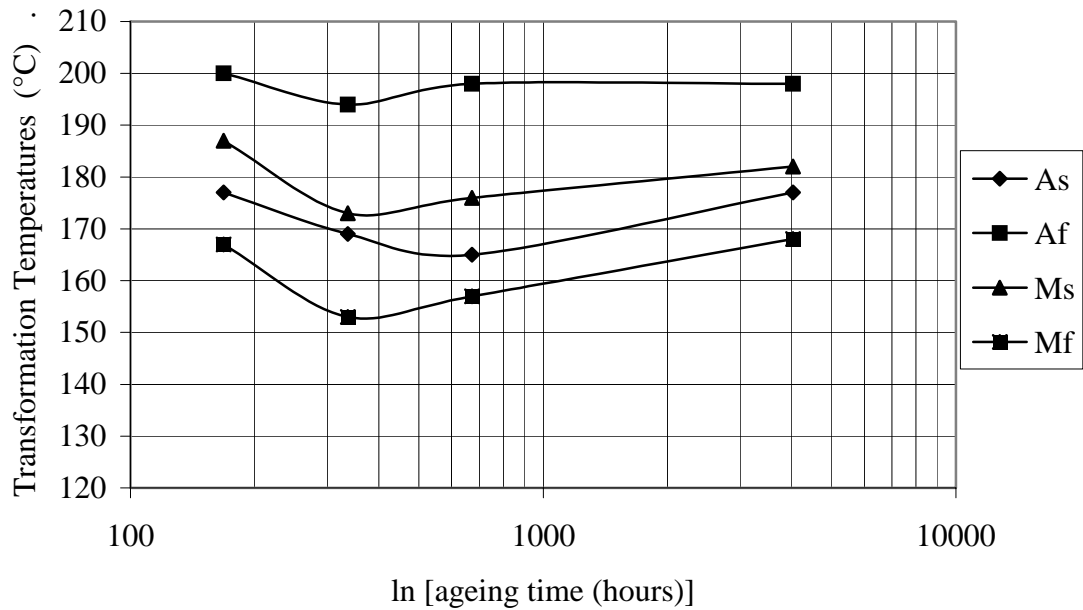
Figure 4.20: Continued.

Additionally, CuAlNi alloys were aged at RT for 168, 336 and 672 hours and the corresponding transformation temperatures were tabulated in Appendix K. Increasing ageing time did not cause any change in transformation temperatures in any of the four CuAlNi alloys. To conclude, CuAlNi alloys were very stable during room temperature ageing.

4.8. Beta Ageing of CuAlNiMn Alloys:

To find out the high temperature ageing behaviour, CuAlNiMn alloys were aged at selected ageing temperatures of 200°C, 230°C, 250°C and 270°C, where they were of Beta (T>A_f) for various times as tabulated in Table 4.5. Corresponding transformation temperatures (A_s, A_f, M_s, M_f) determined by DSC after each ageing time were given in Appendix L.

114

(a) As&Af at 80&100 C for V1
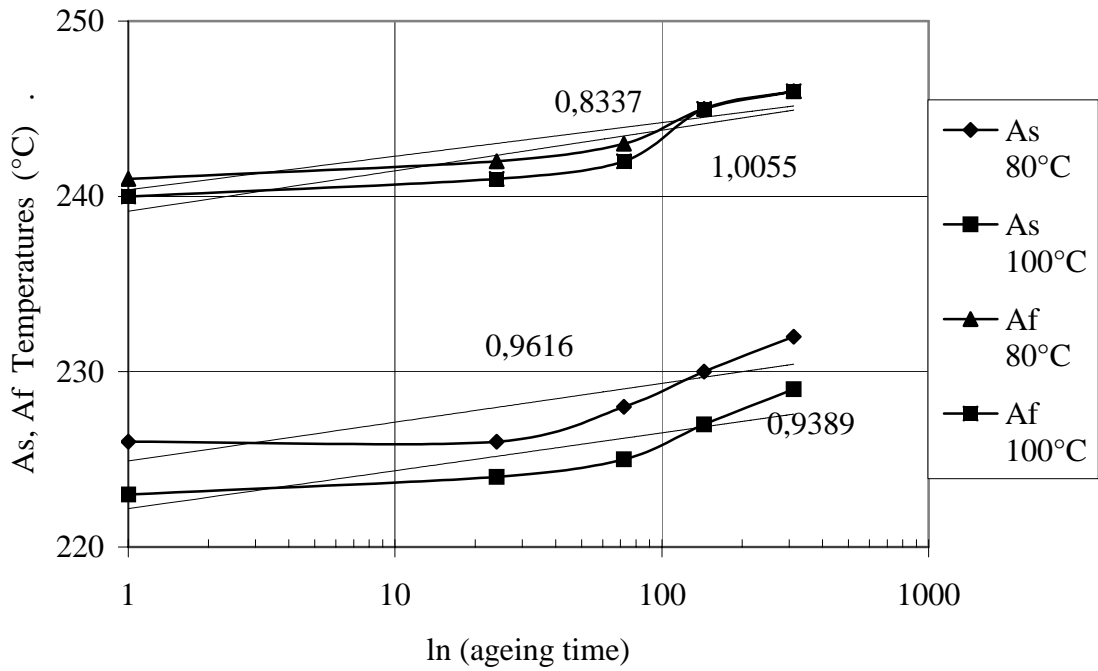
(b) Ms&Mf at 80&100 C for V1
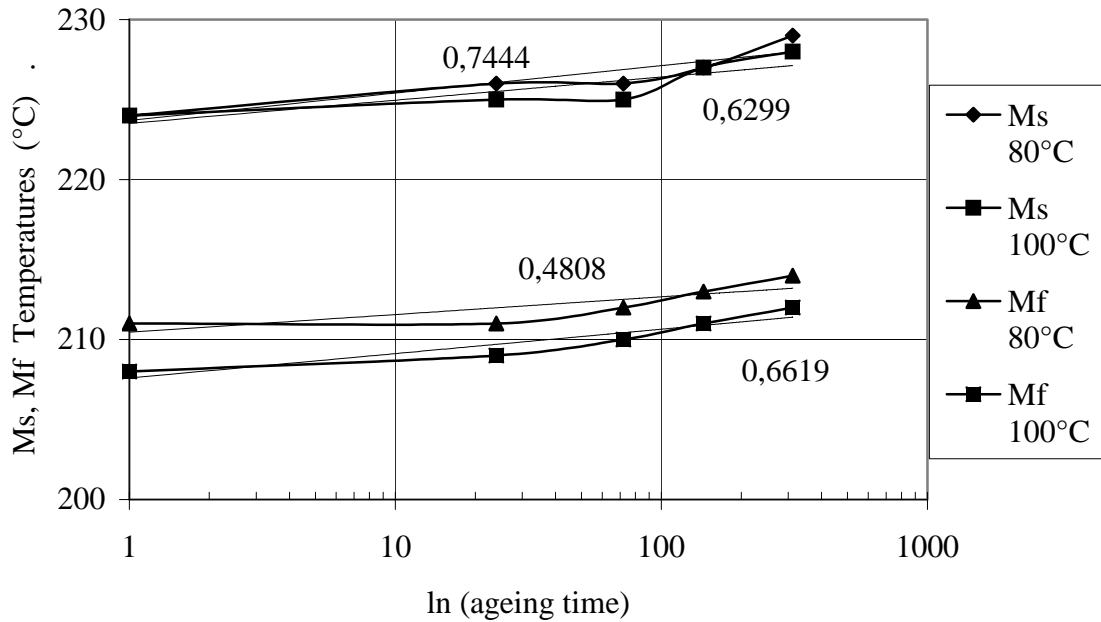
Figure 4.21: The change of the transformation temperatures a) A_s and A_f b) M_s and M_f with ageing time for the ageing temperatures of 80°C and 100°C in Cu-14.0%Al-2.5%Ni (V1) alloy.

(a) As&Af at 80&100 C for V2

0,9482

0,9482

0,7765

1,1294

As, Af Temperatures (°C)

ln (ageing time)

Legend:
- As 80°C
- As 100°C
- Af 80°C
- Af 100°C

(b) Ms&Mf at 80&100 C for V2

0,6392

0,6619

0,694

0,7992

Ms, Mf Temperatures (°C)

ln (ageing time)

Legend:
- Ms 80°C
- Ms 100°C
- Mf 80°C
- Mf 100°C
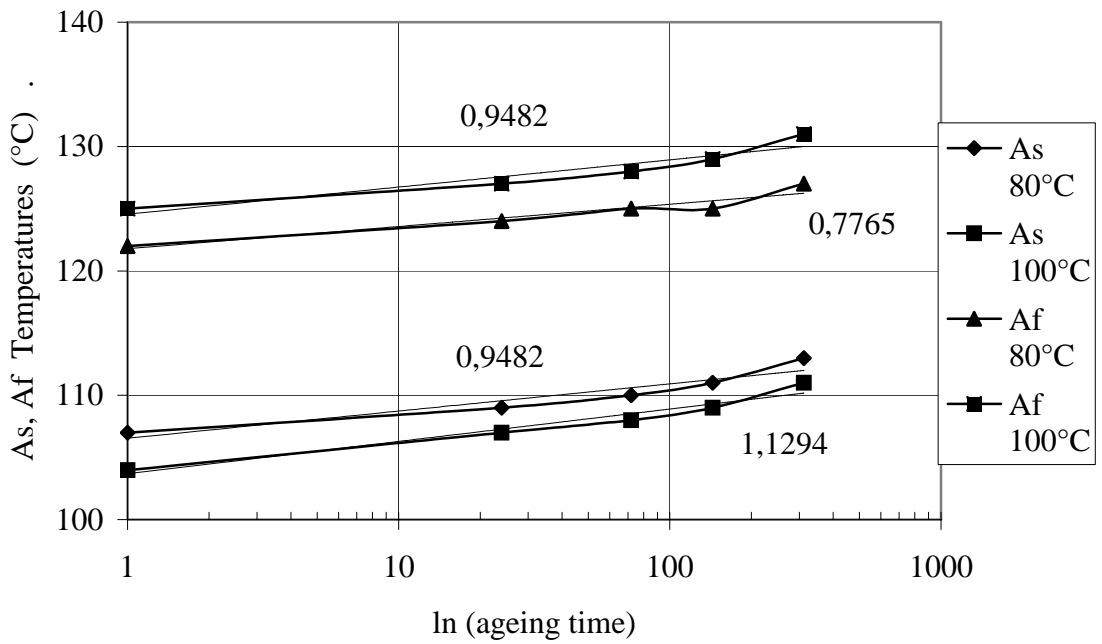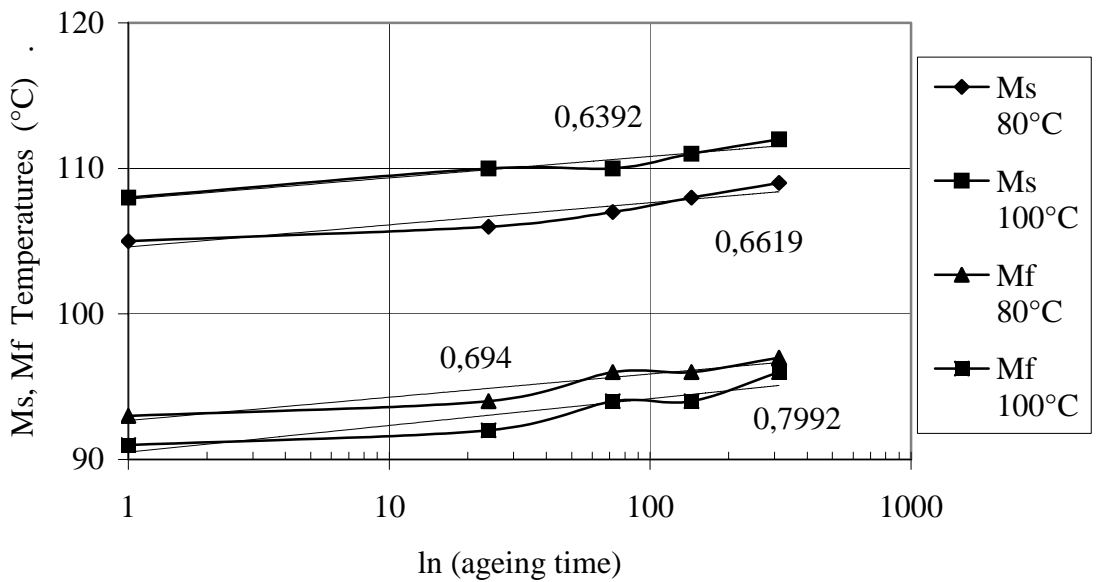
Figure 4.22: The change of the transformation temperatures a) A_s and A_f b) M_s and M_f with ageing time for the ageing temperatures of 80°C and 100°C in Cu-13.9%Al-4.2%Ni (V2) alloy.

(a) As&Af at 80&100 C for V3
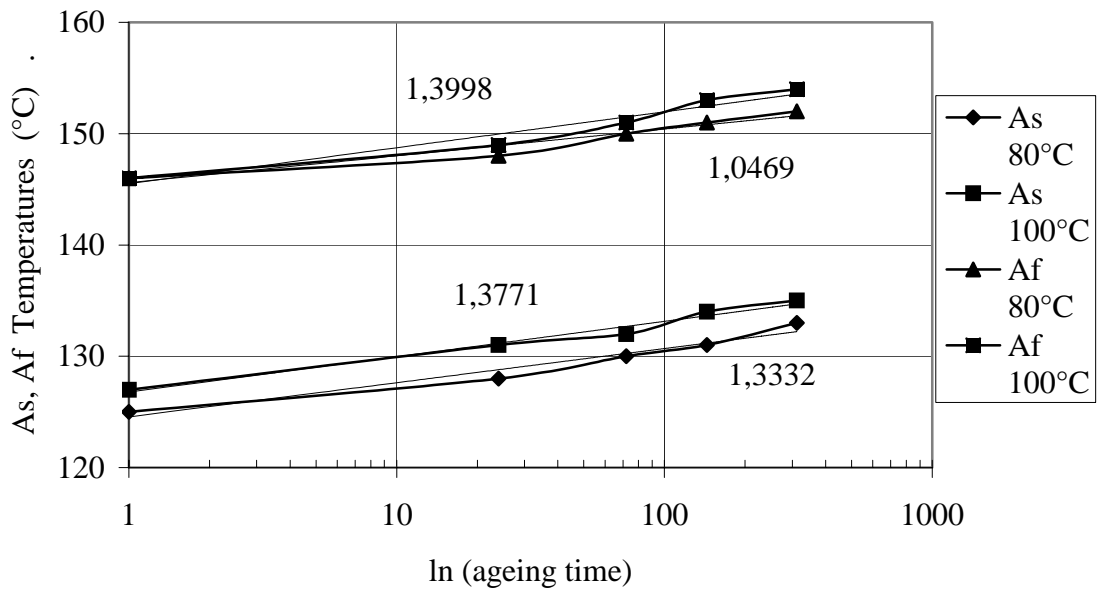
(b) Ms&Mf at 80&100 C for V3
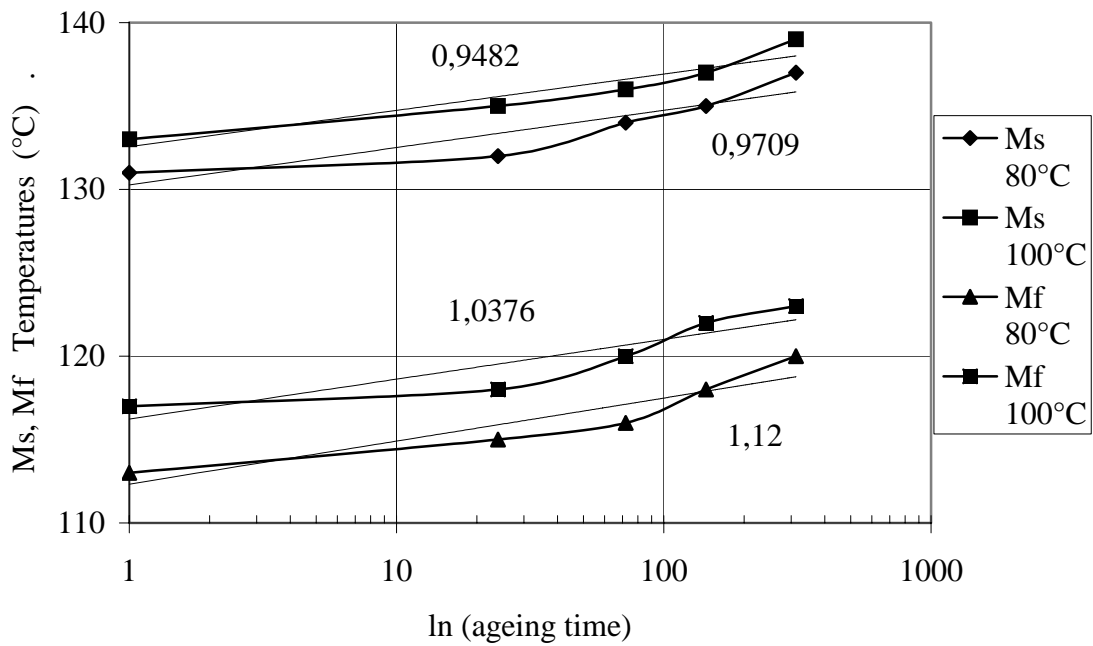
Figure 4.23: The change of the transformation temperatures a) A_s and A_f b) M_s and M_f with ageing time for the ageing temperatures of 80°C and 100°C in Cu-14.2%Al-2.7%Ni (V3) alloy.

117

(a) As&Af at 80&100 C for V4
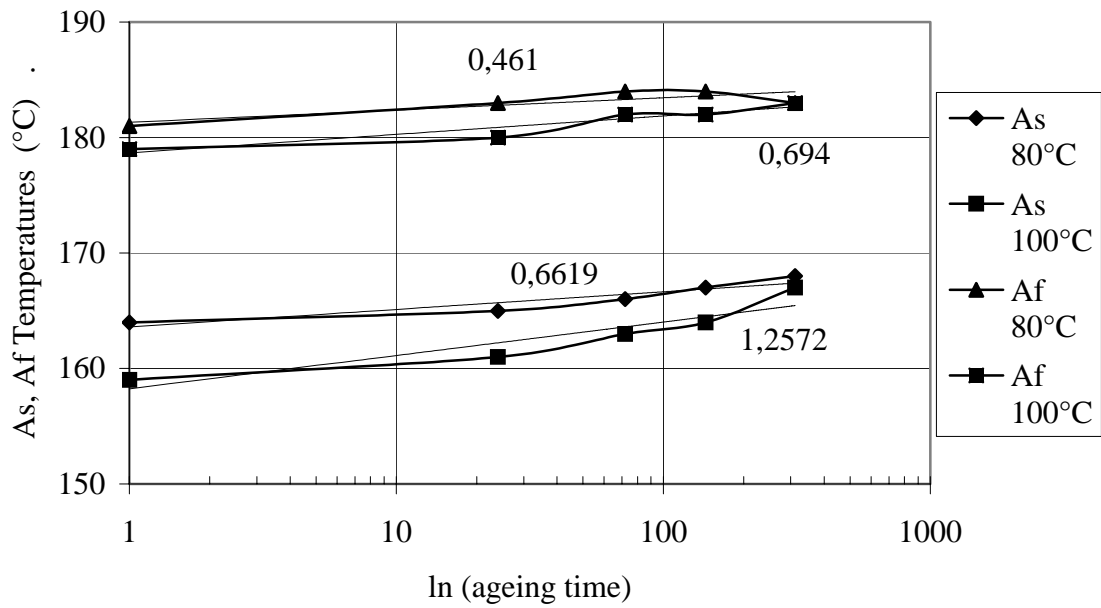
(b) Ms&Mf at 80&100 C for V4
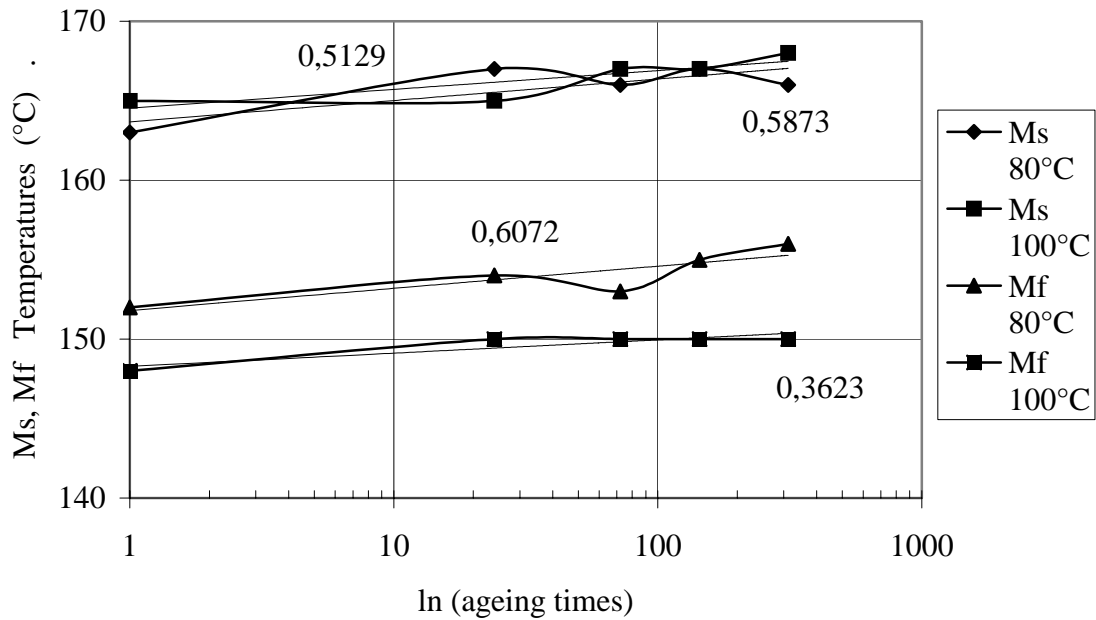
Figure 4.24: The change of the transformation temperatures a) A_s and A_f b) M_s and M_f with ageing time for the ageing temperatures of 80°C and 100°C in Cu-13.6%Al-3.0%Ni (V4) alloy.

Table 4.5: Beta phase ageing schedule for the three CuAlNiMn alloys investigated.

Beta Ageing Temperatures	Beta Phase Ageing Times (minute)		
	VD11	VD12	VD13
200°C	60, 180, 360, 660, 1080, 1560	60, 240, 540, 960, 1560, 2280	60, 180, 360, 660
230°C	15, 45, 105, 225, 405	30, 90, 210, 510	15, 45, 105
250°C	15, 45, 105	15, 45, 105, 285	15, 45
270°C	10, 30, 60	5, 15, 35, 65, 105, 155, 215	5, 15, 35

A general ageing characteristic of the alloys investigated was that, despite the changes in transformation temperatures as will be discussed below, up to a certain ageing period, the peak areas of β→M transformation have not shown any decrease, indicating the lack of any stabilization. Then, with continued ageing the martensite peak area shrinks quite abruptly implying that the amount of martensite transformed is reduced because of Beta phase stabilization. Since determination of the degree of stabilization involves heating and cooling cycles in DSC, which inherently contributes to the ageing phenomena, time at a temperature to stabilization has been determined only approximately and sketched in Figure 4.25 as a function of temperature for the alloys investigated. There seems to be a logarithmic relation between the beta stabilization time and temperature. Beta stabilization time here corresponds to the considerable decrease of β→M transformation peak area or its complete disappearance during DSC measurements. Beta stabilization times at the corresponding Beta phase ageing temperatures were tabulated in Table 4.6. The experiments carried out on alloy VD12 have not been conducted long enough to observe the beta stabilization (maximum 510 minutes ageing at 230°C and 285 minutes ageing at 250°C) in this alloy sample. It was clear from Figure 4.25 that as expected, increasing beta ageing temperatures resulted in shorter beta stabilization times. Alloy VD13 had the shortest beta stabilization time while beta stabilization

time for alloy VD12 was the longest and alloy VD11 was inbetween. With regard to the Manganese contents, highest Manganese bearing Cu-12.9%Al-5.0%Ni-2.2%Mn alloy (VD13) was the one stabilized first and the lowest manganese content Cu-12.6%Al-4.8%Ni-1.1%Mn alloy (VD12) was the longest lasting alloy during beta phase ageing.

According to these results, to introduce CuAlNiMn alloys as potential candidates for high temperature shape memory applications, as it is usually done in literature, is contradictory since Manganese bearing CuAlNi alloys exhibit shorter lifetime above 200°C.

For all three alloys, ageing times were considerably shorter for beta phase ageing as compared to martensite phase ageing. Martensite phase ageing is more sluggish than beta phase ageing, simply because of the higher beta phase ageing temperatures, which imparts the necessary atomic mobility, rather than structural differences between martensite and beta phases. Both phases are ordered and of similar close packing. Exceptionally, martensite with non-cubic crystal structure has lower symmetry than the cubic beta phase. The long period stacking order M18R$_1$
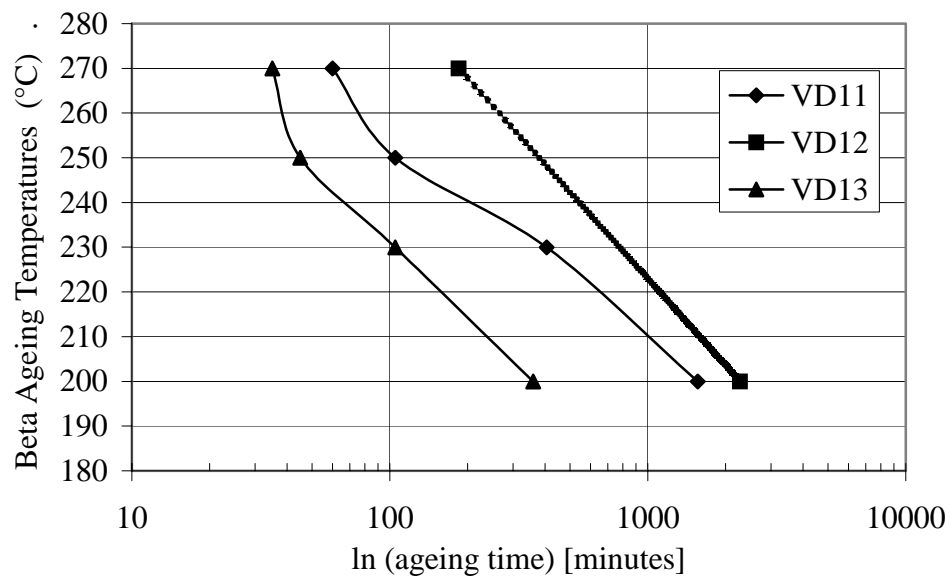
Figure 4.25: Beta Phase stabilization times for three CuAlNiMn alloys at the corresponding Beta ageing temperatures.

Table 4.6: Beta stabilization times at the corresponding beta ageing temperatures for CuAlNiMn alloys.

Beta Ageing Temperatures	Beta Phase Stabilization Times (minutes)		
	VD11	VD12	VD13
200°C	1560	2280	660
230°C	405		105
250°C	105		45
270°C	60	185	35

martensite structure is monoclinic. Under this circumstance, diffusion may be anisotropic due to the non-cubic crystal structure, which may slow down diffusion. Therefore, sluggish martensite ageing as compared to beta phase ageing is primarily due to lower ageing temperatures but anistropic diffusion in martensite may also be contributing.

Change in transformation temperatures with increasing beta ageing times for three CuAlNiMn alloys were plotted in Figure 4.26 to Figure 4.28. Two characteristic and discrete trends of the transformation temperatures common to all three alloys were clearly seen in these figures: Firstly, upon ageing at 200°C, after a certain period of ageing, all transformation temperatures were observed to decrease suddenly just prior to beta stabilization. M_f temperature decreased remarkably as compared to others. On the other hand, upon ageing above 200°C, all transformation temperatures increased except the M_f temperature, which mostly exhibited a gradual decrease. Increase in the transformation temperatures became more obvious at the higher beta ageing temperatures. Increasing A_s and A_f temperatures is probably due to stabilized beta phase. When martensite transforms into beta upon heating, stabilized beta phase regions in the martensite restrict the transformation so that transformation becomes more difficult and A_s and A_f temperatures increase.

(a) 200 °C VD11
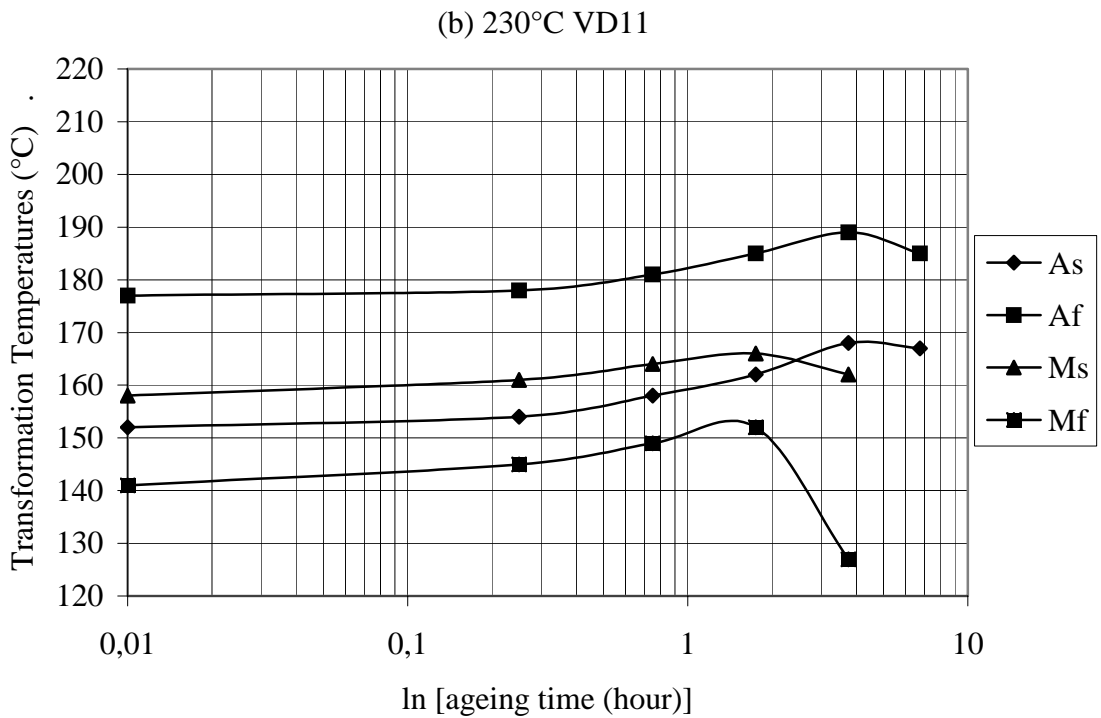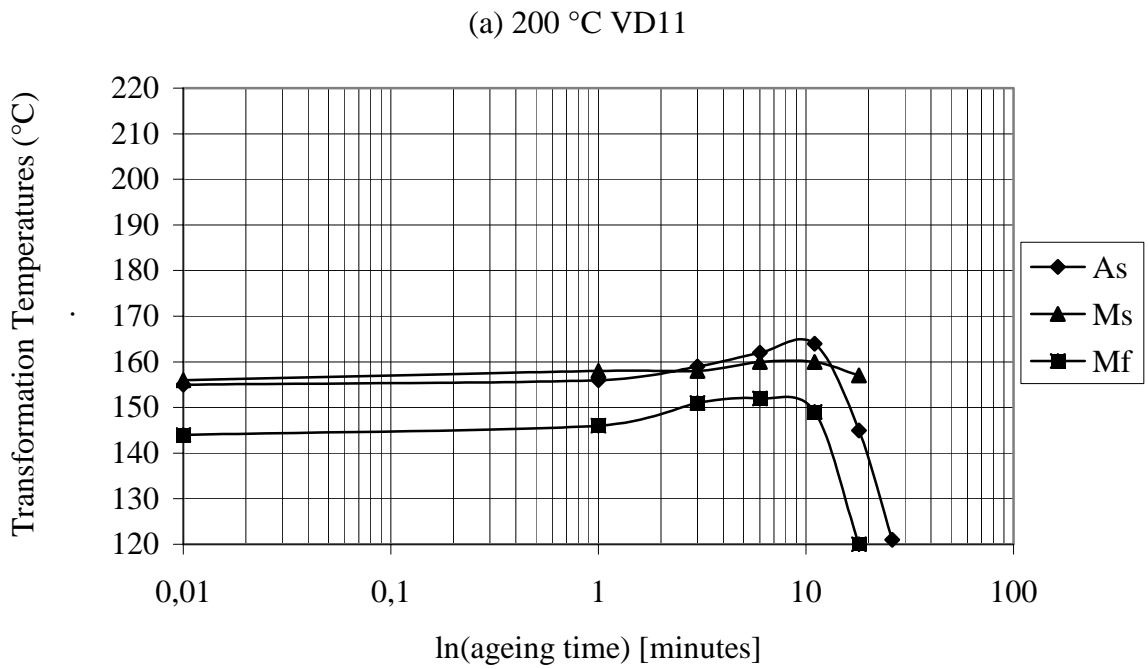
(b) 230°C VD11

Figure 4.26: The change in A_s, A_f, M_s, M_f temperatures of the Cu-12. 6%Al-5.9%Ni-1.8%Mn alloy (VD11) with varying ageing times at the employed ageing temperatures a) 200°C, b) 230°C, c) 250°C and d) 270°C.

(c) 250°C VD11
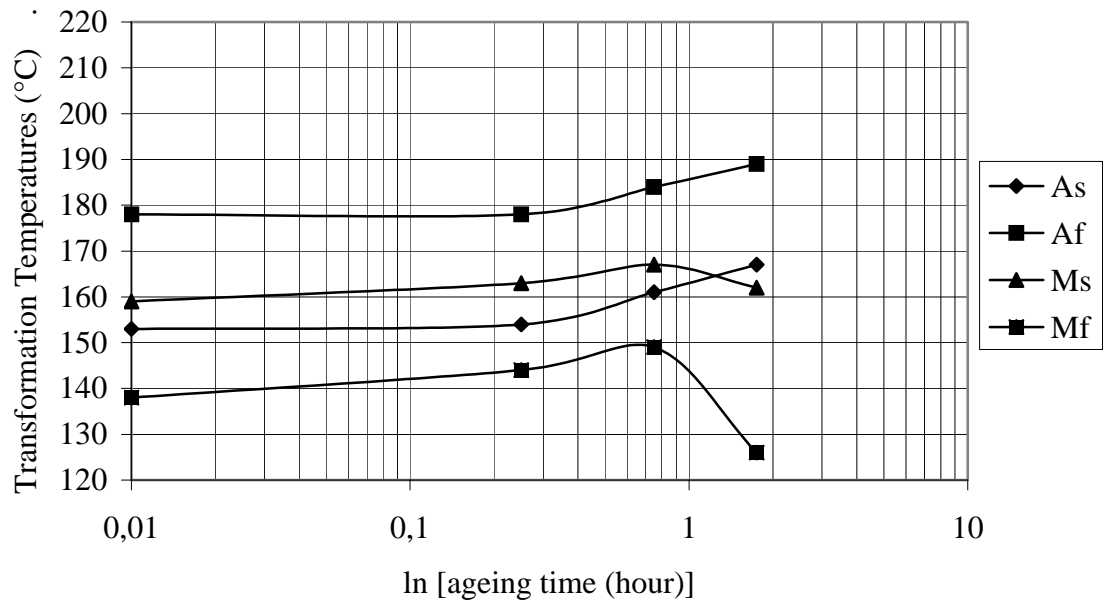
(d) 270°C VD11
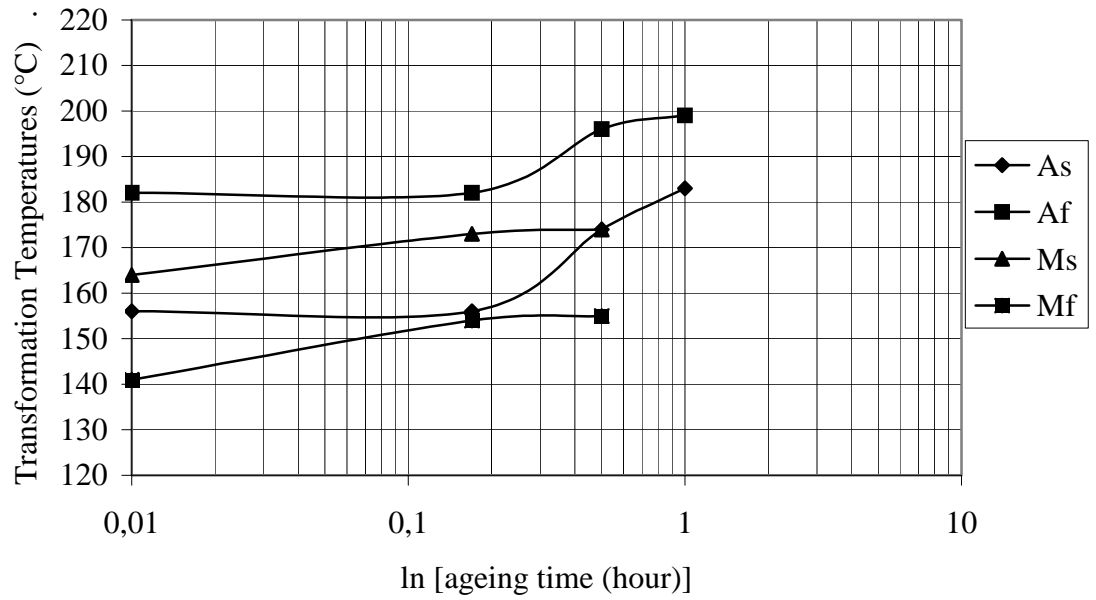
Figure 4.26: Continued.
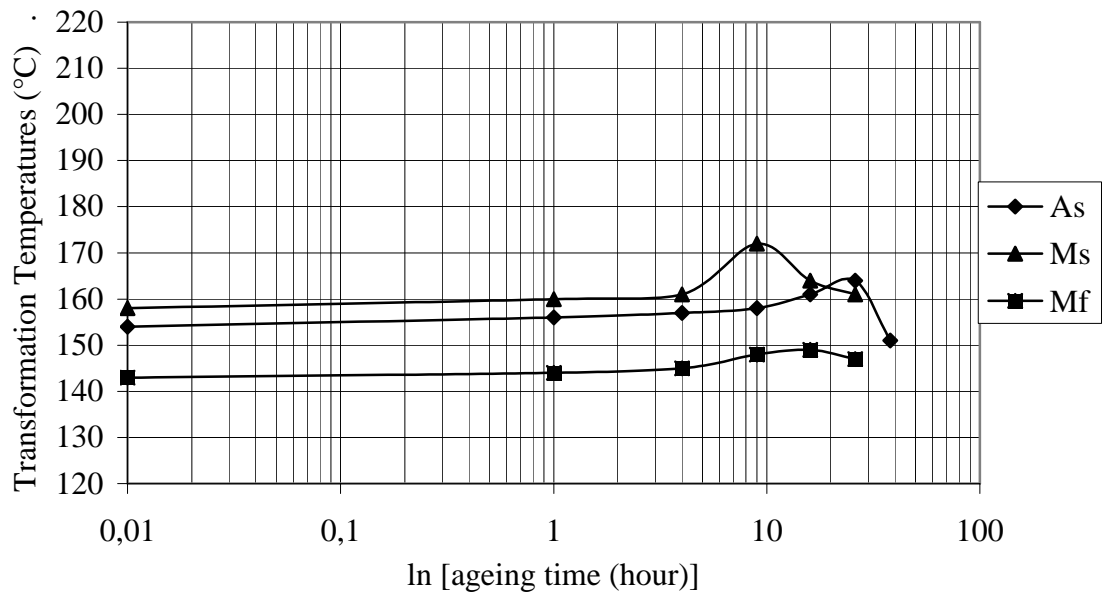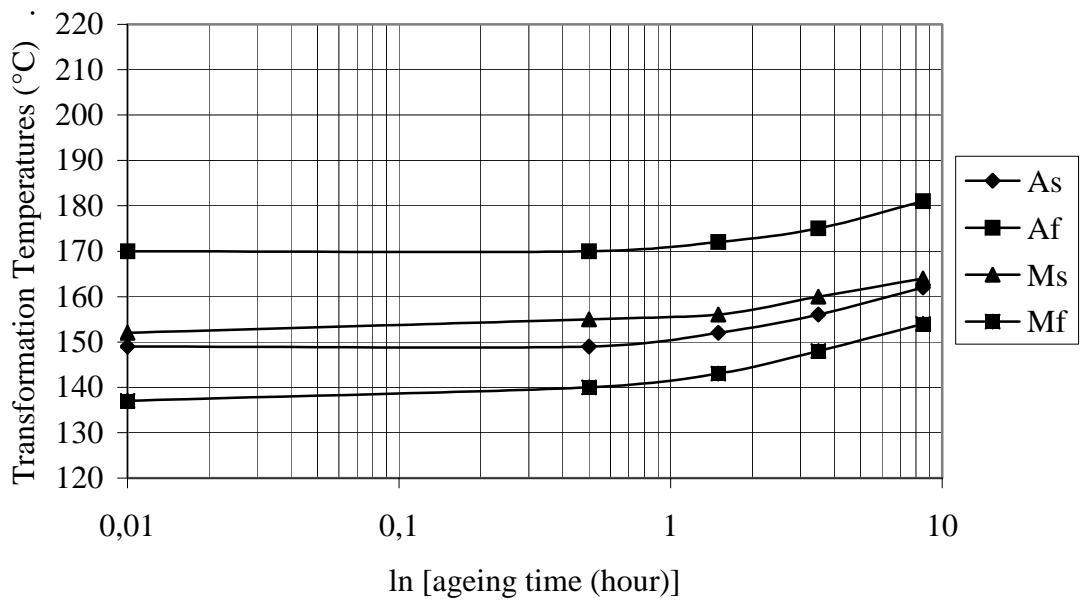
Figure 4.27: The change in A_s, A_f, M_s, M_f temperatures of the Cu-12.6%Al-4.8%Ni-1.1%Mn alloy (VD12) with varying ageing times at the employed ageing temperatures a) 200°C, b) 230°C, c) 250°C and d) 270°C

(c) 250°C VD12
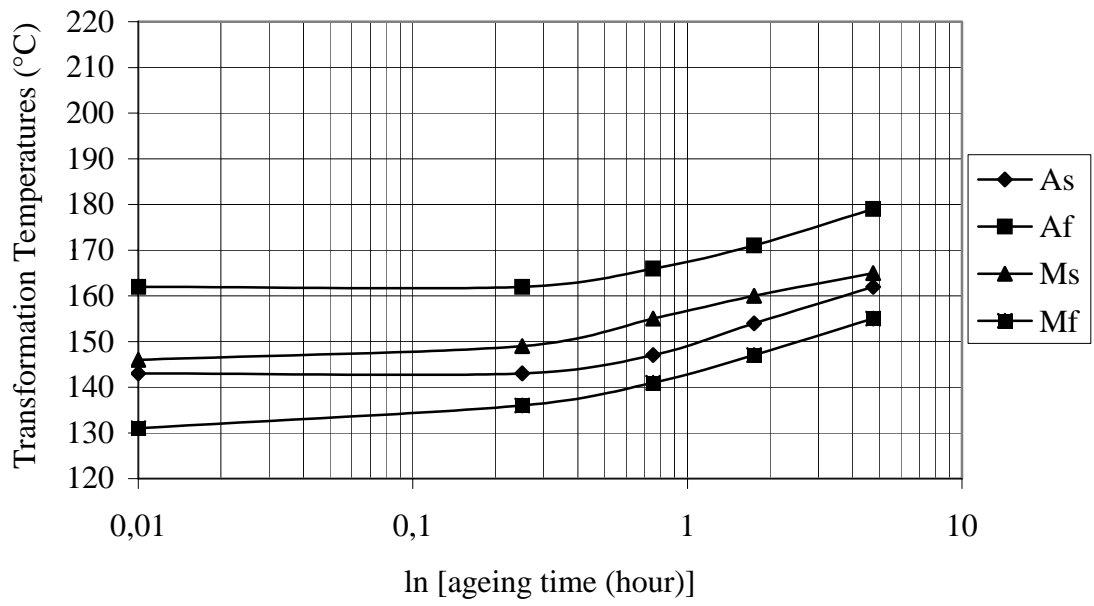
(d) 270°C VD12
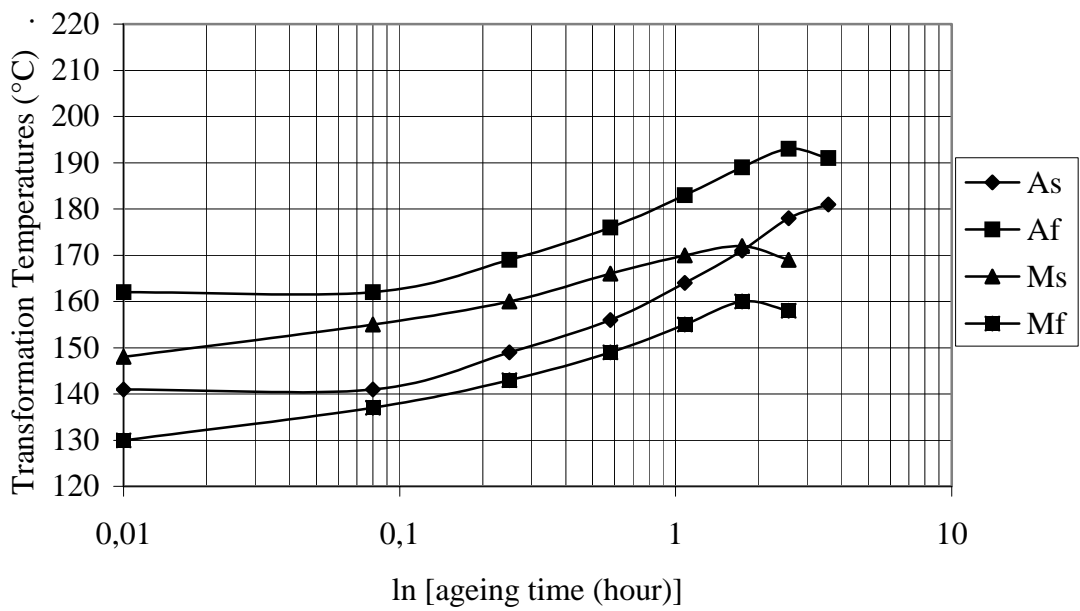
Figure 4.27: Continued

(a) 200°C VD13
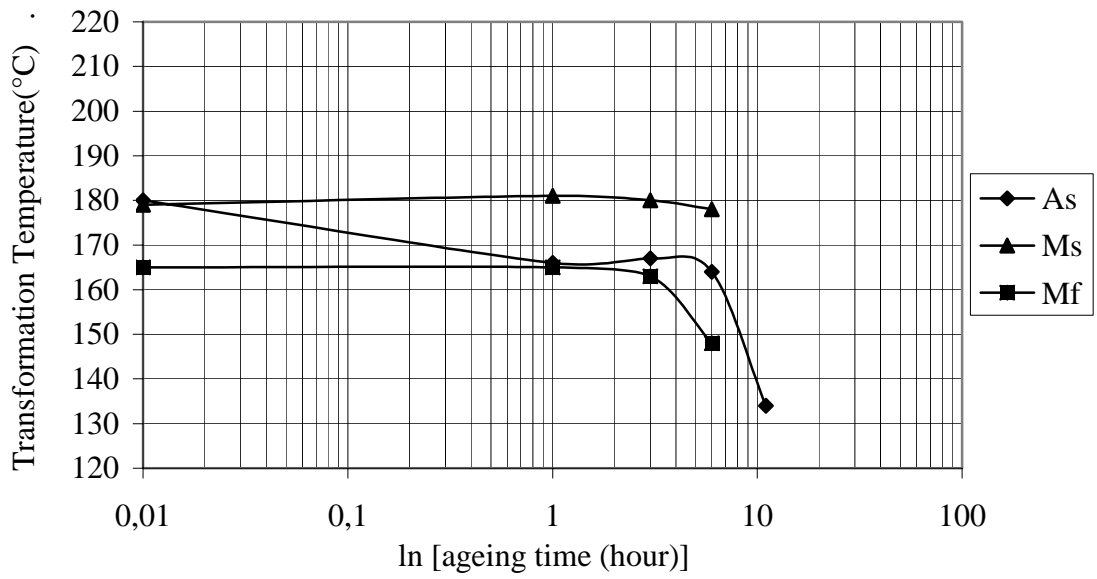
(b) 230°C VD13
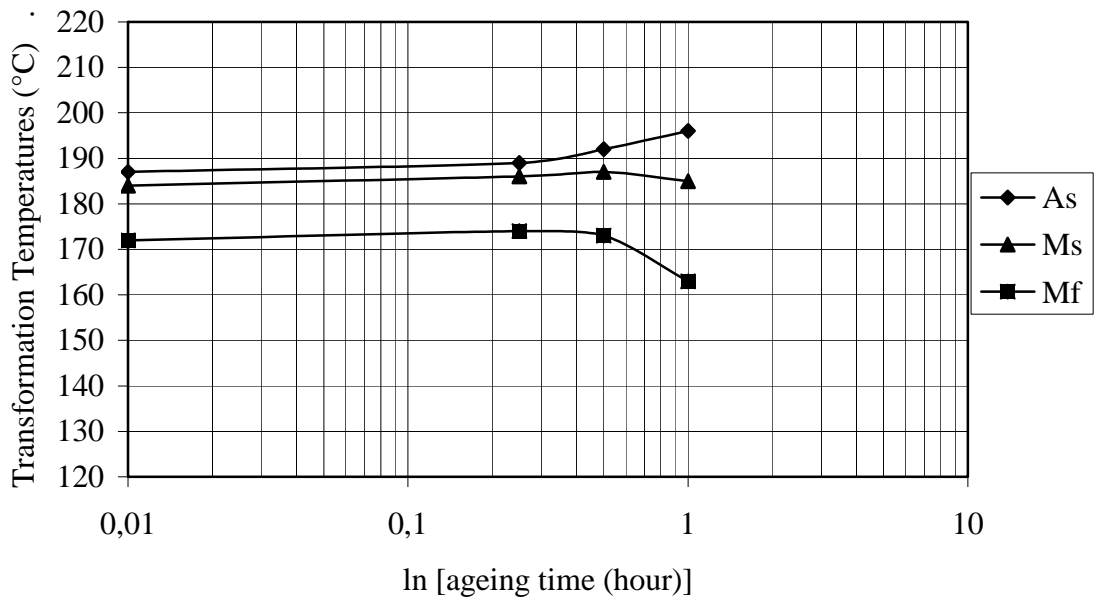
Figure 4.28: The change in A_s, A_f, M_s and M_f temperatures of the Cu-12.9%Al-5.0%Ni-2.2%Mn alloy (VD13) with varying ageing times at the employed ageing temperatures a) 200°C, b) 230°C, c) 250°C and d) 270°C.

126

(c) 250°C VD13
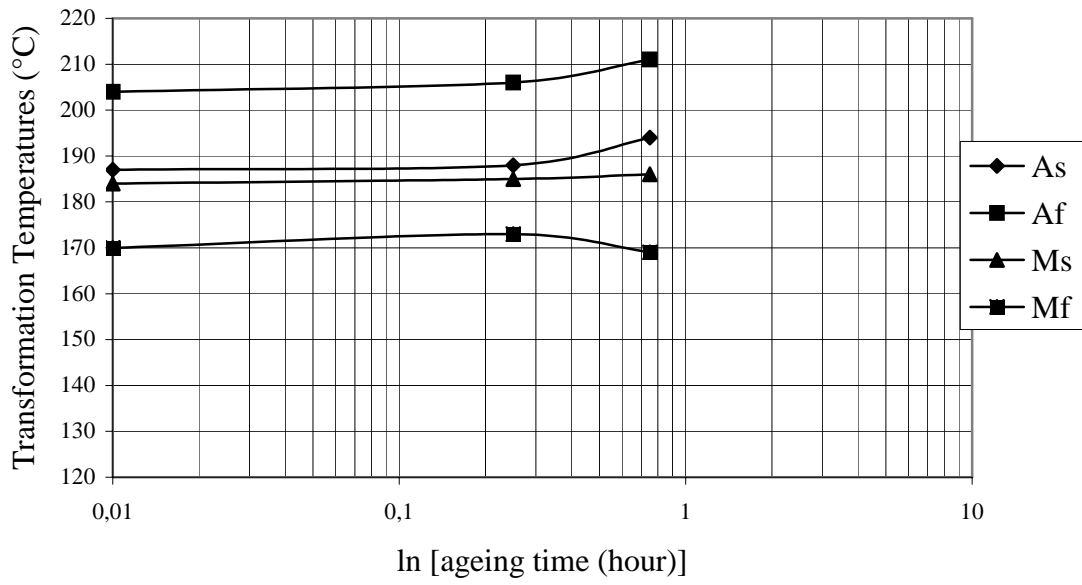
(d) 270°C VD13
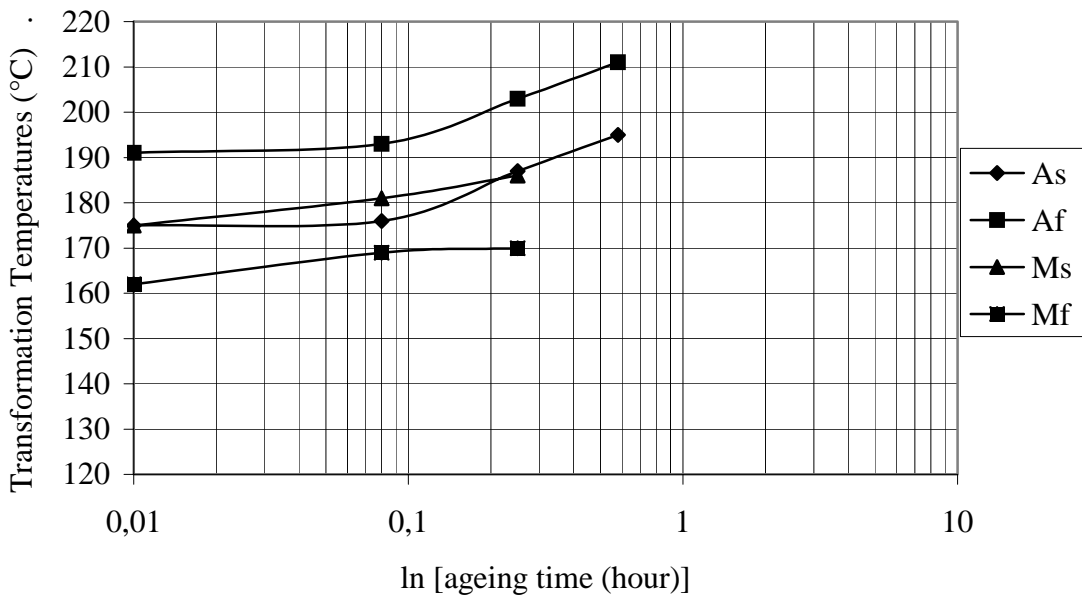
Figure 4.28: Continued

127

4.9. Beta Ageing of CuAlNi Alloys:

Four CuAlNi alloys investigated were aged at 200°C for various times as tabulated in Table 4.7. Changes of transformation temperatures after ageing at 200°C were given in Appendix M. Beta stabilization was not observed in any of the four CuAlNi alloys at the end of 96 hours ageing at 200°C and β→M transformations were still recordable. However, as given in the previous section for the three CuAlNiMn alloys studied, Beta stabilization was realized at the end of 26, 38 and 11 hours ageing at 200°C. In contrast, for CuAlNi alloys beta was not stabilized even after 96 hours ageing at this temperature, indicating that beta phase stabilization times for CuAlNi alloys were considerably longer than that for Mn containing alloys.

In conclusion, on the basis of ageing studies at 200°C, CuAlNi alloys were found to be more resistant to high temperature ageing than CuAlNiMn alloys despite the effort in literature to introduce the CuAlNiMn alloys as potential candidates for high temperature applications.

Change of transformation temperatures with ageing time at 200°C for the four CuAlNi alloys were shown in Figure 4.29. It has been observed that all transformation temperatures consistently increase with ageing time, reaching to as

Table 4.7: Beta phase ageing periods at 200°C for four CuAlNi alloys.

Ageing Temperature (°C)	Beta phase ageing times (minutes)			
	V1	V2	V3	V4
200	15, 45, 105, 345, 765, 1485, 5805	15, 45, 105, 345, 765, 1485, 2925, 5805	15, 45, 105, 405, 825, 1545, 5805	15, 45, 105, 525, 1245, 5805

much as 25-30°C increase after ageing for 96 hours. The rate of increase becomes greater with time. This behaviour was different than the behaviour of CuAlNiMn alloys at the same ageing temperature, showing a decrease in all transformation temperatures that terminates with beta phase stabilization after a certain period of beta ageing. Since beta stabilization has not taken place in CuAlNi alloys all transformation temperatures have continually increased. Transmission Electron Microscope studies of Cu-13.6wt%Al-3.0wt%Ni alloy aged at 210°C for one hour have revealed the γ_2 precipitates. In CuAlNi alloy systems, γ_2 precipitates were known to be enriched by aluminum solute atoms. The remaining matrix has been depleted by aluminum content and enriched by Cu and Ni atoms as a result of formation of γ_2 precipitates. Upon γ_2 precipitates reaching equilibrium, α precipitates form from the Cu and Ni enriched matrix at relatively higher temperatures i.e., 400-500°C. Since α precipitates were not observed in Cu-13.6wt%Al-3.0wt%Ni alloy aged at 210°C for one hour, not even expected at longer ageing periods at this relatively lower temperature, the remaining matrix will be continually decreasing in aluminum content as long as γ_2 precipitation sustained. Therefore, the continual increase of transformation temperatures might have been attributed to matrix concentration change due to γ_2 precipitation. The experimental TEM work on beta phase ageing of CuAlNi alloys was explained in section 4.11.

4.10. Activation Energy Determination For CuAlNiMn Alloys:

Kinetic analysis of the DSC data to determine the activation energy to predict the nature of the processes involved in ageing has been attempted assuming a recovery type homogeneous transformation is responsible. In the relation $f(P-P_0)=A\exp(-Q/RT)t$ expected for such a transformation P is the value of certain property at time t and P_0 is the saturation value, i.e., value after infinite aging time. In the context of the present study, the transformation temperatures can be taken as the property being affected from ageing and at constant value of the property from the slope of $\ln t$ vs. $1/T$ fits one can get the activation energy. But the analysis has not been

(a) V1

ln [ageing time (minutes)]

(b) V2

ln [ageing time (minutes)]
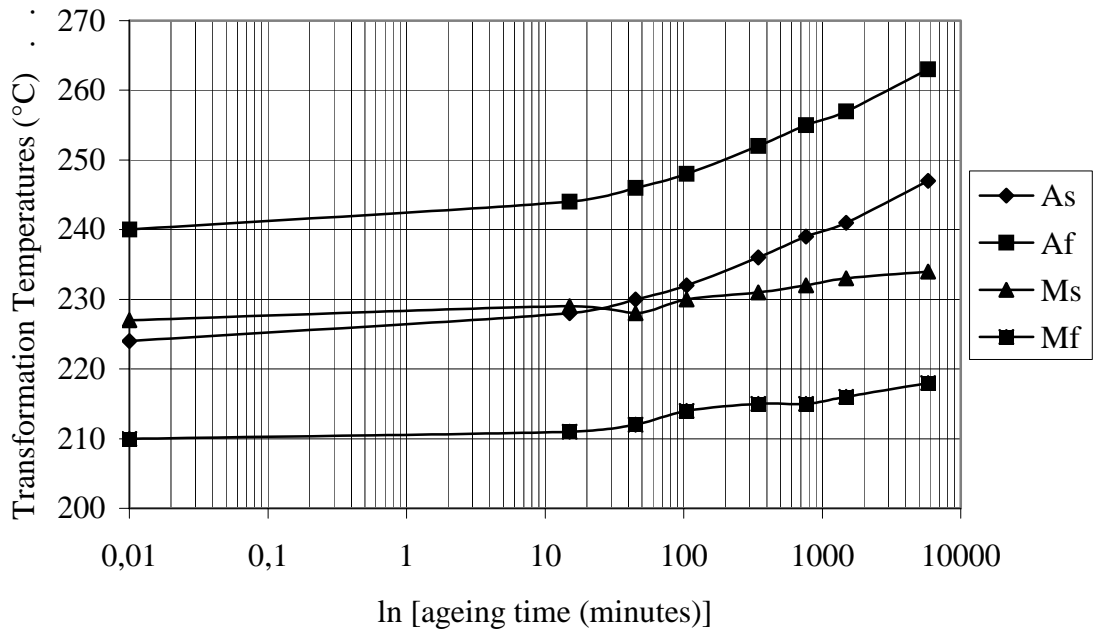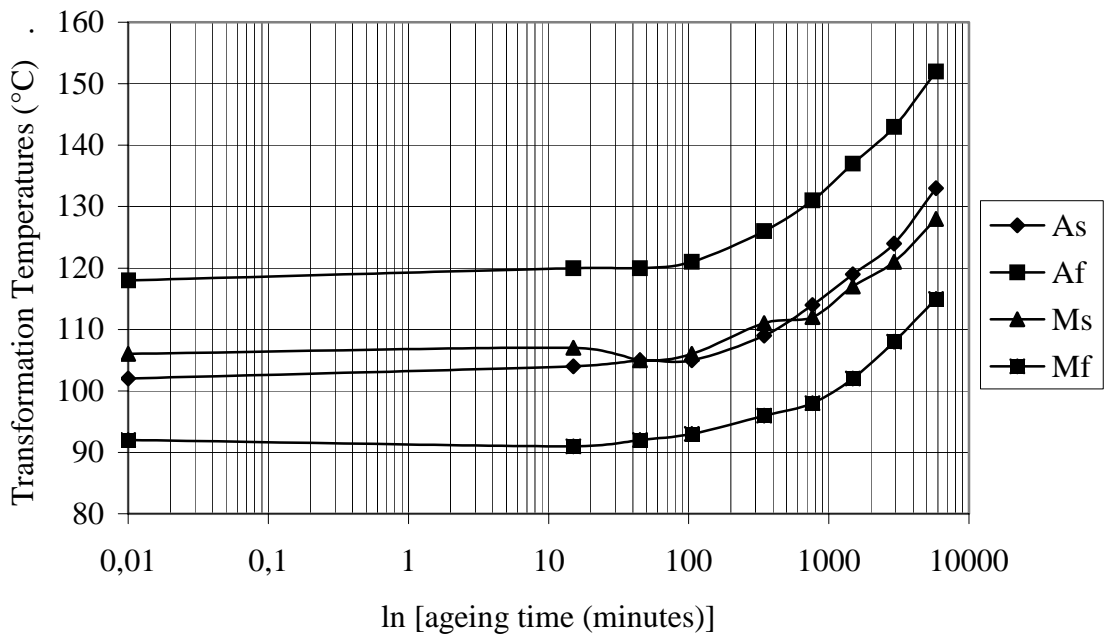
Figure 4.29: The change in A_s, A_f, M_s and M_f temperatures after ageing at 200°C for a) Cu-14.0%Al-2.5%Ni (V1) b) Cu-13.9%Al-4.2%Ni (V2) c) Cu-14.2%Al-2.7%Ni (V3) and d) Cu-13.6%Al-3.0%Ni (V4) alloys

(c) V3
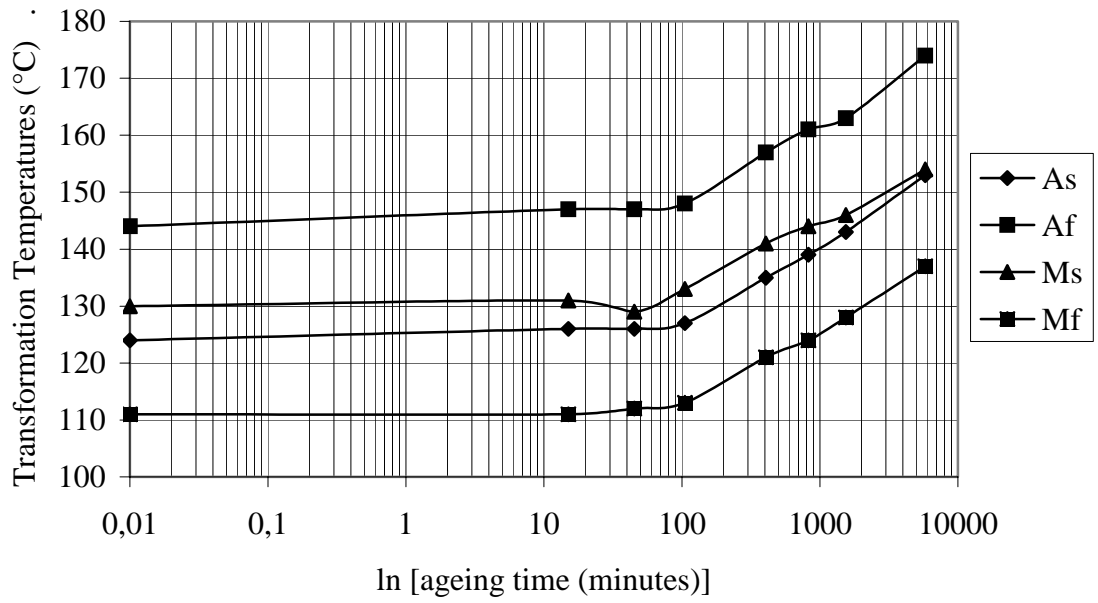
(d) V4
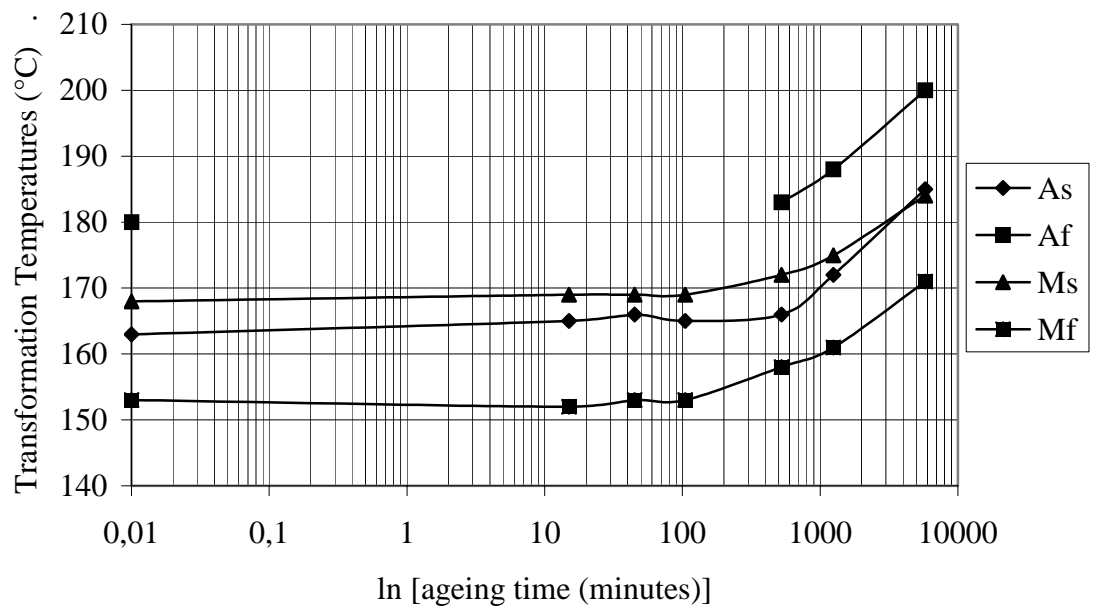
Figure 4.29: Continued.

131

successful because the saturation value, P_0, itself seems to be temperature dependent as can be seen from the examples given in Figure 4.17 a, b to Figure 4.19 a, b. So the only way to determine the activation energy, which most probably would come out to be temperature dependent, is temperature differential testing where change in property is measured as the temperature is instantaneously changed by few degrees. But since the property measured, A_s, A_f is not readily measurable just before and after the temperature change (since their measurement requires extensive heating and cooling), another readily measurable property, such as resistivity or heat capacity, must be employed for the kinetic analysis.

4.11. Transmission Electron Microscope Studies of Ageing Results:

To study the microstructural evolutions during ageing, a Cu-12.6wt%Al-5.9wt%Ni-1.8wt%Mn alloy aged at 150°C for 312 hours was examined by T.E.M. Crystal structure has been found to be still a mixture of $18R_1$ and 2H unaffected from ageing. Generally, martensite plates were coarse and planar and the stacking fault density found to be slightly lower than normally expected, Figure 4.30. Martensite plates in certain regions of the TEM samples were observed to consist of very fine sub plates oriented differently, Figure 4.31-a. Dark field images of the differently oriented sub plates from the same region were shown in Figure 4.31-b, c. Martensite variants were observed to be twin related as shown in Figure 4.32-a, b. Through investigation has revealed only the common features of martensite plates and no sign of precipitate formation has been detected. CuAlNiMn alloys aged at lower temperatures were not examined to check precipitate formation due to kinetic considerations. Based on the fact that precipitates were not observed in this alloy, it was concluded that "precipitates pinning martensite boundaries" was not the mechanism driving martensite stabilization in contrast to literature where precipitate pinning mechanism has been widely offered to be responsible of martensite stabilization. Formation of very fine size coherent grain-refiner rich precipitates in the grain refined copper-based shape memory alloys in the as-quenched condition

has been well known in literature. However, in this study, alloys produced were not grain refined and as-quenched alloys have not exhibited those fine coherent precipitates. Although no precipitates have not been observed at the martensite ageing temperatures in CuAlNi alloys, formation of γ precipitates in CuZnAl alloys has been well known. Thermodynamically, formation of γ precipitates in CuAlNi alloys has been also possible at higher aluminum content however, it might not be achievable kinetically at the considered ageing temperature.

TEM studies to infer precipitation characteristics of a Cu-13.6%Al-3.0%Ni alloy, which has been aged above A_f temperature at selected temperatures of 210°C, 310°C and 410°C for one hour and than water quenched have shown formation of very fine size precipitates at all three beta phase ageing temperatures. Bright field images of fine precipitates, which were formed after ageing at 210°C for one hour were shown in Figure 4.33. Precipitates in coarse and planar martensite plates were very small and of very low density, Figure 4.33-a. Mostly, the martensite plates were so much faulted that they blur the image of precipitates, Figure 4.33-b, c. As well as fine precipitates, some larger precipitates that reveal stain contrast also appear together in Figure 4.33-d (This stain contrast seems to be the effect known as surface precipitation after foil preparation). More densely distributed precipitates were excited by a dark field image in Figure 4.34. These precipitates were spherical and the sizes were around 10-20 nm. However, precipitates as large as 34 nm and as small as 3 nm were present. In Figure 4.35-a, the central dark plate reveals [011] zone diffraction pattern of 2H martensite crystal structure, see Figure 4.35-c and its left neighbor white plate reveals [230] zone diffraction pattern of $18R_1$ martensite crystal structure, illustrated in Figure 4.35-b. Zone axis of each plate was parallel and the orientation relationship between 2H and $18R_1$ martensite phases has been found as:

$$[011]_{2H} \; // \; [230]_{18R1}$$

$$(200)_{2H} \; // \; (0018)_{18R1}$$
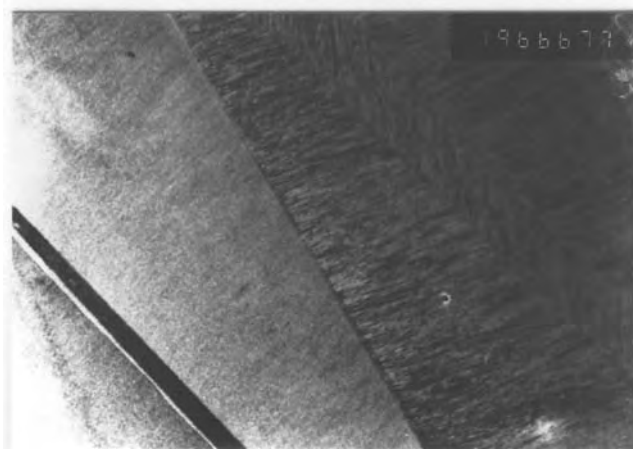
(a)
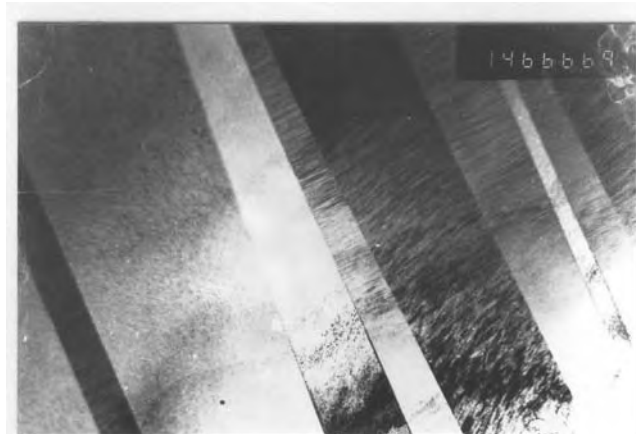
(b)

Figure 4.30: Martensite plates of Cu-12.6wt%Al-5.9wt%Ni-1.8wt%Mn alloy aged at 150°C for 312 hours. a) BF, 19kX, b) BF, 14 kX c) BF, 10 kX, d) BF, 29 kX.
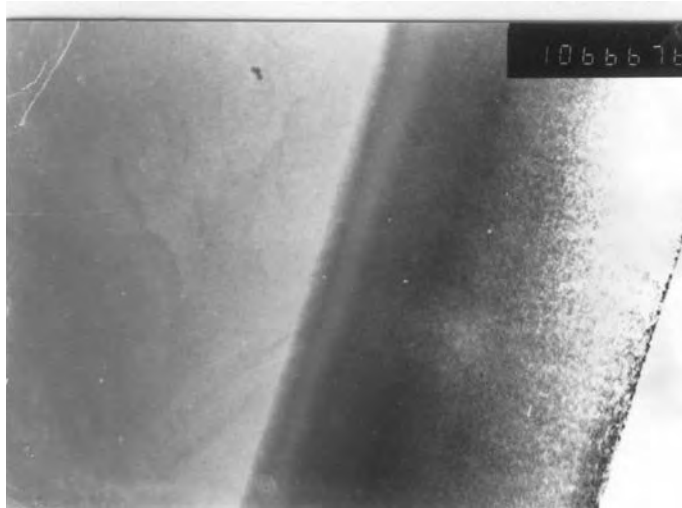
(c)

(d)

Figure 4.30: Continued.

(a)

(b)

(c)

(d)

Figure 4.31: Sub martensite plates observed in Cu-12.6wt%Al-5.9wt%Ni-1.8wt%Mn alloy aged at 150°C for 312 hours. a) BF, 10kX, b) DF, 10 kX, c) DF, 10 kX, d) corresponding diffraction pattern of c.

(a)
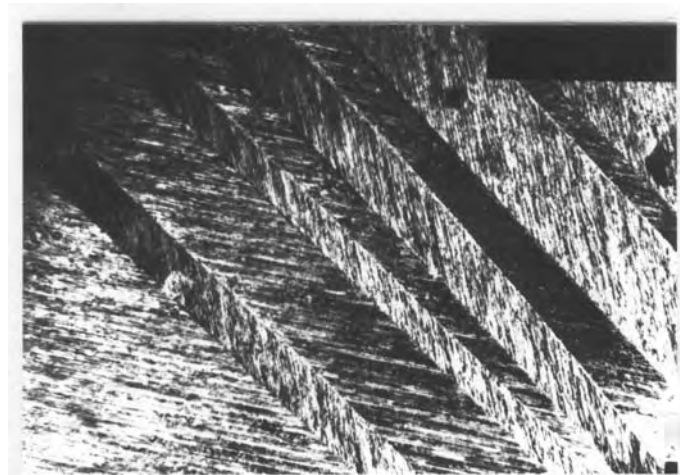
(b)

Figure 4.32: Twin related martensite variants in Cu-12.6wt%Al-5.9wt%Ni-1.8wt%Mn alloy aged at 150°C for 312 hours. a) BF, 19 kX, b) DF, 19 kX.

(a)

(b)

(c)
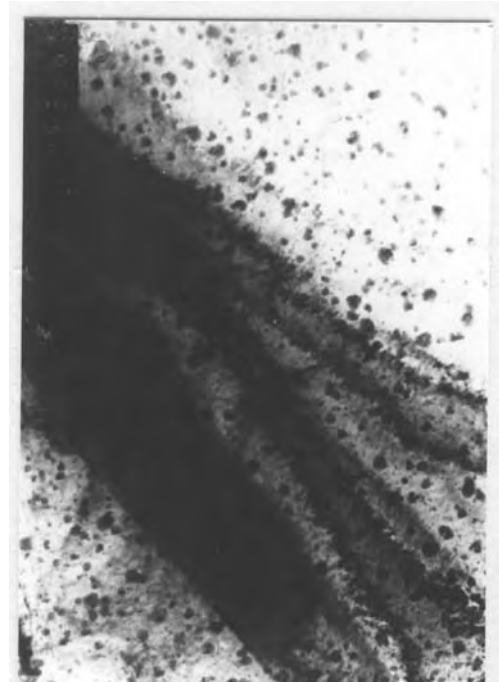
(d)

Figure 4.33: Precipitates observed in Cu-13.6%Al-3.0%Ni alloy aged at 210°C for one hour. a) BF, 10 kX. b) BF, 14 kX. c) BF, 19 kX. d) BF, 19 kX.
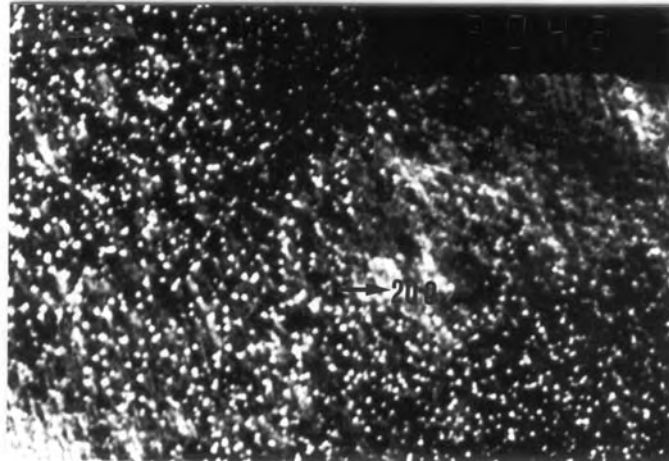
Figure 4.34: More densely distributed precipitates in Cu-13.6%Al-3.0%Ni alloy aged at 210°C for one hour, DF, 30 kX, g(200).

Bright field images of fine precipitates, which were formed after ageing at 310°C for one hour, were shown in Figure 4.36. Martensitic background was very much faulted and the hardly observable faint lines were probably antiphase domain boundaries. Martensite plates were coarse and the precipitates were barely observable. Precipitates as small as 10 nm were seen in the lower right corner of Figure 4.36-d. Centered dark field images of precipitates were shown in Figure 4.37. Observed precipitates were spherical and of sizes in the range 5 to 25 nm. Precipitates (barely seen in bright field images) were seen to be homogeneously distributed in dark field images.

Precipitates, which were formed after ageing at 410°C for 20 minutes were shown in Figure 4.38. In Figure 4.38 c and d some fringes were visible. Precipitates blurred by faulted martensite background were illustrated in Figure 4.38-d. Centered dark field images of precipitates were given in Figure 4.39. Observed precipitates were spherical with 10-20 nm size and homogeneously distributed in martensite plates. An example of precipitates exceptionally located on between the martensite plate boundaries was given in Figure 4.39-d.
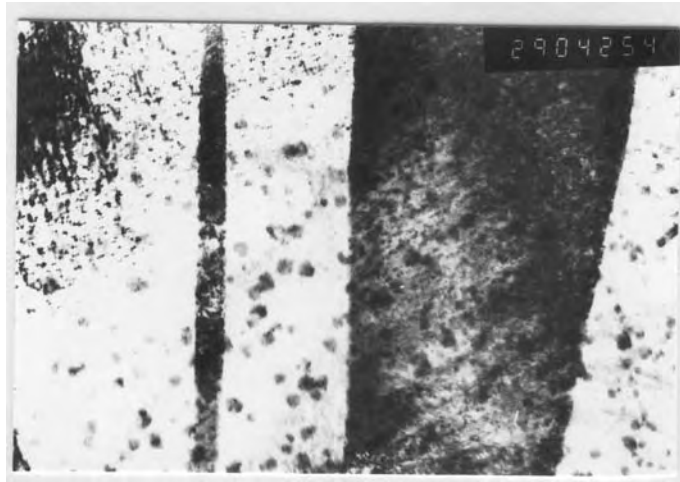
(a)

(b)
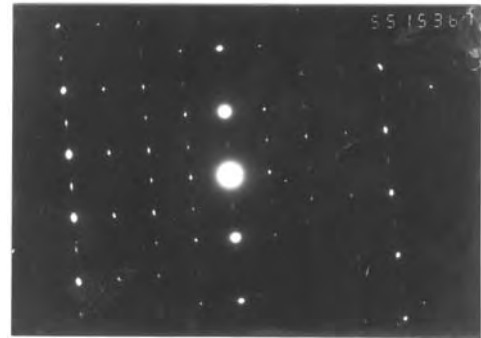
(c)

Figure 4.35: Micrographs showing the 2H and 18R$_1$ martensite phases orientation relationship in Cu-13.6%Al-3.0%Ni alloy aged at 210°C for one hour. a) 2H and 18R$_1$ martensite plates together, BF, 29 kX. b) [230] zone Selected Area Diffraction Pattern (SADP) of 18R$_1$ martensite. c) [011] zone SADP of 2H martensite

(a)
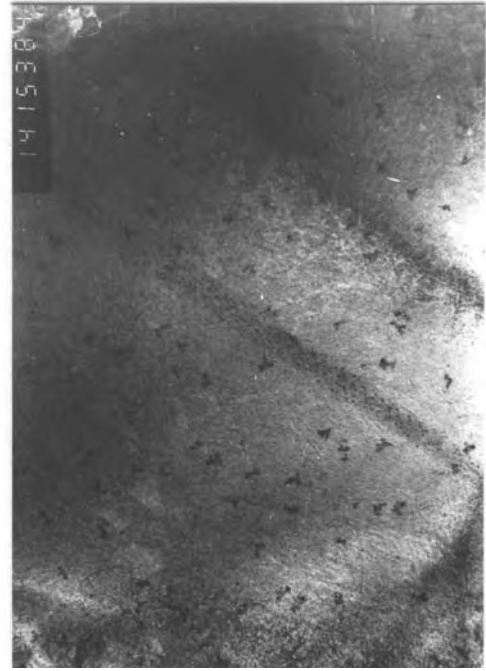
(b)

(c)

(d)

Figure 4.36: Precipitates observed in Cu-13.6%Al-3.0%Ni alloy aged at 310°C for one hour a) BF, 19 kX. b) BF, 14 kX. c) BF, 19 kX. d) BF, 10 kX.
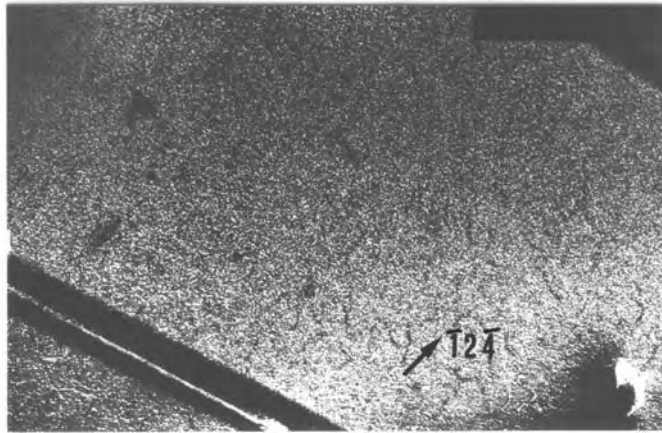
(a)
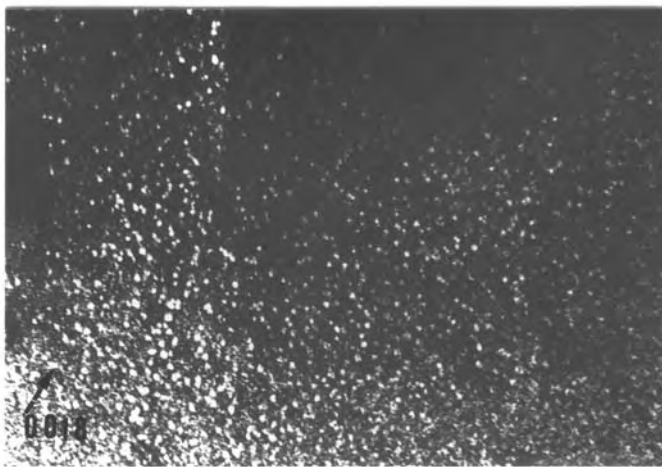
(b)

Figure 4.37: Centered dark field images of precipitates in Cu-13.6%Al-3.0%Ni alloy aged at 310°C for one hour. a) DF, 10 kX, g(-12-4) b) DF, 37 kX, g(0018).

(a)
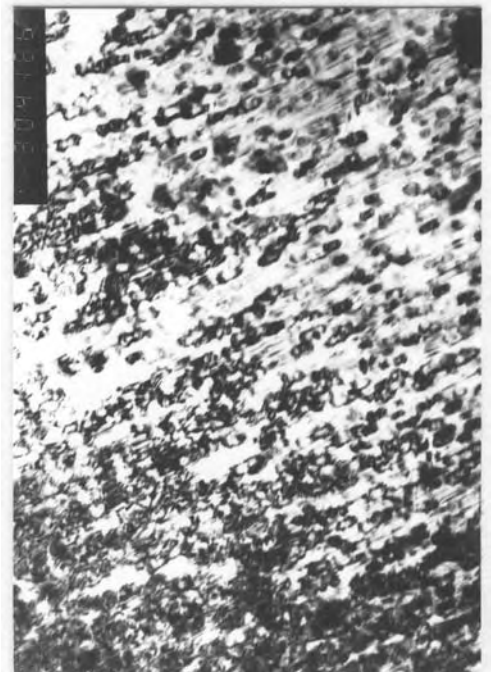
(b)
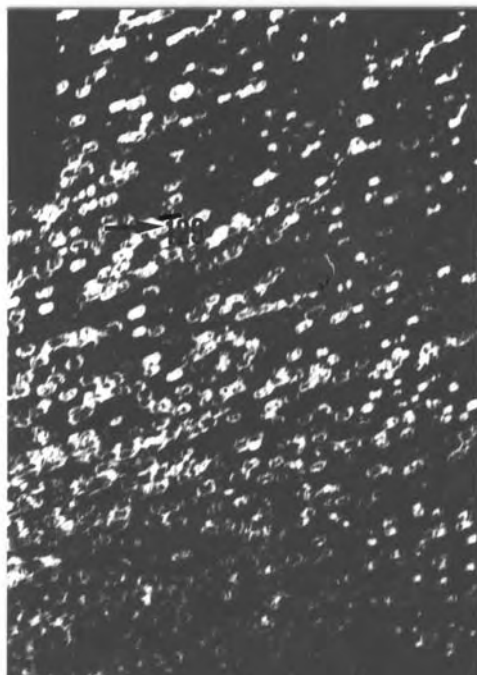
(c)
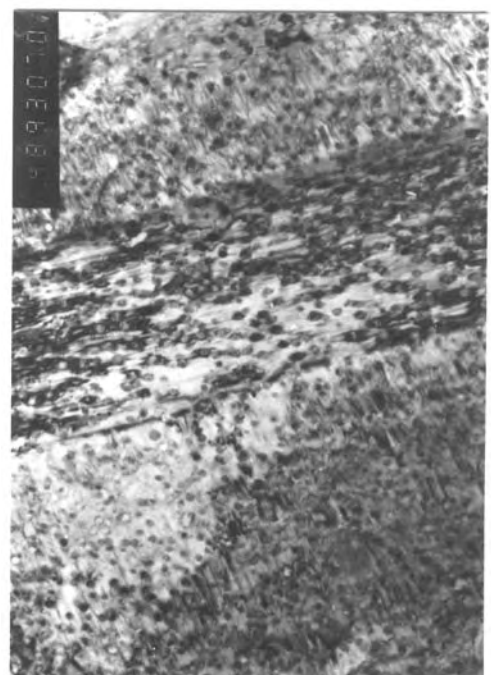
(d)

Figure 4.38: Precipitates observed in Cu-13.6%Al-3.0%Ni alloy aged at 410°C for 20 minutes. a) BF, 14 kX. b) BF, 48 kX. c) Corresponding DF image of c, 48 kX, g(-129). d) BF, 48 kX.

143
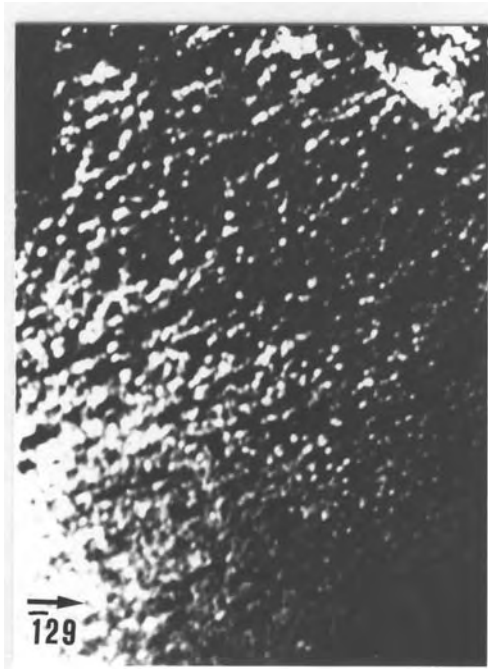
(a)
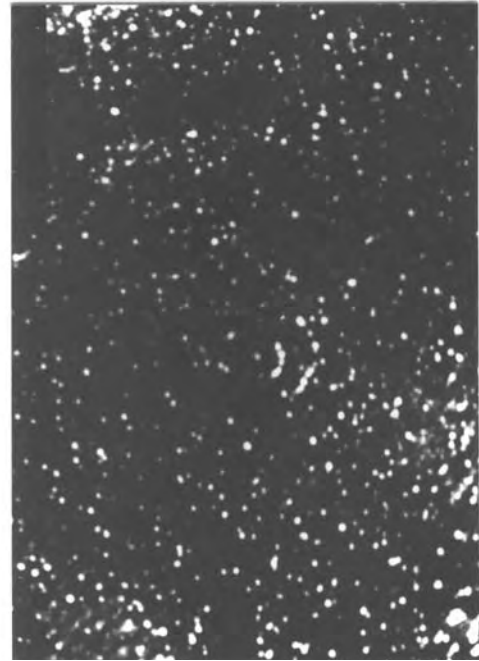
(b)
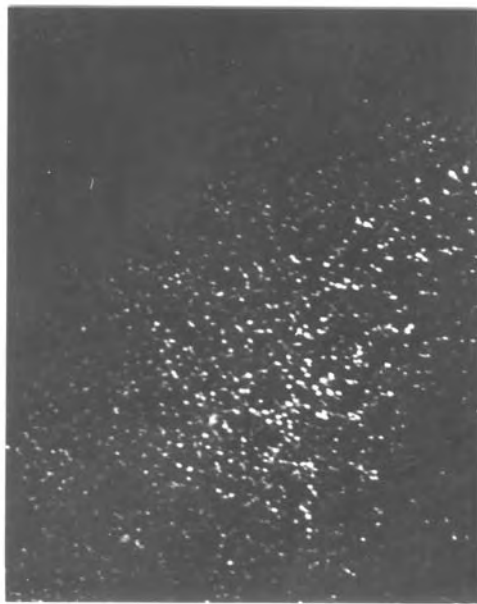
(c)

(d)

Figure 4. 39: Dark field image of precipitates in Cu-13.6%Al-3.0%Ni alloy aged at 410°C for 20 minutes. a) DF, 36 kX, g(-129), b) DF, 29 kX, c) DF, 29 kX, d) DF, 36 kX, g(1-211).

144

Besides finely distributed precipitates similar to those observed in samples aged at 210°C and 310°C for one hour and at 410°C for 20 minutes, a coupled-grown precipitates were observed in samples aged at 410°C for one hour. In addition to coupled-grown precipitates, bulk precipitates of 1200-1500 nm size and cuboidal in morphology were present. Fine precipitates as small as 3 nm with spherical shape were shown in Figure 4.40. Coupled-grown precipitates were illustrated in Figure 4.41. Enlarged micrographs of coupled-grown structure were given in Figure 4.42. Coupled-grown structure consists of lamellar like dark and light sideplates. As can be clearly seen in Figure 4.42-c, dark plates were planar whilst the light plates contains fine precipitates.

<div align="center">(a)   (b)</div>
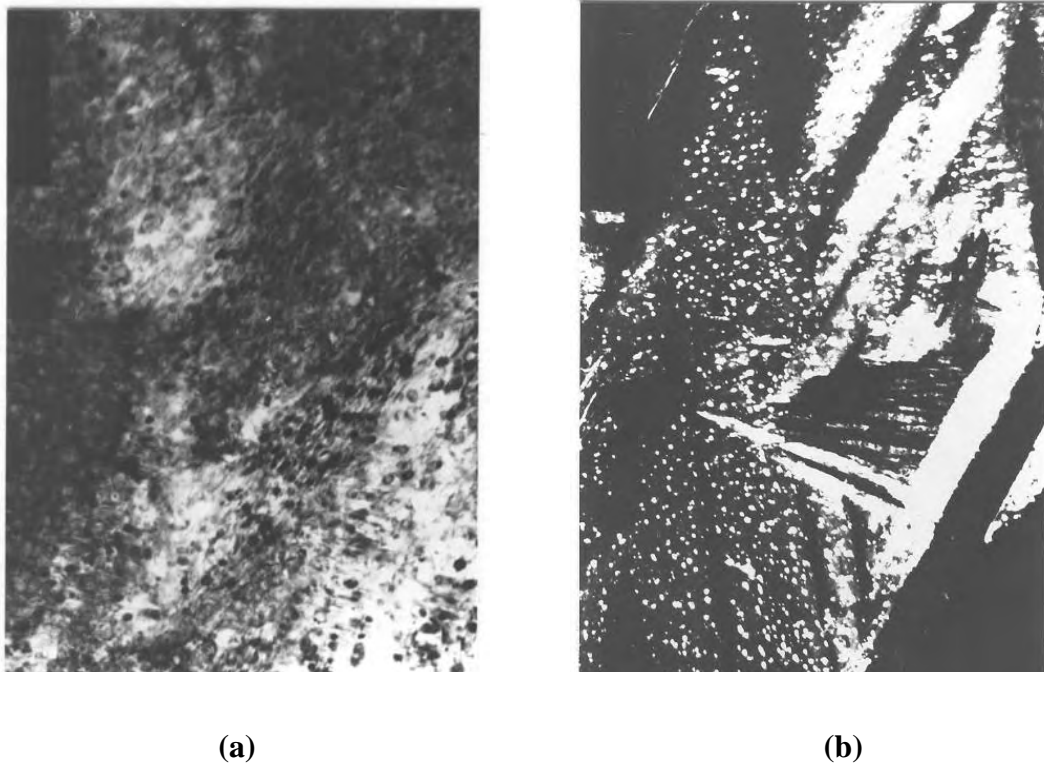
Figure 4.40: Precipitates observed in Cu-13.6%Al-3.0%Ni alloy aged at 410°C for one hour. a) BF, 36 kX. b) DF, 14 kX.
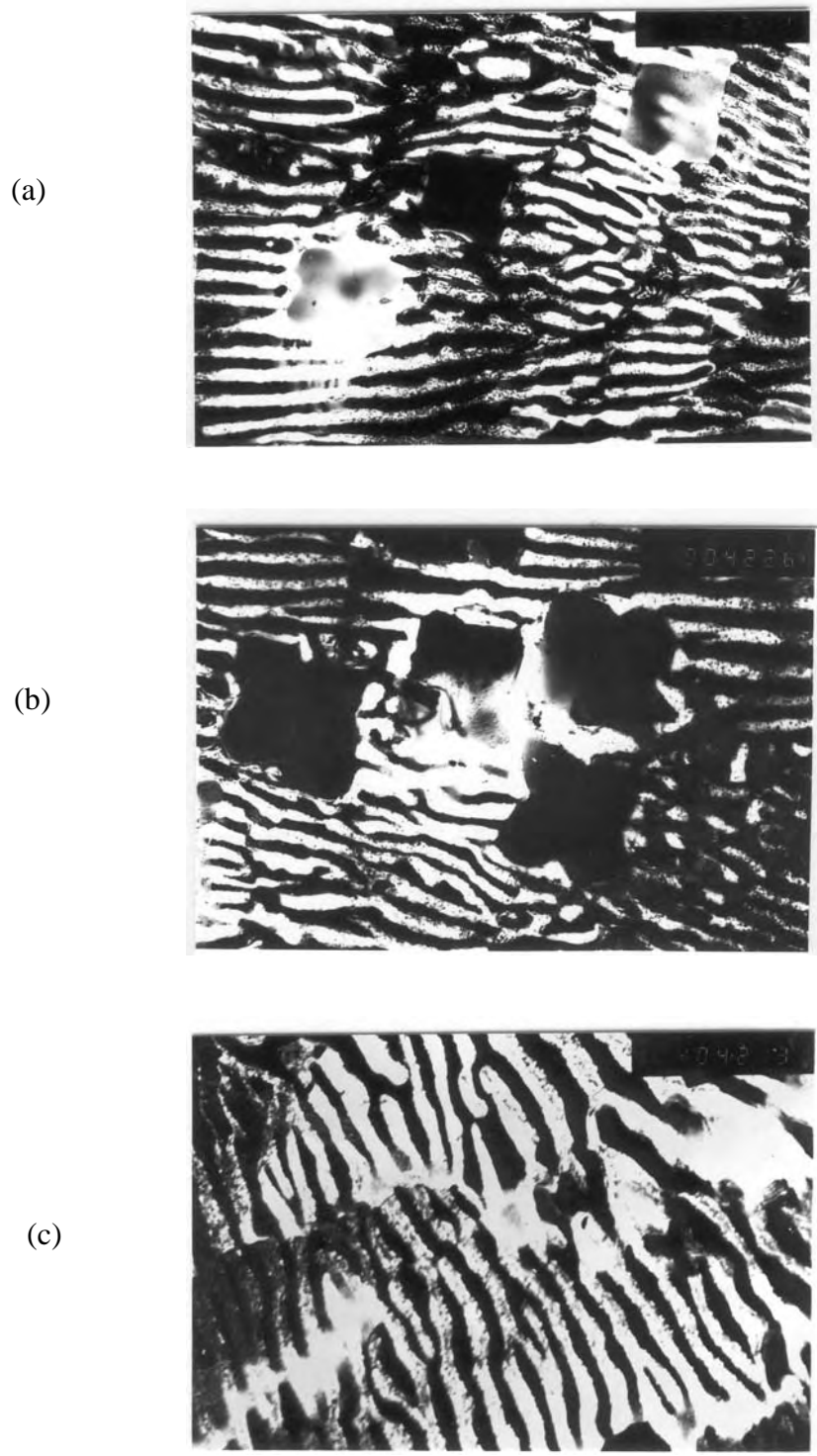
Figure 4.41: Coupled- grown precipitates formed in Cu-13.6%Al-3.0%Ni alloy aged at 410°C for one hour. a) BF, 10 kX b) BF, 10 kX c) DF, 14kX

(a)
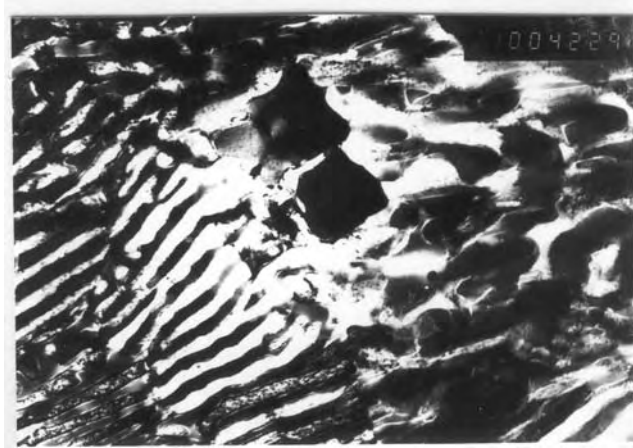
(b)

(c)
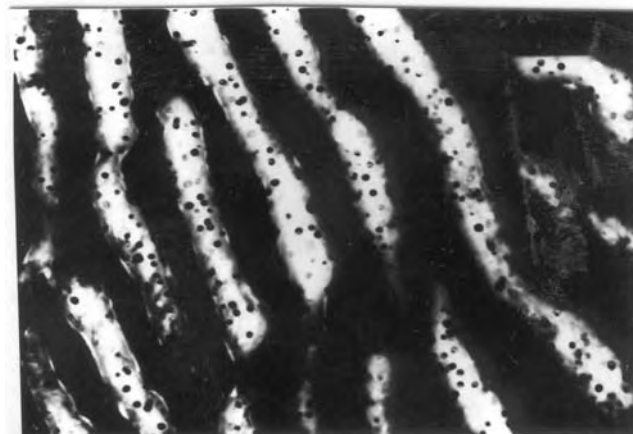
Figure 4.42: Enlarged micrographs of coupled-grown precipitates formed in Cu-13.6%Al-3.0%Ni alloy aged at 410°C for one hour. a) BF, 10kX b) BF, 19 kX c) BF, 36 kX

147

Finally, bulk precipitates were big cuboidals of 1200-1500 nm and they were formed in Cu-13.6%Al-3.0%Ni alloy after ageing at 410°C for one hour. Dark field micrographs of bulk precipitates were exemplified in Figure 4.43 where only the bulk precipitates were excited. Excited bulk precipitates were enlarged in Figure 4.43-b and its corresponding bright field image was given in Figure 4.43-c.

It has been known that crystal structures of γ_2 and α precipitates in CuAlNi alloy systems were ordered bcc and fcc, respectively. Selected area diffraction pattern given in Figure 4.44 was from bulk precipitates and indexed as [-113] zone of bcc crystal structure. For this reason, big bulk precipitates were γ_2 precipitates on the basis of this analysis. Moreover, it was observed in Figure 4.41-a that bulk γ_2 precipitates have connections to dark lamella. Therefore, dark lamella was γ_2, too. It has been well known that equilibrium precipitates of α and γ_2 were thermodynamically stable below eutectoid temperature of approximately 550°C down to room temperature according to phase diagram of CuAlNi alloys. On this thermodynamic basis the accompanying phase of γ_2 precipitates was nothing but equilibrium α precipitates. Hence, the light lamella was α. To conclude, the observed coupled-grown precipitates were equilibrium α and γ_2 precipitates of eutectoid transformation. According to naming here, dark lamella was γ_2 and light lamella was α.

The very fine precipitates observed after ageing at 210°C and 310°C for one hour and at 410°C for 20 minutes, were γ_2 precipitates based on the fact that γ_2 precipitates form kinetically earlier than α precipitates in several Copper-based shape memory alloys. In CuAlNi alloy systems, γ_2 precipitates were known to be enriched by aluminum solute atoms. The remaining matrix has been depleted by Al content and enriched by Cu and Ni atoms as a result of formation of γ_2 precipitates. Upon γ_2 precipitates reaching equilibrium, α precipitates form from the matrix enriched by Cu and Ni atoms at relatively higher temperatures i.e., 400-500°C following the formation of γ_2 precipitates.

(a)

(b)

(c)
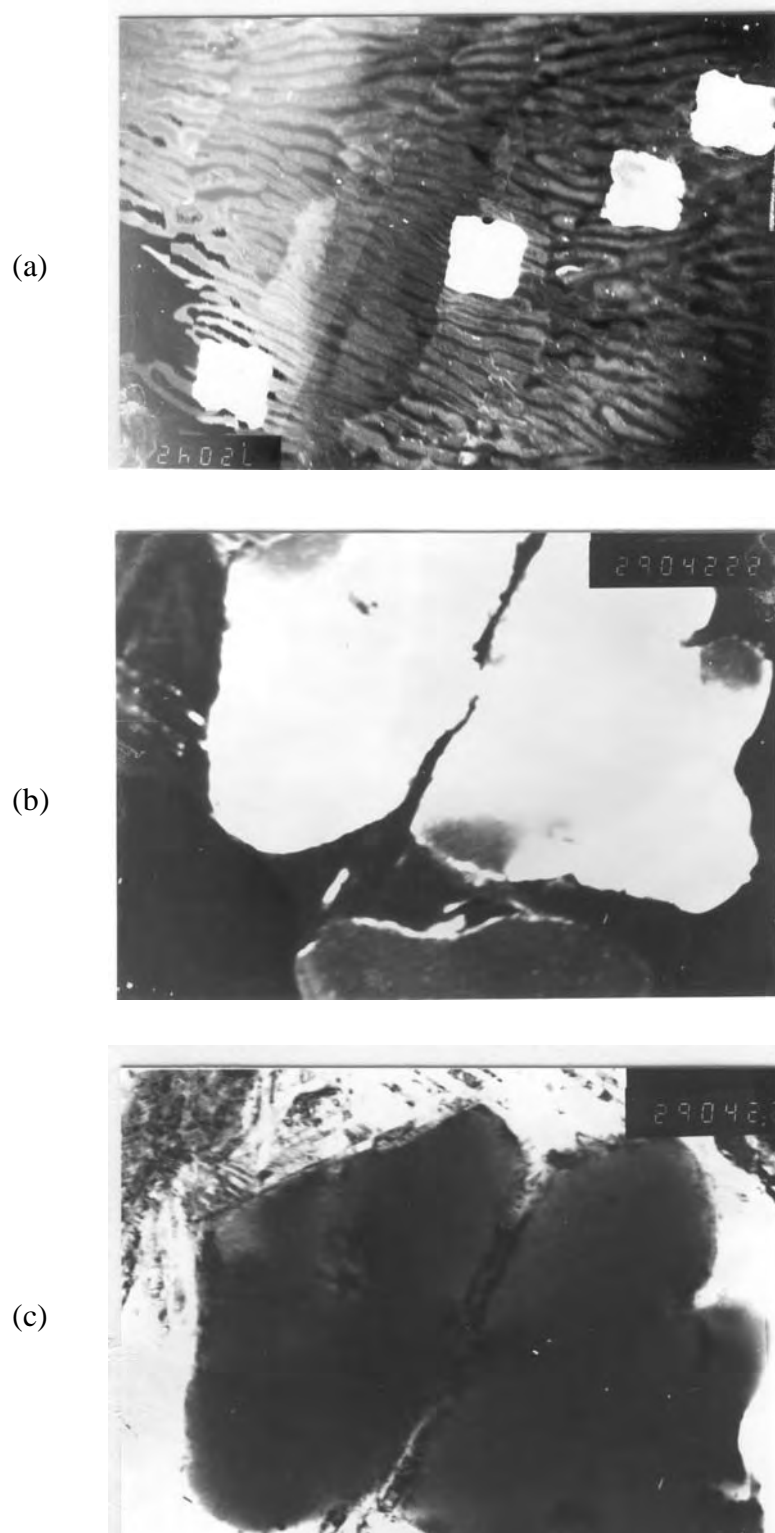
Figure 4.43: Bulk precipitates observed in Cu-13.6%Al-3.0%Ni alloy aged at 410°C for one hour. a) DF, 7,2 kX b) DF, 29 kX c) corresponding bright field image of b, BF, 29 kX.
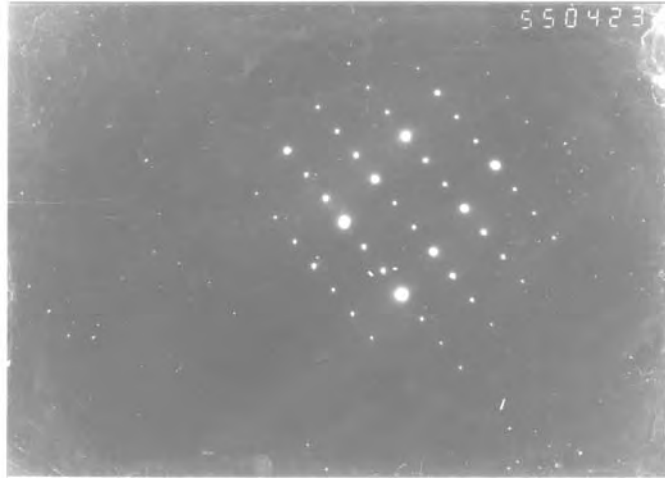
Figure 4.44: Selected area diffraction pattern of bcc crystal structure, [-113] zone, of γ_2 phase (bulk precipitates) observed in Cu-13.6%Al-3.0%Ni alloy after ageing at 410°C for one hour.

Fine spherical precipitates of 5-20 nm size, which were formed after ageing at 210°C and 310°C for one hour and at 410°C for 20 minutes, have grown into 1200-1500 nm size big cuboidal γ_2 precipitates following the ageing at 410°C for one hour.

4.12. Suppositions On Martensite Stabilization Effect in CuAlNiMn Alloys:

In the present study, martensite stabilization mechanism of "precipitates pinning martensite boundaries" has been disproved. It has been well known that neither Martensite nor Beta is equilibrium phase in reversible, thermoelastic, diffusionless M↔β transformations. Therefore, it is not surprising to observe atomic rearrangements in these states during ageing. As a result of atomic rearrangements, relative thermodynamic stability of martensite increases as compared to the parent phase and A_s, A_f temperatures increase. This situation can be simply summarized on a free energy versus temperature curve as shown in Figure 4.11. Since the T_0

temperature has shifted to higher temperatures as a result of lowered free energy of aged martensite, all transformation temperatures have to increase to higher temperatures, as well. At this point, a conflict arise between this picture and experimental results of the present study, which has clearly shown that, M_s and M_f temperatures did not change at all while both A_s and A_f temperatures absolutely increased with increasing ageing temperature and time during martensite ageing. One may explain unchanging M_s, M_f and increasing A_s, A_f temperatures by two different energy states for each phase resulting in different heating/cooling paths depending on state of ageing, as illustrated in Figure 4.45 and Figure 4.46, respectively.

During heating, aged martensite, which has been structurally modified and therefore of lower energy, by a nondiffusional shear mechanism transforms into Beta phase inheriting the modifications energetically unfavorable for itself. However, this Beta
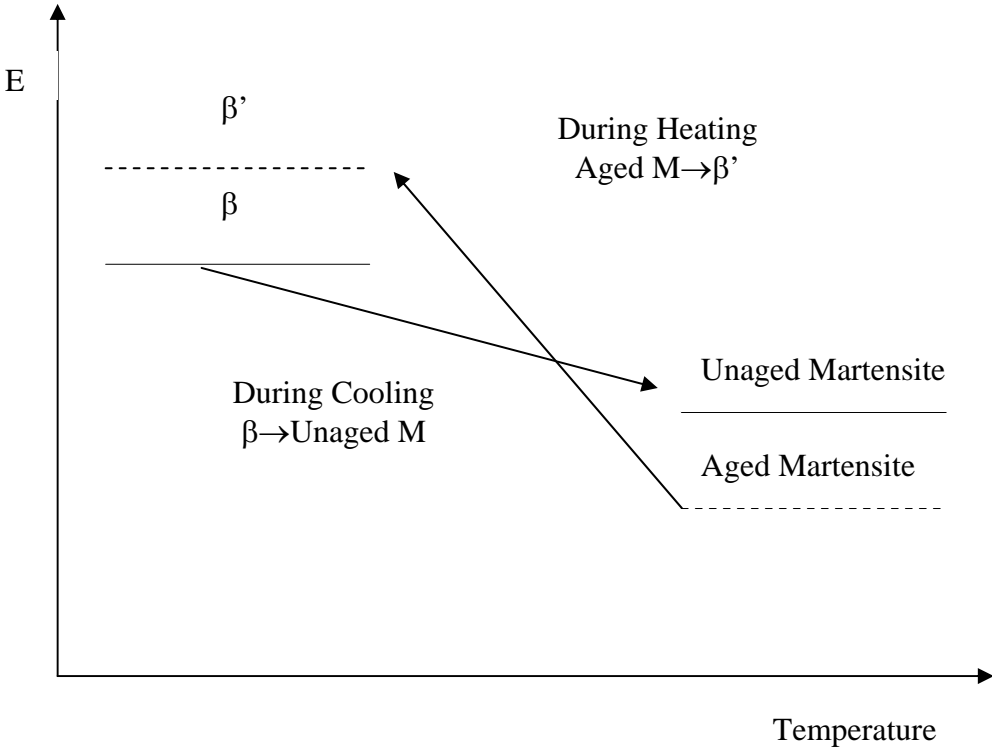
Figure 4.45: Schematic energy level versus temperature curve in the martensite stabilization phenomenon showing the paths of M→β transformation during heating and β→M transformation during cooling.

151
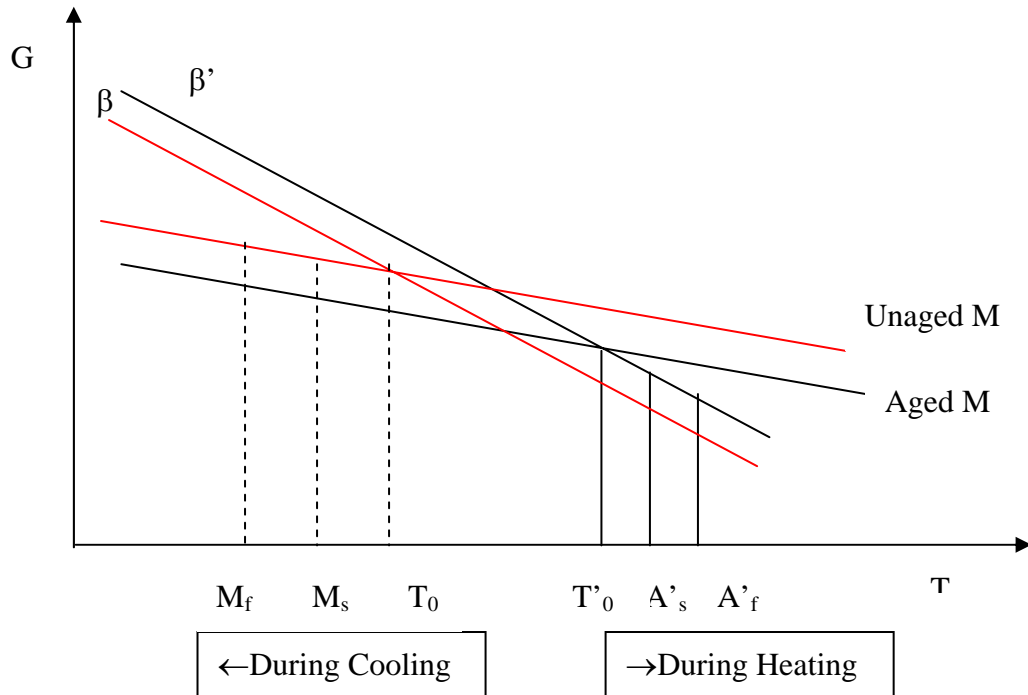
Figure 4.46: Schematic Gibbs free energy versus temperature curve in the martensite stabilization phenomenon showing the increase of A_s and A_f temperatures and stable M_s and M_f temperatures upon heating and cooling, respectively.

phase of higher energy denoted as $\beta^{'}$ is not a long standing state and shortly transforms into stable, original β phase at the end of heating. Transformation during cooling occurs from stable beta to unaged martensite following the original M_s and M_f temperatures. Upon isothermal ageing, martensite again becomes more stable with respect to unaged martensite and lowers its free energy. According to the new equilibrium between $\beta^{'}$ and aged martensite, upon heating the increased $A^{'}_s$ and $A^{'}_f$ are obtained. Hence, two different T_0 temperatures, one corresponding to aged martensite/$\beta^{'}$ and the other to martensite/β equilibria are proposed by this model. T_0 corresponding to the former, which determines A_s, A_f is higher than that corresponding to the later, which determines M_s, M_f. Of course, to this model, one can include the aged beta/martensite equilibria that will yield a third T_0 temperature lower than the other two to explain lowering of M_s, M_f in case of beta ageing.

CHAPTER 5

CONCLUSION

1. Both CuAlNiMn and CuAlNi alloys exhibit thermoelastic martensitic transformation with the transformation temperatures in the order of $M_f<A_s<M_s<A_f$. In the present study, these alloys, unexpectedly, revealed unidentical transformation characteristics in the forward ($M{\rightarrow}\beta$) and backward ($\beta{\rightarrow}M$) directions upon heating and cooling, respectively, as manifested by different slopes of transformation curves and hysteresis widths, both being related with the shape strain involved in the transformation. The difference of start and finish transformation temperatures, i.e., $(A_f - A_s)$ and $(M_s - M_f)$, which are proportional to the slopes of the transformation curves, is known to be inversely proportional with the shape strain involved in shear transformations. When the transformation shape strain is large, more driving force and hence more undercooling is required to complete the transformation, resulting in a wide transformation temperature interval. $(A_f - A_s)$ being unequal to $(M_s - M_f)$ indicates that the shape strains involved and therefore the characteristics of forward and backward reactions are unexpectedly different. $(A_f - M_s)$ and $(A_s - M_f)$ are the measure of hysteresis width, respectively, of the forward and backward transformations and proportional to the shape strain for nucleation. Their difference also indicates a difference between the shape strains involved in the forward and backward transformations. Even though both hysteresis and slopes are the indicator of shear transformation shape

strain, hysteresis width is proportional to the undercooling essential for nucleation while the slopes are related solely to shape strain generated during growth.

DSC studies in both CuAlNiMn and CuAlNi alloys have shown that M→β transformation occurs by an endothermic reaction upon heating while the reverse β→M transformation takes place by an exothermic reaction upon cooling, as expected. M→β transformation enthalpies have found to be greater than that for the corresponding reverse β→M transformation in both alloy groups. Higher enthalpies of M→β than β→M has been realized to be a result of the aferomentioned unidentical transformation characteristics rather than being related to martensite stabilization effect.

2. In CuAlNiMn alloys, each new betatizing treatment has resulted in randomly varying transformation temperatures on the same specimen and an anomalously diffuse and serrated peak shape of the M→β transformation in the first cycle. It has been concluded that each betatizing treatment produces a new and different orientation distribution among the grains, which changes the constraining forces from neighbouring grains during transformation and each time a different strain distribution takes effect, yielding different transformation temperatures on the same sample. Therefore, it has been necessary, especially for CuAlNiMn alloys, to thermally cycle each as quenched alloy sample for three times in DSC prior to ageing to obtain thermally more stable, reproducible transformation temperatures and to eliminate the anomalous effect of betatizing on the transformation temperatures.

In addition to the anomalous serrated and diffuse first cycle peaks, anomalously increasing transformation temperatures during the first few cycles was very distinct. In CuAlNiMn alloys, while the rise in A_s and A_f temperatures between first and second thermal cycles is 15-20°C, after

second cycle, the rise has been detected to be only 1-2°C and rise in transformation temperatures has been found to rapidly decrease with increasing number of thermal cycles but not cease totally even after ten cycles.

During the first few thermal cycles, relative to A_s and A_f temperatures, M_s and M_f temperatures of both CuAlNiMn and CuAlNi alloys have only slightly changed because of the experimental fact that the actual first cycle referring to first $\beta \rightarrow M$ transformation has been taking place during quenching from 950°C and can not be monitored by DSC measurements.

It has been recognized that Manganese has a major role in the formation of diffuse and serrated first cycle peaks based on the fact that this anomalous effect has been observed uniquely in CuAlNiMn alloys, but not in Mn free CuAlNi alloys. Serrations remind repeating attempts for shrinkage of martensite crystals upon heating and their successive suppression by a mechanism involving the manganese atoms. Manganese atoms may be interacting with excess quenched-in vacancies and producing Mn-vacancy couples, which pin the shrinking martensite boundaries and result in the observed serrations. If such a mechanism is really operative, upon heating the samples above A_f temperature at the end of the first cycle, excess vacancies would anneal out diminishing the Manganese-vacancy interactions; serrations and diffuse nature would disappear in the following cycles.

3. During martensite ageing of CuAlNiMn alloys, M_s and M_f temperatures have not changed with increasing ageing time at the ageing temperatures in the range 80°C to 150°C. On the other hand, both A_s and A_f temperatures have increased with increasing ageing temperature and time, and the most obvious increase in A_s and A_f temperatures observed during 150°C was approximately 40-45°C at the end of the 312 hours ageing period. During

room temperature ageing apart from the effect of betatizing on transformation temperatures, CuAlNiMn alloys were quite stable. Transformation temperatures of CuAlNi alloys, on the other hand, have not changed at all during martensite ageing and they were very stable during room temperature ageing. In this respect, it should be noted that CuAlNiMn alloys were more prone to martensite stabilization than the CuAlNi alloys.

Through T.E.M investigation in the Cu-12.6wt%Al-5.9wt%Ni-1.8wt%Mn alloy aged at 150°C for 312 hours has revealed no sign of precipitate formation and based on this fact it has been concluded that the most widely and frequently offered "precipitates pinning martensite boundaries" mechanism could not be responsible of martensite stabilization.

4. Beta phase ageing of CuAlNiMn alloys at temperatures 200°C, 230°C, 250°C and 270°C, have drastically shortened ageing periods for stabilization to the extent that $\beta \rightarrow M$ transformation completely ceases. With regard to the Manganese content, highest Manganese bearing Cu-12.9%Al-5.0%Ni-2.2%Mn alloy (VD13) was the one stabilized first and the lowest manganese containing Cu-12.6%Al-4.8%Ni-1.1%Mn alloy (VD12) was the longest lasting alloy during beta phase ageing. This demonstrates that introducing CuAlNiMn alloys as potential candidates for high temperature shape memory applications, as it is usually done in literature, is also contradictory to the above results.

All transformation temperatures of CuAlNiMn alloys, upon ageing above 200°C, increased except the M_f temperature, which mostly exhibited a slight decrease. Increase in the transformation temperatures became more obvious at the higher beta ageing temperatures.

During beta phase ageing of CuAlNi alloys, it has been observed that all transformation temperatures consistently increased with time, reaching to as

much as 25-30°C increase after ageing at 200°C for 96 hours, but complete stabilization has not occurred in the periods investigated. On the basis of Transmission Electron Microscope studies on Cu-13.6wt%Al-3.0wt%Ni alloy aged at 210°C for one hour that revealed the γ_2 precipitates, the persistent increase of transformation temperatures with aging time has been attributed to matrix concentration change in relation to γ_2 precipitation.

Beta stabilization was not observed in any of the four CuAlNi alloys at the end of 96 hours ageing at 200°C indicating that beta phase stabilization times for CuAlNi alloys were considerably longer than that for Mn containing alloys; for the three CuAlNiMn alloys studied, Beta stabilization was realized at the end of 26, 38 and 11 hours ageing at 200°C. In conclusion, on the basis of ageing studies at 200°C, with regard to beta stabilization, CuAlNi alloys were found to be more resistant to high temperature ageing than CuAlNiMn alloys.

5. All alloys were found to consist of a mixture of martensite phases with $M18R_1$ and 2H long period stacking order crystal structures. Quantitative amounts of martensite with each crystal structure was not assessable due to the textured microstructure. But on a qualitative basis, martensite with $M18R_1$ structure was dominant in relatively lower aluminium and higher nickel content CuAlNiMn alloys and martensite with 2H structure was abundant in relatively higher aluminium and lower nickel content CuAlNi alloys.

The orientation relationship between the $M18R_1$ and 2H martensite structures in Cu-13.6%Al-3.0%Ni alloy aged at 210°C for one hour has been found to be:

$$[011]_{2H} \parallel [230]_{18R1}$$
$$(200)_{2H} \parallel (0018)_{18R1}$$

Fine spherical precipitates of 5-20 nm size, which were observed after ageing at 210°C and 310°C for one hour and at 410°C for 20 minutes were γ_2 precipitates and in Cu-13.6%Al-3.0%Ni alloy, they have found to be grown into 1200-1500 nm size big cuboidal γ_2 precipitates after ageing at 410°C for one hour.

Equilibrium γ_2 and α phase of eutectoid transformation were observed as coupled-grown lamellar morphologies in Cu-13.6%Al-3.0%Ni alloy aged at 410°C for one hour.

6. One of the predicted mechanisms of martensite stabilization, namely "precipitates pinning martensite boundaries" has been disproved in the present study. Hence, martensite stabilization effect might be a consequence of a mechanism based on "atomic rearrangements in martensite". One may explain unchanging M_s, M_f and increasing A_s, A_f temperatures as a result of martensite ageing by two different energy states for each phase resulting in different heating/cooling paths depending on state of ageing. During heating, aged martensite, which has been structurally modified and therefore of lower energy, by a nondiffusional shear mechanism transforms into Beta phase inheriting the modifications energetically unfavorable for itself. However, this Beta phase of higher energy denoted as β' is not a long-standing state and shortly transforms into stable, original β phase at the end of heating. Transformation during cooling occurs from stable beta to unaged martensite following the original M_s and M_f temperatures. Upon isothermal ageing, martensite again becomes more stable with respect to unaged martensite and lowers its free energy. According to the new equilibrium between β' and aged martensite, upon heating the increased A'_s and A'_f are obtained. Hence, two different T_0 temperatures, one corresponding to aged martensite/β' and the other to martensite/β equilibria are proposed by this model. T_0 corresponding to the former, which determines A_s, A_f is higher than that corresponding to the later, which determines M_s, M_f. Of course, to

this model, one can include the aged beta/martensite equlibria that will yield a third T_0 temperature lower than the other two to explain lowering of M_s, M_f in case of beta ageing.

CHAPTER 6

SUGGESTIONS FOR FUTURE WORK

Martensite stabilization of copper-based shape memory alloys being the major factor limiting their practical applications has been a long-term unsolved problem for these alloys. In this study, except disproving the predicted mechanism of "precipitates pinning martensite boundaries", it has not been possible to offer a genuine ageing mechanism for CuAlNiMn alloys. Basically the unexpected and unpredictable experimental findings, such as the effects of betatizing and early thermal cycling on transformation temperatures of CuAlNiMn alloys, which has been overlooked in literature, required considerable time to be spent on these topics rather than stabilization mechanism itself.

Since the copper-based shape memory martensites are non-equilibrium phases, they have an inborn tendency to change. Aged martensite becomes more stable with respect to unaged martensite phase due to some atomic rearrangements during ageing. As a result, transformation temperatures increase due to the increased equilibrium temperature, T_0, between the aged martensite and beta phase. Without clarifying the origin and preventing martensite stabilization, practical applications of copper-based shape memory alloys will be delayed. To my opinion, the subject of martensite stabilization may attract attention only for academic interest for the eager of the topic in the today's world where technology and marketing of the product are always one step ahead of scientific research. Moreover, it has been

noticed that research on TiNi alloys, despite their higher cost, has increased in the last couple of years at the expense of that on copper based alloys because of the unresolvable nature of stabilization problem. Continuing with this subject has the risk that a unified ageing mechanism to make a contribution to the subject. can not be found.

A similar change has been taking place in the SMA research group of this department. Studies on production of copper-based shape memory alloys and most of the mechanic characterization of these alloys, such as one way shape memory effect under free and constrained recovery conditions, pseudoelasticity, modification of ternary alloys by fourth element additions have been carried out. The present study seems to be the last one on the copper-based shape memory alloys in the department. In the beginning, this study to test the success of CuAlNiMn alloys was promising. However, the martensite and beta ageing results of these alloys are not supporting or enhancing the proposal of CuAlNiMn alloys as potential candidates for high temperature shape memory alloy applications. CuAlNiMn alloys have not exhibited a better thermal stability than CuAlNi alloys, which resulted in shift of interest to the production and characterization of TiNi shape memory alloys.

Martensite stabilization is a vacancy-assisted diffusional phenomenon. For the future work on the subject, finding out the behaviour of vacancies by using different techniques may be helpful for the solution. In this respect, electrical resistivity measurement technique is recommended due to its sensitivity to lattice defects. Positron annihilation is known to be a direct technique to determine vacancy concentration and its change. Differential Scanning Calorimetry technique has prime importance for the close control of transformation temperatures of alloys. The subject of hot rolling known to be an inhibition method of stabilization may be interesting again in relation to vacancies. Since the CuZnAl alloys are known to be more prone to ageing effects, the studies must be concentrated on CuAlNi alloys.

REFERENCES

1. K.Sugimoto, K.Kamei, M.Nakaniwa, <u>Engineering Aspects of Shape Memory Alloys</u>, Edited by Duerig, Butterworth-Heinemann Ltd., 1990, p:89-95.

2. V.Recarte, R.B.Saez, E.H.Bocanegra, M.L.No, J.San Juan, Mat.Sci.and Eng. A, 273/275, 1999, p: 380-384.

3. D.P.Dunne and N.F.Kennon, Metals Forum, 1981, 4, p.176.

4. L. Delaey, A. Deruyttere, N. Aernoudt, and J. R. Roos, <u>Shape Memory Effect, Super-Elasticity and Damping in Cu-Zn-Al Alloys</u>, INCRA Research Report (Project No. 238), February, 1978.

5. C. M. Friend, Scripta Met., 23, 1989, p:1817-1820.

6. C. M. Friend, J. Ortin, A. Planes, L. Manosa, M. Yoshikawa, Scipta Met., 24, 1990, p:1641-1645.

7. D. Adnyana, Metallography, 18, 1985, p:187-196.

8. J. V. Wood, P. H. Shingu, Met.Trans. A, 15, 1984, p:471-480.

9. C. Castillo, B. G. Mellor, M. L. Blazquez, C. Gomez, Scripta Met., 21, 1987, p:1711-1716.

10. Y. F. Hsu, W. Wang, C. M. Wayman, Met.Trans.A, 22, 1991, p:1473-1478.

11. Elif Tarhan, M.Sc. Thesis, Middle East Technical University, 1996.

12. V. Recarte, O. A. Lambri, R. B. Perez-Saez, M. L. No, J. San Juan, Appl. Phys.Lett.,70, 26, 1997, p: 3513-3515.

13. C. Segui, E. Cesari, J.of Mat.Sci., 30, 1995, p:5770-5776.

14. C. Segui and E. Cesari, J.of Mat.Science, 30, 1995, p:5770-5776.

15. Hurtado, D. Segers, J. Van Humbeeck, L. Dorikens and C. Dauwe, Scripta Metal. Et Mat., 33,5, 1995, p:741-747.

16. V. Recarte, O. A. Lambri, R. B. Perez-Saez, M. L. No, J. San Juan, J.of Applied Phsycs, 86, 1999, p:5467-5473.

17. V. Recarte, R. B. Perez-Saez, M. L. No, J. San Juan, J. of Mater.Res., 14, 7, 1999, p: 2806-2813.

18. W. Salgueiro, R. Romero, A. Somoza and M. Ahlers, Phys. Stat. Sol. A, 1993, 138, p. 111.

19. M. L. Castro, R. Romero, Mat.Sci. and Eng A, 1998, 255, p. 1.

20. Y. S. Han, Y. G. Kim, J. of Materials Science, 21, 1986, p:2711.

21. Planes, J. L. Macquerin, M. Morin and G. Guenin, Mat. Sci. and Eng., 1981, 50, p: 53.

22. Z. G. Wei and D. Yang, Mat. Sci. and Eng., 1989, A119, pp. 145.

23. R. Rapacioli and M. Ahlers, Scripta Met., 1977, 11, pp. 1147.

24. S. C. Singh, Y. Murakami and L. Delaey, Scripta Met., 1978, 12, pp. 435.

25. D. Schofield and A. P. Miodownik, Metals Tech., 1980, pp. 167.

26. M. H. Wu and C. M. Wayman, Scripta Met. Et Mater., 1991, 25, p. 1635.

27. S. Miyazaki and K. Otsuka, Shape Memory Alloys Edited By H.Funakubo, Gordon and Breach Science Publishers, 1984, p. 116.

28. J. Singh, H. Chen and C. M. Wayman, Met. Trans. A, 1986, 17A, p. 65.

29. J. Singh, H. Chen and C. M. Wayman, Scripta Met., 1985, 19, p. 231.

30. N. Kuwano and C. M. Wayman, Met. Trans. A, 1984, 15A, pp. 621

31. M. A. Dvorack, N. Kuwano, S. Polat, H. Chen and C. M. Wayman, Scripta Met., 1983, 17, p. 1333

32. E. S. Lee and Y. G. Kim, Met. Trans. A, 1990, 21A, p. 1681.

33. E. S. Lee and Y. G. Kim, Scripta Met. Et Mater., 1990, 24, p. 745.

34. S. S. Leu and C. T. Hu, Met. Trans. A, 1991, 22A, p. 25.

35. N. F. Kennon, D. P. Dunne and L. Middleton, Met. Trans. A, 1982, 13A, pp. 551.

36. T. Tadaki, <u>Shape Memory Materials</u>, Edited By K.Otsuka and C.M.Wayman, Cambridge University Press, 1998, p. 97.

37. M. Ahlers, <u>ICOMAT'86</u>, The Japan Institute of Metals, 1986, p:786

38. M. Chandrasekaran, E.Cesari, J.Wolska, I.Hurtado, R.Stalmans and J.Dutkiewicz, <u>ESOMAT'94</u>, J.de Phy. IV, 1995, 5, pp. 143.

39. X. Ren and K. Otsuka, Phase Transitions, 1999, 69, p: 329.

40. K. Otsuka and X. Ren, Mat.Sxci. and Eng., 2001, A312, p:207.

41. M. Ahlers, J. L. Pelegrina, Mat.Sci. and Eng. A, 2003, p:1.

42. H. Morawiec and M. Gigla, <u>ESOMAT'94</u>, J. De Phys.,C2, 5, 1995, p. C2-193.

43. P. Rodriguez and G. Guenin, Mat. Sci. and Eng., 1990, A129, p. 273

44. V. Pelosin, A. Riviere, J.of Alloys and Compounds, 1998, 268, p. 166.

45. Z. G. Wei, H. Y. Peng, D. Z. Yang, C. Y. Chung and J. K. L. Lai, Acta Met., 1996, 44, pp. 1189.

46. Hurtado, J. V. Humbeeck, P. Ratchev and L. Delaey, Mat. Trans. JIM, 1996, 37, p. 1371.

47. Hurtado, P. Ratchev, J. V. Humbeeck and L. Delaey, Acta Met., 1996, 44, p. 3299.

48. W. H. Zou, H. Y. Peng, R. Wang, J. Gui and D. Z. Yang, Acta Met., 1995, 43, p. 3009.

49. P. Ratchev, J. V. Humbeeck and L. Delaey, Acta Metall. Mater., 1993, 41, p. 2441.

50. C. Y. Chung, W. H. Zou, X. D. Han, C. W. H. Lam, M. Gao, X. F. Duan and J. K. L. Lai, Acta Met., 1988, 46, pp. 5541.

51. W. H. Zou, C. W. H. Lam, C. Y. Chung and J. K. L. Lai, Met. Trans. A, 1998, 29A, pp. 1865.

52. Z. G. Wei, H. Y. Peng, W. H. Zou and D. Z. Yang, Met. Trans. A, 1997, 28A, p. 955

53. K. Marukawa, K. Tsuchiya and Y. Arai, ICOMAT'95, 1995, pp. C8-841.

54. Y. Nakata, O. Yamamoto and K. Shimizu, Mat. Trans. JIM, 1993, 34, p. 429.

55. Y. Bai, X. G. Xu, Y. X. Liu, L. M. Xiao, G. L. Geng, Mat.Sci. and Eng.A, 2002, 334, p:49

56. M. Graef, J. V. Humbeeck, M. Andrade and L. Delaey, Scripta Met., 1985, 19, p:644.

57. M. De Graef, J. Van Humbeeck and L. Delaey, ICOMAT'86, 1986, pp. 850.

58. M. Mantel, R. Rapacioli and G. Guenin, Japan Inst. Of Metals, ICOMAT'86, 1986, p:880.

59. J. Jansen, J. Van Humbeeck, M. Chandrasekaran, N. Mwamba and L. Delaey, ICOMAT'82, 1982, p. C4-715.

60. C. Segui, Scripta Met.,32, 1995, p:565-570.

61. C. W. H. Lam, C. Y. Chung, W. H. Zou and J. K. L. Lai, Met. And Mat.Trans. A, 1997, 28A, p:2765.

62. J. Van Humbeeck, D. Segers and L. Delaey, Scripta Met., 1985, 19, p: 477.

63. D. Segers, J. Van Humbeeck, L. Dorikens-Vanpraet, I. Lernahieu and M. Dorikens, Scripta Met., 1988, 22, p: 521.

64. T. M. Wang, B. Y. Wang, B. X. Feng, C. L. Liu, B. H. Jiang and Z. Y. Xu, Phys. Stat. Sol. A, 1989, 114, p: 451.

65. Y. Kong, B. Jiang, T. Y. Hsu, B. Wang and T. Wang, Phys. Stat. Sol. A, 1992, 133, p:269.

66. Y. Kong, B. Jiang, T. Y. Hsu, B. Wang and T. Wang, MRS Sym.Proc.,1992, 246, p:25.

67. Q. Xuan, J. Bohong and T. Y. Hsu, Mat. Sci. and Eng., 1987, 93, p: 205.

68. Abu Arab and M. Ahlers, Acta Met., 1988, 9, p. 2627.

69. Y. Hashiguchi, H. Higuchi, I. Matsui, T. Niitani, H. Tokunoh, Y. Ikai, Japan Inst. Of Metals, 1986, ICOMAT'86, p:832

70. C. M. Cook and L. M. Brown, Scripta Met., 1978, 12, pp. 949.

71. V. Recarte, P. Saez, M. L. No, J. S. Huan, J.of Mat.Res., 1999, 14, p:2806

72. Y. Nakata, T. Tadaki and K. Shimizu, Mat. Trans. JIM, 1990, 31, p. 652.

73. M. Ahlers, G. Barcelo, R. Rapacioli, Scripta Met., 1978, 12, p:1075.

74. K. Marukawa, K. Tsuchiya, Scripta Met. Et Mat., 1995, 32,p:77.

75. K. Marukawa, K. Tsuchiya, K. Takezawa, H. Hoshi, Mat. Sci.and Eng. A, 1999, 273,p:568.

76. X. Y. Lu and M. S. Cao, Japan Inst. Of Metals, ICOMAT'86, 1986, p:856.

77. T. Suzuki, R. Kojima, Y. Fuji and A. Nagasawa, Acta Met., 1989, 37, p. 163.

78. Hurtado, J. V. Humbeeck and L. Delaey, ESOMAT'91, 1991, pp. C4-247.

79. X. Ren, K. Otsuka, Physical Rev. Let., 2000, 85,5, p: 1016.

80. X. Ren, K. Otsuka, Letters to Nature, 1997, 389/9, p:579.

81. K. Otsuka and X. Ren, Scripta Met.,2004, 50, p: 207-212.

82. K. Shimizu and T. Tadaki, Mat. Trans. JIM, 1992, 33, pp. 165.

83. Y. Nakata, O. Yamamoto, K. Shimizu and T. Tadaki, Mat. Charac., 1994, 32, pp. 205.

84. K. Shimizu, Y. Nakata and O. Yamamoto, MRS Symposium Proceedings, 1992, 246, pp. 43.

85. D. B. Williams and C. B. Carter, Transmission Electron Microscopy, 1996, p:616.

86. G. Scarsbrook, J. M. Cook and W. M. Stobbs, Met.Trans A, 1984, 15A, p.1977.

87. L. Delaey, T. Suzuki and J. V. Humbeeck, Scripta Met., 1984, 18, pp. 899.

88. J. Van Humbeeck, L. Delaey and D. Roedolf, ICOMAT'86, 1986, p. 862.

89. S. Chakravorty and C. M. Wayman, Acta Met., 1977, 25, p:989-1000.

90. E. S. Lee and S. Ahn, Acta Met., 1998, 46, p:4357-4368.

91. K. Shimizu and T. Tadaki, Shape Memory Alloys, edited by H.Funakubo, 1987, p:18.

92. D. W. Roh, E. S. Lee, Y. G. Kim, Met.Trans. A, 1992, 23A, p:2753-2760.

93. G. Scarsbrook, J. Cook and W. M. Stobbs, Journal De Phys. C4, 12, ICOMAT'82, 1982, p:C4-703.

94. X. Duan and W. M. Stobbs, Scripta Met., 1989, 23, p. 441.

95. J. Wolska, M. Chandrasekaran and E. Cesari, Scripta Met. Et Mater., 1993, 28, p. 779.

96. S. Miyazaki and K. Otsuka, <u>Shape Memory Alloys</u> Edited By H.Funakubo, Gordon and Breach Science Publishers, 1984, p. 129.

97. Y. Nakata, T. Tadaki and K. Shimizu, Mat. Trans. JIM, 1985, 26, pp. 646-652.

98. Y. Gao, M. Zhu and J. K. L. Lai, J.of Mat. Sci., 1998, 33, p. 3579-3584.

99. M. A. Morris and S. Gunter, Scripta Met. Et Mater., 1992, 26, p: 1663-1668.

100. J. C. Li and G. S. Ansel, Met. Trans. A, 14, 1983, p:1293-1297.

101. J. Perkins and W. E. Muesing, Met. Trans. A, 14, 1983, p:33-36.

102. J. Garcia R., Scripta Met., 42, 2000, p: 531-536.

103. J. Garcia, J. Pons and E. Cesari, Scripta Met., 37, 1997, p:1783-1788.

104. T. Tadaki, M. Takamori and K. Shimizu, Trans. Jap. Inst. Of Met., 1987, 28, pp. 120.

105. J. Pons, F. C. Lovey, E. Cesari, Acta Met., 38, 1990, p:2733-2740.

106. J. Pont, J. Muntasel, J. Pons and E. Cesari, J.of Mar.Res., 12, 1997, p:2288-2297.

107. L. Manosa, M. Jurado, A. Comas, E. Obrado, A. Planes, C. Stassis, R. Romero, A. Somoza, M. Morin, Acta Mater., 1998, 46, p: 1045-1053.

108. M. Morris and T. Lipe, Acta Met., 42, 1994, p:1583-1594.

APPENDIX A

THERMAL ANALYSİS

A generally accepted definition of thermal analysis is "a group of techniques in which a physical property of a substance and/or its reaction products is measured as a function of temperature whilst the substance is subjected to a controlled temperature program". The most popular and widely used thermal analysis methods are Differential Thermal Analysis (DTA) and Differential Scanning Calorimetry (DSC). The basic difference between DSC and DTA is that former is a calorimetric method in which differences in energy between sample and reference are measured, later records the differences in temperature between sample and reference while both are subjected to a controlled temperature program.

In terms of basic principles there is a classical DTA and two types of DSC, namely Power Compensation DSC and Heat Flux DSC.

1. DTA/DSC INSTRUMENTATION:

a. Classical DTA:

In classical DTA, there is a single heating furnace where the sample and reference are placed on individual bases and thermocouple junctions are attached directly to these bases, or into the sample and reference material. In addition to separate sample and reference thermocouples, a third thermocouple is used to measure furnace temperature to control the heating rates and temperature programmes. When the temperature of sample equals to the temperature of reference both thermocouples produce identical voltages and the net voltage output is zero. When sample and reference temperatures differ, resultant net voltage output reflects the difference in temperature between the sample and reference. As the furnace

temperature changed, the temperatures of sample and reference also change. In the absence of any physical or chemical changes, the temperature difference ($\Delta T = T_S - T_R$) remains zero. When there is a physical or chemical change in the sample, but not in reference material, the sample temperature no longer equals to reference temperature and a temperature difference, ΔT results. Figure A.1 shows a-classical DTA and b-heat flux configuration. A schematic DTA cell is illustrated in Figure A.2.
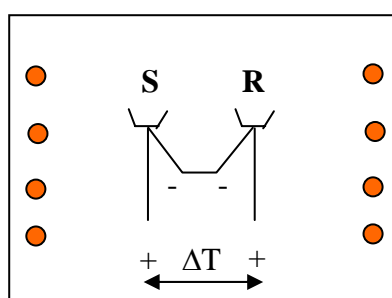
(a)
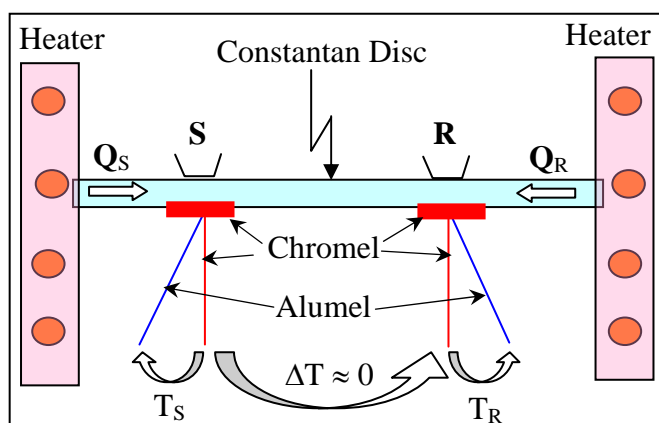
(b)

Figure A.1: Differential Thermal Analysis a) classical DTA and b)heat flux configuration.
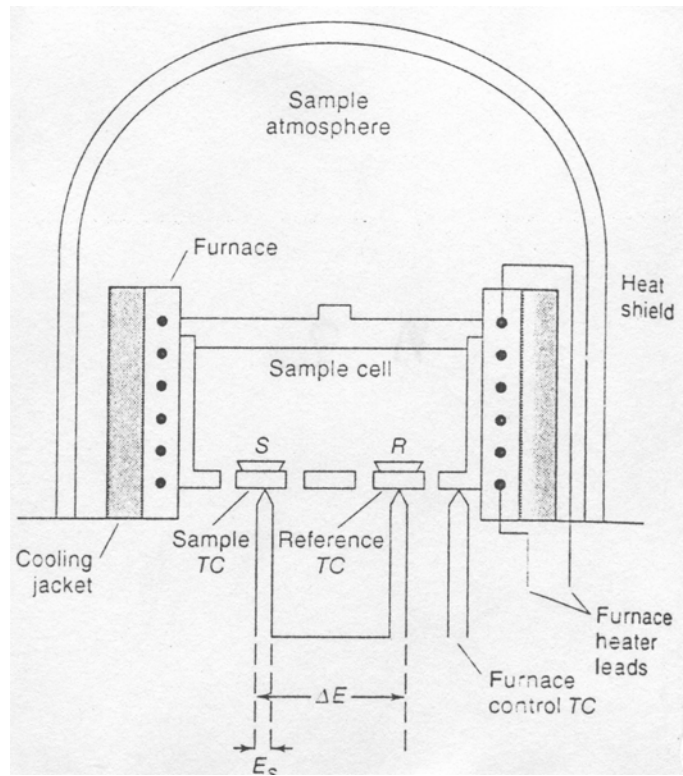
Figure A.2: A schematic DTA cell.
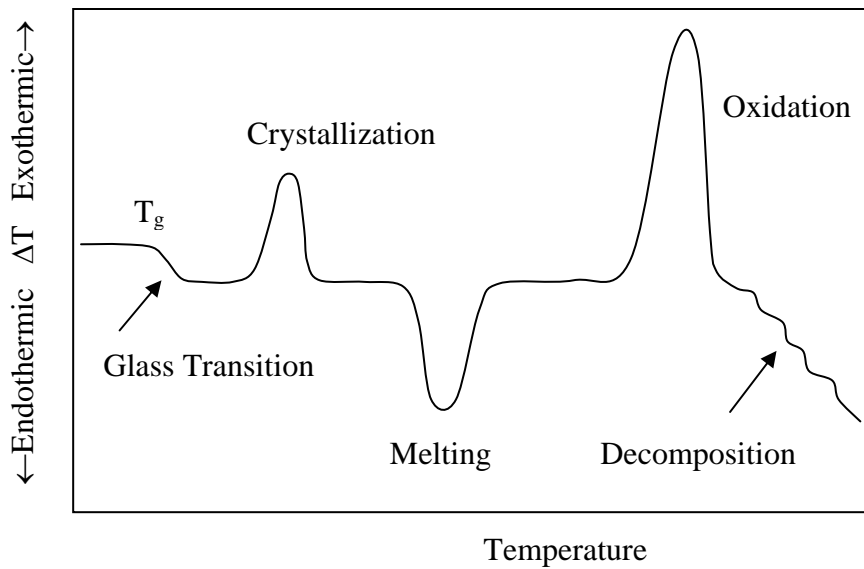
Figure A.3: Schematic DTA curve showing types of changes.

A plot of ΔT as a function of either time or sample temperature is known as a DSC curve. Figure A.3 is a schematic DSC curve showing types of changes. As can be seen melting is an endothermic reaction whereas oxidation and crystallization are examples of exothermic reaction.

DTA and DSC have found valuable application in the study of phase diagrams both in the pharmaceuticals and more widely in the general area of material science.

b. Power Compensation DSC:

In Power Compensation DSC, the aim is to maintain the sample and reference material at the same temperature ($\Delta T = T_S - T_R \approx 0$) throughout the controlled temperature programme. There are separate heaters for sample and reference as shown in Figure A.4. When there is a temperature difference arising between sample and reference, differential thermal power is supplied to the heaters to eliminate the difference in temperature and to maintain temperature at the programmed value. This power supply difference is recorded as the output of DSC.
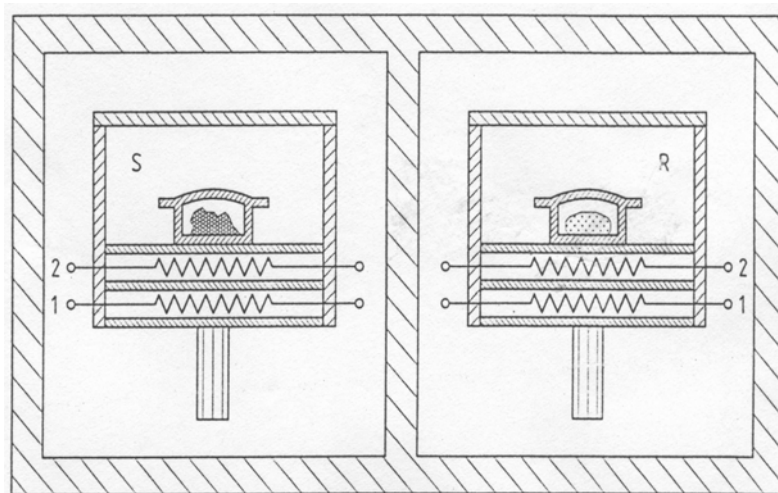
Figure A.4: Power Compensation DSC.

c. Heat Flux DSC:

In Heat Flux DSC, signal is derived from the temperature difference established when the sample and reference are heated in the same furnace. Heat flows into both the sample and the reference material through an electrically heated constantan thermoelectric disc. Heat is transferred through the disks up into the sample and reference via the two pans. The differential heat flow to the sample and reference is monitored by chromel constantan area thermocouples formed by the junction between the constantan platform and chromel discs attached to the underside of platforms. Differential heat flow into the two pans is directly proportional to the difference in output of the two thermocouple junctions. Figure A.1-b is the heat flux differential scanning calorimeter and Figure A.5 demonstrates the schematic heat flux DSC cell showing constantan disc and thermocouple junctions.
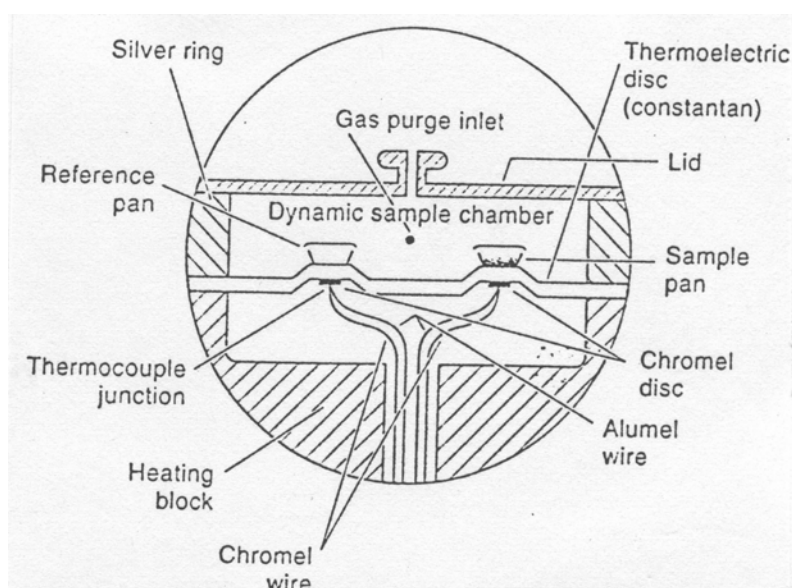
Figure A.5: A schematic Heat-flux DSC cell.

The change in Enthalphy, ΔH, of the sample is equal to the difference between the heat flow to or from the sample, Q_s, and the heat flow to or from the reference material, Q_r.

$$\Delta H = Q_s - Q_r$$

According to the heat flux equation

$$Q = (T_2 - T_1)/R$$

Heat flow is proportional to the driving force, i.e., the temperature difference, and inversly proportional to the thermal resistance . Therefore,

$$\Delta H = Q_s - Q_r = (T_c - T_s)/R - (T_c - T_r)/R$$

where T_c is temperature external to sample and reference, T_s is the sample temperature and T_r is the reference temperature. The system is so designed that T_c and R values are identical. Finally,

$$\Delta H = -(T_s - T_r)/R$$

The measured signal is the voltage from thermocouples which is proportional to the temperature difference.

2. FACTORS AFFECTING DTA/DSC CURVES:

Thermal analysis results depend closely on the instrumental parameters selected for each run. Thus results are not reproducible if similar conditions are not selected. The optimization of sample, crucible, rate of heating, atmosphere and mass of sample for each run enable the user to obtain good and reproducible results.

The sample: Chemical description, the source and pretreatments of the sample must be given. The previous history of sample, impurities present can all affect the results.

The crucible: The material and shape of the crucible (pan) is important. The most frequently used crucibles for low and moderate temperatures –150 to 600°C are made of aluminum. Crucibles made of silver, gold, quartz, alumina, graphite and stainless steel are available commercially. Especially stainless steel ones are relatively massive and considerably increase the effective response time of the

equipment. Crucibles can be of a shallow or deep design. Deep crucibles may restrict gas flow more than flat, wide ones.

The Rate of Heating: Most important changes in DSC curves are critically dependent on the rate of heating. A very slow heating rate allows the reaction come closer to equilibrium and there will be less thermal lag in the apparatus. Conversely, high heating rate results in a faster experiment, deviates more from equilibrium and causes greater thermal lag. It is generally found that an increase in heating rate increases the peak temperature and often increases peak areas slightly and peak shape becomes narrower and sharper. Figure A.6 shows the effect of heating rate and related change in peak position and shape for fusion of indium. Increasing heating rate often decreases the resolution between two adjacent peaks so slower heating rates are preferable. At very low heating rates, the peak areas become very small or nonexisting. Sensitivity is ability of an instrument to detect thermal effects of low magnitude. Resistivity and sensitivity of DSC intruments are controversial; increasing heating rate is at the expense of resolution and decreasing heating rate is at the expense of sensitivity.

The Atmosphere: Both heat transfer and the supply and removal of gaseous reactants depend on the chemical nature of the atmosphere and its flow. Oxidation reactions occur well in oxygen, less in air and not at all in argon. Product removal by a rapid gas flow may prevent occurence of reverse reactions.

The Mass of the Sample: A large sample mass requires more energy and heat transfer is determined by sample mass and dimensions including volume, packing, particle size of sample. Comparisons of runs had better make using similar sample masses, sizes and shapes. Small amounts of sample yields maximum resolution of peaks and most regular shapes and permit best thermal contact with sample container, minimizes the thermal gradients within sample.

Use of small samples, slow heating/cooling rates, good contact between sample, crucible and temperature sensors reduce thermal gradients and thermal lag as much as possible.
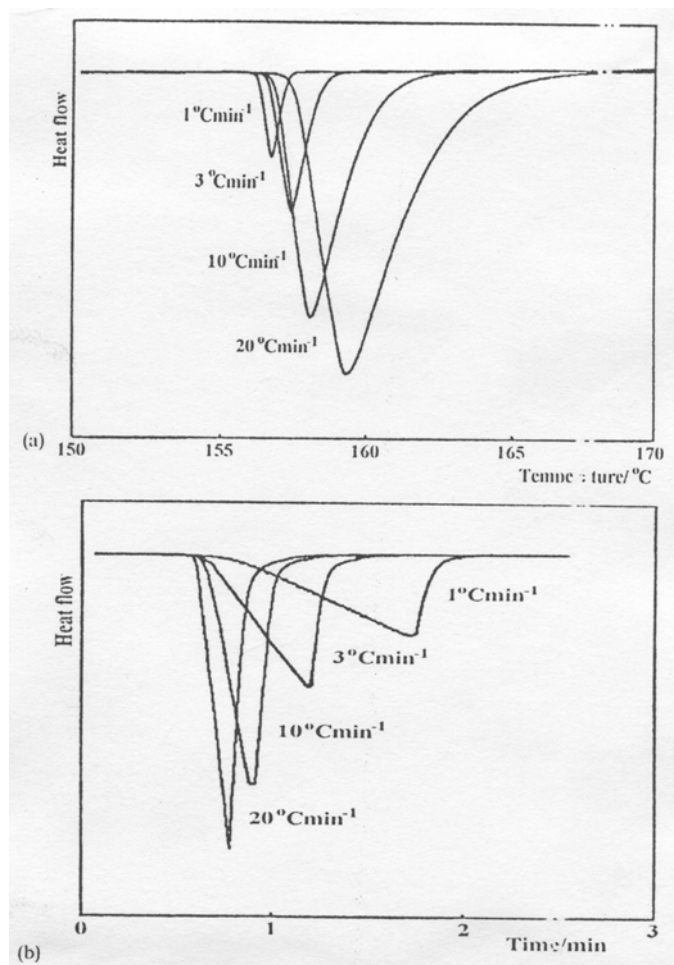
Figure A.6: Influence of heating rate on the thermal analysis curves for the fusion of indium a) plotted against temperature, b) plotted against time.

3. DSC CURVES:

DSC curves record the differential heat input to the sample on the ordinate, against temperature or time on the abscissa. An idealised representation of endothermic and exothermic reactions is given in Figure A.7.

C_p change for the sample resulting from any physical or chemical reaction may be detected by the displacement of the baseline from one horizontal position to another as can be seen in Figure A.7.

175

Peak area in DSC is proportional to the enthalphy change,

$$Peak\ Area = \Delta H.m.K$$

Where ΔH is sample enthalpy change, m is sample mass, K is the calibration constant.
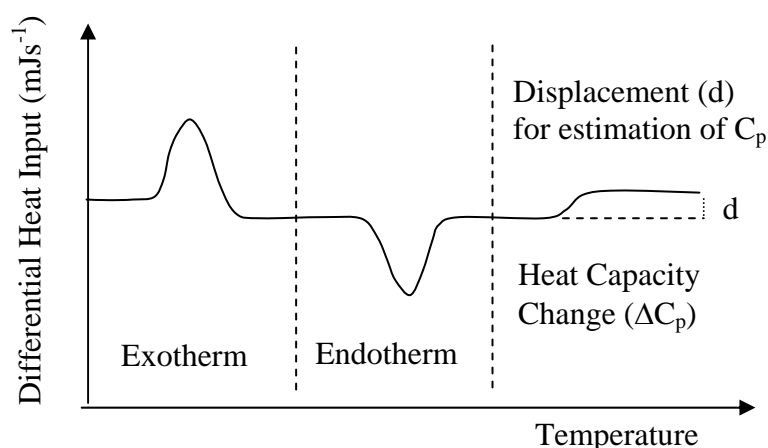
Figure A.7: An idealised representation of endothermic, exothermic reactions and Cp change in DSC.

4. INTERPRETATION OF DTA/DSC PEAKS:

The zero line is the curve measured with the instrument empty, i.e. without samples and crucibles or with crucibles empty. The (interpolated) baseline is the line constructed connecting the measured curve before and after a peak. In the literature, extrapolated onset and offset temperatures are used. Extrapolated onset temperature (T_e) is the intersection of baseline with the line drawn through the almost linear section of ascending peak slope. Extrapolated offset temperature (Tc) is the intersection of baseline with the line drawn through the descending peak slope. All can be seen in Figure A.8.
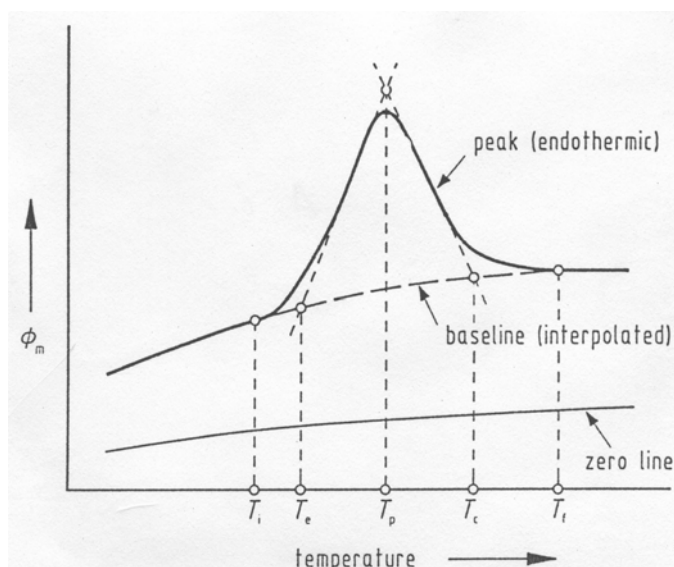
Figure A.8: Schematic DSC curve showing baselines and extrapolated temperatures.

A small thermal lag normally develops between sample and reference material due to the thermal capacity of the sample. So there is a gradual increase of ΔT with temperature initially (AB) until sample begins to undergo an exothermic effect at B. Point B where the curve begin to deviate from the baseline corresponds to the onset temperature at which the exothermic effect is first detectable. The peak temperature C corresponds to the maximum rate of heat evolution detection. It does not necessarily represent the maximum rate of reaction, nor the completion of the exothermic process. The exotherm causing peak BCD is completed some temperature between C and D. One can note that the levels of baselines AB and DE are different. It is a consequence of the fact that the heat capacity of the sample has changed as a result of exothermic process and they are all shown in Figure A.9.

The Baseline for signal integration can be selected in different ways but mostly used one is the linear from first to last point such that baseline is a straight line joining the two extreme points selected on the curve. The other ways are the

177
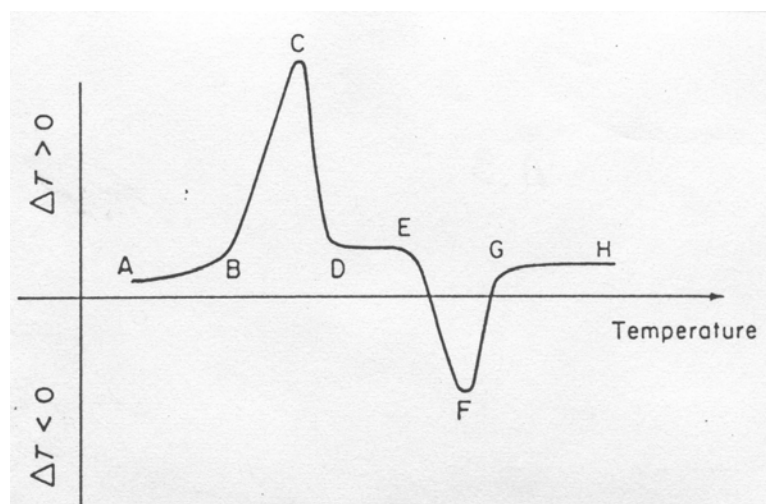
Figure A.9: An idealized DTA/DSC curve showing endotherm, exotherm, baseline change, onset and ofset temperatures and peak temperatures.

horizontal drawn from first or last point, equal to zero i.e. integration in relation to original baseline, curve baseline. For peak area calculations two points must be selected first, one referring to onset temperature, the other referring to offset temperature. Than baseline is the line connecting those points.

References:

A1. Thermal Methods of Analysis by Wesley Wendlant, 1974,p.134.

A2. Principles of Instrumental Analysis by Skoog, Leary, , p.568.

A3. Instrumental Methods of Analysis by Willard, Merritt, Dean, Settle, ,p.761.

A4. Thermal Methods by Dodd, Tonge, 1987,p.110.

A5. Introduction to Thermal Analysis by M.E. Brown, Kluwer Academic Publishers, 2001,p.55.

A6. Principles of Thermal Analysis, by P.J. Haines, The Royal Society of Chemistry, 2002, p.55.

A7. R.C. Mackenzi, Thermochimica Acta, 1979,28,1.

A8. Differential Scanning Calorimetry an introduction for practitioners, by G.Höhne, W.Hemminger, H.J.Flammersheim, Springer-Verlag, 1996, p.21.

A9. Setaram DSC131 User Handbook.

APPENDIX B

TRANSFORMATION TEMPERATURES AT THE END OF THIRD CYCLE

The transformation temperatures of CuAlNiMn and CuAlNi alloys at the end of third cycle ,which were thermally cycled prior to ageing temperatures of 80°C, 100°C, 120°C, 150°C, 200°C, 230°C, 250°C, 270°C.

Table B.1: Transformation temperatures referring to third cycle for alloy VD11.

Alloy	Temperature	A_s	A_f	M_s	M_f
VD11	80°C	155	173	158	144
	100°C	144	168	150	139
	120°C	152	172	160	140
	150°C	151	174	159	139
	200°C	155	169	156	144
	230°C	152	177	158	141
	250°C	153	178	159	138
	270°C	156	182	164	141

Table B.2: Transformation temperatures referring to third cycle for alloy VD12.

Alloy	Temperature	A_s	A_f	M_s	M_f
VD12	80°C	142	163	143	128
	100°C	143	164	145	130
	120°C	145	165	149	134
	150°C	145	168	148	133
	200°C	154	177	158	143
	230°C	149	170	152	137
	250°C	143	162	146	131
	270°C	141	162	148	130

Table B.3: Transformation temperatures referring to third cycle for alloy VD13.

Alloy	Temperature	A_s	A_f	M_s	M_f
VD13	80°C	184	204	182	168
	100°C	177	197	179	162
	120°C	174	189	172	159
	150°C	173	194	176	158
	200°C	180	197	179	165
	230°C	187	206	184	172
	250°C	187	204	184	170
	270°C	175	191	175	162

Table B.4: Transformation temperatures referring to third cycle for alloy V1.

Alloy	Temperature	A_s	A_f	M_s	M_f
V1	80°C	226	241	224	211
	100°C	223	240	224	208
	120°C	225	239	225	212
	150°C	227	240	226	212
	200°C	224	240	227	210
	230°C	225	239	225	210
	250°C	223	239	224	209
	270°C	225	240	225	210

Table B.5: Transformation temperatures referring to third cycle for alloy V2.

Alloy	Temperature	A_s	A_f	M_s	M_f
V2	80°C	107	122	105	93
	100°C	104	125	108	91
	120°C	104	118	105	93
	150°C	106	120	105	93
	200°C	102	118	106	92
	230°C	112	125	111	98
	250°C	116	134	120	103
	270°C	114	132	116	100

Table B.6: Transformation temperatures referring to third cycle for alloy V3.

Alloy	Temperature	A_s	A_f	M_s	M_f
	80°C	125	146	131	113
	100°C	127	146	133	117
	120°C	124	145	132	114
V3	150°C	127	142	128	116
	200°C	124	144	130	111
	230°C	131	148	136	120
	250°C	129	149	135	118
	270°C	127	145	131	115

Table B.7: Transformation temperatures referring to third cycle for alloy V4.

Alloy	Temperature	A_s	A_f	M_s	M_f
	80°C	164	181	163	152
	100°C	159	179	165	148
	120°C	164	182	169	153
V4	150°C	164	181	168	152
	200°C	163	180	168	153
	230°C	166	184	171	154
	250°C	164	184	169	153
	270°C	164	182	168	152

APPENDIX C

ENTHALPY CHANGES DURING THREE THERMAL CYCLES

Endothermic and Exothermic Enthalpy changes of CuAlNi and CuAlNiMn alloys at the end of third cycle for ageing temperatures of 80°C, 100°C, 120°C, 150°C, 200°C, 230°C, 250°C, 270°C.

Table C.1: Enthalpy values of applied cycles for alloy V1

Number of Cycles		First Cycle		Second Cycle		Third Cycle	
Temperature (°C)	Alloy	ΔH_{endo} (J/gr)	ΔH_{exo} (J/gr)	ΔH_{endo} (J/gr)	ΔH_{exo} (J/gr)	ΔH_{endo} (J/gr)	ΔH_{exo} (J/gr)
80	V1	10,6	-9,3	11,2	-8,6	11,1	-9,5
100	V1	10,1	-8,9	11,2	-9,3	11,0	-9,4
120	V1	10,5	-8,9	11,0	-8,7	11,2	-8,4
150	V1	9,8	-9,1	10,8	-8,9	10,9	-8,9
200	V1	10,3	-8,9	11,0	-8,8	11,1	-9,4
230	V1	9	-8,3	10,2	-7,9	10,1	-8,4
250	V1	8,2	-7,9	10,5	-7,6	10,3	-7,7
270	V1	9,0	-8,5	10,4	-7,9	10,2	-8,3

Table C.2: Enthalpy values of applied cycles for alloy V2

Number of Cycles		First Cycle		Second Cycle		Third Cycle	
Temperature (°C)	Alloy	ΔH_{endo} (J/gr)	ΔH_{exo} (J/gr)	ΔH_{endo} (J/gr)	ΔH_{exo} (J/gr)	ΔH_{endo} (J/gr)	ΔH_{exo} (J/gr)
80	V2	7,8	-7,0	7,9	-6,9	7,8	7,2
100	V2	6,8	-5,7	7,2	-6,3	7,1	-6,3
120	V2	6,7	-6,0	7,2	-6,3	7,1	-6,2
150	V2	7,5	-6,1	7,6	-7,2	7,5	-6,7
200	V2	7,5	-5,6	7,8	-5,8	7,7	-5,8
230	V2	6,4	-6,3	7,1	-6,7	7,0	-6,1
250	V2	6,7	-7,2	7,4	-7,2	7,4	-7,0
270	V2	7,1	-7,2	7,4	-6,0	7,6	-6,4

Table C.3: Enthalpy values of applied cycles for alloy V3

Number of Cycles		First Cycle		Second Cycle		Third Cycle	
Temperature (°C)	Alloy	ΔH_{endo} (J/gr)	ΔH_{exo} (J/gr)	ΔH_{endo} (J/gr)	ΔH_{exo} (J/gr)	ΔH_{endo} (J/gr)	ΔH_{exo} (J/gr)
80	V3	8,1	-8,1	8,9	-7,7	9,1	-7,3
100	V3	8,0	-7,2	8,5	-7,2	8,6	-6,7
120	V3	7,7	-8,5	8,3	-6,4	8,4	-7,4
150	V3	7,6	-8,3	8,0	-6,8	8,3	-6,4
200	V3	7,8	-9,3	8,4	-8,3	8,6	-7,9
230	V3	7,5	-6,9	8,2	-6,5	8,1	-6,8
250	V3	7,9	-6,9	8,5	-7,0	8,4	-6,9
270	V3	7,8	-7,0	8,2	-6,6	8,3	-6,3

Table C.4: Enthalpy values of applied cycles for alloy V4

Number of Cycles		First Cycle		Second Cycle		Third Cycle	
Temperature (°C)	Alloy	ΔH_{endo} (J/gr)	ΔH_{exo} (J/gr)	ΔH_{endo} (J/gr)	ΔH_{exo} (J/gr)	ΔH_{endo} (J/gr)	ΔH_{exo} (J/gr)
80	V4	9,3	-8,7	10,2	-8,3	10,2	-9,0
100	V4	8,8	-8,2	10,0	-8,0	9,9	-8,0
120	V4	9,2	-8,4	9,9	-8,6	9,9	-8,3
150	V4	8,4	-7,8	9,9	-8,4	9,8	-8,1
200	V4	8,6	-8,0	9,6	-7,9	9,8	-8,1
230	V4	8,9	-7,7	9,3	-8,0	9,3	-8,1
250	V4	7,8	-8,1	8,9	-7,4	8,4	-7,2
270	V4	8,3	-7,5	9,2	-7,7	9,0	-7,2

Table C.5: Enthalpy values of applied cycles for alloy VD11

Number of Cycles		First Cycle		Second Cycle		Third Cycle	
Temperature (°C)	Alloy	ΔH_{endo} (J/gr)	ΔH_{exo} (J/gr)	ΔH_{endo} (J/gr)	ΔH_{exo} (J/gr)	ΔH_{endo} (J/gr)	ΔH_{exo} (J/gr)
80	VD11	7,6	-7,7	9,0	-8,0	9,0	-8,2
100	VD11	5,0	-7,2	8,2	-7,1	8,6	-7,4
120	VD11	6,2	-5,2	8,9	-5,7	9,1	-7,5
150	VD11	6,7	-7,0	8,2	-7,2	8,2	-7,3
200	VD11	6,0	-7,1	8,8	-6,8	9,2	-7,6
230	VD11	6,8	-6,9	8,9	-5,6	8,8	-5,6
250	VD11	6,6	-6,8	7,8	-7,1	7,9	-6,7
270	VD11	6,9	-7,5	8,4	-7,1	8,4	-7,3

Table C.6: Enthalpy values of applied cycles for alloy VD12

Number of Cycles		First Cycle		Second Cycle		Third Cycle	
Temperature (°C)	Alloy	ΔH_{endo} (J/gr)	ΔH_{exo} (J/gr)	ΔH_{endo} (J/gr)	ΔH_{exo} (J/gr)	ΔH_{endo} (J/gr)	ΔH_{exo} (J/gr)
80	VD12	6,1	-7,4	8,5	-7,4	8,3	-7,2
100	VD12	6,2	-6,8	8,6	-6,9	8,6	-6,9
120	VD12	7,7	-8,1	9,1	-8,1	8,9	-8,3
150	VD12	7,5	-8,1	9,1	-8,6	8,9	-8,2
200	VD12	7,9	-8,7	9,4	-8,8	9,4	-8,2
230	VD12	7,8	-8,3	9,4	-8,0	9,2	-8,3
250	VD12	6,0	-7,7	8,2	-7,5	8,3	-7,4
270	VD12	7,3	-8,0	8,9	-8,6	9,0	-8,0

Table C.7: Enthalpy values of applied cycles for alloy VD13

Number of Cycles		First Cycle		Second Cycle		Third Cycle	
Temperature (°C)	Alloy	ΔH_{endo} (J/gr)	ΔH_{exo} (J/gr)	ΔH_{endo} (J/gr)	ΔH_{exo} (J/gr)	ΔH_{endo} (J/gr)	ΔH_{exo} (J/gr)
80	VD13	6,0	-6,7	7,5	-6,3	7,5	-6,4
100	VD13	6,1	-7,7	8,4	-7,6	8,0	-6,8
120	VD13	4,1	-5,5	6,1	-5,1	6,1	-4,9
150	VD13	7,1	-7,9	8,8	-8,6	8,7	-7,9
200	VD13	7,6	-7,9	8,7	-7,8	8,7	-7,8
230	VD13	7,1	-7,8	8,6	-7,4	8,4	-6,8
250	VD13	5,1	-5,1	6,4	-4,8	5,7	-4,5
270	VD13	5,6	-7,0	7,8	-6,5	7,5	-6,0

RESULTS OF THREE THERMAL CYCLES APPLIED TO CuAlNiMn ALLOYS PRIOR TO AGEING

Table D.1: Three thermal cycles applied to alloys VD11, VD12 and VD13 before ageing at 80°C

Alloy	Cycle	A_s	A_f	ΔH_{endo}	M_s	M_f	ΔH_{exo}
VD11	1	139	156	7.6	155	139	-7.7
	2	153	171	9.0	155	142	-8,0
	3	155	173	9,0	158	144	-8.2
VD12	1	125	147	6.1	142	127	-7.4
	2	142	162	8.5	141	128	-7.4
	3	142	163	8.3	143	128	-7.2
VD13	1	169	188	6.0	179	163	-6.7
	2	182	200	7.5	180	166	-6.3
	3	184	204	7.5	182	168	-6.4

Table D.3: Three thermal cycles applied to alloys VD11, VD12 and VD13 before ageing at 120°C

Alloy	Cycle	A_s	A_f	ΔH_{endo}	M_s	M_f	ΔH_{exo}
VD11	1	129	147	6.2	155	139	-5.2
	2	150	170	8.9	154	141	-5.7
	3	152	172	9.1	160	140	-7.5
VD12	1	134	154	7.7	148	133	-8.1
	2	145	164	9.1	151	133	-8.1
	3	145	165	8.9	149	134	-8.3
VD13	1	170	186	4.1	171	155	-5.5
	2	171	187	6.1	172	158	-5.1
	3	174	189	6.1	172	159	-4.9

Table D.2: Thermal cycles applied to alloys VD11, VD12 and VD13 before ageing at 100°C

Alloy	Cycle	A_s	A_f	ΔH_{endo}	M_s	M_f	ΔH_{exo}
VD11	1	68	94	5,0	139	116	-7.2
	2	130	147	8.2	143	130	-7.1
	3	133	158	8.3	144	133	-6.8
	4	136	160	8.3	145	133	-7.1
	5	137	162	8.5	148	125	-7.1
	6	139	163	8.4	147	137	-7.3
	7	140	165	8.5	148	133	-7.4
	8	141	166	8.4	150	129	-7.4
	9	143	167	8.5	149	138	-6.9
	10	144	168	8.6	150	139	-7.4
VD12	1	133	160	6.2	143	129	-6.8
	2	142	162	8.6	145	130	-6.9
	3	142	163	8.5	145	130	-7,0
	4	143	163	8.4	-	-	-
	4	143	164	8.7	145	130.85	-6.9
VD13	1	164	186	6.1	174	154	-7.7
	2	172	192	8.4	176	157	-7.6
	3	174	195	8.3	177	160	-7.0
	4	175	196	8.2	178	161	-6.8
	5	177	197	8.0	179	162	-6.8

Table D.4: Three thermal cycles applied to alloys VD11, VD12 and VD13 before ageing at 150°C

Alloy	Cycle	A_s	A_f	ΔH_{endo}	M_s	M_f	ΔH_{exo}
VD11	1	134	156	6.7	155	135	-7.0
	2	149	172	8.2	155	137	-7.2
	3	151	174	8.3	159	139	-7.4
VD12	1	131	153	7.5	153	132	-8.1
	2	145	167	9.1	151	133	-8.6
	3	145	168	8.9	148	133	-8.2
VD13	1	165	184	7.1	173	154	-7.9
	2	171	191	8.8	175	157	-8.6
	3	173	194	8.7	176	158	-7.9

Table D.5: Three thermal cycles applied to alloys VD11, VD12 and VD13 before ageing at 200°C

Alloy	Cycle	A_s	A_f	ΔH_{endo}	M_s	M_f	ΔH_{exo}
VD11	1	136	152	6,0	152	138	-7,1
	2	152	167	8,8	153	144	-6,8
	3	155	169	9,2	156	144	-7,6
VD12	1	143	162	7,9	157	140	-8,7
	2	155	177	9,4	161	141	-8,8
	3	154	177	9,4	158	143	-8,2
VD13	1	175	192	7,6	176	161	-7,9
	2	178	195	8,8	177	164	-7,4
	3	180	197	8,7	179	165	-7,8

Table D.6: Three thermal cycles applied to alloys VD11, VD12 and VD13 before ageing at 230°C

Alloy	Cycle	A_s	A_f	ΔH_{endo}	M_s	M_f	ΔH_{exo}
VD11	1	135	159	6,8	155	137	-6,9
	2	151	174	8,9	157	139	-5,6
	3	152	177	8,8	158	141	-5,6
VD12	1	137	156	7,8	153	137	-8,3
	2	148	169	9,4	151	136	-8,0
	3	149	170	9,2	152	137	-8,3
VD13	1	179	197	7,1	182	168	-7,8
	2	185	202	8,6	184	170	-7,4
	3	187	206	8,4	184	172	-6,8

Table D.7: Three thermal cycles applied to alloys VD11, VD12 and VD13 before ageing at 250°C

Alloy	Cycle	A_s	A_f	ΔH_{endo}	M_s	M_f	ΔH_{exo}
VD11	1	135	160	6,6	153	131	-6,8
	2	147	172	7,8	154	134	-7,1
	3	149	175	7,8	157	136	-6,7
	4	151	176	7,9	158	137	-6,8
	5	153	178	7,9	159	138	-6,7
VD12	1	131	153	6,0	144	129	-7,7
	2	142	160	8,2	145	129	-7,5
	3	142	160	8,5	145	130	-7,3
	4	142	161	8,4	146	130	-6,7
	5	143	162	8,3	146	131	-7,4
VD13	1	169	191	5,1	180	164	-5,1
	2	181	199	6,4	181	166	-4,8
	3	184	202	6,0	182	168	-4,7
	4	185	205	6,1	183	169	-4,7
	5	187	204	5,7	184	170	-4,5

Table D.8: Three thermal cycles applied to alloys VD11, VD12 and VD13 before ageing at 270°C

Alloy	Cycle	A_s	A_f	ΔH_{endo}	M_s	M_f	ΔH_{exo}
VD11	1	140	165	6,9	158	138	-7,5
	2	153	179	8,4	161	141	-7,1
	3	156	182	8,4	164	141	-7,3
VD12	1	129	150	7,3	147	128	-8,0
	2	140	161	8,9	148	129	-8,6
	3	141	162	9,0	148	130	-8,0
VD13	1	165	192	5,6	172	156	-7,0
	2	173	189	7,8	174	160	-6,5
	3	175	191	7,5	175	162	-6,1

APPENDIX E

RESULTS OF THREE THERMAL CYCLES APPLIED TO
CuAlNi ALLOYS PRIOR TO AGEING

Table E.1: Three thermal cycles applied to alloys V1, V2, V3 and V4 before ageing at 80°C

Alloy	Cycle	A_s	A_f	ΔH_{endo}	M_s	M_f	ΔH_{exo}
V1	1	222	257	10,6	220	207	-9,3
	2	222	238	11,2	222	210	-8,6
	3	226	241	11,1	224	211	-9,5
V2	1	92	108	7,8	101	90	-7,0
	2	104	120	7,9	103	92	-6,9
	3	107	122	7,8	105	93	-7,2
V3	1	120	142	8,1	126	107	-8,1
	2	122	142	8,9	129	111	-7,7
	3	125	146	9,1	131	113	-7,5
V4	1	158	178	9,3	161	148	-8,7
	2	161	180	10,2	161	151	-8,3
	3	164	181	10,2	163	152	-9,0

Table E.2: Three thermal cycles applied to alloys V1, V2, V3 and V4 before ageing at 100°C

Alloy	Cycle	A_s	A_f	ΔH_{endo}	M_s	M_f	ΔH_{exo}
V1	1	217	250	10,1	220	204	-8,9
	2	219	237	11,2	222	206	-9,3
	3	223	240	11,0	224	208	-9,4
V2	1	89	110	6,8	105	88	-5,7
	2	102	123	7,2	107	90	-5,8
	3	104	125	7,1	108	91	-6,3
V3	1	119	139	8,0	128	112	-7,2
	2	124	143	8,5	131	115	-7,2
	3	127	146	8,6	133	117	-6,7
V4	1	160	189	8,8	162	144	-8,2
	2	157	178	10,0	164	146	-8,0
	3	159	179	9,9	165	148	-8,0

Table E.3: Three thermal cycles applied to alloys V1, V2, V3 and V4 before ageing at 120°C

Alloy	Cycle	A_s	A_f	ΔH_{endo}	M_s	M_f	ΔH_{exo}
V1	1	225	262	10,5	221	207	-8,9
	2	222	236	11,0	223	210	-8,7
	3	225	239	11,2	225	212	-8,4
V2	1	92	105	6,7	101	89	-6,0
	2	101	116	7,2	103	91	-6,3
	3	104	118	7,1	105	93	-6,2
V3	1	117	138	7,7	127	107	-8,5
	2	121	142	8,3	130	112	-6,4
	3	124	145	8,4	132	114	-7,4
V4	1	160	178	9,2	167	149	-8,4
	2	162	181	9,9	168	152	-8,6
	3	164	182	9,9	169	153	-8,3

Table E.4: Three thermal cycles applied to alloys V1, V2, V3 and V4 before ageing at 150°C

Alloy	Cycle	A_s	A_f	ΔH_{endo}	M_s	M_f	ΔH_{exo}
V1	1	221	254	9,8	222	208	-9,1
	2	224	238	10,8	224	211	-8,9
	3	227	240	10,9	226	212	-8,9
V2	1	92	107	7,5	102	90	-6,1
	2	103	118	7,6	104	91	-7,2
	3	106	120	7,5	105	93	-6,7
V3	1	122	139	7,6	124	110	-8,3
	2	124	139	8,0	127	113	-6,8
	3	127	142	8,3	128	116	-6,4
V4	1	160	179	8,4	166	149	-7,8
	2	162	179	9,9	168	151	-8,4
	3	164	181	9,8	168	152	-8,1

Table E.5: Three thermal cycles applied to alloys V1, V2, V3 and V4 before ageing at 200°C

Alloy	Cycle	A_s	A_f	ΔH_{endo}	M_s	M_f	ΔH_{exo}
V1	1	222	268	10,3	222	205	-8,9
	2	221	237	11,0	225	208	-8,8
	3	224	240	11,1	227	210	-9,4
V2	1	85	102	7,5	102	88	-5,6
	2	100	116	7,8	104	90	-5,8
	3	102	118	7,7	106	92	-5,8
V3	1	117	138	7,8	126	105	-9,3
	2	120	141	8,4	128	109	-8,3
	3	124	144	8,6	130	111	-7,9
V4	1	164	181	8,6	165	150	-8,0
	2	162	179	9,6	167	152	-7,9
	3	163	180	9,8	168	153	-8,1

Table E.6: Three thermal cycles applied to alloys V1, V2, V3 and V4 before ageing at 230°C

Alloy	Cycle	A_s	A_f	ΔH_{endo}	M_s	M_f	ΔH_{exo}
V1	1	218	249	9,0	221	205	-8,3
	2	222	237	10,2	223	209	-7,9
	3	225	239	10,1	225	210	-8,4
V2	1	99	113	6,4	107	95	-6,3
	2	110	124	7,1	109	96	-6,7
	3	112	125	7,0	111	98	-6,1
V3	1	123	140	7,5	130	115	-6,9
	2	128	145	8,2	134	118	-6,5
	3	131	148	8,1	136	120	-6,8
V4	1	160	180	8,9	169	151	-7,7
	2	164	183	9,3	170	152	-8,0
	3	166	184	9,3	171	154	-8,1

Table E.7: Three thermal cycles applied to alloys V1, V2, V3 and V4 before ageing at 250°C

Alloy	Cycle	A_s	A_f	ΔH_{endo}	M_s	M_f	ΔH_{exo}
V1	1	217	253	8,2	219	203	-7,9
	2	220	236	10,5	222	207	-7,6
	3	223	239	10,3	224	209	-7,7
V2	1	102	121	6,7	115	100	-7,2
	2	114	133	7,4	119	102	-7,2
	3	116	134	7,4	120	103	-7,0
V3	1	120	140	7,9	130	113	-6,9
	2	126	145	8,5	133	116	-7,0
	3	129	149	8,4	135	118	-6,9
V4	1	158	180	7,8	166	148	-8,1
	2	162	183	8,9	169	151	-7,4
	3	164	184	8,4	169	153	-7,2

Table E.8: Three thermalcycles applied to alloys V1, V2, V3 and V4 before ageing at 270°C

Alloy	Cycle	A_s	A_f	ΔH_{endo}	M_s	M_f	ΔH_{exo}
V1	1	222	262	9,0	221	205	-8,5
	2	222	238	10,4	223	208	-7,9
	3	225	240	10,2	225	210	-8,3
V2	1	98	117	7,1	114	97	-7,2
	2	112	131	7,4	114	99	-6,0
	3	114	132	7,6	116	100	-6,4
V3	1	118	138	7,8	127	109	-7,0
	2	124	142	8,2	129	113	-6,6
	3	127	145	8,3	131	115	-6,3
V4	1	156	177	8,3	164	149	-7,5
	2	162	181	9,2	167	150	-7,7
	3	164	182	9,0	168	152	-7,2

X-RAY DIFFRACTION ANGLES AND DIFFRACTOGRAMS OF CuAlNiMn AND CuAlNi ALLOYS

The measured Diffraction Angles of three CuAlNiMn alloys and their corresponding X-ray Diffractogrammes are seen in Table F.1 and Figure F.1, respectively.

Table F.1: The measured Diffraction Angles of three CuAlNiMn alloys.

$2\theta_{calculated}$	2H	$18R_1$	$2\theta_{measured}$ VD11	$2\theta_{measured}$ VD12	$2\theta_{measured}$ VD13
30.7	(110)		30.5	30.5	
31.4	(011)			31.4	
45.5	(120)				45.8
47.2		(127)	47.2	47.8	47.3
49.9		(0018)	49.9	49.9	49.6
51.3		(204)			51.2
52.7	(121)		52.6	52.9	52.7
53		(1211)	52.9		
53.5		(1017)	54	53.9	53.6
54.9		(208)		54.8	55.5
56.7	(201)		56.6		
65.3		(1217)	65.5		
67.7		(1218)			67.8
84.6		(013)	84.9	84.8	84.5
93.8		(0418)/(329)			93.8
94		(242)		94.1	
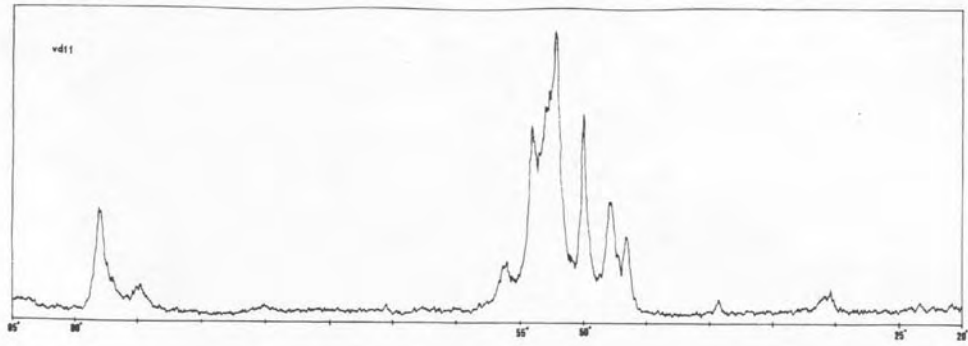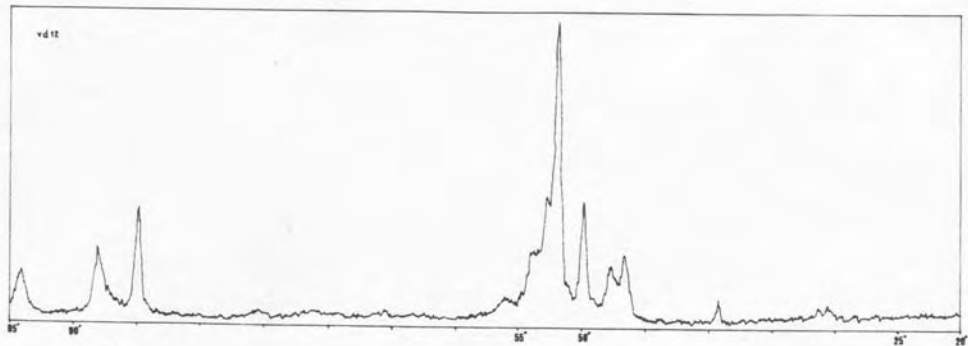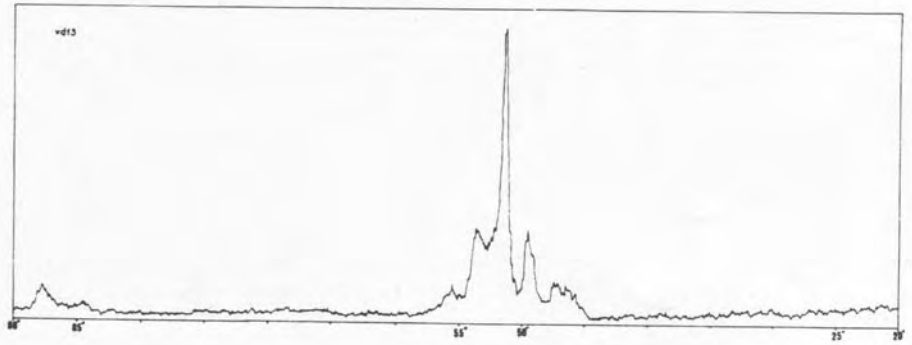
Figure F.1: X-ray diffractogrammes of three CuAlNiMn alloys;
a) Cu-12. 6%Al-5.9%Ni-1.8%Mn, b)Cu-12.6%Al-4.8%Ni-1.1%Mn,
c) Cu-12.9%Al-5.0%Ni-2.2%Mn .

194

The measured Diffraction Angles of three CuAlNiMn alloys and their corresponding X-ray Diffractogrammes are given in Table F.2 and Figure F.2, respectively.

Table F.2: The measured Diffraction Angles of four CuAlNi alloys.

$2\theta_{calculated}$	2H	$18R_1$	$2\theta_{measured}$ V1	$2\theta_{measured}$ V2	$2\theta_{measured}$ V3	$2\theta_{measured}$ V4
25.2	(001)				25.4	
30.7	(110)		30.2	30.6	30.7	30.6
31.4	(011)		31.2	31.4	31.3	31.4
40.1	(111)			39.3	39.4	
45.5	(120)		45.8			
47.2		(127)		47.5	47.2	47.5
49.9		(0018)	49.7			
50.0	(200)					50
50.2		(202)		50.1	50.2	
52.7	(121)		52.8	52.5	52.2	52.2
53		(1211)			53	
53.5		(1017)	53.5			
54.9		(208)				54.2
56.7	(201)			56.4	56.2	
65.3		(1217)	65.2	65.3		
70.3	(221)	(1219)	70.2		70.8	
75.9		(0318)		75.8		
84.6		(013)		84.6	84.8	
94		(242)	94			
94.8		(244)		94.4		
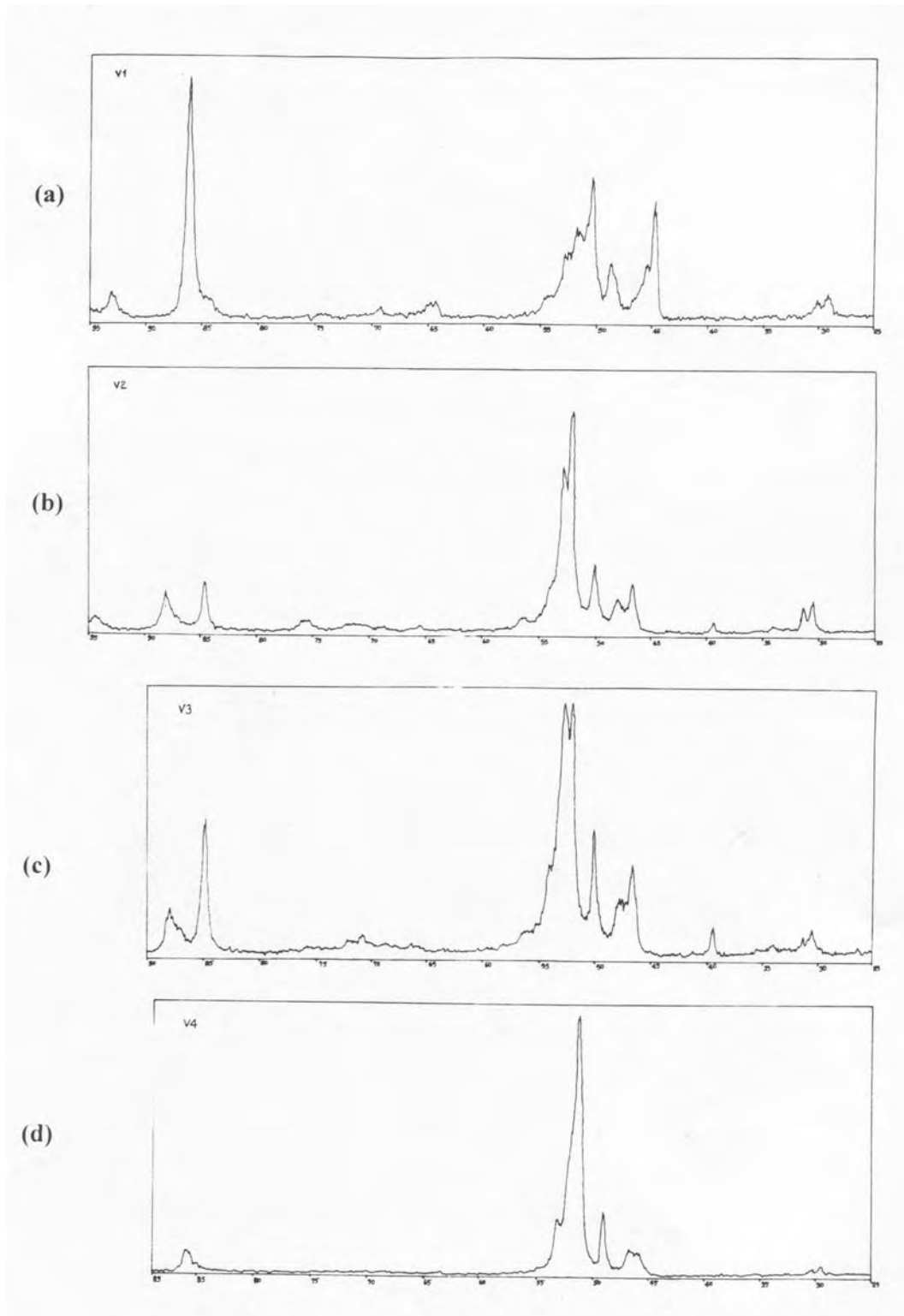
Figure F.2: X-ray diffractogrammes of four CuAlNi alloys;
a) Cu-14.0%Al-2.5%Ni, b) Cu-13.9%Al-4.2%Ni, c) Cu-14.2%Al-2.7%Ni,
d) Cu-13.6%Al-3.0%Ni.

APPENDIX G

TRANSFORMATION TEMPERATURES OF
CuAlNiMn ALLOYS AFTER MARTENSITE AGEING

Table G.1: Alloy VD11 after ageing at 80°C.

80°C,VD11	A_s	A_f	ΔH_{endo}	M_s	M_f	ΔH_{exo}
0 hour	155	173	9,0	158	144	-8,2
24 hour	157	175	8,7	159	144	-7,5
72 hour	159	178	7,9	159	144	-6,7
144 hour	160	179	8,4	160	146	-7,8
312 hour	162	180	8,6	161	147	-6,9

Table G.2: Alloy VD12 after ageing at 80°C.

80°C,VD12	A_s	A_f	ΔH_{endo}	M_s	M_f	ΔH_{exo}
0 hour	142	163	8,3	143	128	-7,2
24 hour	142	163	8,6	144	129	-7,5
72 hour	143	164	7,7	144	129	-7,4
144 hour	143	163	8,7	144	131	-8,0
312 hour	145	164	8,4	144	131	-7,3

Table G.3: Alloy VD13 after ageing at 80°C.

80°C,VD13	A_s	A_f	ΔH_{endo}	M_s	M_f	ΔH_{exo}
0 hour	184	204	7,5	182	168	-6,4
24 hour	186	204	7,9	183	170	-6,9
72 hour	187	207	7,4	184	169	-5,9
144 hour	188	208	8,3	184	170	-6,8
312 hour	189	208	8,0	185	171	-6,2

Table G.4: Alloy VD11 after ageing at 100°C.

100°C,VD11	A_s	A_f	ΔH_{endo}	M_s	M_f	ΔH_{exo}
0 hour	144	168	8,6	150	139	-7,4
24 hour	146	169	8,6	146	137	-6,8
72 hour	147	170	8,8	152	141	-7,1
144 hour	148	171	8,9	154	137	-7,3
312 hour	150	172	8,8	154	143	-7,5

Table G.5: Alloy VD12 after ageing at 100°C.

100°C,VD12	A_s	A_f	ΔH_{endo}	M_s	M_f	ΔH_{exo}
0 hour	143	164	8,7	145	130	-6,9
24 hour	144	164	8,8	146	131	-7,6
72 hour	144	165	9,0	146	132	-8,1
144 hour	145	164	9,1	146	134	-6,6
312 hour	146	166	8,8	148	133	-7,1

Tablo G.6: Alloy VD13 after ageing at 100°C.

100°C,VD13	A_s	A_f	ΔH_{endo}	M_s	M_f	ΔH_{exo}
0 hour	177	197	8,0	179	162	-6,8
24 hour	178	199	8,4	179	164	-6,3
72 hour	180	201	7,9	180	165	-6,5
144 hour	181	199	8,0	180	165	-6,1
312 hour	183	203	8,1	180	165	-6,5

Table G.7: Alloy VD11 after ageing at 120°C.

120°C,VD11	A_s	A_f	ΔH_{endo}	M_s	M_f	ΔH_{exo}
0 hour	152	172	9,1	160	140	-7,5
24 hour	157	179	9,3	157	145	-7,0
72 hour	160	182	9,5	158	143	-6,4
144 hour	163	185	9,6	161	144	-7,1
312 hour	163	188	8,7	160	145	-7,6

Table G.8: Alloy VD12 after ageing at 120°C.

120°C,VD12	A_s	A_f	ΔH_{endo}	M_s	M_f	ΔH_{exo}
0 hour	145	165	8,9	149	134	-8,3
24 hour	148	169	9,5	149	135	-7,8
72 hour	149	170	9,4	150	136	-8,1
144 hour	151	172	9,7	151	137	-7,8
312 hour	153	174	8,6	151	136	-8,1

Table G.9: Alloy VD13 after ageing at 120°C.

120°C,VD13	A_s	A_f	ΔH_{endo}	M_s	M_f	ΔH_{exo}
0 hour	174	189	6,1	172	159	-4,9
24 hour	177	193	5,8	173	160	-4,9
72 hour	181	195	5,7	174	160	-4,7
144 hour	183	199	5,9	174	160	-4,4
312 hour	186	201	6,1	175	160	-3,3

Table G.10: Alloy VD11 after ageing at 150°C.

150°C,VD11	A_s	A_f	ΔH_{endo}	M_s	M_f	ΔH_{exo}
0 hour	151	174	8,3	159	139	-7,4
24 hour	179	196	7,9	159	140	-7,2
72 hour	186	203	8,2	160	141	-7,2
144 hour	190	207	8,0	162	143	-6,8
312 hour	194	214	8,7	162	144	-7,0

Table G.11: Alloy VD12 after ageing at 150°C.

150°C,VD12	A_s	A_f	ΔH_{endo}	M_s	M_f	ΔH_{exo}
0 hour	145	168	8,9	148	133	-8,2
24 hour	170	180		152	135	-8,5
72 hour	170	180		149	137	-8,5
144 hour	171	189	8,6	150	137	-8,5
312 hour	174	192	9,1	154	138	-8,1

Table G.12: Alloy VD13 after ageing at 150°C.

150°C,VD13	A_s	A_f	ΔH_{endo}	M_s	M_f	ΔH_{exo}
0 hour	173	194	8,8	176	158	-7,9
24 hour	195	216	9,3	178	160	-7,6
72 hour	204	-	9,0	178	161	-7,8
144 hour	210	-	7,9	180	162	-7,5
312 hour	220	-	1,3	180	163	-6,5

APPENDIX H

TRANSFORMATION TEMPERATURES OF CuAlNiMn ALLOYS AFTER AGEING AT ROOM TEMPERATURE

Transformation Temperatures of CuAlNiMn alloys after ageing at Room Temperature for ageing times of 168, 336, 672, 2016 and 4032 hours, for the applied two thermal cycles.

Table H.1: VD11 alloy after ageing at RT

RT-VD11	hours	No.of cycles	A_s	A_f	ΔH_{endo}	M_s	M_f	ΔH_{exo}
1 week	168	Cyc1	132	152	6,1	150	133	-7,4
		Cyc2	148	170	8,2	153	136	-7,1
2 week	336	Cyc1	130	149	5,4	150	133	-6,6
		Cyc2	149	168	7,7	153	136	-6,9
1 month	672	Cyc1	134	147	6,8	154	140	-7,3
		Cyc2	152	170	8,8	156	142	-7,3
3 months	2016	Cyc1	137	153	6,7	153	133	-7,8
		Cyc2	146	172	8,9	156	135	-8,5
6 months	4032	Cyc1	136	166	7,2	161	139	-6,9
		Cyc2	155	179	8,9	161	142	-7,0

Table H.2: VD12 alloy after ageing at RT

RT-VD12	hours	No.of cycles	A_s	A_f	ΔH_{endo}	M_s	M_f	ΔH_{exo}
1 week	168	Cyc1	151	178	7,4	168	145	-7,6
		Cyc2	159	172	8,4	170	146	-7,7
2 week	336	Cyc1	139	168	7,9	157	133	-8,6
		Cyc2	149	176	8,8	157	134	-7,8
1 month	672	Cyc1	138	160	8,4	147	134	-7,7
		Cyc2	146	167	9,0	148	134	-8,1
3 months	2016	Cyc1	150	170	8,5	160	143	-8,2
		Cyc2	155	175	9,2	160	144	-7,4
6 months	4032	Cyc1	142	170	8,4	154	136	-8,1
		Cyc2	150	178	9,3	165	137	-7,3

Table H.3: VD13 alloy after ageing at RT

RT-VD13	hours	No.of cycles	A_s	A_f	ΔH_{endo}	M_s	M_f	ΔH_{exo}
1 week	168	Cyc1	177	200	5,8	187	167	-5,6
		Cyc2	185	212	6,7	188	167	-5,9
2 week	336	Cyc1	169	194	5,2	173	153	-5,8
		Cyc2	172	189	6,4	174	158	-5,6
1 month	672	Cyc1	165	198	5,7	176	157	-6,5
		Cyc2	175	192	7,2	176	161	-6,1
6 months	4032	Cyc1	177	198	6,4	182	168	-5,3
		Cyc2	187	205	6,9	185	170	-5,6

TRANSFORMATION TEMPERATURES OF CuAlNi ALLOYS
AFTER MARTENSITE AGEING

Transformation Temperatures of CuAlNi Alloys after ageing at 80°C and 100°C.

Table J.1: V1 alloy after ageing at 80°C

80 V1	A_s	A_f	ΔH_{endo}	M_s	M_f	ΔH_{exo}
0	226	241	11,1	224	211	-9,5
24	226	242	-	226	211	-8,4
72	228	243	10,9	226	212	-8,2
144	230	245	11,2	227	213	-8,7
312	232	246	11,1	229	214	-8,6

Table J.2: V2 alloy after ageing at 80°C

80 V2	A_s	A_f	ΔH_{endo}	M_s	M_f	ΔH_{exo}
0	107	122	7,8	105	93	-7,2
24	109	124	7,9	106	94	-6,9
72	110	125	7,8	107	96	-6,3
144	111	125	7,9	108	96	-7,2
312	113	127	7,7	109	97	-6,7

Table J.3: V3 alloy after ageing at 80°C

80 V3	A_s	A_f	ΔH_{endo}	M_s	M_f	ΔH_{exo}
0	125	146	9,0	131	113	-7,5
24	128	148	9,1	132	115	-7,4
72	130	150	8,9	134	116	-6,9
144	131	151	8,9	135	118	-7,3
312	133	152	9,0	137	120	-7,3

Table J.4: V4 alloy after ageing at 80°C

80 V4	A_s	A_f	ΔH_{endo}	M_s	M_f	ΔH_{exo}
0	164	181	10,2	163	152	-8,9
24	165	183	9,8	167	154	-7,7
72	166	184	9,5	166	153	-7,8
144	167	184	9,6	167	155	-7,4
312	168	183	9,5	166	156	-7,9

Table J.5: V1 alloy after ageing at 100°C

100 V1	A_s	A_f	ΔH_{endo}	M_s	M_f	ΔH_{exo}
0	223	240	11,0	224	208	-9,3
24	224	241	-	225	209	-8,3
72	225	242	10,7	225	210	-8,7
144	227	245	10,7	227	211	-9,0
312	229	246	10,8	228	212	-8,3

Table J.6: V2 alloy after ageing at 100°C

100 V2	A_s	A_f	ΔH_{endo}	M_s	M_f	ΔH_{exo}
0	104	125	7,1	108	91	-6,3
24	107	127	6,9	110	92	-7,3
72	108	128	7,1	110	94	-6,2
144	109	129	7,2	111	94	-6,7
312	111	131	7,1	112	96	-5,3

Table J.7: V3 alloy after ageing at 100°C

100 V3	A_s	A_f	ΔH_{endo}	M_s	M_f	ΔH_{exo}
0	127	146	8,6	133	117	-6,7
24	131	149	8,6	135	118	-7,3
72	132	151	8,9	136	120	-6,9
144	134	153	8,6	137	122	-7,0
312	135	154	8,9	139	123	-6,8

Table J.8: V4 alloy after ageing at 100°C

100 V4	A_s	A_f	ΔH_{endo}	M_s	M_f	ΔH_{exo}
0	159	179	9,8	165	148	-7,9
24	161	180	9,7	165	150	-7,3
72	163	182	9,0	167	150	-6,4
144	164	182	9,2	167	150	-7,9
312	167	183	8,9	168	150	-7,8

TRANSFORMATION TEMPERATURES OF CuAlNi ALLOYS
AFTER AGEING AT ROOM TEMPERATURE

Transformation Temperatures of CuAlNi alloys after ageing at Room Temperature
for ageing times of 168, 336 and 672 hours.

Table K.1: V1 alloy after ageing at RT

RT-V1	hours	Cycles	A_s	A_f	ΔH_{endo}	M_s	M_f	ΔH_{exo}
1 week	168	1	220	253	9,5	219	203	-8,7
		2	221	239	10,8	222	206	-8,2
2 week	336	1	221	241	10,4	221	205	-8,7
		2	221	237	10,8	221	209	-8,3
1 month	672	1	222	249	9,9	222	206	-8,7
		2	223	238	10,7	225	209	-9,0

Table K.2: V2 alloy after ageing at RT

RT-V2	hours	Cycles	A_s	A_f	ΔH_{endo}	M_s	M_f	ΔH_{exo}
1 week	168	1	99	119	7,0	113	97	-6,3
		2	112	131	7,2	113	99	-5,3
2 week	336	1	97	114	7,2	110	95	-6,7
		2	110	128	7,9	111	96	-7,2
1 month	672	1	101	116	7,3	114	99	-7,4
		2	115	130	7,7	115	101	-6,4

Table K.3: V3 alloy after ageing at RT

RT-V3	hours	Cycles	A_s	A_f	ΔH_{endo}	M_s	M_f	ΔH_{exo}
1 week	168	1	122	142	7,4692	128	113	-5,6641
		2	127	147	7,7307	132	116	-6,744
2 week	336	1	121	139	7,9511	130	114	-6,5195
		2	127	146	8,2588	133	117	-6,976
1 month	672	1	117	136	8,0657	128	110	-7,0541
		2	123	143	8,5255	129	114	-6,6161

Table K.4: V4 alloy after ageing at RT

RT-V4	hours	Cycles	A_s	A_f	ΔH_{endo}	M_s	M_f	ΔH_{exo}
1 week	168	1	160	184	8,9	171	151	-8,1
		2	166	187	9,5	173	153	-7,6
2 week	336	1	161	182	8,5	167	149	-7,8
		2	162	183	9,4	170	151	-7,7
1 month	672	1	159	179	9,1	166	149	-8,4
		2	162	182	9,6	165	151	-7,9

APPENDIX L

TRANSFORMATION TEMPERATURES OF CuAlNiMn ALLOYS AFTER BETA PHASE AGEING

Transformation temperatures of CuAlNiMn alloys after ageing at Beta ageing temperatures of 200°C, 230°C, 250°C and 270°C.

Table L.1: VD11 alloy after ageing at 200°C

200°C,VD11	A_s	A_f	ΔH_{endo}	M_s	M_f	ΔH_{exo}
0 hour	155	169	9,2	156	144	-7,5
1hour	156	171	8,8	158	146	-6,8
3 hour	159	-	8,9	158	151	-6,5
6 hour	162	-	8,8	160	152	-6,8
11 hour	164	-	8,3	160	149	-7,0
18 hour	145	173	5,8	157	115	-3,5
26 hour	117	168		No transf.		

Table L.2: VD12 alloy after ageing at 200°C

200°C,vd12	A_s	A_f	ΔH_{endo}	M_s	M_f	ΔH_{exo}
0 hour	154	177	9,4	158	143	-8,1
1 hour	156	-	6,0	160	144	-7,9
4 hour	157	-	4,9	161	145	-8,1
9 hour	158	179	7,9	172	148	-6,7
16 hour	161	183	7,6	164	149	-6,5
26 hour	164	177	5,9	161	147	-3,7
38 hour	151	175		No Transf.		

Table L.3: VD13 alloy after ageing at 200°C

200°C,vd13	A_s	A_f	ΔH_{endo}	M_s	M_f	ΔH_{exo}
0 hour	180	197	8,7	179	165	7,8
1 hour	166	-	-	181	165	-5,8
3 hour	167	-	-	180	163	-3,3
6 hour	164	-		178	148	-1,1
11 hour	134	187	1,0	NO TRANSF.		

Table L.4: VD11 alloy after ageing at 230°C

230°C,vd11	A_s	A_f	ΔH_{endo}	M_s	M_f	ΔH_{exo}
0 hour	152	177	8,7	158	141	-5,6
0,25 hour	154	178	8,8	161	145	-8,0
0,75 hour	158	181	8,9	164	149	-8,0
1,75 hour	162	185	8,7	166	152	-7,6
3,75 hour	168	189	8,6	162	127	-5,4
6,75 hour	167	185		No Transf.		

Table L.5: VD12 alloy after ageing at 230°C

230°C,vd12	A_s	A_f	ΔH_{endo}	M_s	M_f	ΔH_{exo}
0 hour	149	170	9,2	152	137	-8,3
0,5 hour	149	170	9,2	155	140	-7,6
1,5 hour	152	172	9,3	156	143	-8,0
3,5 hour	156	175	9,2	160	148	-8,1
8,5 hour	162	181	9,1	164	154	-6,8

Table L.6: VD13 alloy after ageing at 230°C

230°C,vd13	A_s	A_f	ΔH_{endo}	M_s	M_f	ΔH_{exo}
0 hour	187	206	8,4	184	172	-6,8
0,25 hour	189	-	7,2	186	174	-6,9
0,5 hour	192	-	5,6	187	173	-5,8
1 hour	196	-	4,8	185	163	-0,8

Table L.7: VD11 alloy after ageing at 250°C

250°C,vd11	A_s	A_f	ΔH_{endo}	M_s	M_f	ΔH_{exo}
0 hour	153	178	7,9	159	138	-6,7
0,25 hour	154	178	7,7	163	144	-6,9
0,75 hour	161	184	7,7	167	149	-6,9
1,75 hour	167	189	7,7	162	126	-4,2

Table L.8: VD12 alloy after ageing at 250°C

250°C,vd12	A_s	A_f	ΔH_{endo}	M_s	M_f	ΔH_{exo}
0 hour	143	162	8,3	146	131	-7,3
0,25 hour	143	162	8,0	149	136	-7,1
0,75 hour	147	166	8,1	155	141	-7,4
1,75 hour	154	171	8,3	160	147	-6,9
4,75 hour	162	179	8,4	165	155	-5,4

Table L.9: VD13 alloy after ageing at 250°C

250°C,vd13	A_s	A_f	ΔH_{endo}	M_s	M_f	ΔH_{exo}
0 hour	187	204	5,6	184	170	-4,5
0,25 hour	188	206	5,7	185	173	-3,2
0,75 hour	194	211	4,8	186	169	-0,4

Table L.10: VD11 alloy after ageing at 270°C

270°C,vd11	A_s	A_f	ΔH_{endo}	M_s	M_f	ΔH_{exo}
0 hour	156	182	8,3	164	141	-7,3
0,17hour	156	182	8,9	173	154	-7,6
0,5hour	174	196	8,7	174	155	-4,9
1hour	183	199	7,7	No transf.		

Table L.11: VD12 alloy after ageing at 270°C

270°C,vd12	A_s	A_f	ΔH_{endo}	M_s	M_f	ΔH_{exo}
0 hour	141	162	8,9	148	130	-7,9
0,08 hour	141	162	8,9	155	137	-8,3
0,25hour	149	169	9,0	160	143	-7,6
0,58hour	156	176	8,6	166	149	-7,9
1,08hour	164	183	9,0	170	155	-7,6
1,74hour	171	189	8,8	172	160	-7,1
2,57hour	178	193	8,5	169	158	-6,1
3,57hour	181	191		No transf.		

Table L.12: VD13 alloy after ageing at 270°C

270°C,vd13	A_s	A_f	ΔH_{endo}	M_s	M_f	ΔH_{exo}
0 hour	175	191	7,5	175	162	-6,0
0,08 hour	176	193	7,4	181	169	-5,7
0,25hour	187	203	6,6	186	170	-3,2
0,58hour	195	211		No transf.		

APPENDIX M

TRANSFORMATION TEMPERATURES OF CuAlNi ALLOYS AFTER BETA PHASE AGEING

Transformation Temperatures of CuAlNi Alloys after ageing at Beta Phase ageing temperature of 200°C for the ageing periods (minutes) given in the left column.

Table M.1: V1 alloy after ageing at 200°C

200,V1	A_s	A_f	ΔH_{endo}	M_s	M_f	ΔH_{exo}
0	224	240	11,1	227	210	-9,4
15	228	244	9,9	229	211	-8,8
45	230	246	10,9	228	212	-8,8
105	232	248	11,3	230	214	-8,0
345	236	252	10,1	231	215	-8,2
765	239	255	11,4	232	215	-8,0
1485	241	257	11,7	233	216	-8,7
5805	247	263	11,8	234	218	-8,4

Table M.2: V2 alloy after ageing at 200°C

200,V2	A_s	A_f	ΔH_{endo}	M_s	M_f	ΔH_{exo}
0	102	118	7,7	106	92	-5,8
15	104	120	7,6	107	91	-7,6
45	105	120	7,8	105	92	-6,5
105	105	121	7,8	106	93	-6,6
345	109	126	7,7	111	96	-7,1
765	114	131	8,1	112	98	-7,5
1485	119	137	7,9	117	102	-7,5
2925	124	143	7,7	121	108	-8,6
5805	133	152	8,1	128	115	-7,8

Table M.3: V3 alloy after ageing at 200°C

200,V3	A_s	A_f	ΔH_{endo}	M_s	M_f	ΔH_{exo}
0	124	144	8,6	130	111	-7,9
15	126	147	8,7	131	111	-8,6
45	126	147	8,7	129	112	-8,0
105	127	148	8,7	133	113	-9,1
405	135	157	9,0	141	121	-8,7
825	139	161	8,8	144	124	-8,5
1545	143	163	8,9	146	128	-7,6
5805	153	174	9,5	154	137	-7,6

Table M.4: V4 alloy after ageing at 200°C

200,V4	A_s	A_f	ΔH_{endo}	M_s	M_f	ΔH_{exo}
0	163	180	9,8	168	153	-8,1
15	165	-	8,7	169	152	-8,4
45	166	-	8,1	169	153	-8,3
105	165	-	8,5	169	153	-7,9
525	166	183	9,6	172	158	-8,1
1245	172	188	9,6	175	161	-7,9
5805	185	200	9,3	184	171	-6,9

VITA

Elif Tarhan was born in Ankara on January 16, 1971. She graduated from Metallurgical and Materials Engineering Department of Middle East Technical University, Ankara, Turkey in 1993. She received her Master of Science degree in the same department in 1996. She has been working as a research assistant in the Department since 1993. Since 1995 she has been in charge of the Transmission Electron Microscopy Laboratory of the Department. She is a member of the Chamber of Metallurgical Engineers. Her main research interest is the phase transformations in metallic systems and copper based shape memory alloys.

PUBLICATIONS

1. Elif Tarhan ve Şakir Bor, CuAlNiMn Alaşımlarında Kritik Dönüşüm Sıcaklıklarının DSC Yöntemiyle Belirlenmesi ve Isıl Döngü Etkileri, 11. Metalurji Kongresi, Haziran 2002, Bildiriler E-Kitabı, sayfa: 367.

2. Nurcan Artunç, Neşe Elgün, Alexy Vizir, Ian Brown, Şakir Bor, Elif Tarhan, Electrical and Structural Properties of Cr ion-implanted thin Au films, Materials Chemistry and Physics, 1999, 60, page:182.

3. Elif Tarhan ve Şakir Bor, Karmaşık Kristal Yapıların Geçirmeli Elektron Mikroskobunda Bilgisayar Yardımı ile Çözümlenmesi, Metalurji Dergisi, 1997, 111, sayfa: 40.

4. Elif Tarhan ve Şakir Bor, Bakır Esaslı Şekil Bellekli Alaşımlarda Mikroyapı İncelemeleri, 9. Metalurji Kongresi, Haziran 1997, Kongre Bildiri Kitabı, sayfa:1361

5. Gamze Saranlı, Yusuf Karabay, Elif Tarhan, Şakir Bor, Cu-Zn-Al Şekil Bellekli Alaşımların Üretim ve Karakterizasyonu, 9. Metalurji Kongresi, Haziran 1997, Kongre Bildiri Kitabı, sayfa:1293

6. Elif Tarhan ve Şakir Bor, Chrystallography of Cu-Based Shape Memory Alloys, 13. Ulusal Elektron Mikroskobi Kongresi, Eylül 1997, Kongre Bildiri Kitabı, sayfa:670

7. Elif Tarhan ve Şakir Bor, Structure and Morphology of Stress Induced Long Period Ordered Martensitic Structures, 12. Ulusal Elektron Mikroskobi Kongresi, Eylül 1995, Kongre Bildiri Kitabı, sayfa175.

8. Elif Tarhan ve Şakir Bor, Ordered Domain Structures in DO_3 Lattices, 12. Ulusal Elektron Mikroskobi Kongresi, Eylül 1995, Kongre Bildiri Kitabı, sayfa174.

9. Elif Tarhan ve Şakir Bor, Structure and Morphology of Thermally Induced Long Period Ordered Martensitic Structures, 12. Ulusal Elektron Mikroskobi Kongresi, Eylül 1995, Kongre Bildiri Kitabı, sayfa173.

10. Ş.Bor, T.Öztürk, A.Şahin, E.Tarhan ve Ö. Tekinli, Sıcak DaldırmaAlüminyum Kaplama Sırasında Oluşan Fe-Al Ara Fazları ve İç Yapıları, 7. Metalurji Kongresi, Mayıs 1993, Kongre Bildiri Kitabı, sayfa:1303.